EPS-meteograms
ENS-meteograms

EPS=Ensemble Prediction System

ENS=Ensemble (new name at ECMWF)

Oslo 17.01.2017 00utc ana + 0-10 d

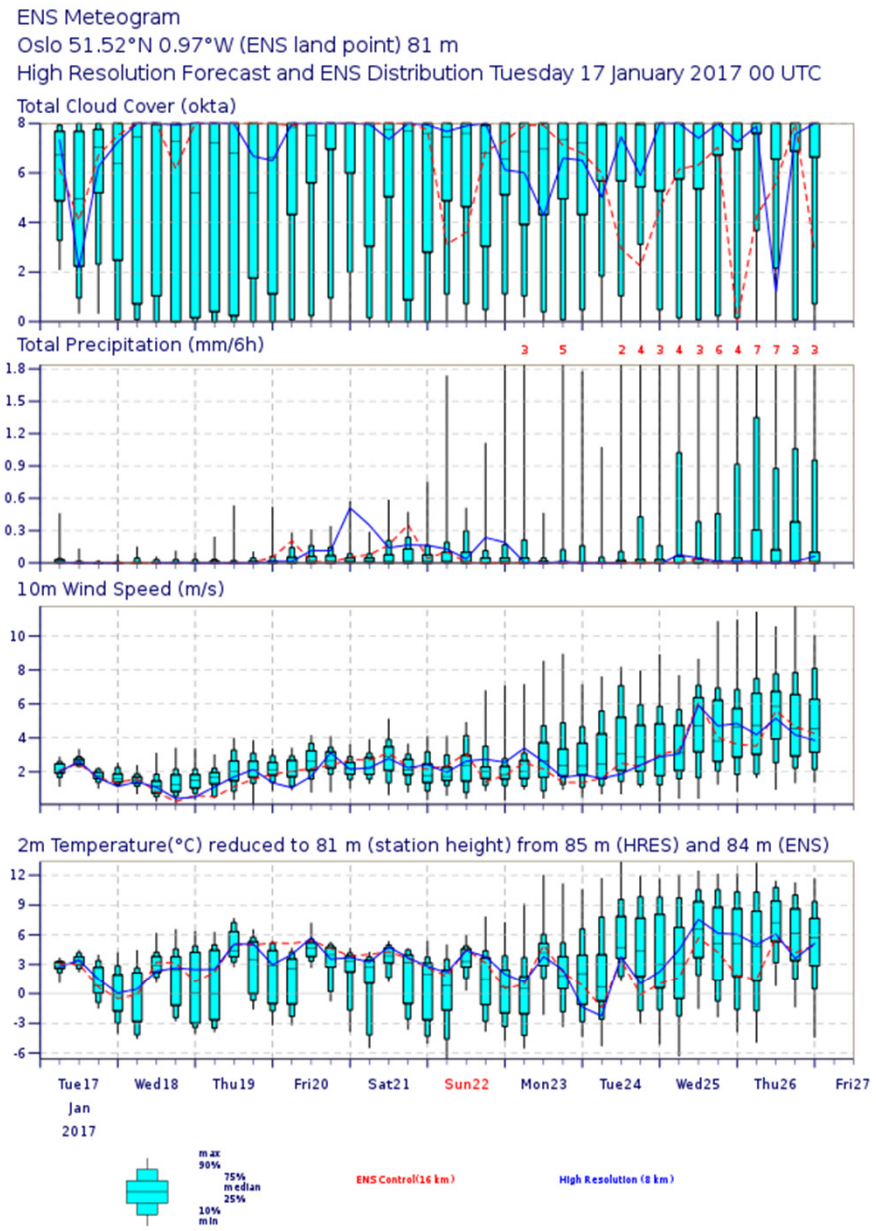

Oslo 17.01.2017 00utc ana + 0-15 d

Røst 17.01.2016 00utc ana +

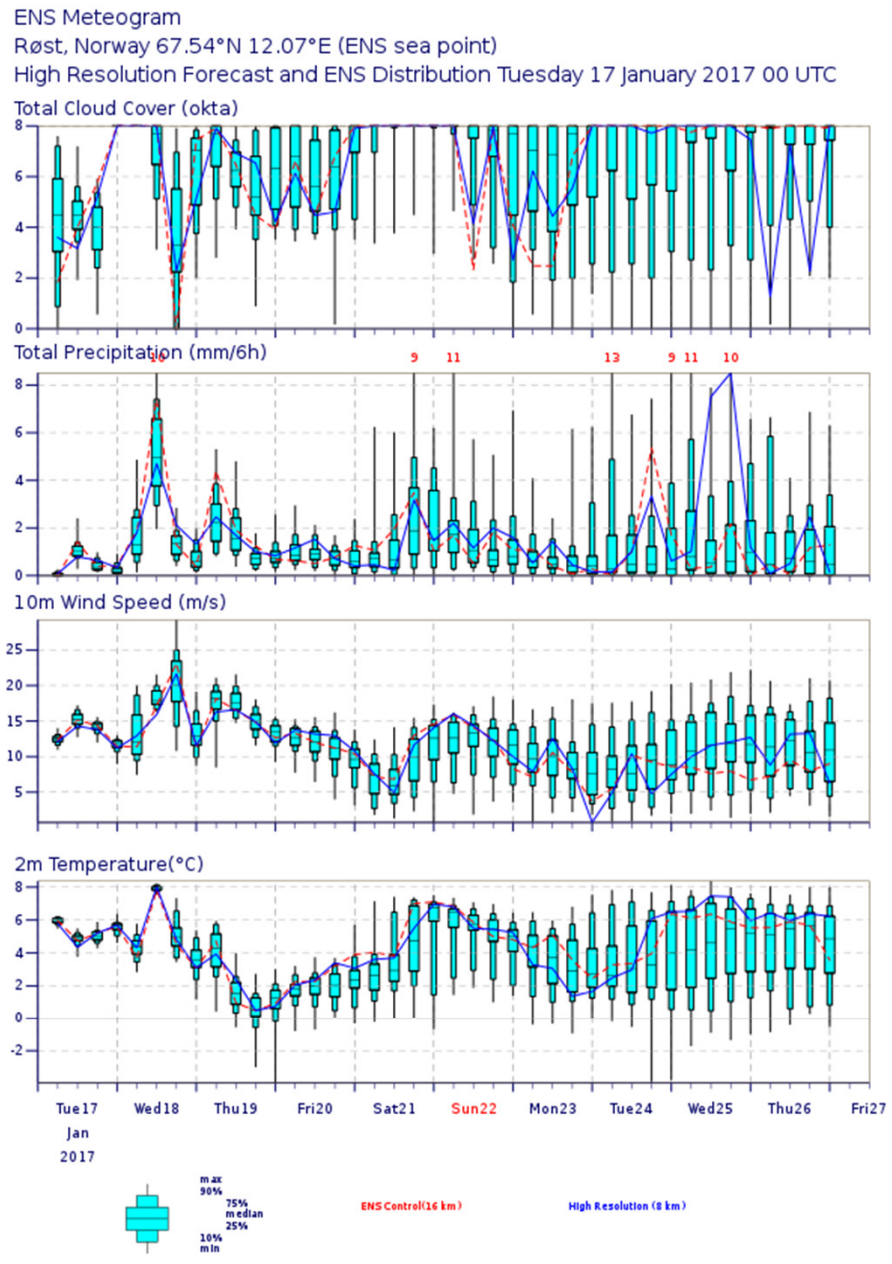

Røst 15.01.2016 00utc ana +

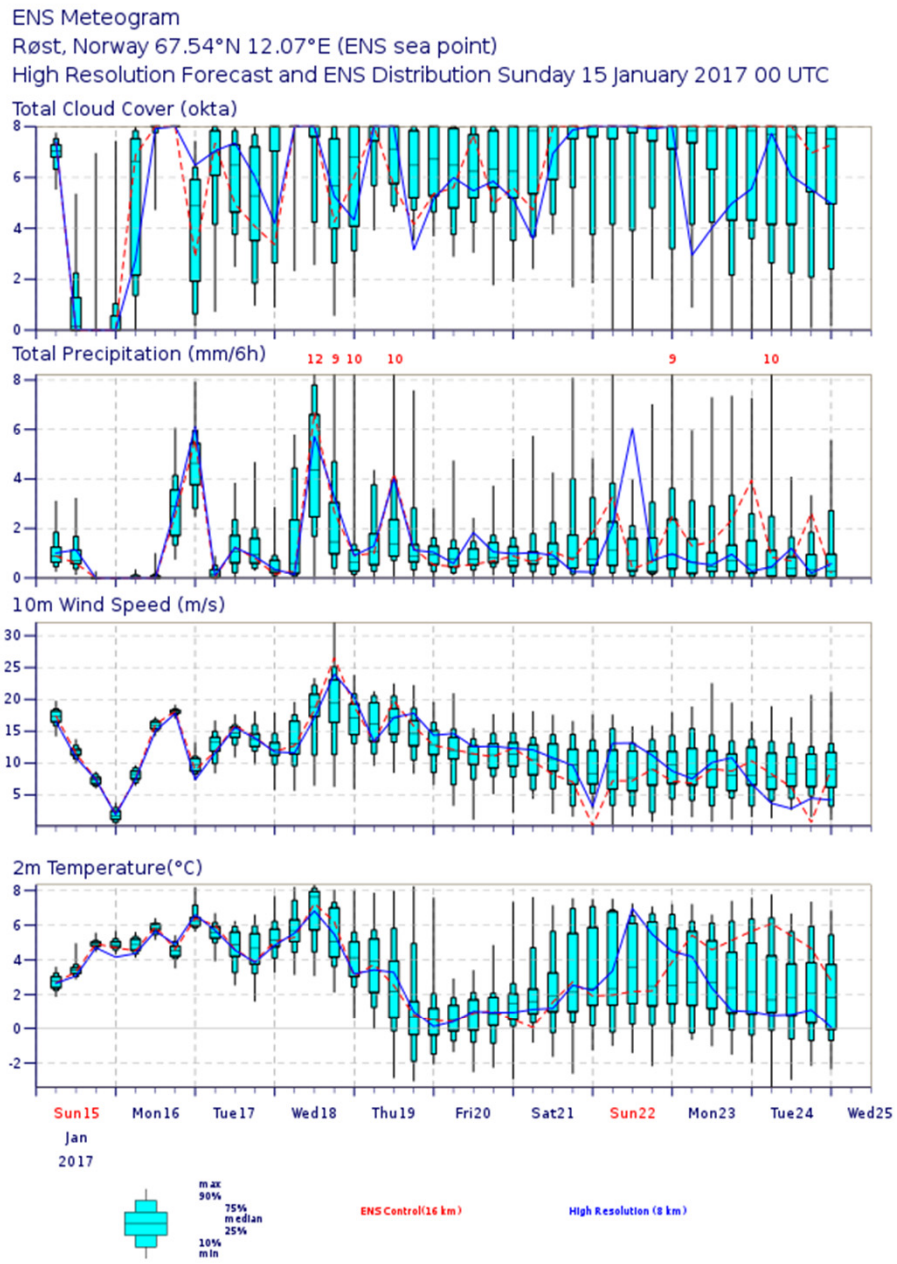

16.01.2016 00utc ana +

ENS Meteogram
Oslo, Norway 60°N 10.67°E (EPS land point) 11 m
High Resolution Forecast and ENS Distribution Saturday 16 January 2016 00 UTC

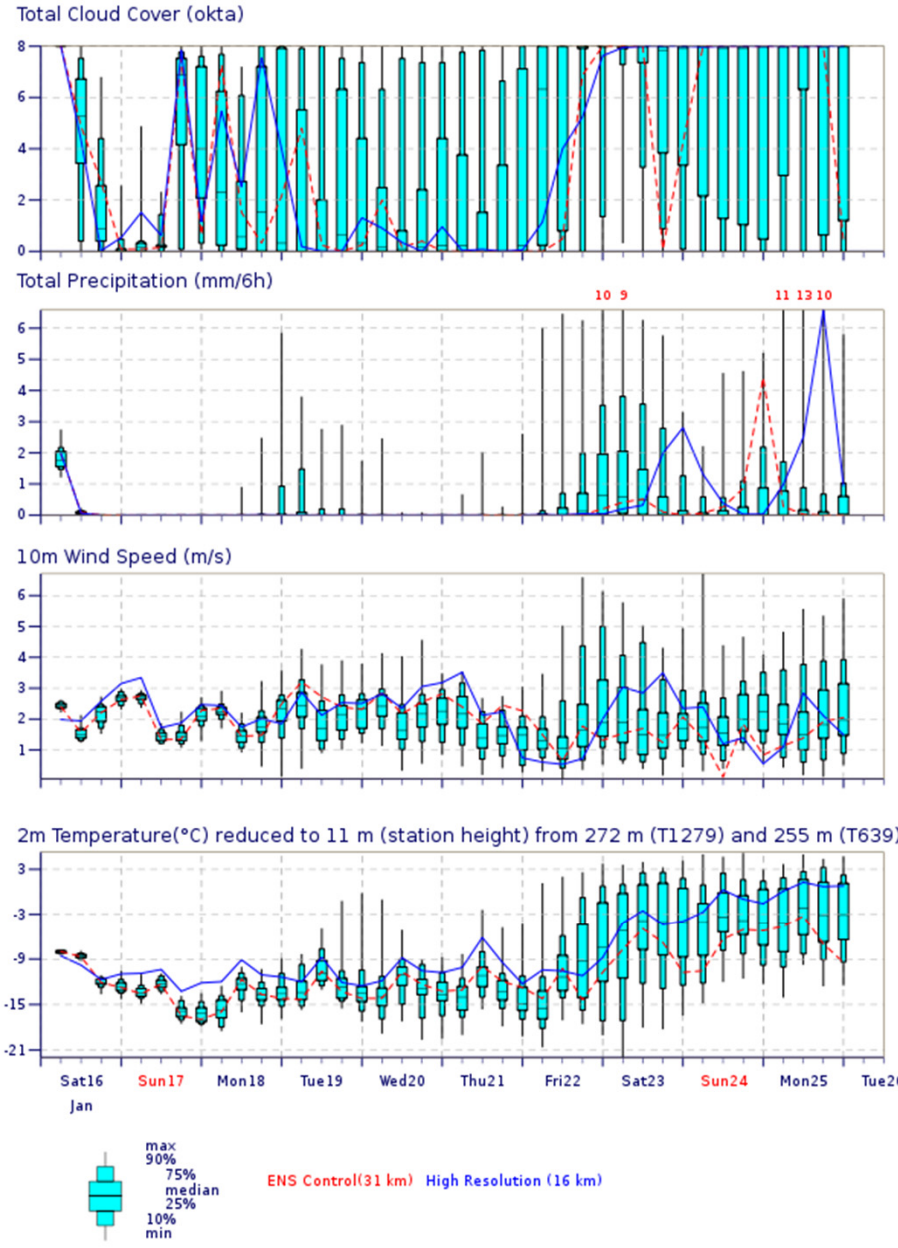

18.01.2016 00utc ana +

ENS Meteogram
Oslo, Norway 60°N 10.67°E (EPS land point) 11 m
High Resolution Forecast and ENS Distribution Monday 18 January 2016 00 UTC

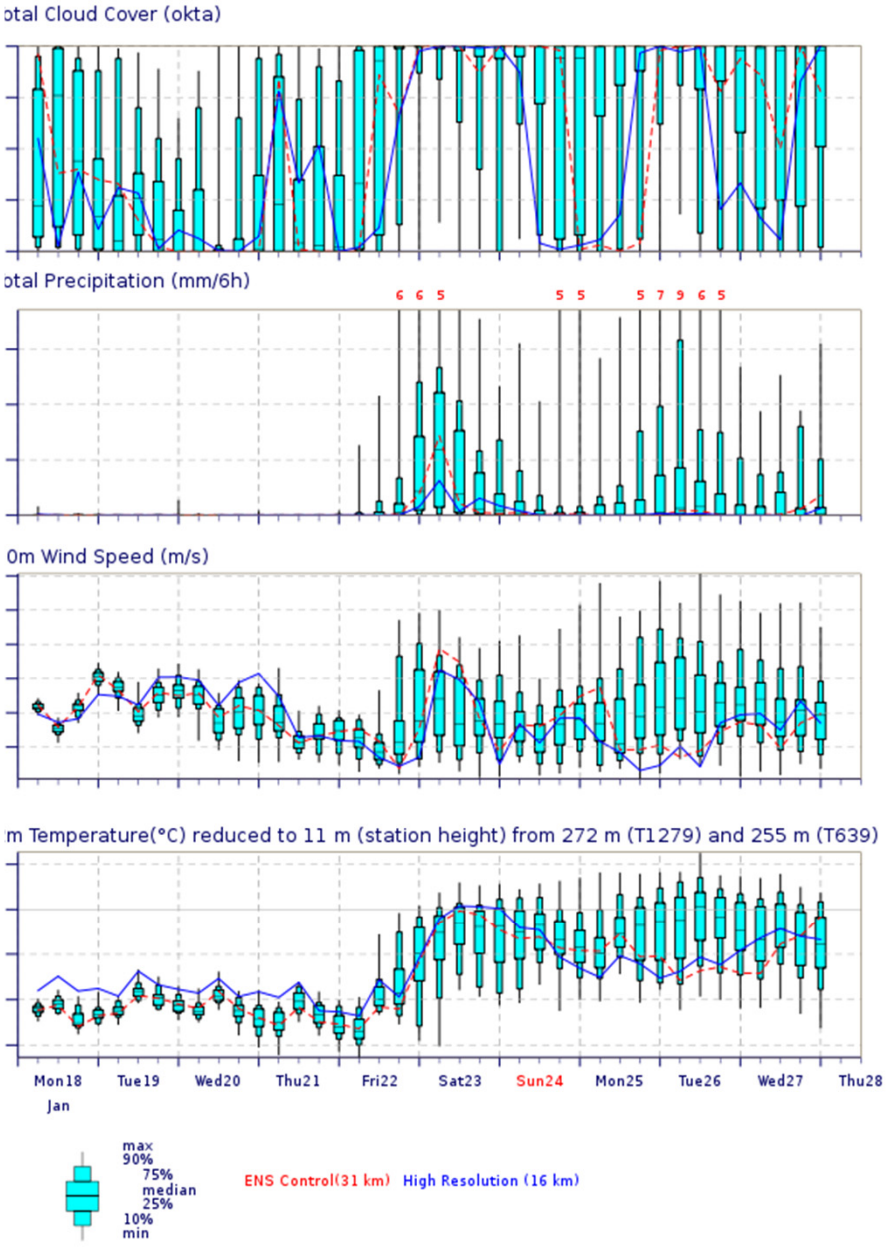

16.01.2016 00utc ana +

ENS Meteogram
Oslo, Norway 59.81°N 11°E (EPS land point) 11 m
Extended Range Forecast based on ENS distribution Saturday 16 January 2016 00 UTC

Daily mean of Total Cloud Cover (okta)

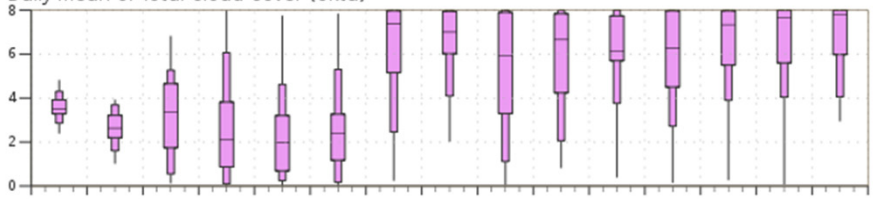

Total Precipitation (mm/24h)

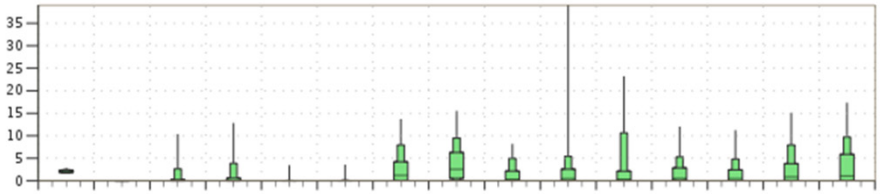

Daily Distribution of 10m Wind Direction

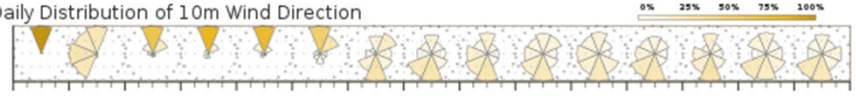

Daily mean of 10m Wind Speed (m/s)

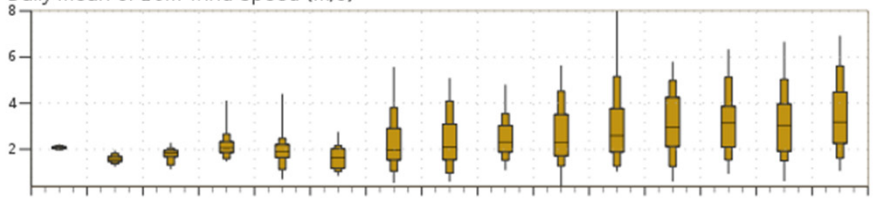

2m min/max Temperature (°C) reduced to 11 m (station height) from 186 m (T319)

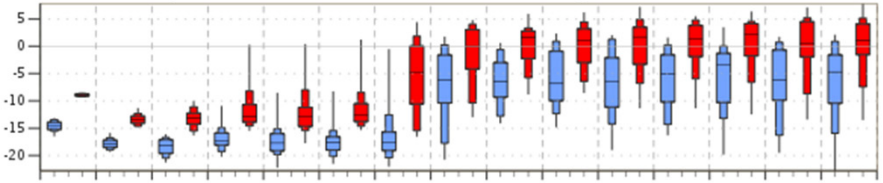

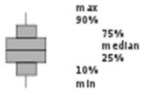

18.01.2016 00utc ana +

ENS Meteogram
Oslo, Norway 59.81°N 11°E (EPS land point) 11 m
Extended Range Forecast based on ENS distribution Monday 18 January 2016 00 UTC

Daily mean of Total Cloud Cover (okta)

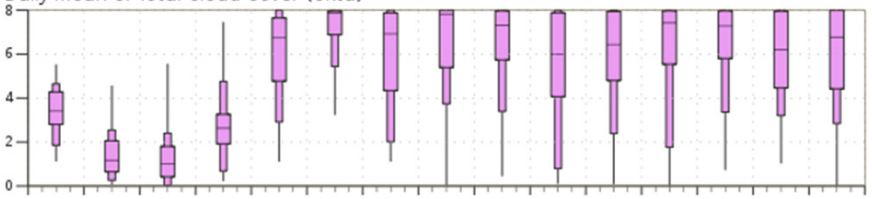

Total Precipitation (mm/24h)

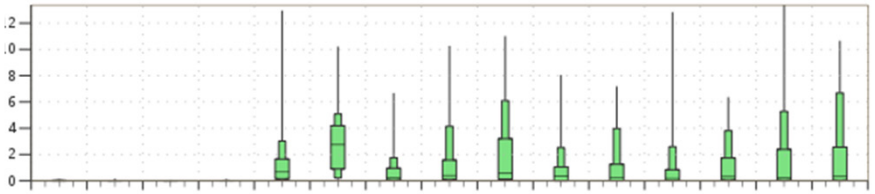

Daily Distribution of 10m Wind Direction

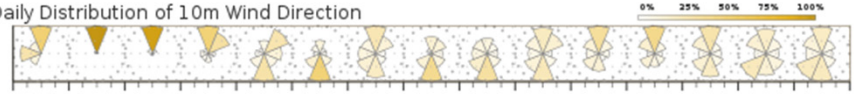

Daily mean of 10m Wind Speed (m/s)

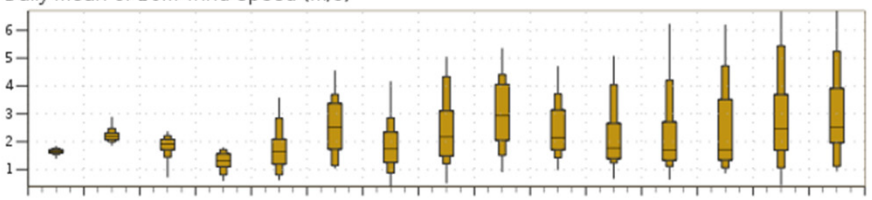

2m min/max Temperature (°C) reduced to 11 m (station height) from 186 m (T319)

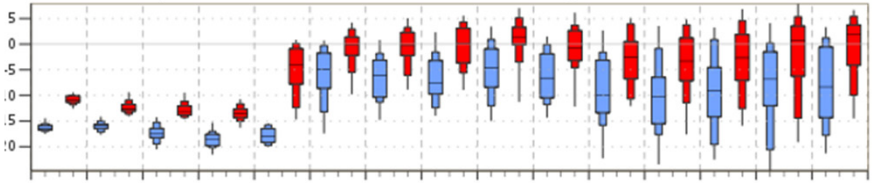

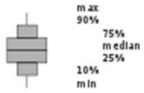

ENS Meteogram

ENS Meteogram

Oslo, Norway 59.81°N 11°E (EPS land point) 11 m

Extended Range Forecast based on ENS distribution Saturday 16 January 2016 00 UTC

16.01.2016 00utc ana +

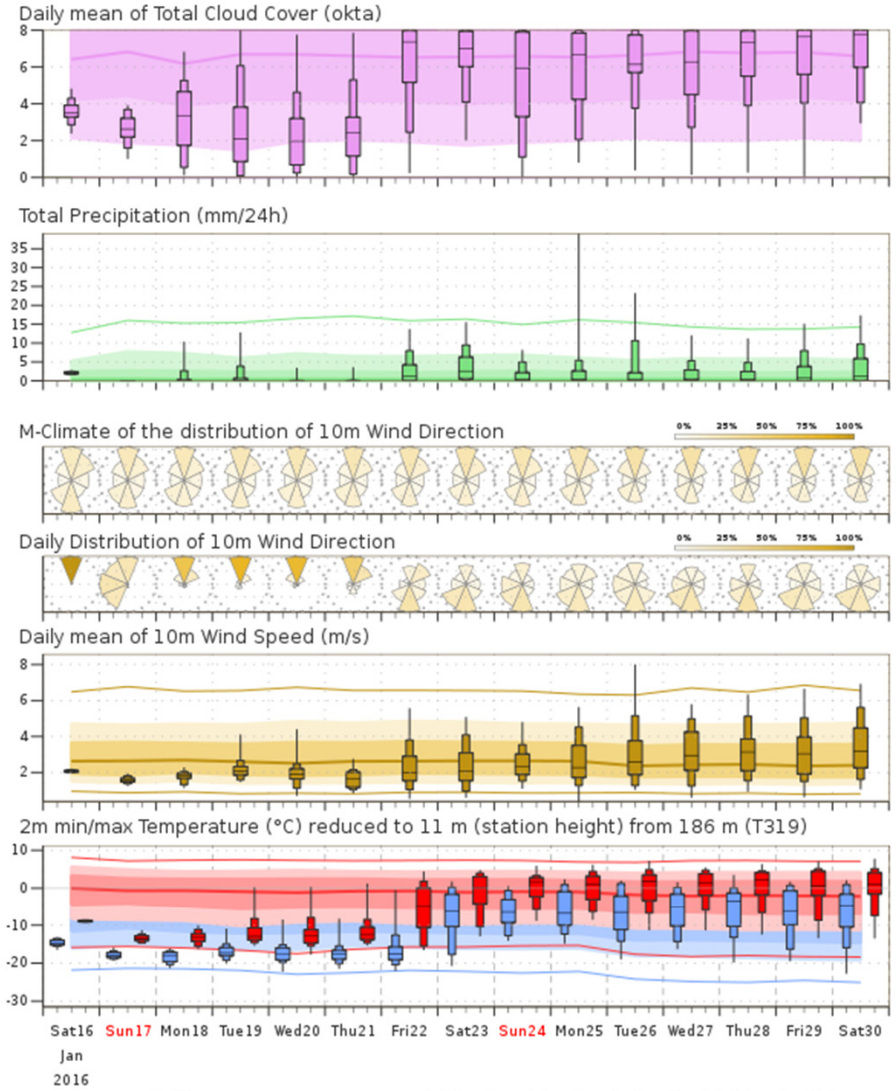

M-Climate: this stands for Model Climate. It is a function of lead time, date (+/-15days), and model version. It is derived by rerunning a 11 member ensemble over the last 20 years twice a week (1980 realisations). M-Climate is always from the same model version as the displayed ENS data.

ENS Meteogram

ENS Meteogram

slo, Norway 59.81°N 11°E (EPS land point) 11 m

xtended Range Forecast based on ENS distribution Monday 18 January 2016 00 UTC

18.01.2016 00utc ana +

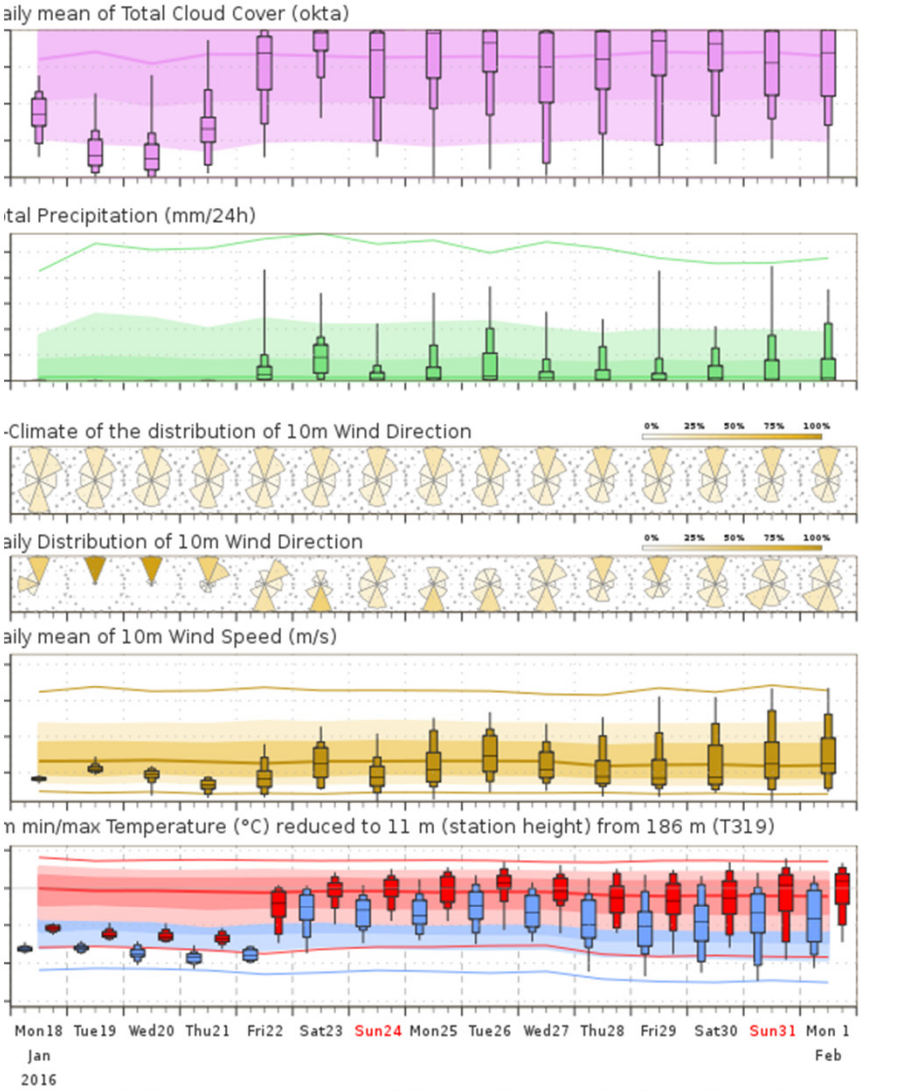

M-Climate: this stands for Model Climate. It is a function of lead time, date (+/-15days), and model version. It is derived by rerunning a 11 member ensemble over the last 20 years twice a week (1980 realisations). M-Climate is always from the same model version as the displayed ENS data.

NWP Historics

Vilhelm F. K. Bjerknes (1904)

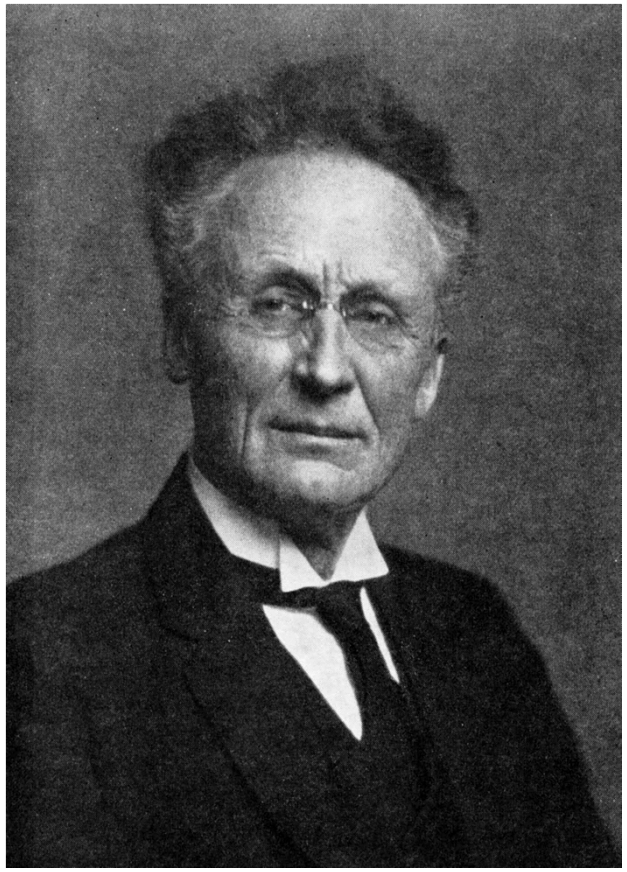

"Das Problem von der Wettervorhersage, betrachtet vom Standpunkt der Mechanik und der Physik"

Founded the basis for WP as an exact science:

Classical fluid dynamics

\+ classical thermodynamics

= "Physical fluid dynamics"

Number of unknowns = number of equations.

PDE: Only first order in time

Exact Science Paradigm in 1904:

Observe at t=0 ➔Calculate every variable at any time t.

Determinism IN PRINCIPLE!

Lewis Fry Richardson (1881-1953)

Lewis Fry Richardson (1881-1953)

Richardson(1922)

Weather Prediction by Numerical Process Cambridge Univ. Press

The first numerical weather forecast – manual (!)

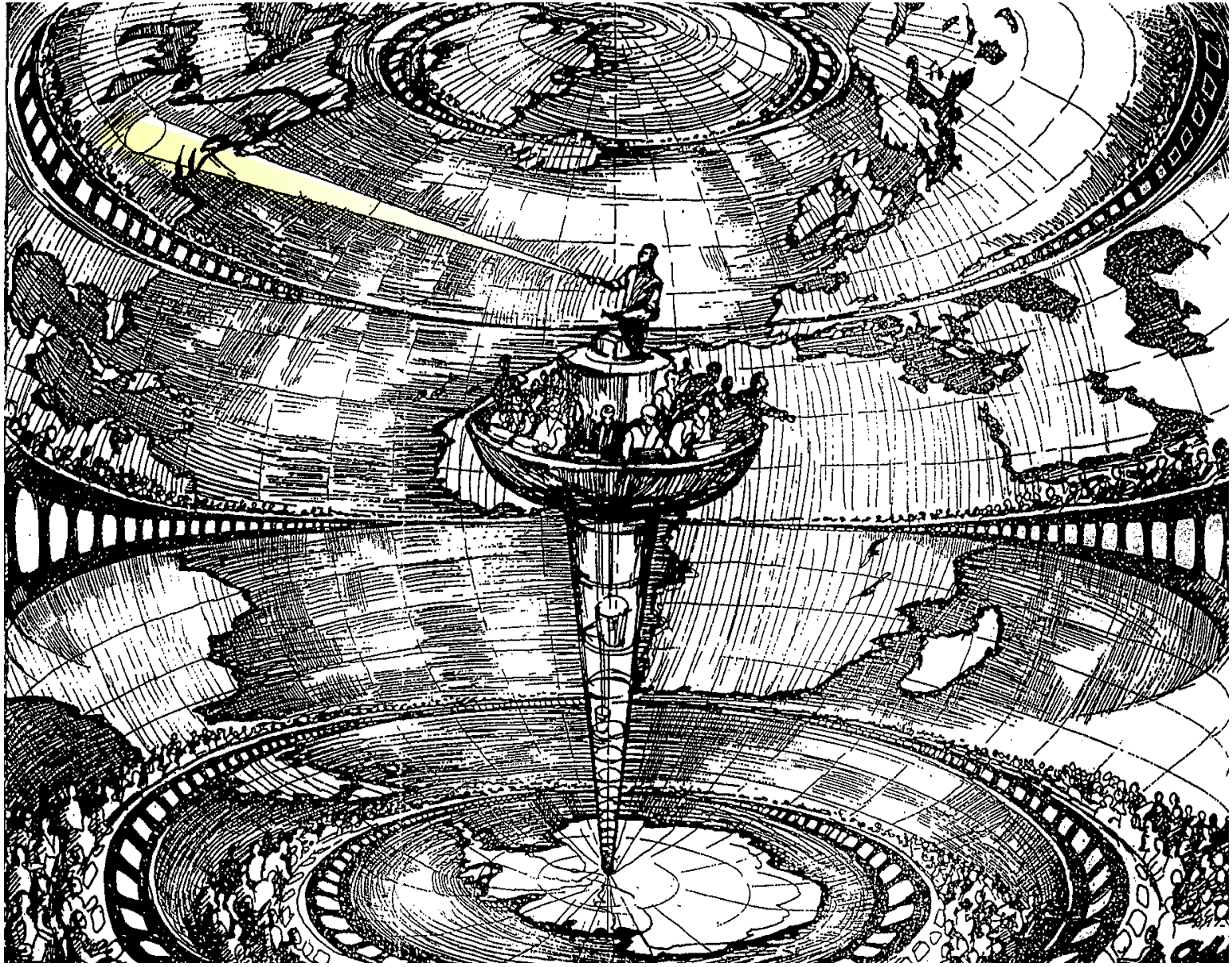

Meteorological «noise» and Richardson's failure

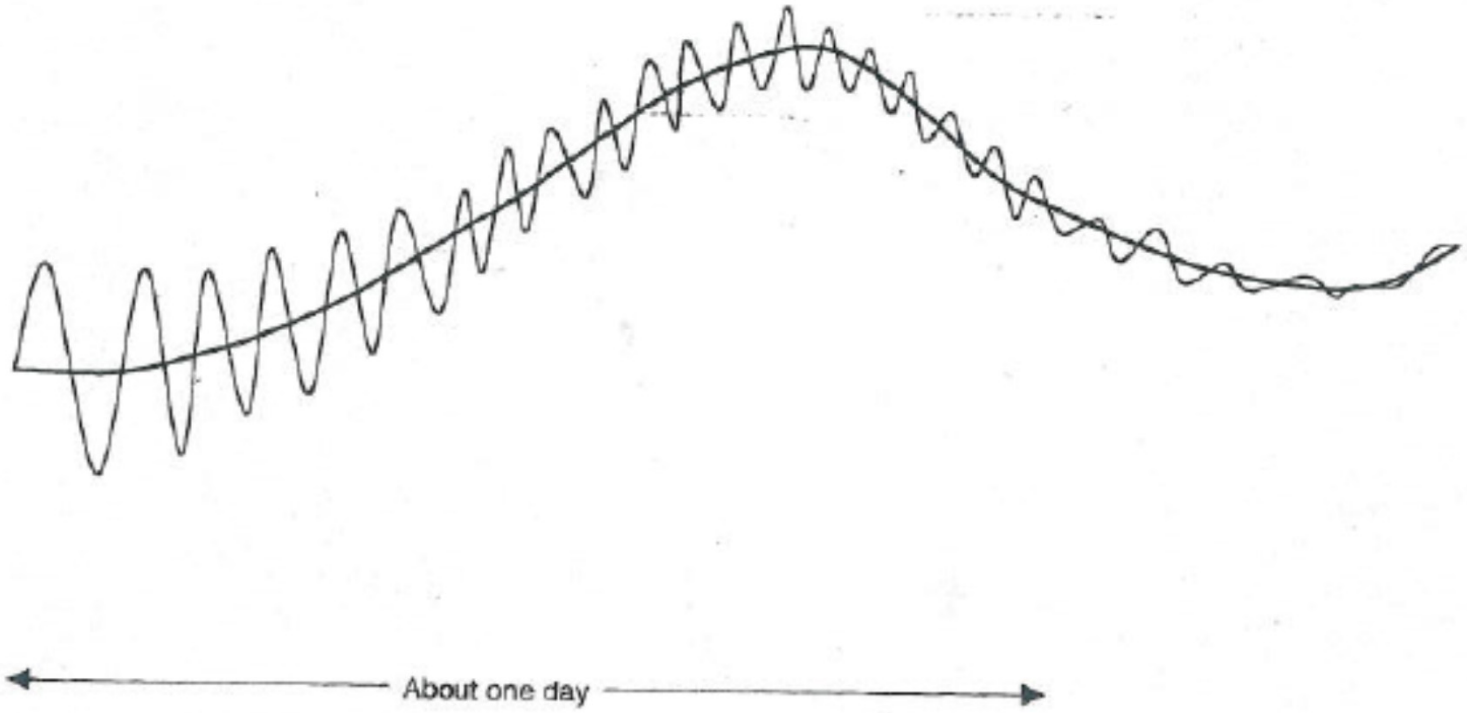

Figure 1.2.1: Schematic of a forecast with slowly varying weather-related variations and superimposed high-frequency gravity waves. Note that even though the forecast of the slow waves is essentially unaffected by the presence of gravity waves, the initial time derivative is much larger in magnitude, as obtained in the Richardson (1922) experiment.

The world's first successful, purely calculated weather forecast
Institute of Advanced Study, Princeton Univ., USA,1946→1950

John von Neuman

Jule Charney

Ragnar Fjørtoft

Arnt Eliassen

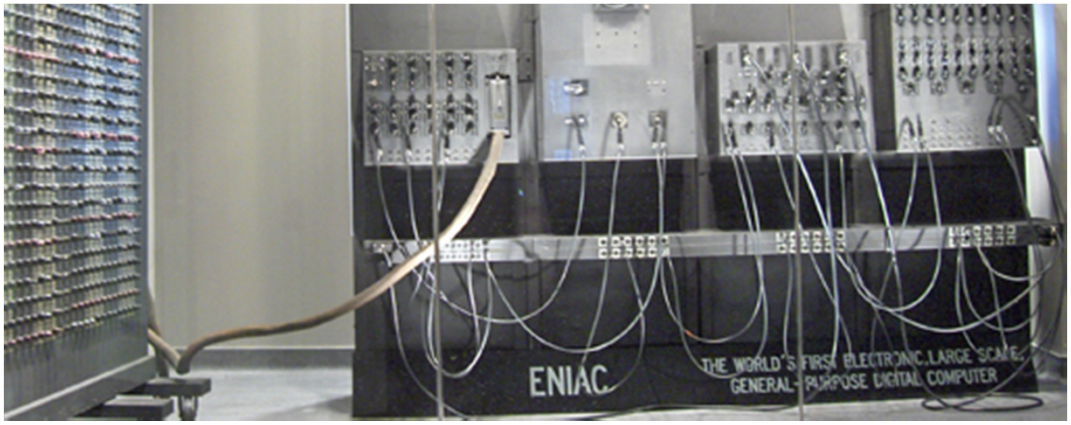

ENIAC
The computer

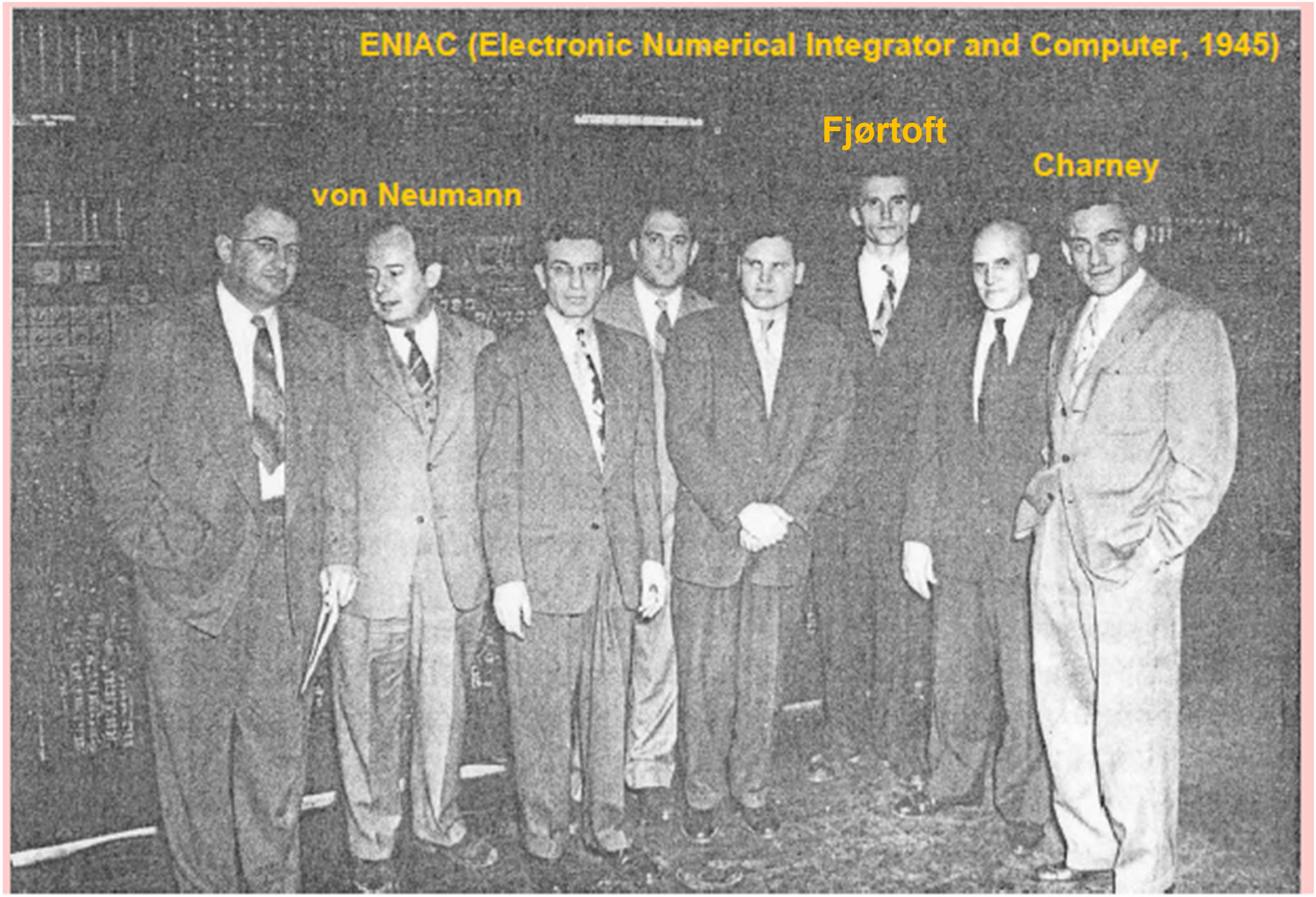
ENIAC (Electronic Numerical Integrator and Computer, 1945)
Fjørtoft
Charney
von Neumann

Z_500 t=0, analysis t=+24h, verifying analysis

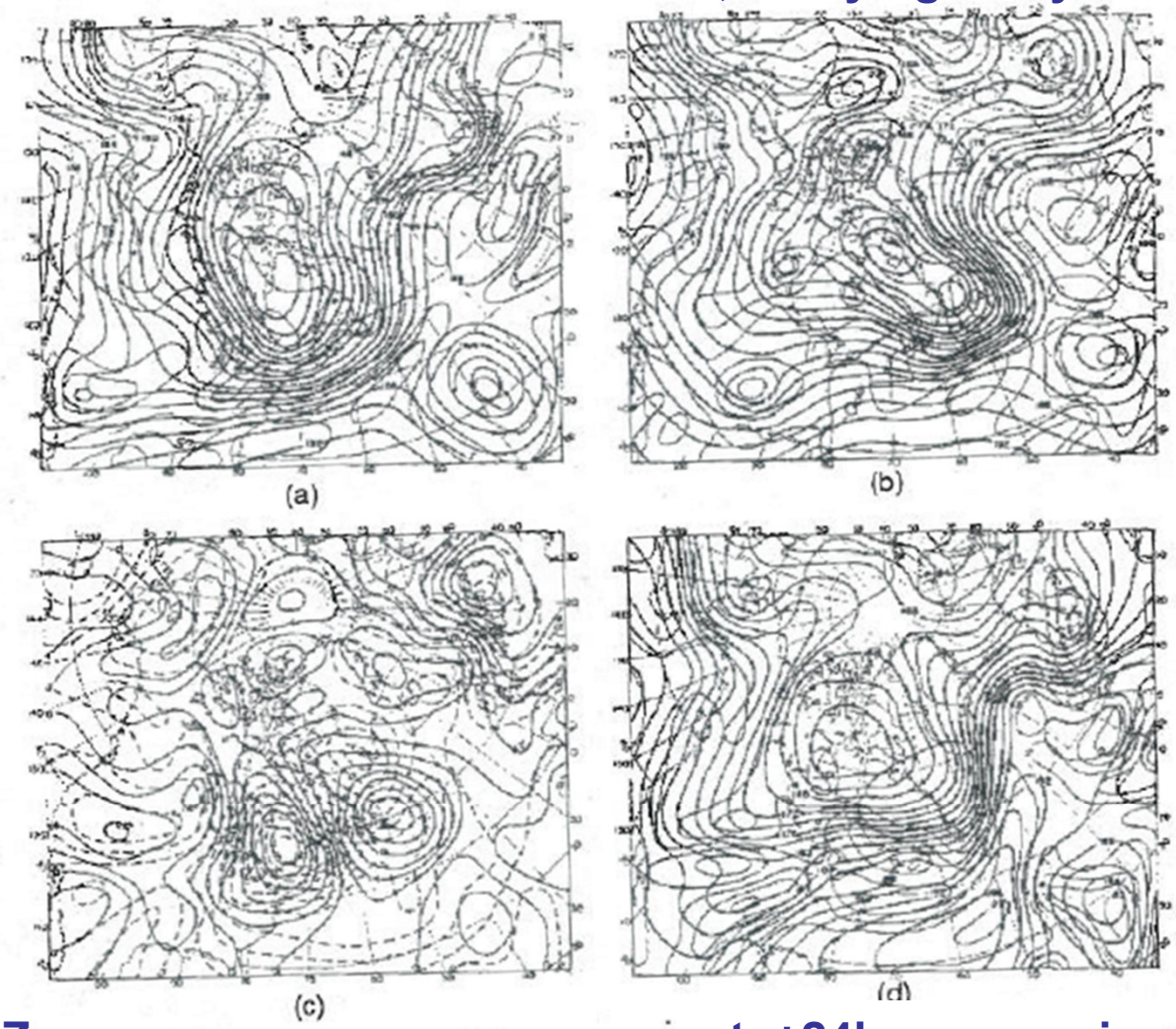

ΔZ, ana t=+24h, prognosis

Figure 1.2.2: Forecast of 30 January 1949, 0 z and $\zeta + f$ at $t = 0$; (b) observed z and $\zeta + f$ at $t = 24$ h; (c) observed (continuous lines) and computed (broken lines) 24-h height change; (d) computed z and $\zeta + f$ at $t = 24$ h. The height unit is 100 ft and the unit of vorticity is $1/3 \times 10^{-4}$ s^{-1}. (Reproduced from the *Compendium of Meteorology*, with permission of the American Meteorological Society.)

Edward N. Lorenz (1963 and 1969)

Founder of Dynamic System Science

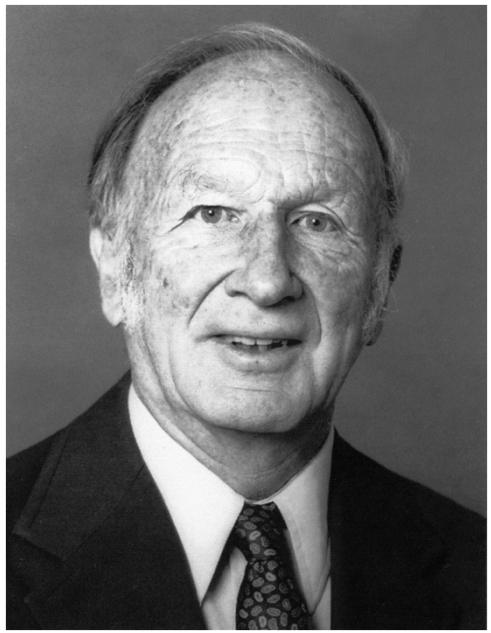

Deterministic chaos =
A deterministic system whose time development is critically sensitive to initial conditions

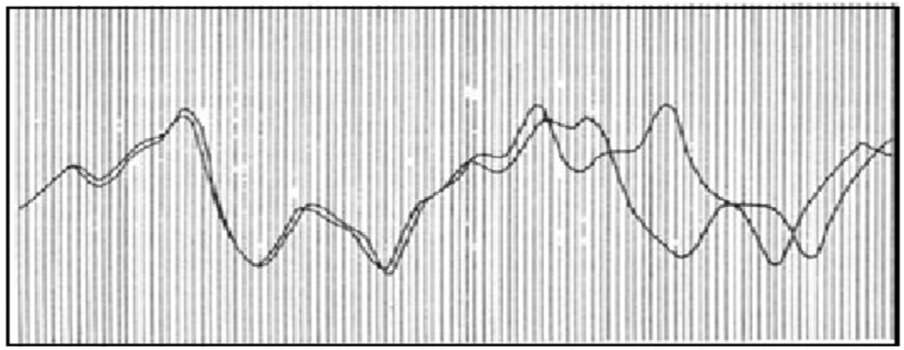

Figur 1. Lorenz' grafiske framstilling av to tidsutviklinger for en variabel i sin overforenklede regnemaskinmodell for atmosfæren. Ved utgangstilstanden til venstre på figuren er verdiene ikke til å skille fra hverandre. Ettersom tiden går øker forskjellen og utviklingene går i helt forskjellig retning.

"… one flap of a sea-gull's wing may forever change the future course of the weather"

(Lorenz, 1969)

"The Butterfly Effect"

«The Lorenz-model»:

$$\dot{X} = -\sigma X + \sigma Y$$

$$\dot{Y} = -XZ + rX - Y$$

$$\dot{Z} = XY - bZ$$

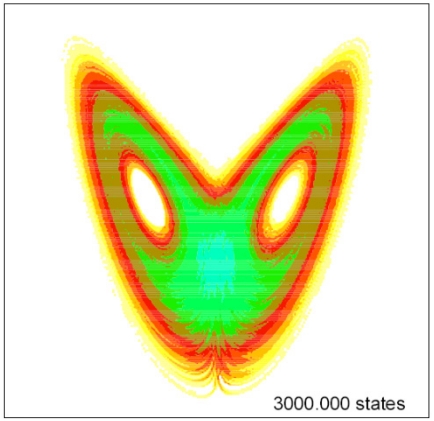

Meteorologisk institutt met.no

The Lorenz (1963) attractor, the prototype chaotic model…..

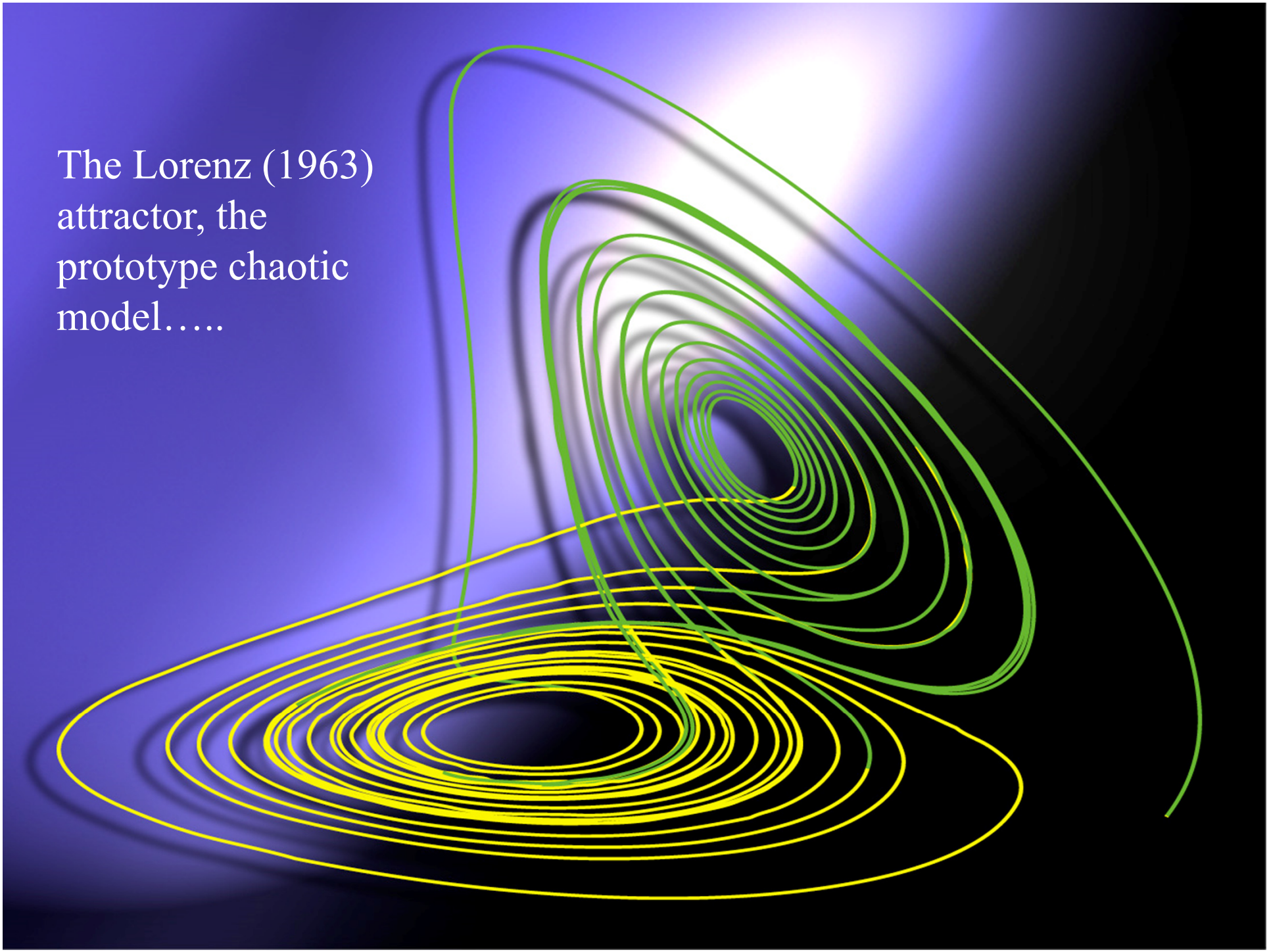

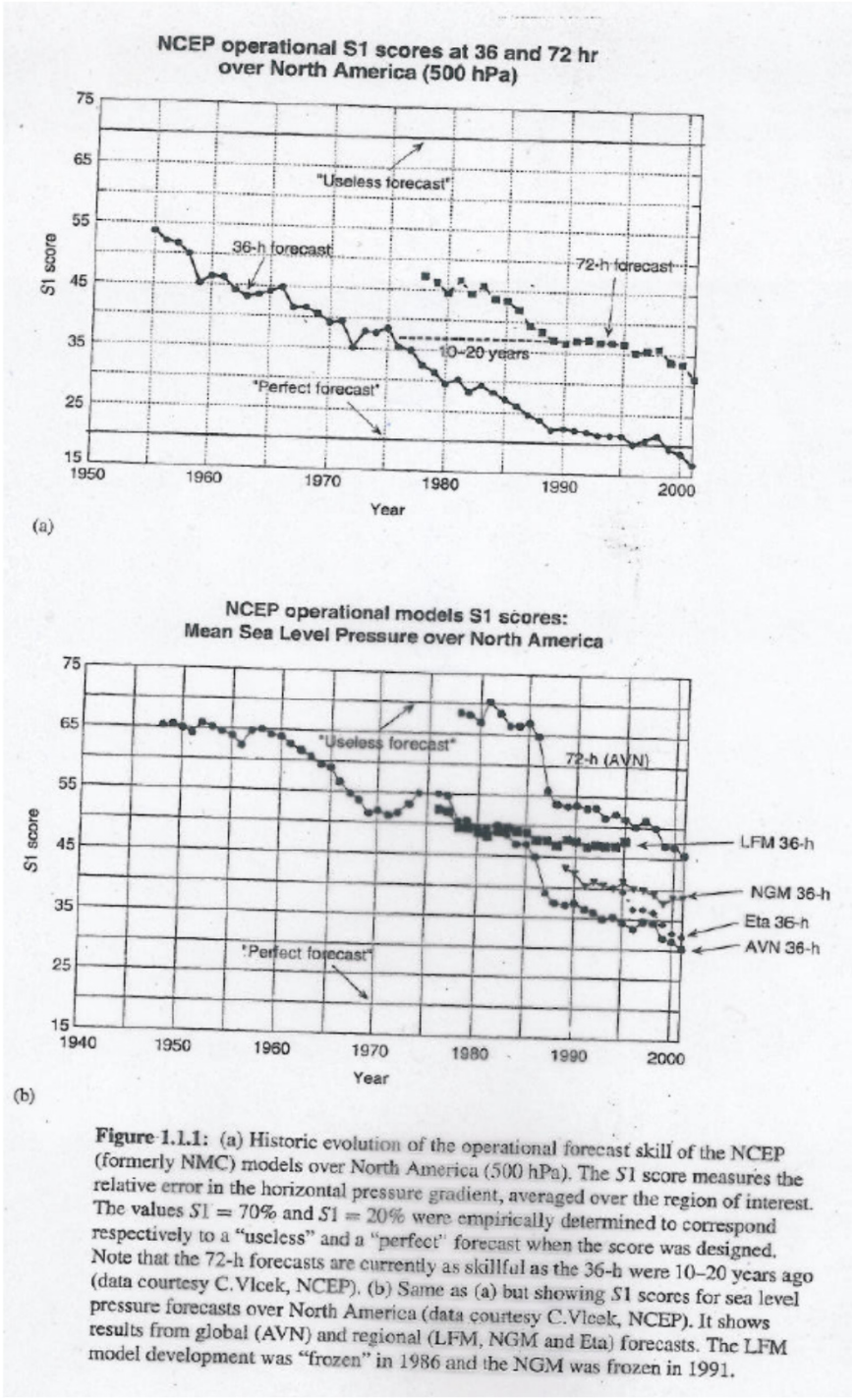

Figure 1.1.1: (a) Historic evolution of the operational forecast skill of the NCEP (formerly NMC) models over North America (500 hPa). The *S1* score measures the relative error in the horizontal pressure gradient, averaged over the region of interest. The values $S1 = 70\%$ and $S1 = 20\%$ were empirically determined to correspond respectively to a "useless" and a "perfect" forecast when the score was designed. Note that the 72-h forecasts are currently as skillful as the 36-h were 10–20 years ago (data courtesy C.Vlcek, NCEP). (b) Same as (a) but showing *S1* scores for sea level pressure forecasts over North America (data courtesy C.Vlcek, NCEP). It shows results from global (AVN) and regional (LFM, NGM and Eta) forecasts. The LFM model development was "frozen" in 1986 and the NGM was frozen in 1991.

Development of the

S1-scores for Z500hPa and MSLP
For different forecast lengths

S1=70% =>useless forecast
S1=20%=>perfect forecast

Development if RMS error of predicted geop. Height of 500 hPa

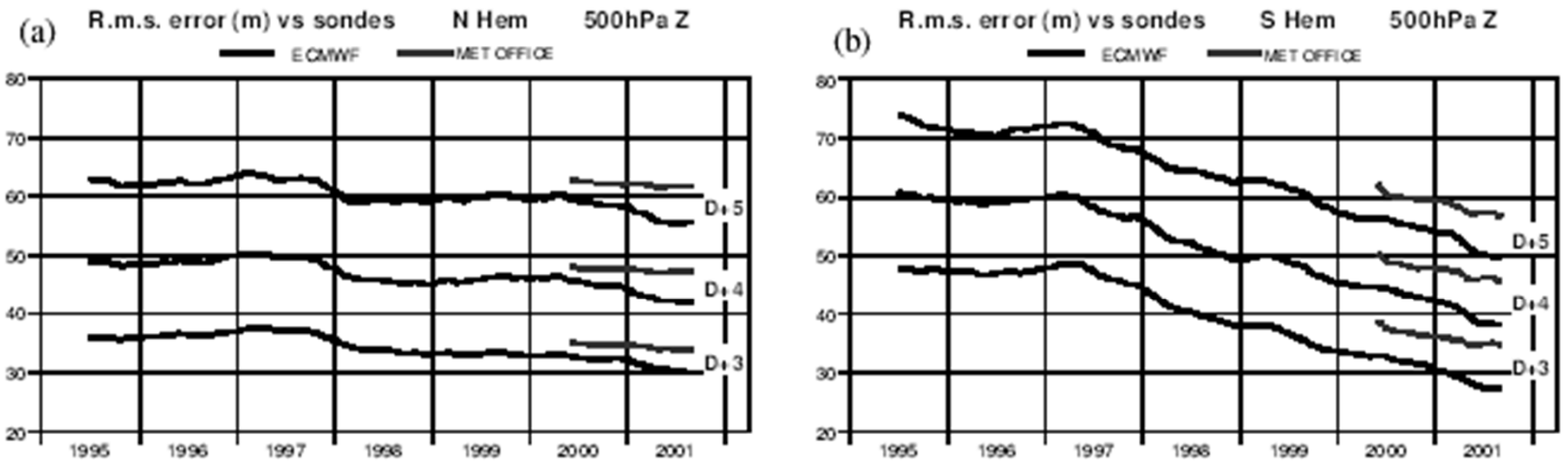

Figure 3. R.m.s. errors of 3-, 4- and 5-day ECMWF 500 hPa height (m) forecasts for the extratropical: (a) northern, and (b) southern hemispheres, plotted in the form of annual running means of monthly data for verification against radiosondes from July 1994 to August 2001. Recent Met Office forecast errors are also shown. Values plotted for a particular month are averages over that month and the 11 preceding months.

ECMWF

ECMWF has been producing operational medium-range weather forecasts since 1 August 1979.

- Corresponding developments of numerical models
  - 1950: Charney, Fjörtoft and von Neumann
  - 1950s: 3-D numerical weather prediction (NWP) models
  - 1960s: atmospheric general circulation models (GCM)
  - 1970s: atmosphere-ocean coupled GCM
    start of operational NWP
  - 1980s: operational NWP with global models
    data assimilation with numerical models
  - 1990s: global warming simulations with coupled GCM
    operational ensemble NWPs
  - 2000s: Earth system modeling
    interactions of multiple components in multiple scales

24h summary of observations received at ECMWF, 5 July 2004

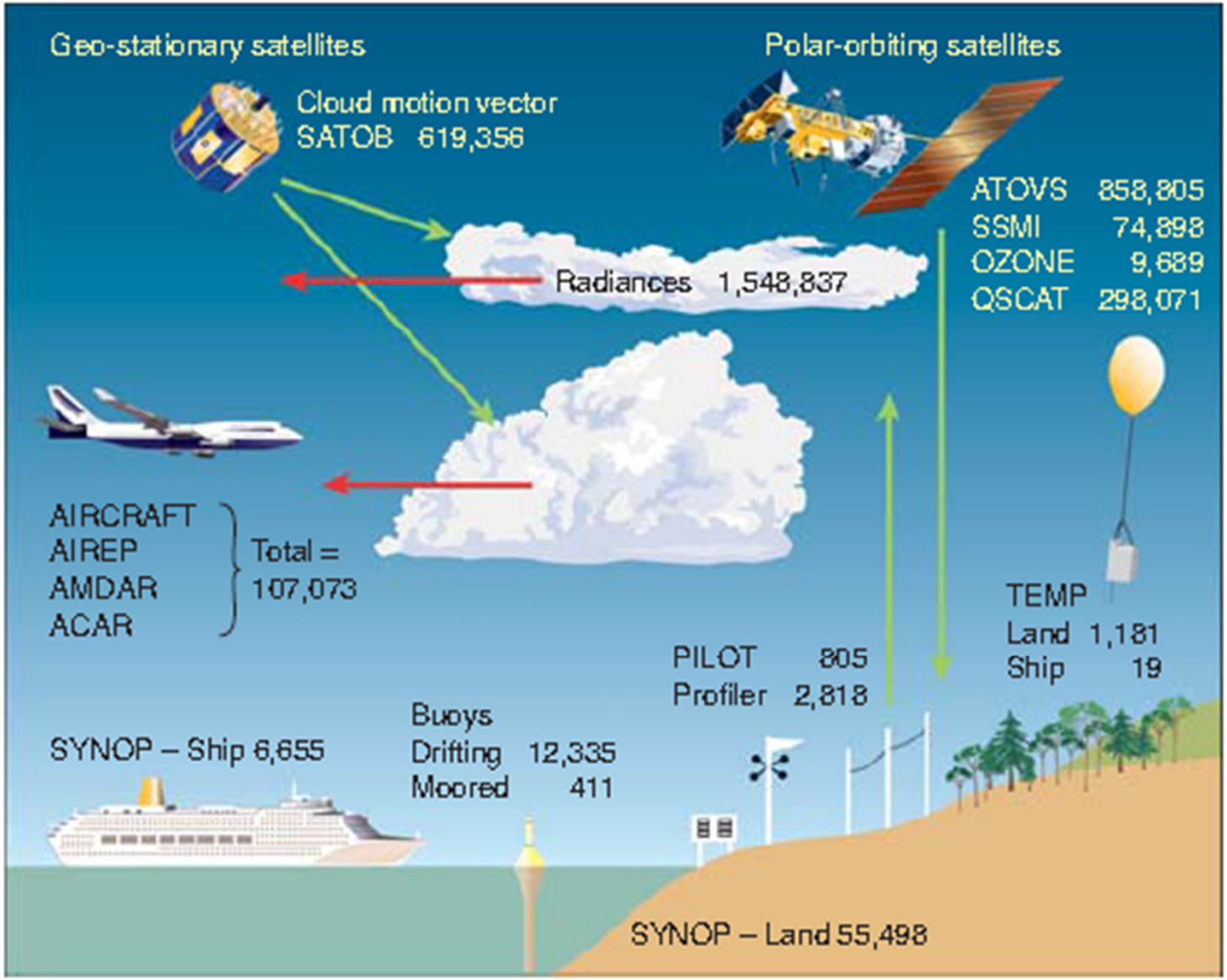

RMSE and Anomaly correlation

The rms error E_j of the day j forecast is defined by

$$E_j = \sqrt{\overline{(f_j - a)^2}}$$

$$(E_j)^2 = \overline{((f_j - c) - (a - c))^2}$$

$$= \overline{(f_j - c)^2} + \overline{(a - c)^2} - 2\,\overline{(f_j - c)(a - c)}$$

$$= (A_j)^2 + (A_a)^2 - 2\,\overline{(f_j - c)(a - c)}$$

Anomaly correlation coefficient

$$ACC_j = \frac{\overline{(f_j - c)(a - c)} - \overline{(f_j - c)}\,\overline{(a - c)}}{\sqrt{[\overline{(f_j - c)^2} - \overline{(f_j - c)}^2]\,[\overline{(a - c)^2} - \overline{(a - c)}^2]}}$$

$$AC_j = \frac{\overline{(f_j - c)(a - c)}}{\sqrt{[\overline{(f_j - c)^2}]\,[\overline{(a - c)^2}]}}$$

Assuming:

$\overline{(a - c)}$ and $\overline{(f_i - c)} = 0$

The normalized error N_j is given by

$$N_j = \frac{(E_j)^2}{(A_a)^2 + (A_j)^2}$$

$$N_j = 1 - \frac{2 A_j A_a}{(A_j)^2 + (A_a)^2} AC_j$$

$$= 1 - AC_j \left(1 - \frac{(A_j - A_a)^2}{(A_j)^2 + (A_a)^2} \right)$$

Assume

A_j is close to A_a

$$N_j \approx 1 - AC_j$$

Or:

$$E_j^2 = 2A_a^2 (1 - AC_j)$$

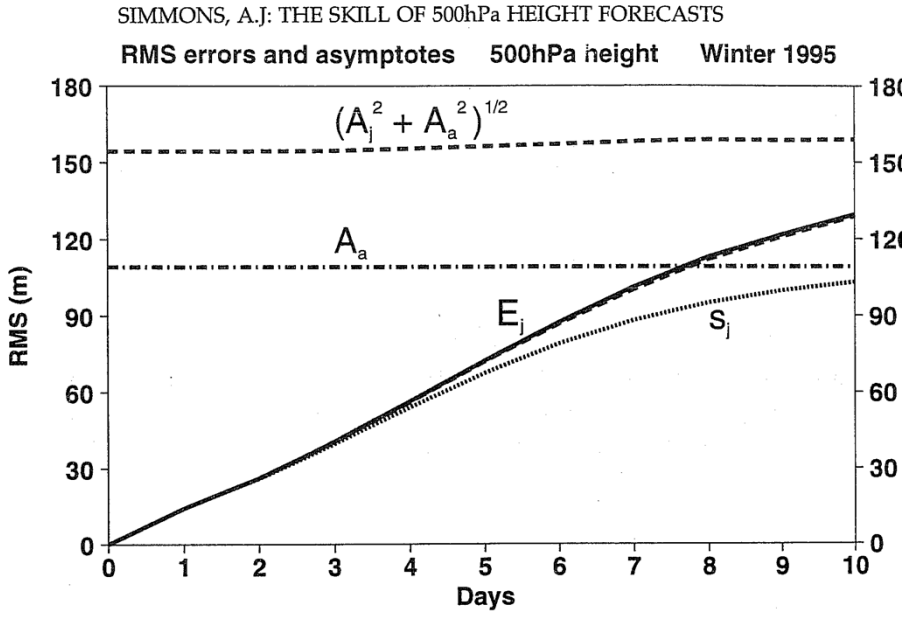

$$E_j^2 = 2A_a^2\,(1 - AC_j)$$

E=RMS Error

AC=Anomaly Correlation

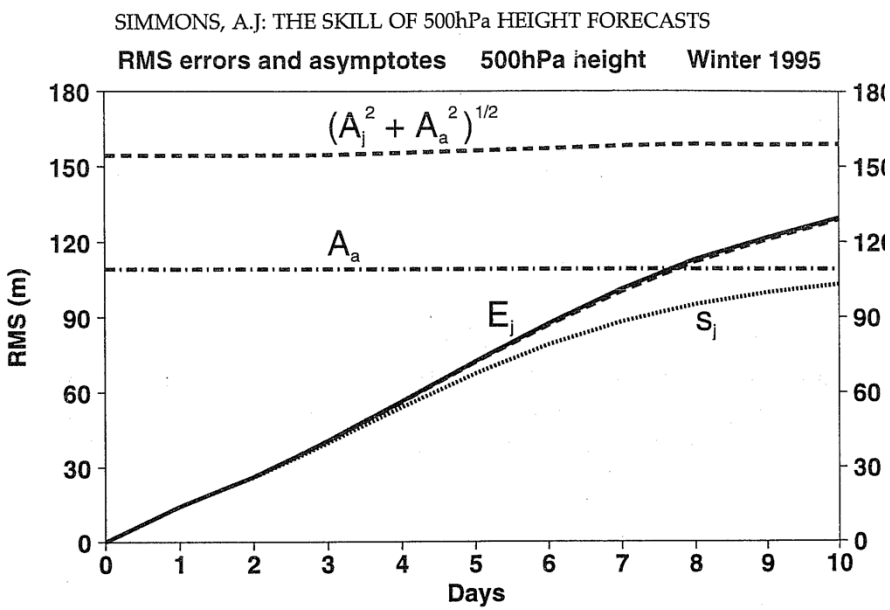

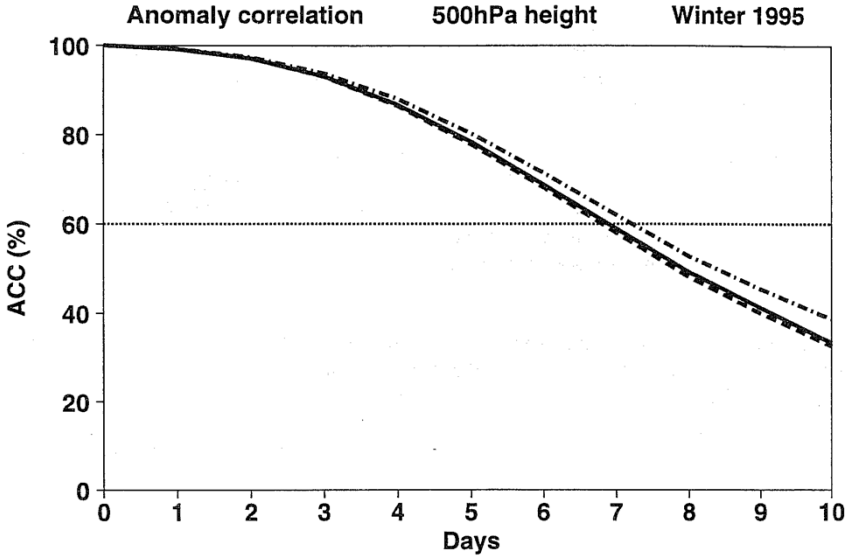

Evolution of ECMWF scores over NH and SH for Z500

The combination of improved data-assimilation and forecasting models, the availability of more/better observations (especially from satellites), and higher computer power have led to increasingly accurate weather forecasts. **Today, over NH (SH) a day-7 single forecast of the upper-air atmospheric flow has the same accuracy as a day-5 in 1985 (day-3 in 1981).**

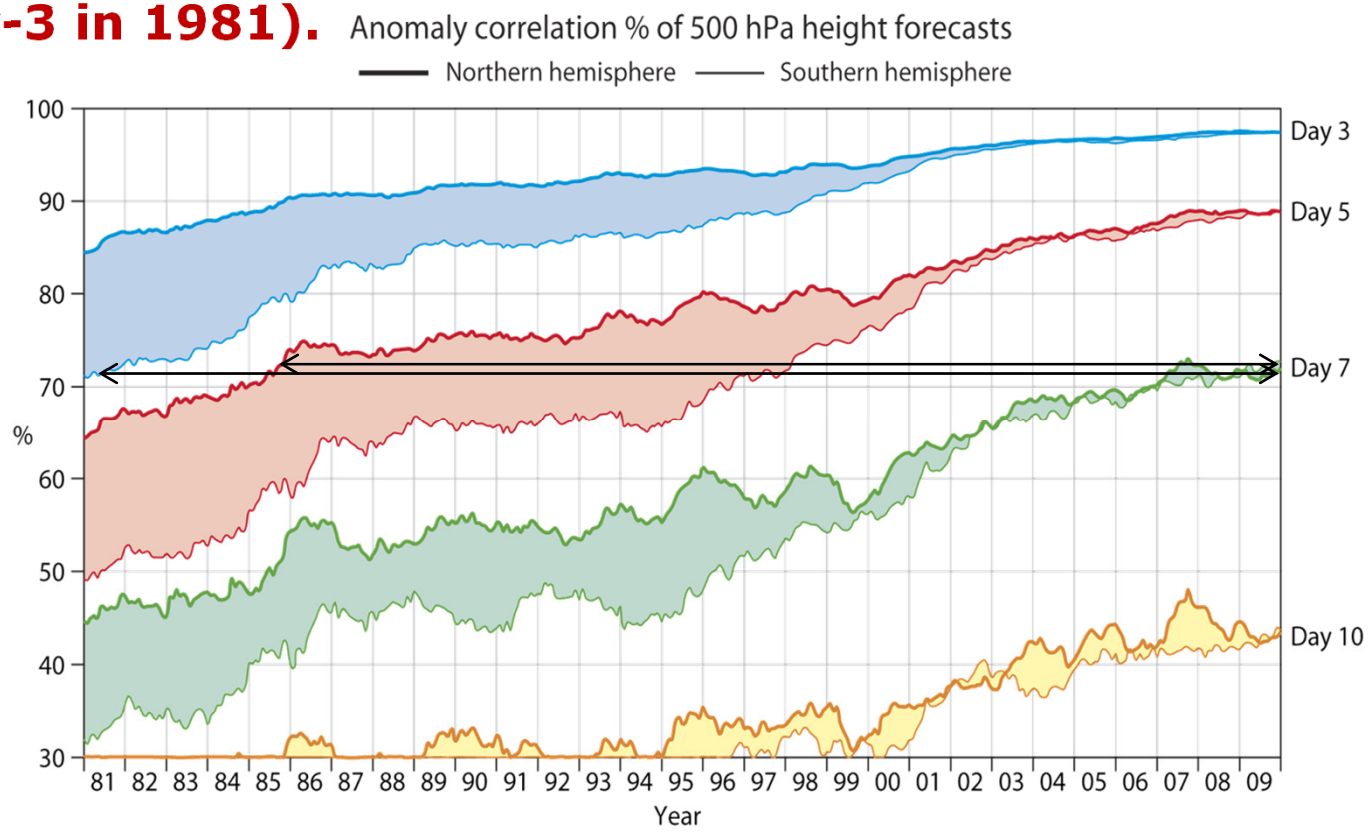

Evolution of ECMWF scores over NH and SH for Z500 II

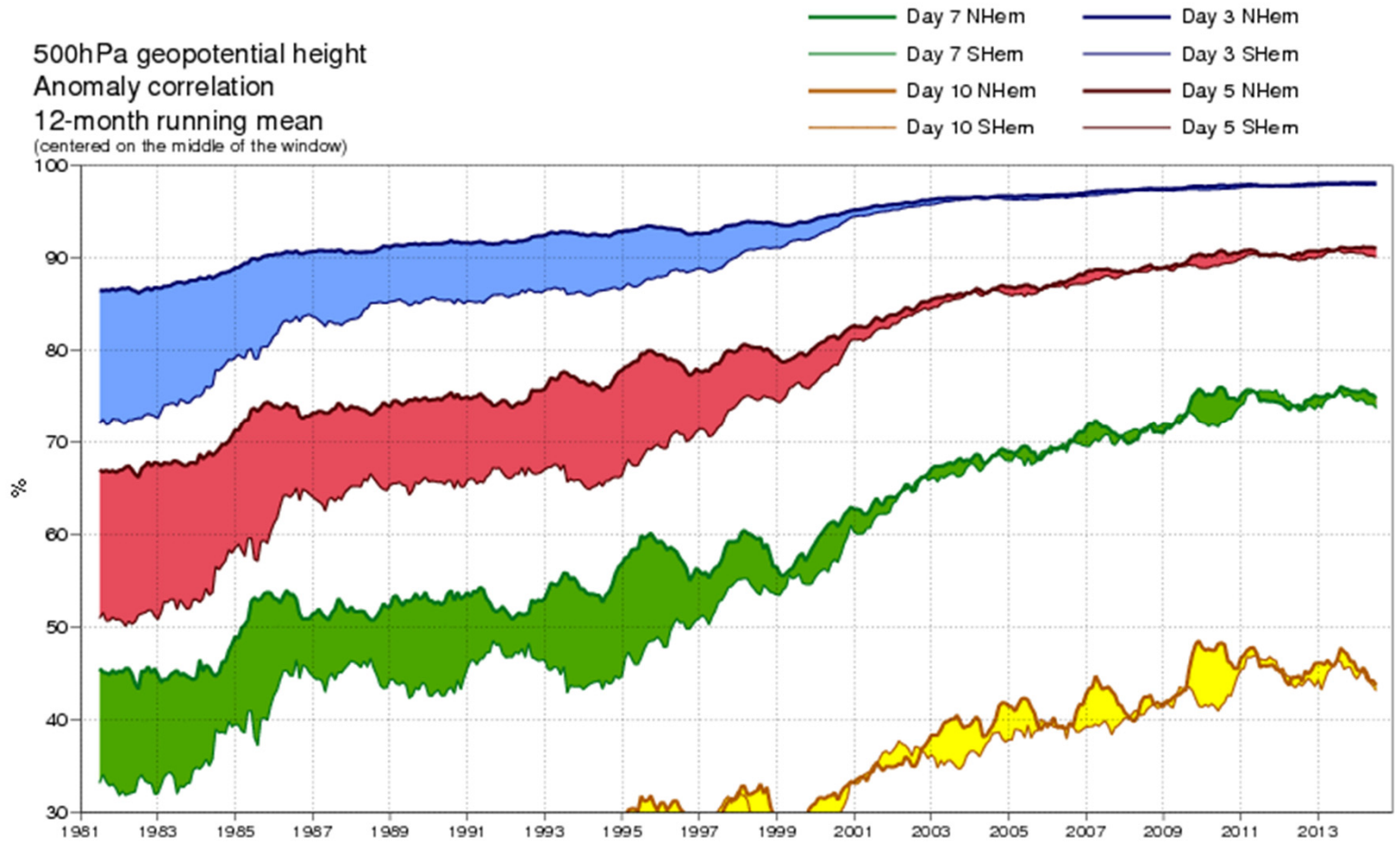

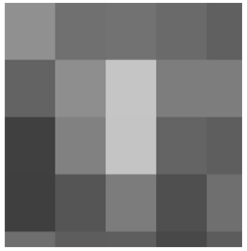

~210km

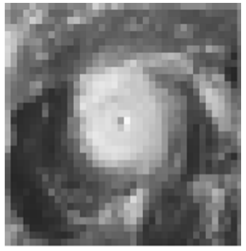

~16km

Quality of numerical model forecasts for the geopotential height of 500 hPa

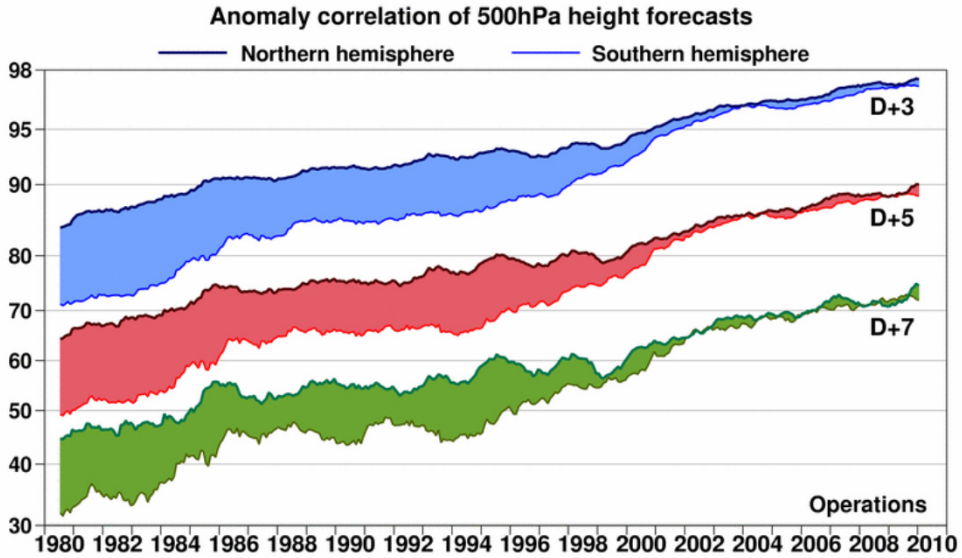

Anomaly-correlation for forecasted Z(500hPa) from ECMWF's operational, global model snce 1980

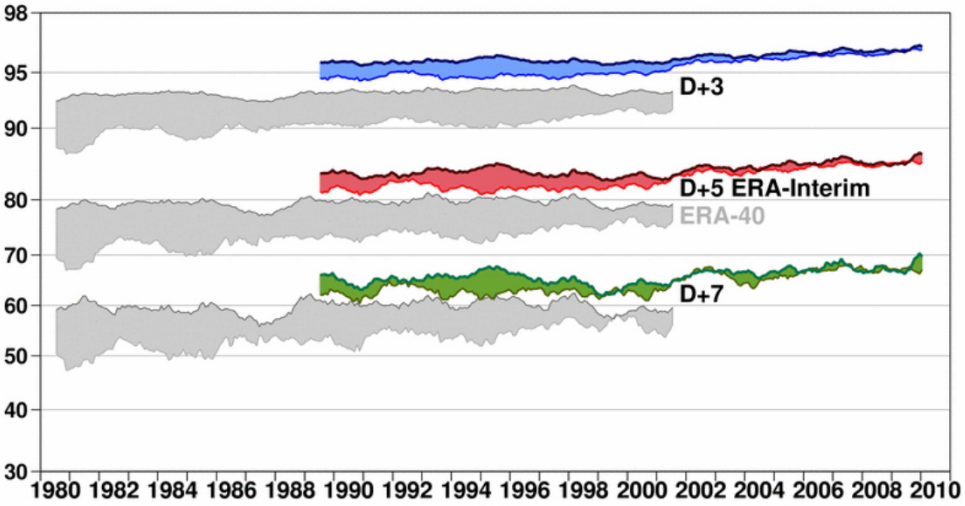

Same results if the same («frozen») model- and analysis-system is used for all years (here: ECMWF's re-analysis, «ERA»):

Changes are only due to
-Random fluctuations (internal variability)
-observational changes

Courtesy: P.Kållberg, A. Simmons; ECMWF

Re-analyses & Re-forecasts in NWP verification

HRES and ERA Interim 00,12UTC forecast skill
500hPa geopotential
Lead time of Anomaly correlation reaching 80%
NHem Extratropics (lat 20.0 to 90.0, lon -180.0 to 180.0)

Z500 : Forecast time when ACC=80% N hemisphere

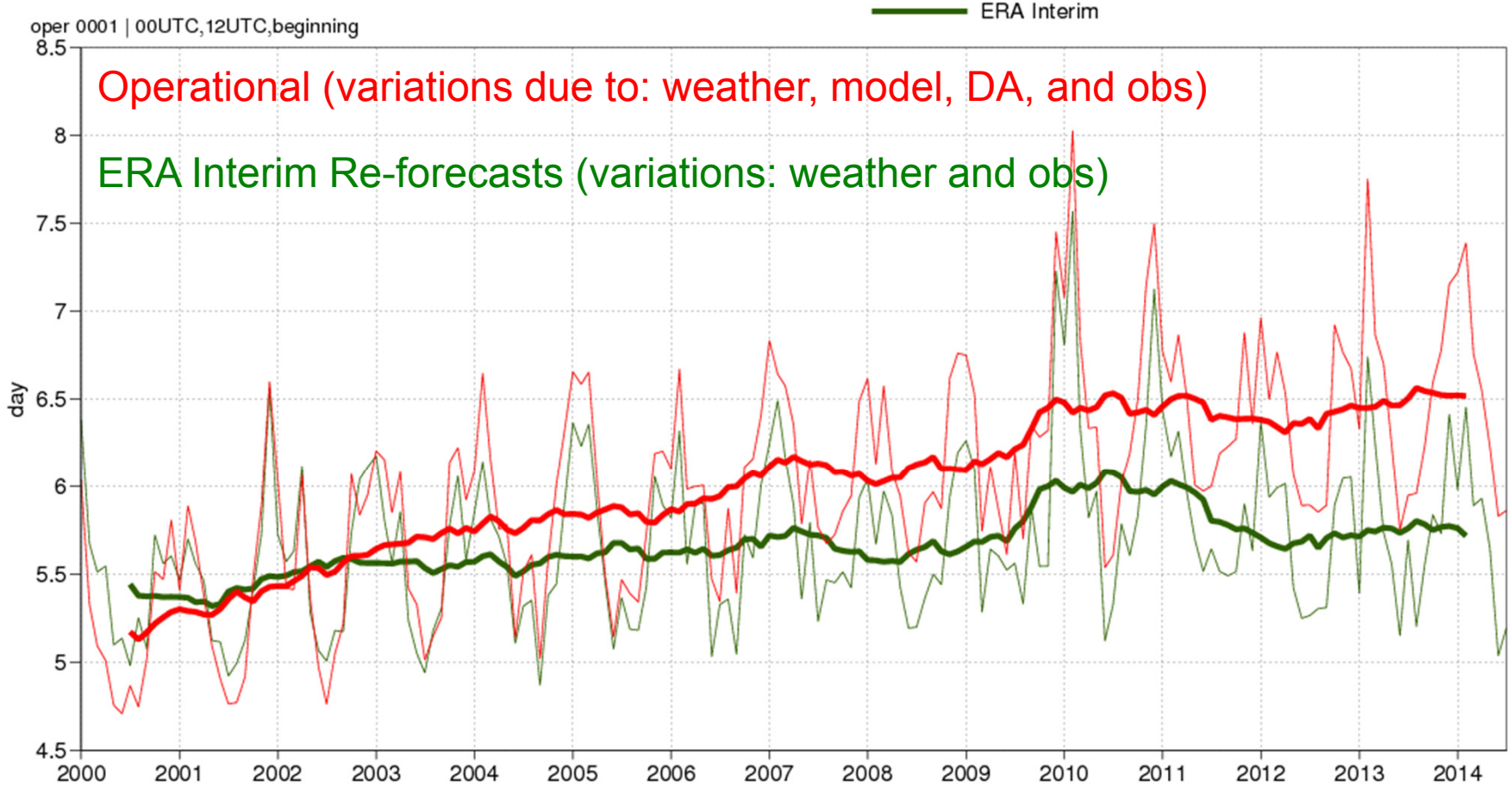

Improved predictions over since 2000
due to system improvements (and observation changes)

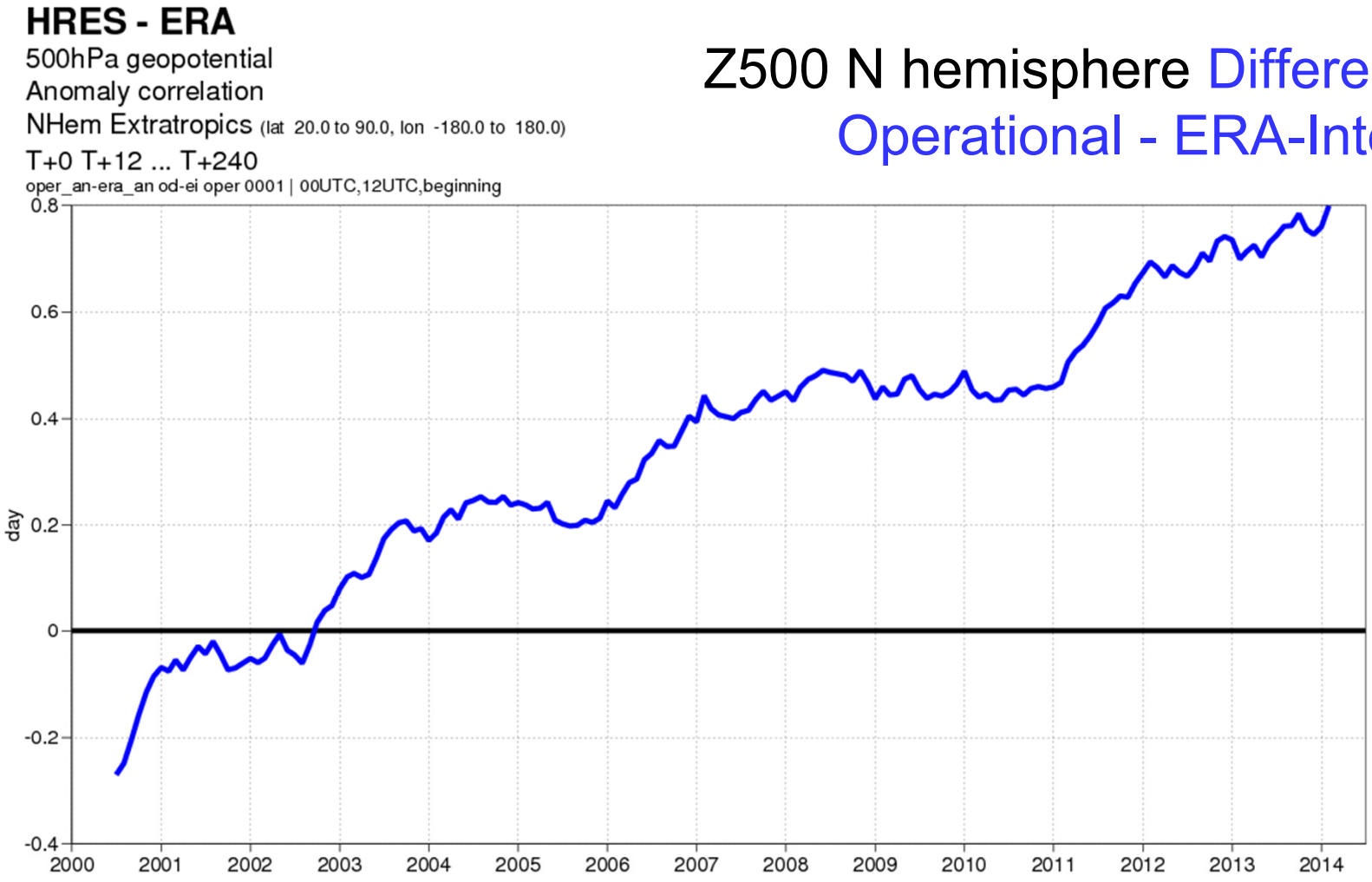

Z500 N hemisphere Difference:
Operational - ERA-Interim

Forecast improvements for T_{850} caused by systems and obs for different regions

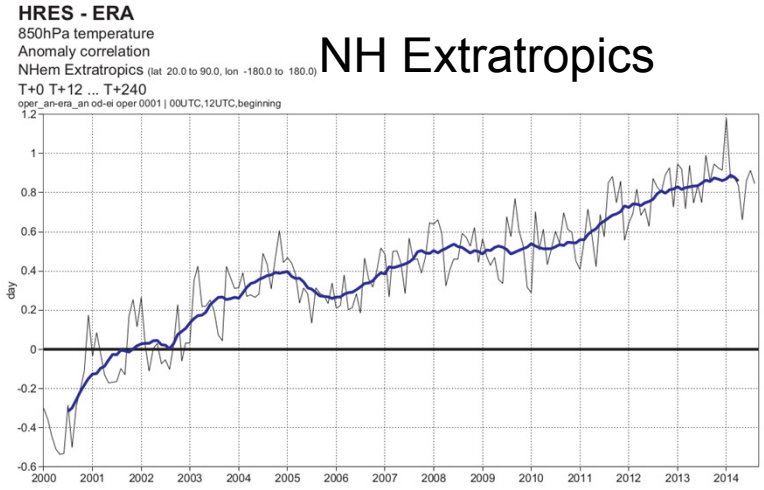

NH Extratropics

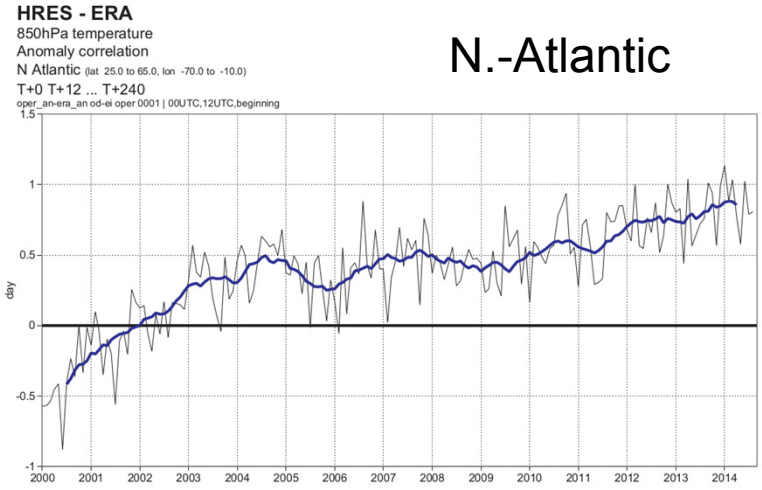

N.-Atlantic

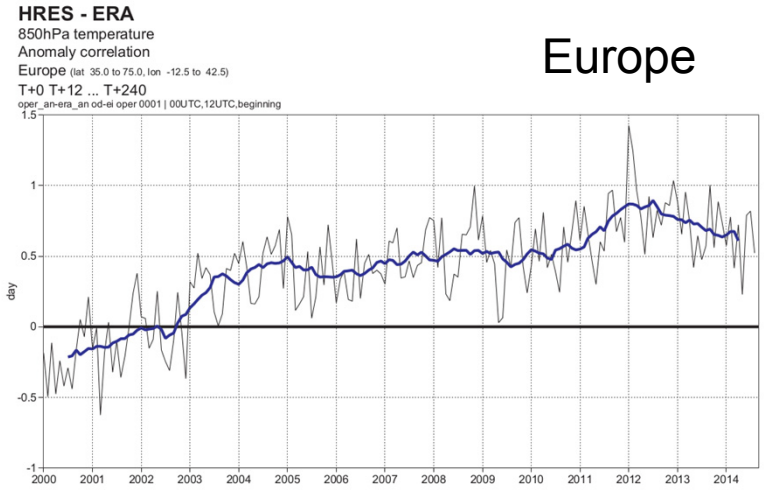

Europe

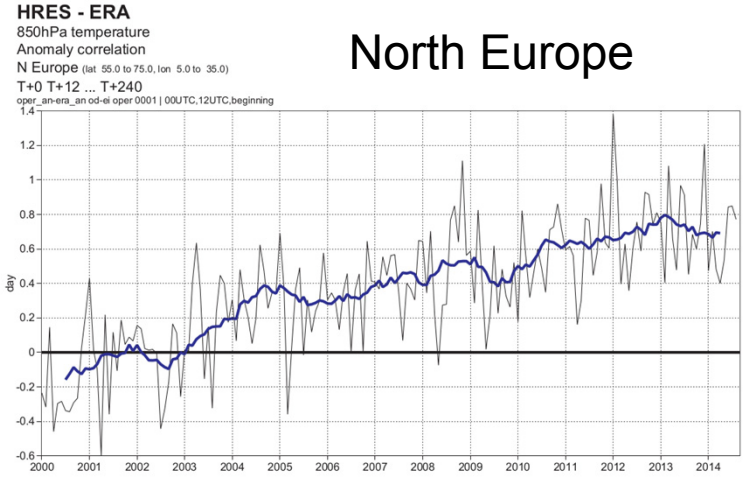

North Europe

Upward Trend in EPS (now: ENS)

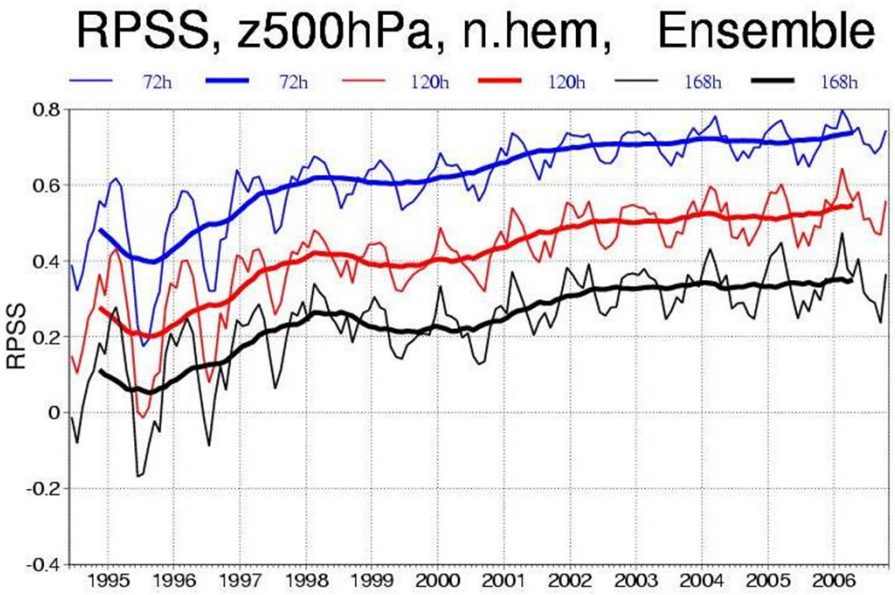

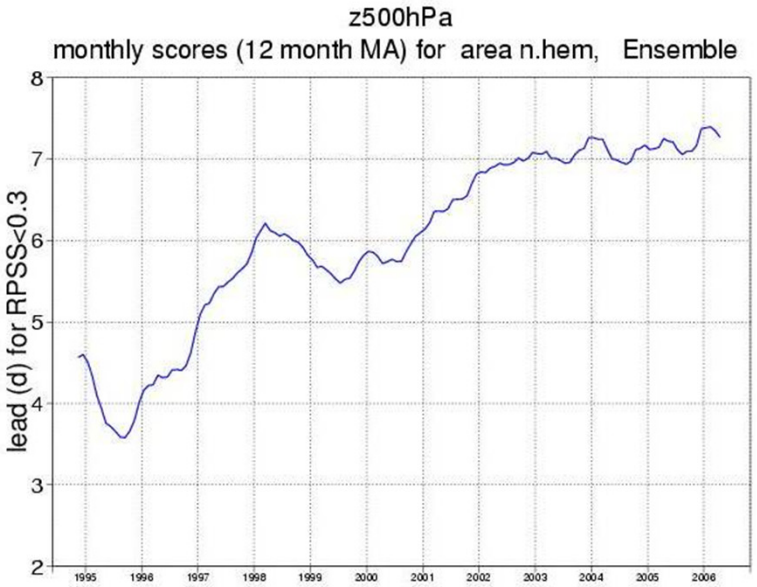

Upward Trend in High Res Deterministic over Last Decade

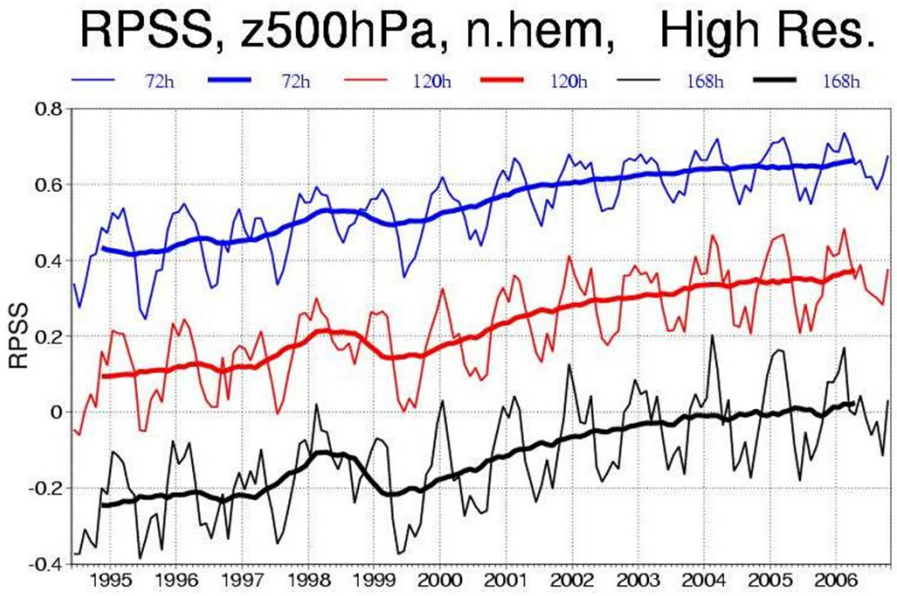

Simple mathematical systems possessing chaos

Logistic map

Lorenz «Butterfly»

Logistic map

$$x_{n+1} = r\,x_n(1-x_n)$$

population at year n

combined rate for reproduction and starvation

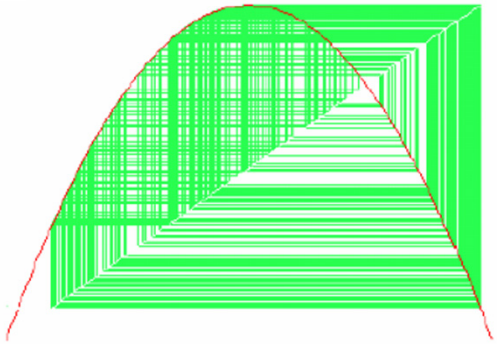

havior is chaos. There is another way to easier see these bifurcations. If the stable points, or stable

$X_n(r)$ when $n \to \infty$

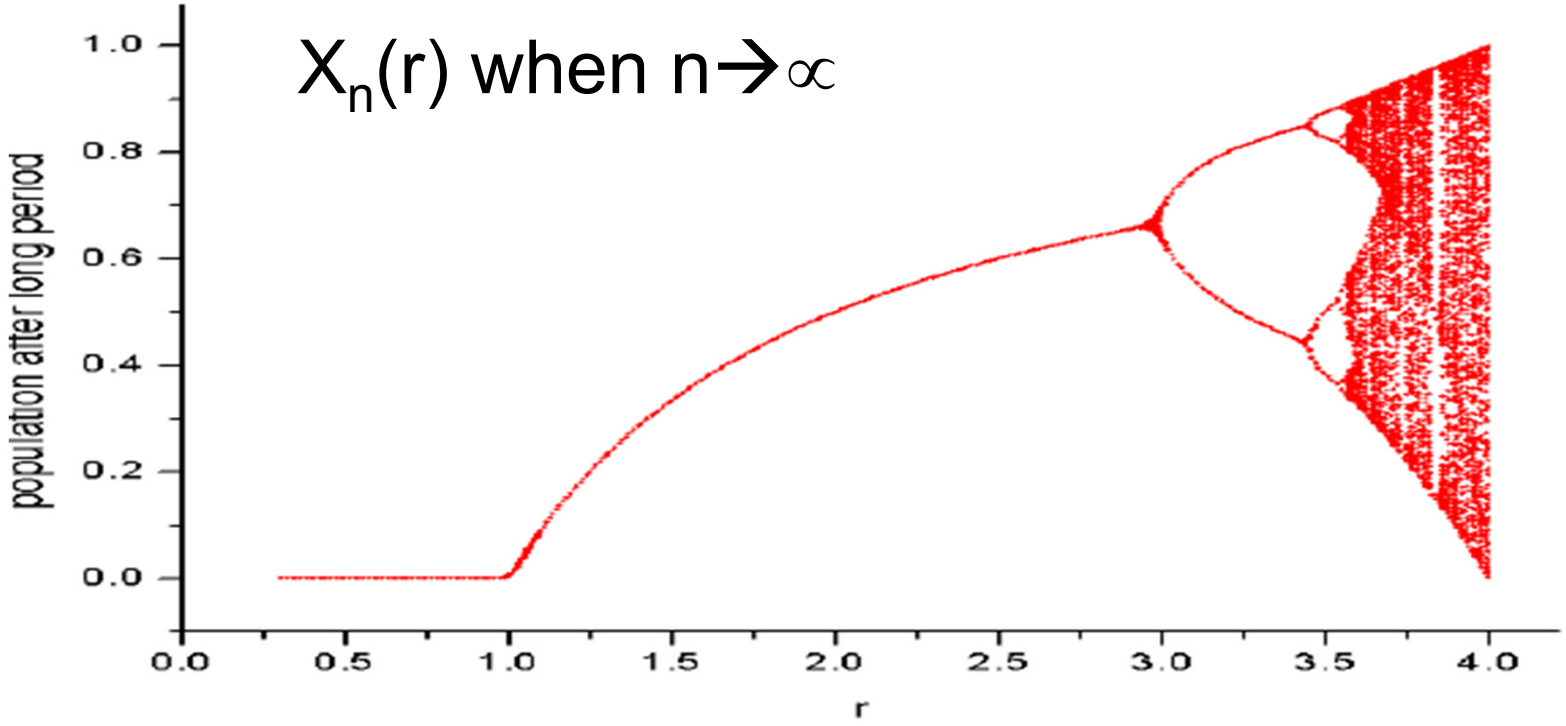

The Lyapunov exponent for the logistic map (estimated numerically)

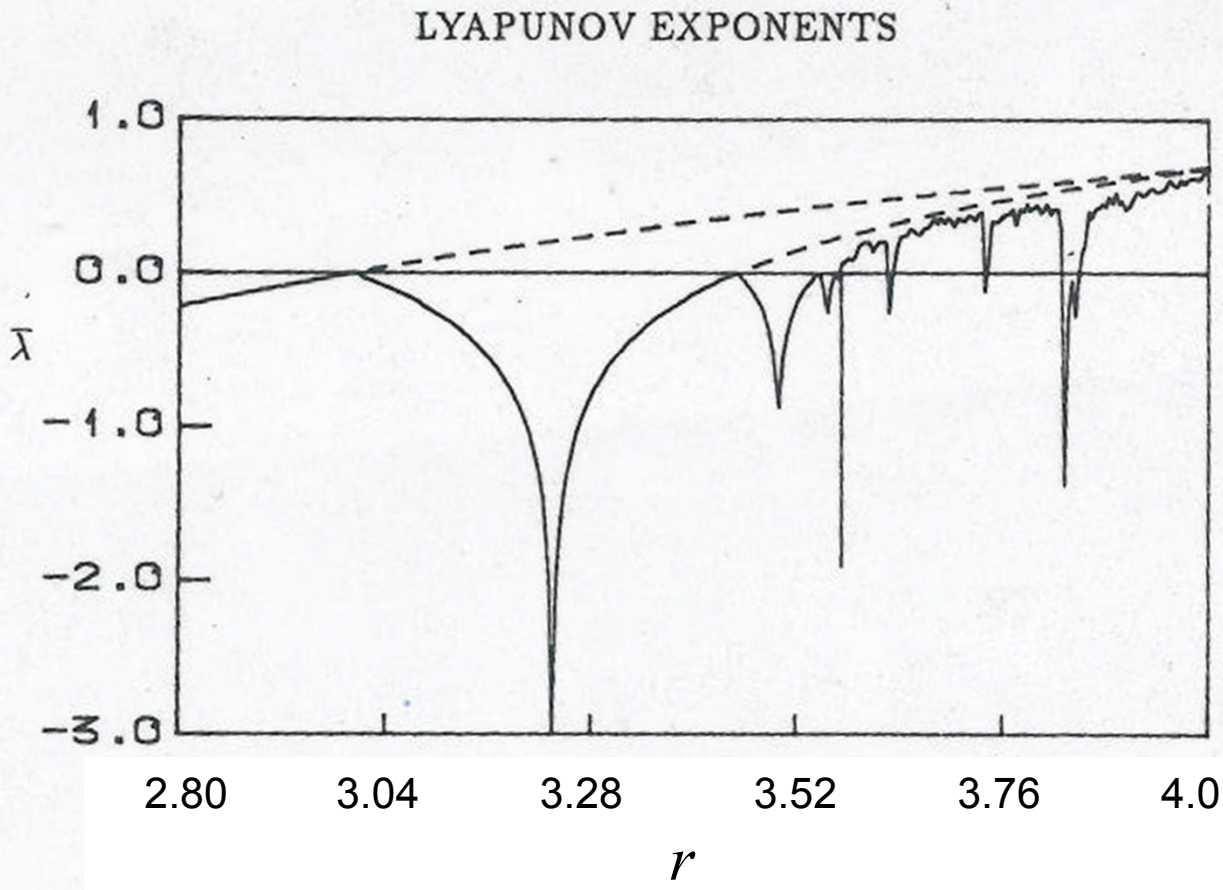

Figure 3.8 The Lyapunov characteristic exponent for the logistic map. The broken curves show the Lyapunov exponents for the unstable period one and period two orbits.

Chaos Theory concepts

Kalnay Ch 6.2-6.3

Phase space representation of the atmosphere as a dynamical system

Assume a phase space of dimension N where $\boldsymbol{X} = \begin{bmatrix} X_1 \\ \vdots \\ X_N \end{bmatrix}$ is a state vector.

Autonomous governing equations with initial state:

$$\frac{d\boldsymbol{X}}{dt} = \boldsymbol{F}(\boldsymbol{X}); \boldsymbol{X}(t_0) = \boldsymbol{X}_0; \boldsymbol{F} = \begin{bmatrix} F_1 \\ \vdots \\ F_N \end{bmatrix}$$

Unique solution for an arbitrary time $t > t_0$: $\boldsymbol{X}(t) = \boldsymbol{M}(\boldsymbol{X}_0)$; *i.e.* ***the trajectory***.

Conditions for stability with respect to small perturbations of the initial state are investigated by adding small increments to X_0 , integrate forward in time and neglect non-linear terms:

$$\frac{d}{dt}[\boldsymbol{X} + \boldsymbol{\delta x}] = \boldsymbol{F}(\boldsymbol{X} + \boldsymbol{\delta x}) \; ; \; \boldsymbol{\delta x}(t_0) = \boldsymbol{\delta x}_0$$

$$\Leftrightarrow \frac{d\boldsymbol{X}}{dt} + \frac{d}{dt}\boldsymbol{\delta x} \approx \boldsymbol{F}(\boldsymbol{X}) + \boldsymbol{J} \cdot \boldsymbol{\delta x} \; ; \boldsymbol{\delta x}(t_0) = \boldsymbol{\delta x}_0;$$

Tangent-Linear Model (TL) and its Propagator from time 0 to t

where the jacobian is evaluated along the non-linear solution trajectory:

$$\boldsymbol{J} = \left[\frac{\partial \boldsymbol{F}}{\partial \boldsymbol{X}}\right]_{\boldsymbol{X}(t)} = \begin{bmatrix} \frac{\partial F_1}{\partial X_1} & \cdots & \frac{\partial F_1}{\partial X_N} \\ \vdots & \ddots & \vdots \\ \frac{\partial F_N}{\partial X_1} & \cdots & \frac{\partial F_N}{\partial X_N} \end{bmatrix}_{\boldsymbol{X}(t)}$$

The ***Tangent-Linear Model (TL),*** is then:

$$\frac{d}{dt}\boldsymbol{\delta x} = \boldsymbol{J} \cdot \boldsymbol{\delta x}; \quad \boldsymbol{\delta x}(t_0) = \boldsymbol{\delta x}_0$$

and the solution is: $\boldsymbol{\delta x}(t) = \boldsymbol{L}(t_0, t) \cdot \boldsymbol{\delta x}_0$, where the ***propagator*** *or* ***resolvent*** is:

$$\boldsymbol{L}(t_0, t) = \left[\frac{\partial \boldsymbol{M}}{\partial \boldsymbol{X}}\right]_{\boldsymbol{X}(t)} = \begin{bmatrix} \frac{\partial M_1}{\partial X_1} & \cdots & \frac{\partial M_1}{\partial X_N} \\ \vdots & \ddots & \vdots \\ \frac{\partial M_N}{\partial X_1} & \cdots & \frac{\partial M_N}{\partial X_N} \end{bmatrix}_{\boldsymbol{X}(t)}$$

Tangent-Linear Model (TL) and its Propagator from time 0 to t

If $X(t)$ is a fixed point (a constant), then J is a constant, and we can formally write:

$$L(t_0, t) = e^{J(t-t_0)}$$

If the eigenvalues of J are μ_i, then the eigenvalues of L are $\Lambda_i = e^{\mu_i (t-t_0)}$, $i=1, \ldots, N$.

and for non-constant $X(t)$ and J, this can be generalized to:

$$L(t_0, t) = e^{\int_{t_0}^{t} J\, dt}$$

For numerical integrations, time is stepped forward in K steps, Δt , and we can define:

$$L(t_0, t) = L_{K-1} \cdot \ldots \cdot L_k \cdot \ldots \cdot L_0 = \prod_{k=0}^{K-1} L_k = exp\left[\sum_{k=0}^{K-1} J_k \, \Delta t\right]$$

where $L_k = L(t_k, t_k + \Delta t)$.

Assume that eigenvalue no. i of L_k and J_k are Λ_i^k and μ_i^k respectively, and define:

$$\Lambda_i(t) = \prod_{k=0}^{K-1} \Lambda_i^k \, ; i = 1, \ldots, N$$

Lyapunov exponents

Assume that eigenvalue no. i of $\boldsymbol{L}_k$ and $\boldsymbol{J}_k$ are Λ_i^k and μ_i^k respectively, and define:

$$\Lambda_i(t) = \prod_{k=0}^{K-1} \Lambda_i^k \; ; i = 1, \ldots, N$$

The Lyapunov exponent no. i is then:

$$\lambda_i = \lim_{t\to\infty} \frac{1}{t - t_0} ln|\Lambda_i(t)| = \lim_{t\to\infty} \frac{1}{t - t_0} \sum_{k=0}^{K-1} ln\left|\Lambda_i^k\right|$$

= the growth-rate of small perturbations averaged over the attractor. This is a **global** property; i.e. it represents an average property for the entire attractor set of the dynamic system. If one or more $\lambda_i > 0$, there are at list some directions in phase-space along which arbitrary initial perturbations will grow.

$\frac{1}{\Delta t} ln\left|\Lambda_i^k\right|$ is the ***local Lyapunov exponent no. i at time-step k.***

LOCAL LYAPUNOV VECTORS

$$\boldsymbol{l}_1(t) = \lim_{s\to\infty} \boldsymbol{L}(t-s,t)\,\boldsymbol{y}(t-s)$$

the leading local Lyapunov exponent (i.e. no. 1): $l_1 = \frac{1}{\Delta t} ln \frac{\|\boldsymbol{l}_1(t+\Delta t)\|}{\|\boldsymbol{l}_1(t)\|}$

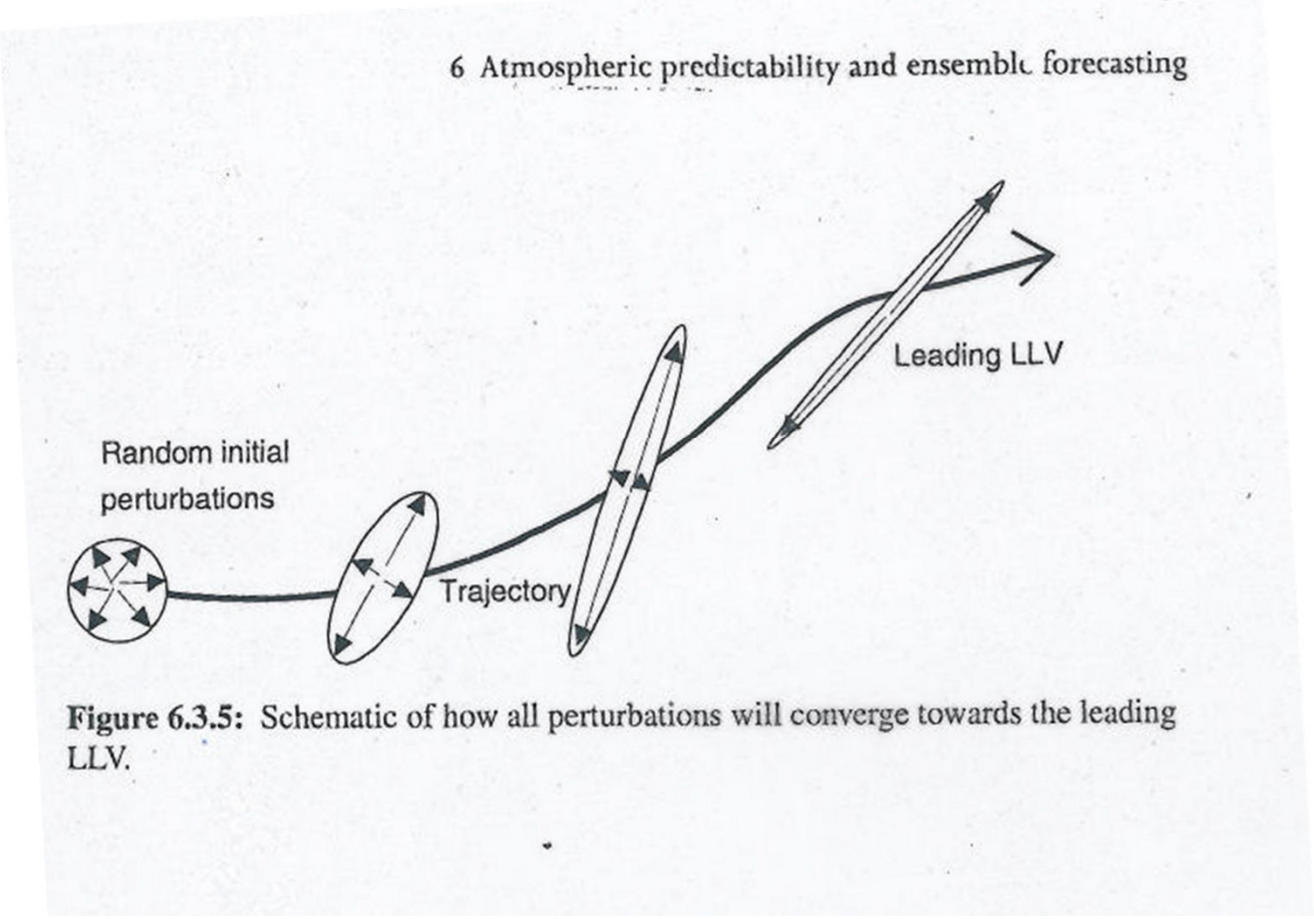

Figure 6.3.5: Schematic of how all perturbations will converge towards the leading LLV.

The Lorenz three-parameter model. «Butterfly»

$$\begin{aligned} \dot{X} &= -\sigma(X - Y) \\ \dot{Y} &= rX - Y - XZ \\ \dot{Z} &= b(XY - Z) \end{aligned}$$

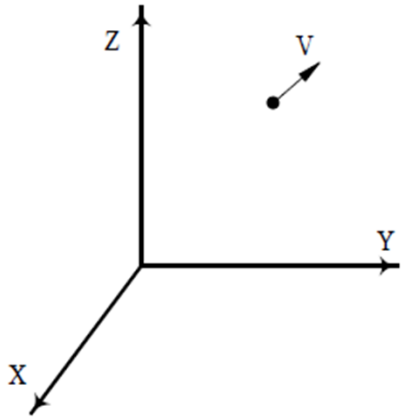

Setting $\dot{x} = \dot{y} = \dot{z} = 0$ gives fixed points at:

- the origin, (0,0,0); stable for $0 < r < 1$
- C^+, $(\sqrt{b(r-1)}, \sqrt{b(r-1)}, r-1)$;
- C^-, $(-\sqrt{b(r-1)}, -\sqrt{b(r-1)}, r-1)$.

The C^+ and C^- fixed points only exist for $r > 1$

C^+ and C^- are stable for

$$1 < r < r_H = \frac{\sigma(\sigma + b + 3)}{\sigma - b - 1}$$

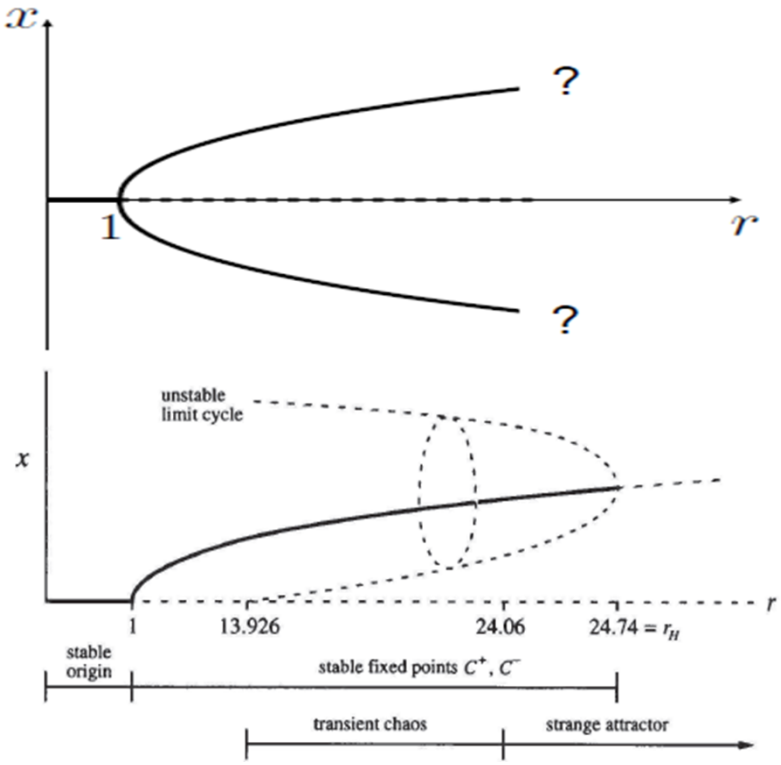

The Lorenz three-parameter model. «Butterfly»

$(r = 28, \sigma = 10, b = 8/3)$:

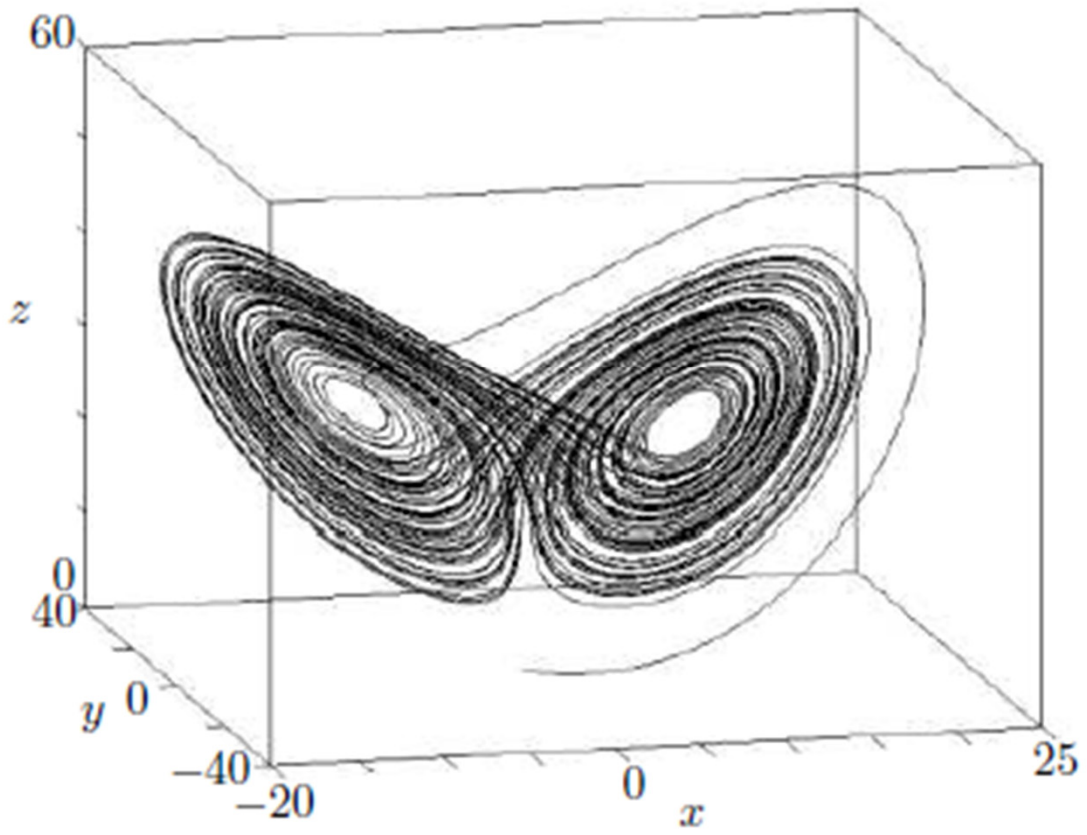

The growth of perturbations:
linear – weakly non-linear – strongly non-linear

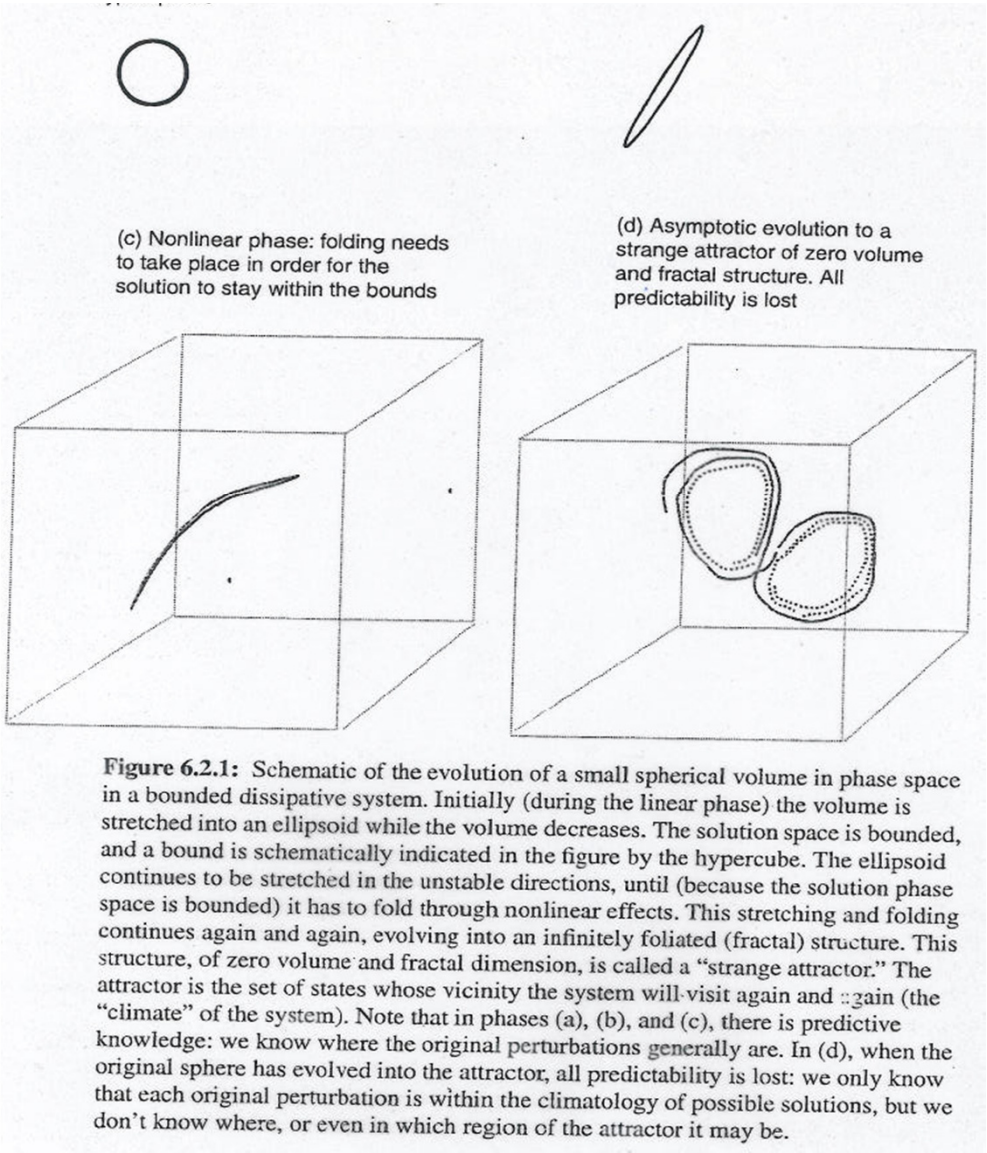

Figure 6.2.1: Schematic of the evolution of a small spherical volume in phase space in a bounded dissipative system. Initially (during the linear phase) the volume is stretched into an ellipsoid while the volume decreases. The solution space is bounded, and a bound is schematically indicated in the figure by the hypercube. The ellipsoid continues to be stretched in the unstable directions, until (because the solution phase space is bounded) it has to fold through nonlinear effects. This stretching and folding continues again and again, evolving into an infinitely foliated (fractal) structure. This structure, of zero volume and fractal dimension, is called a "strange attractor." The attractor is the set of states whose vicinity the system will visit again and again (the "climate" of the system). Note that in phases (a), (b), and (c), there is predictive knowledge: we know where the original perturbations generally are. In (d), when the original sphere has evolved into the attractor, all predictability is lost: we only know that each original perturbation is within the climatology of possible solutions, but we don't know where, or even in which region of the attractor it may be.

Why probabilistic weather prediction?

Why not categorical («deterministic») forecasts

Example case: State-dependent forecast quality

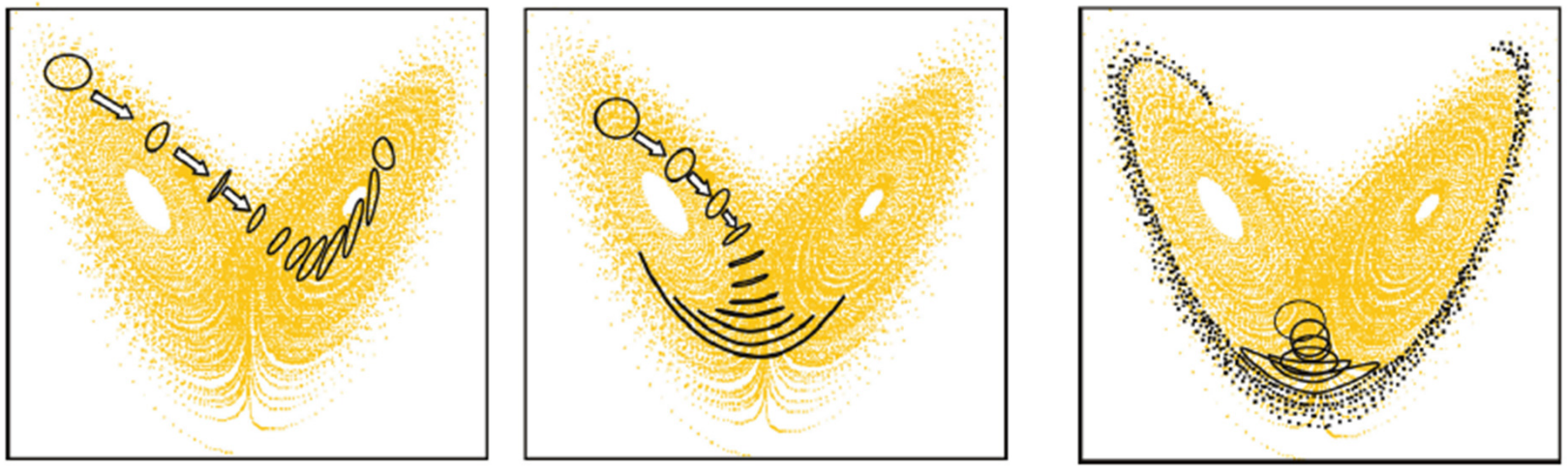

Figure 2: Phase-space evolution of an ensemble of initial points on the *Lorenz* (1963) attractor, for three different sets of initial conditions. Predictability is a function of initial state.

Example case: diagnose state dependence, ensemble spread and forecast uncertainty

«plumes»

For London UK

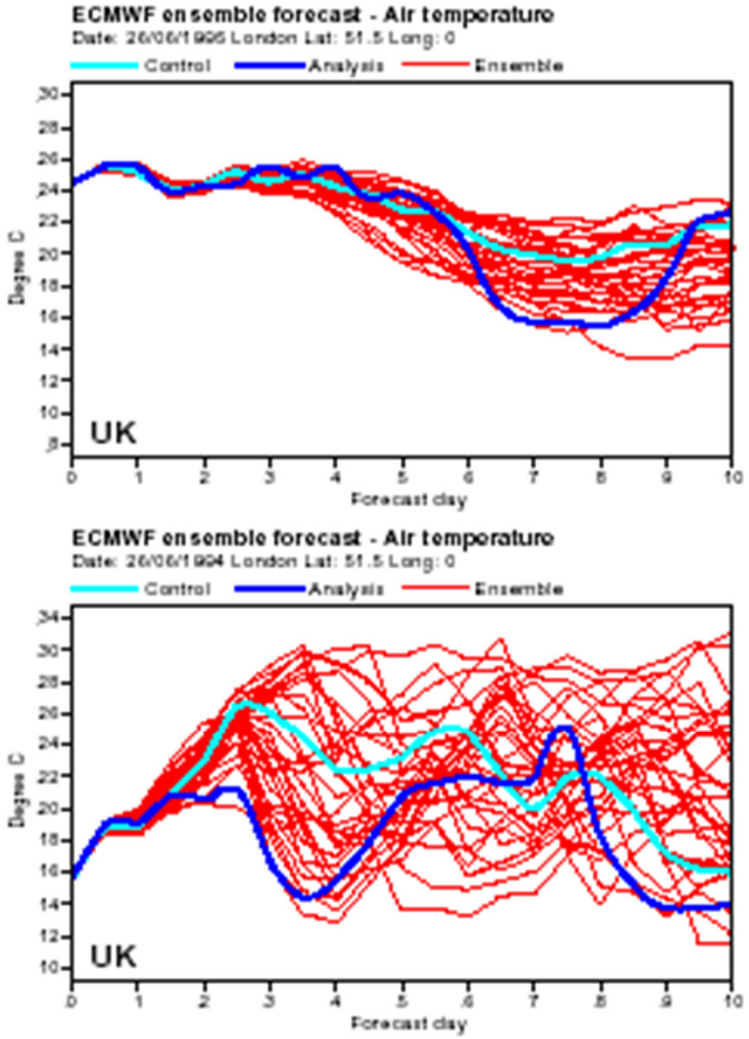

26.06.1995 00utc

26.06.1994 00utc

Figure 4. ECMWF forecasts for air temperature in London started from (a) 26 June 1995 and (b) 26 June 1994.

Example case: diagnose state dependence, ensemble spread and forecast uncertainty

«spaghetti maps»

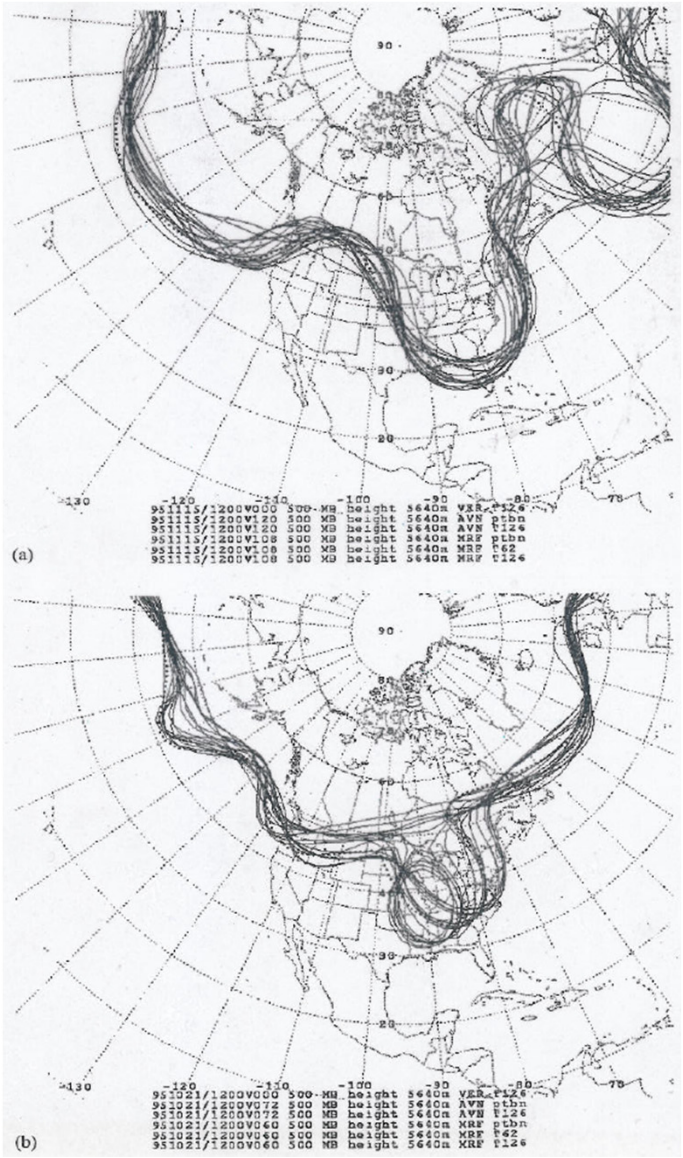

15.11.1995 12utc + 5days

22.10.1995 12utc + 2.5days

Example: sensitive dependence of initial conditions

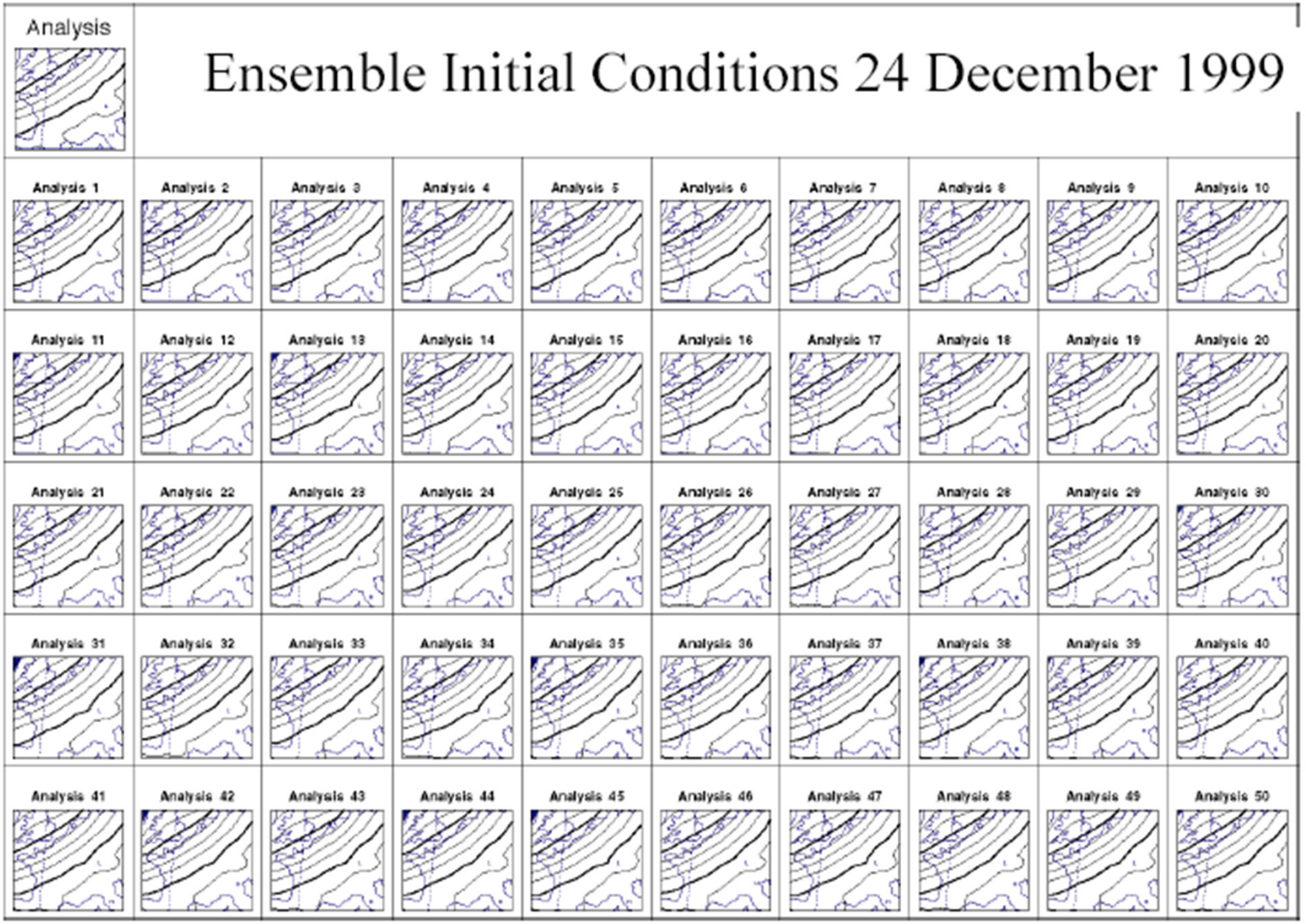

Example: sensitive dependence of initial conditions

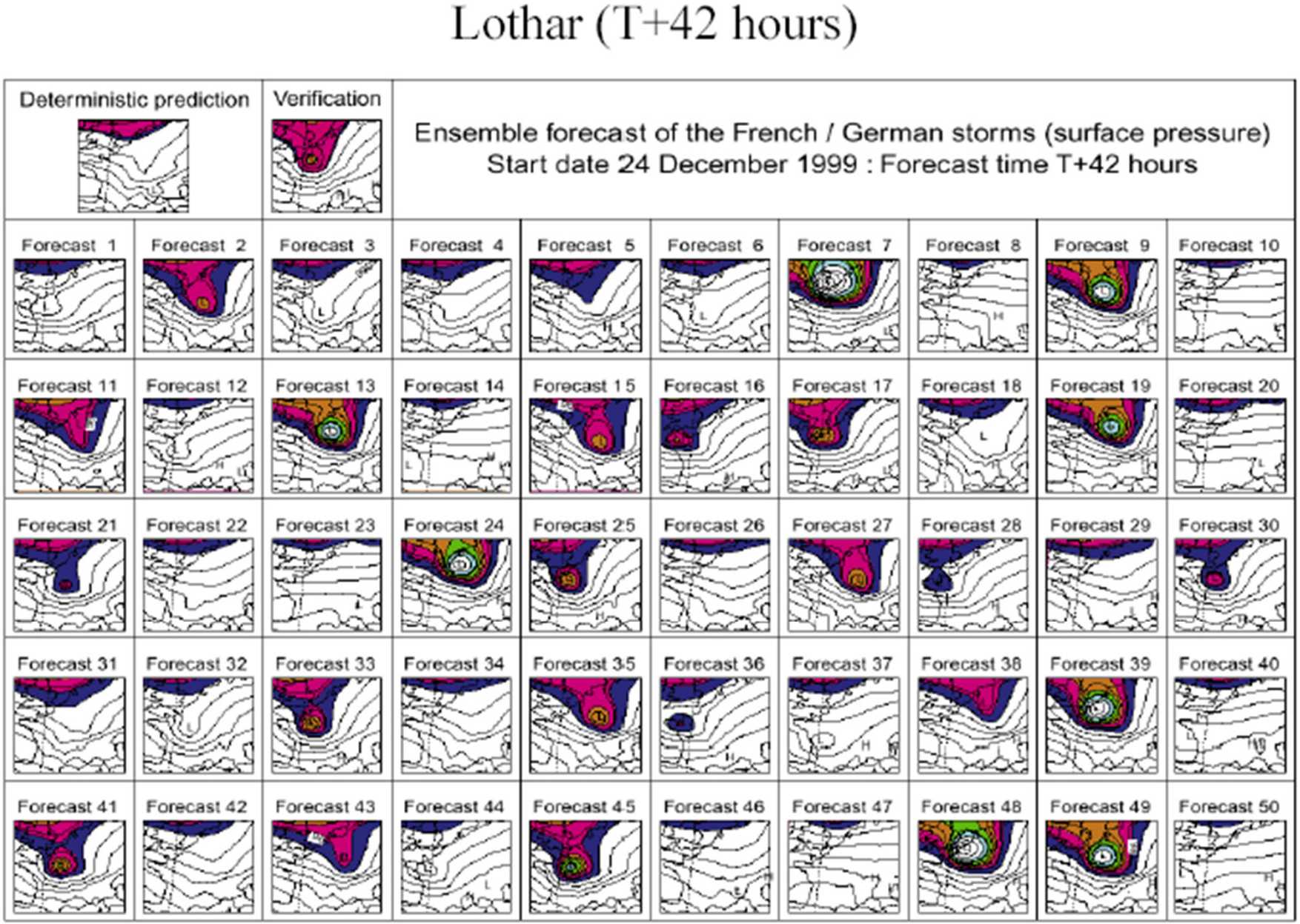

But: Deterministic forecasts for 1-2 days are nearly perfect !
- for z500

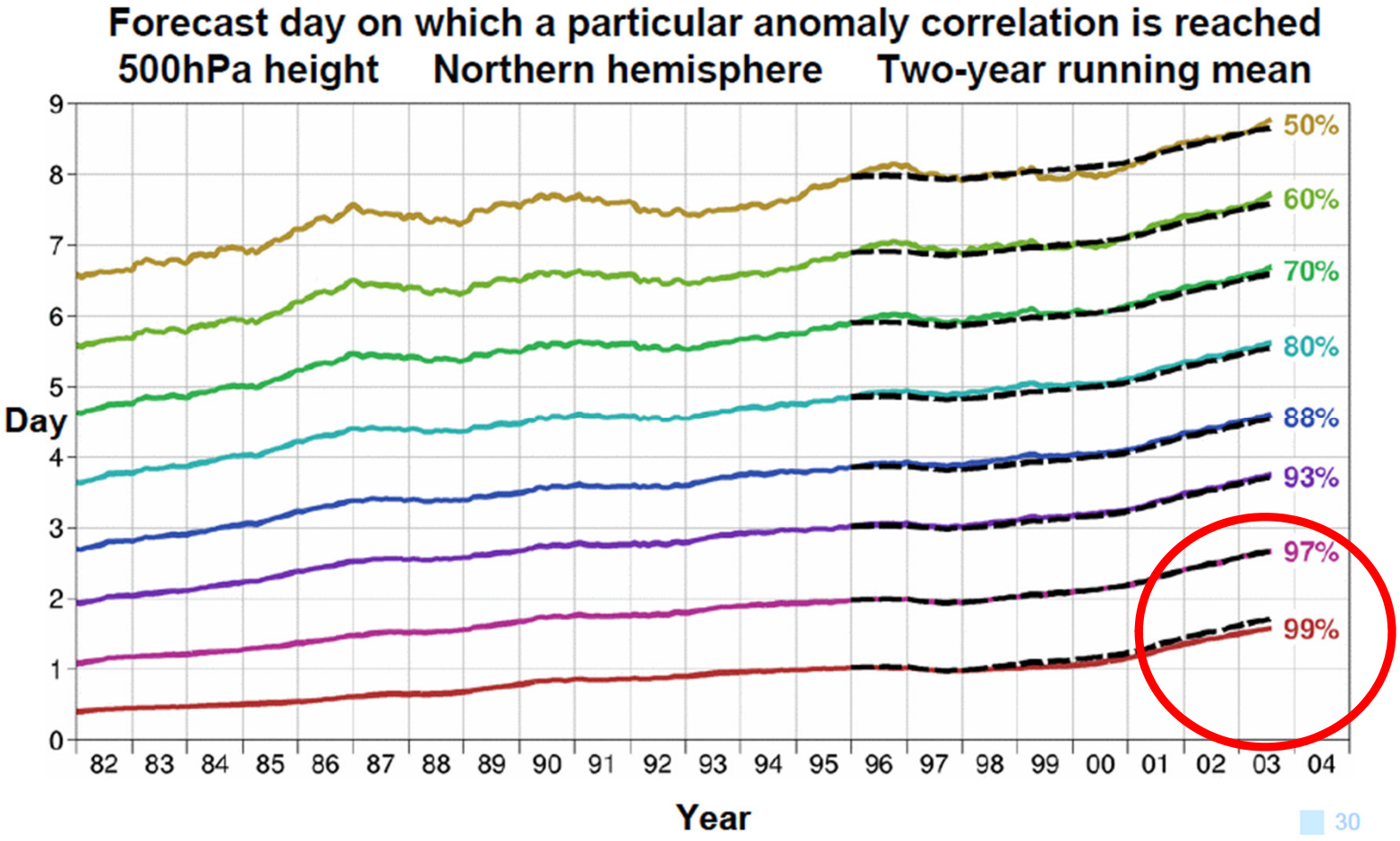

NWP quality for 500hPa geopotential heights

Courtesy: A. Simmons; ECMWF

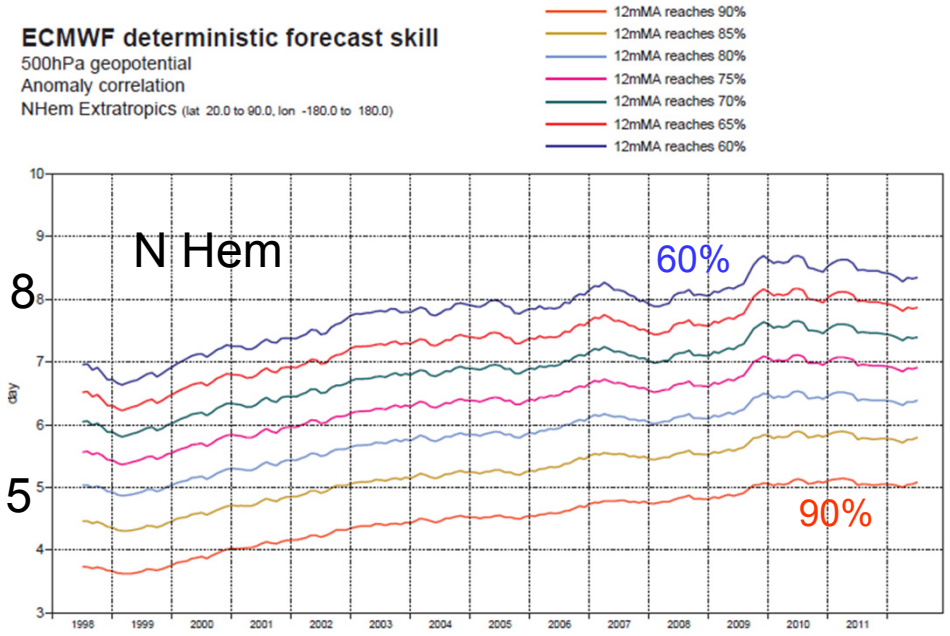

Deterministic forecasts for 1-2 days are nearly perfect !

- for z500

Forecast length when ACC=x%

X=90,85,80,75,70,65,60

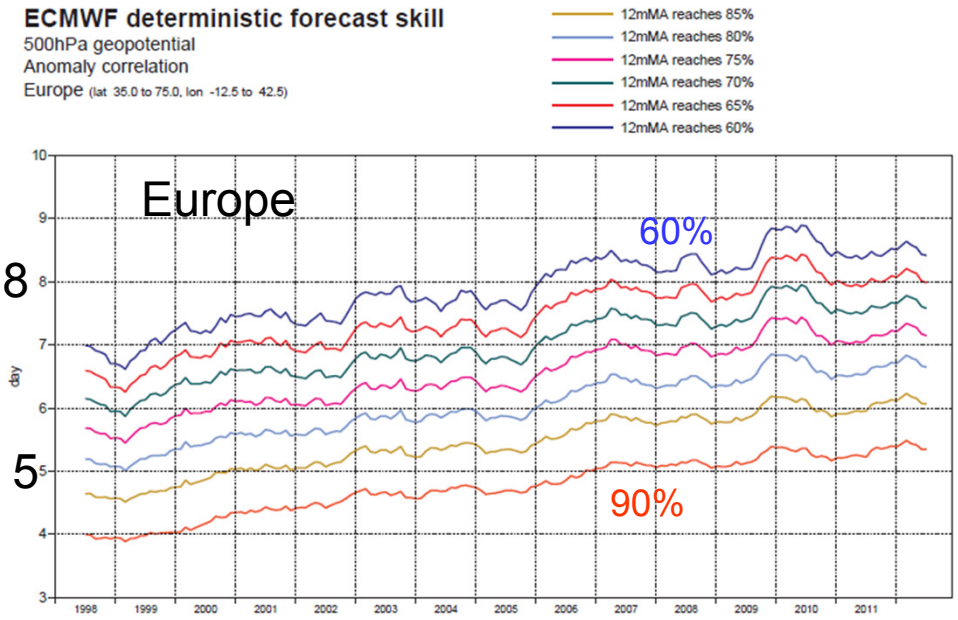

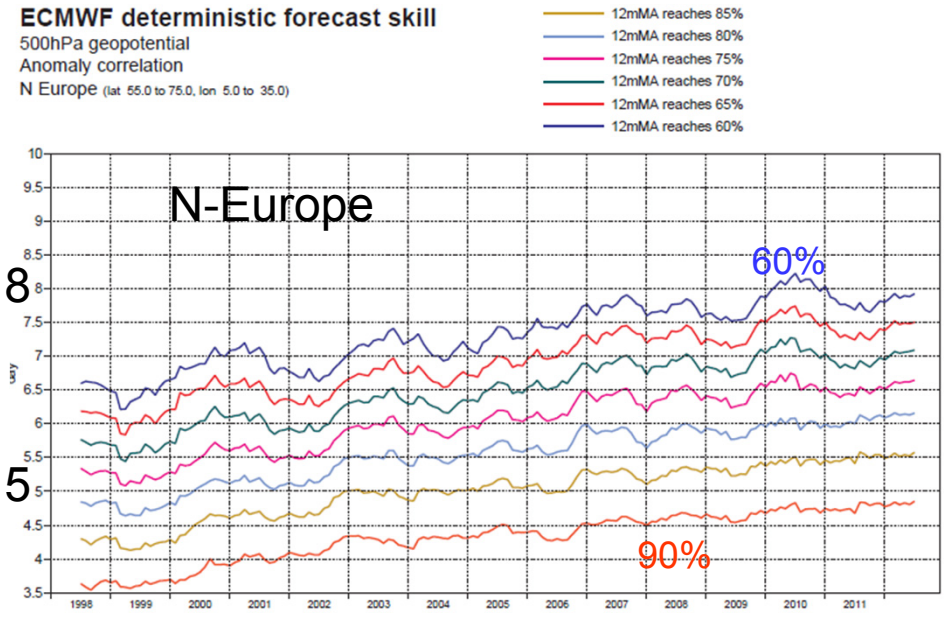

ECMWF operational verification

Brier Skill Score for 96h ECMWF EPS for selected events

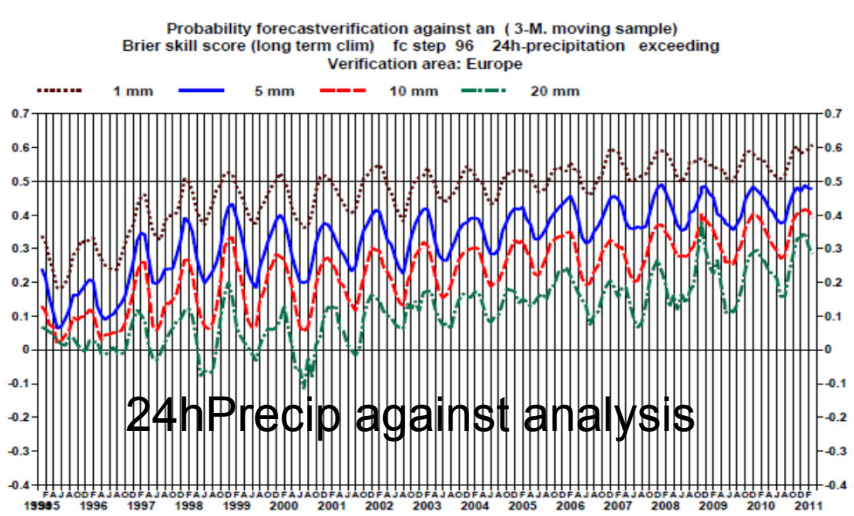

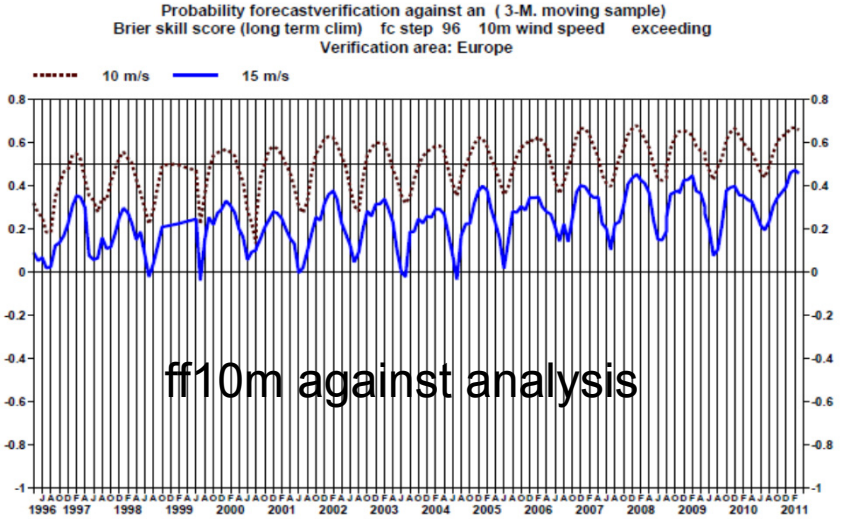

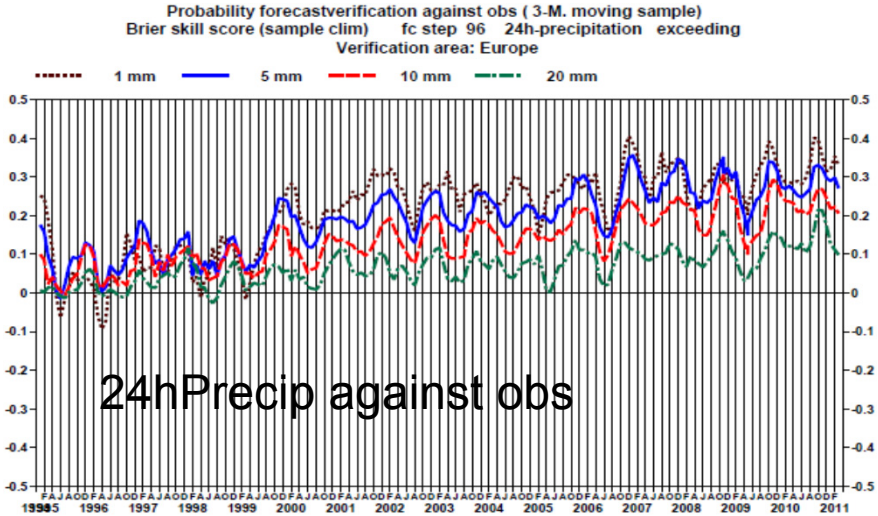

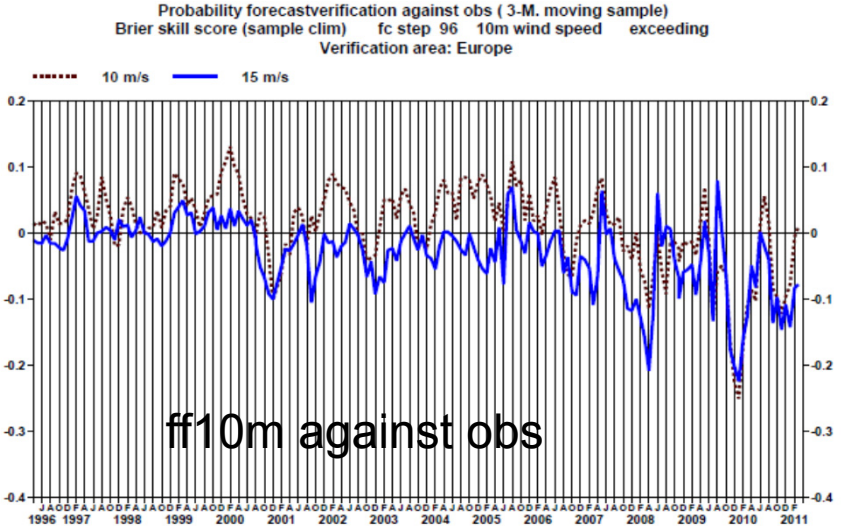

The predictability depends on the spatial scales

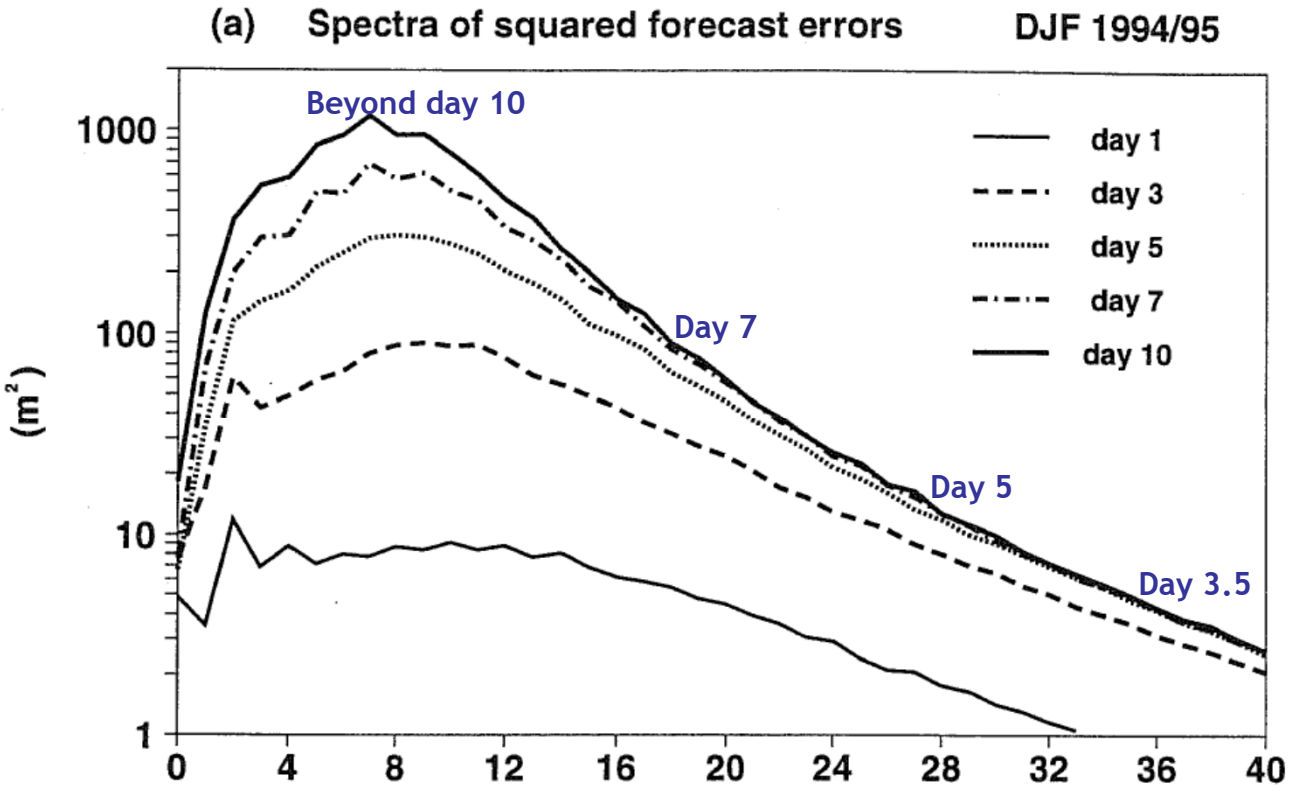

Except: Strong local forcing which are well described increases the predictability also for smaller scales (adjustments og large-scale patterns to local forcing: topography, coastlines, land-use contrasts etc.)

Predictability as a function of the spatial extension of weather systems

Spectra of mean-square 850hPa temperature errors

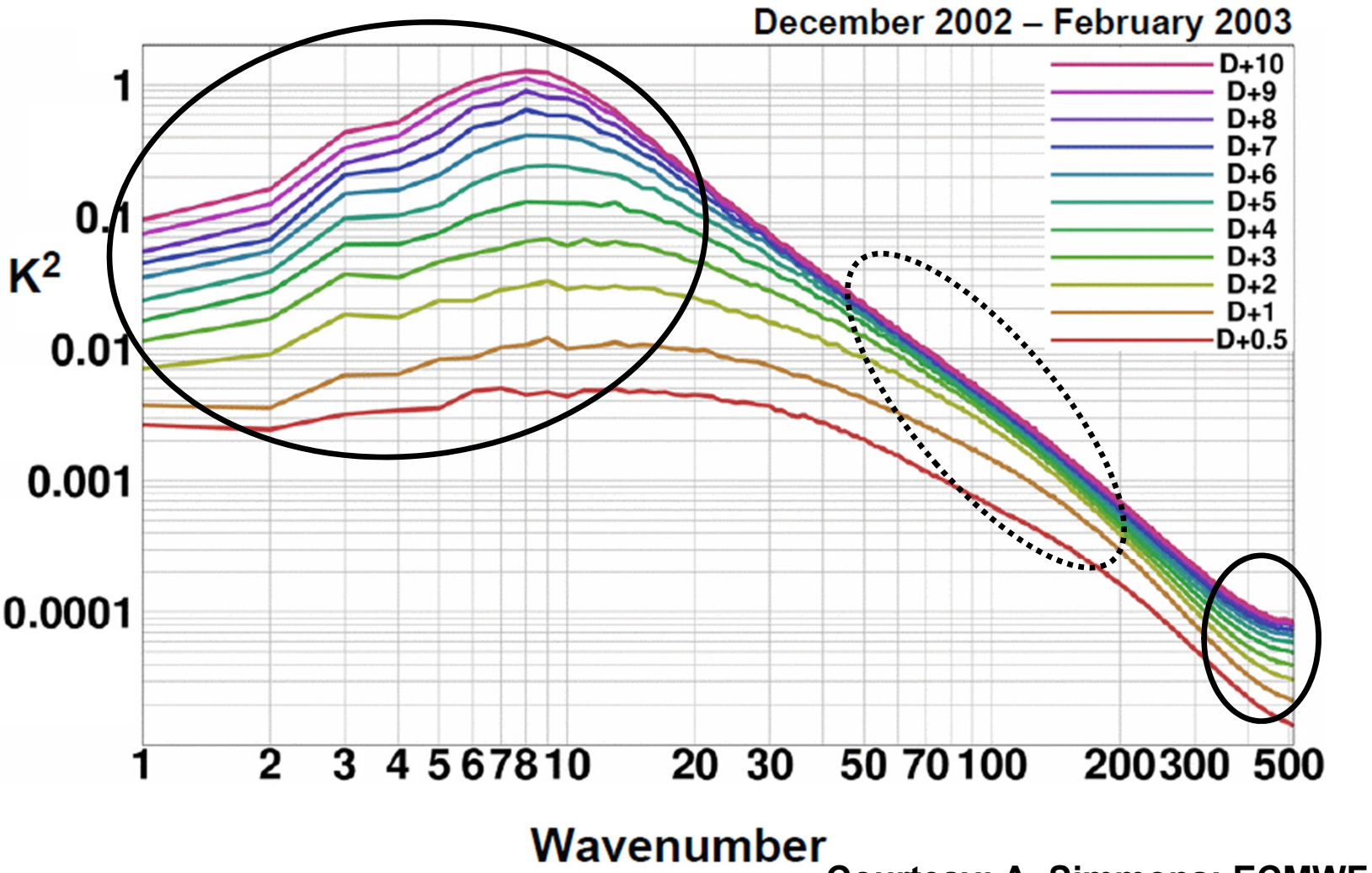

Courtesy: A. Simmons; ECMWF

Predictability as a function of the spatial extension of weather systems II

Forecast lead time when Rank Probability Skill Score (RPSS) for EC EPS of $Z_{500} < 0.3$

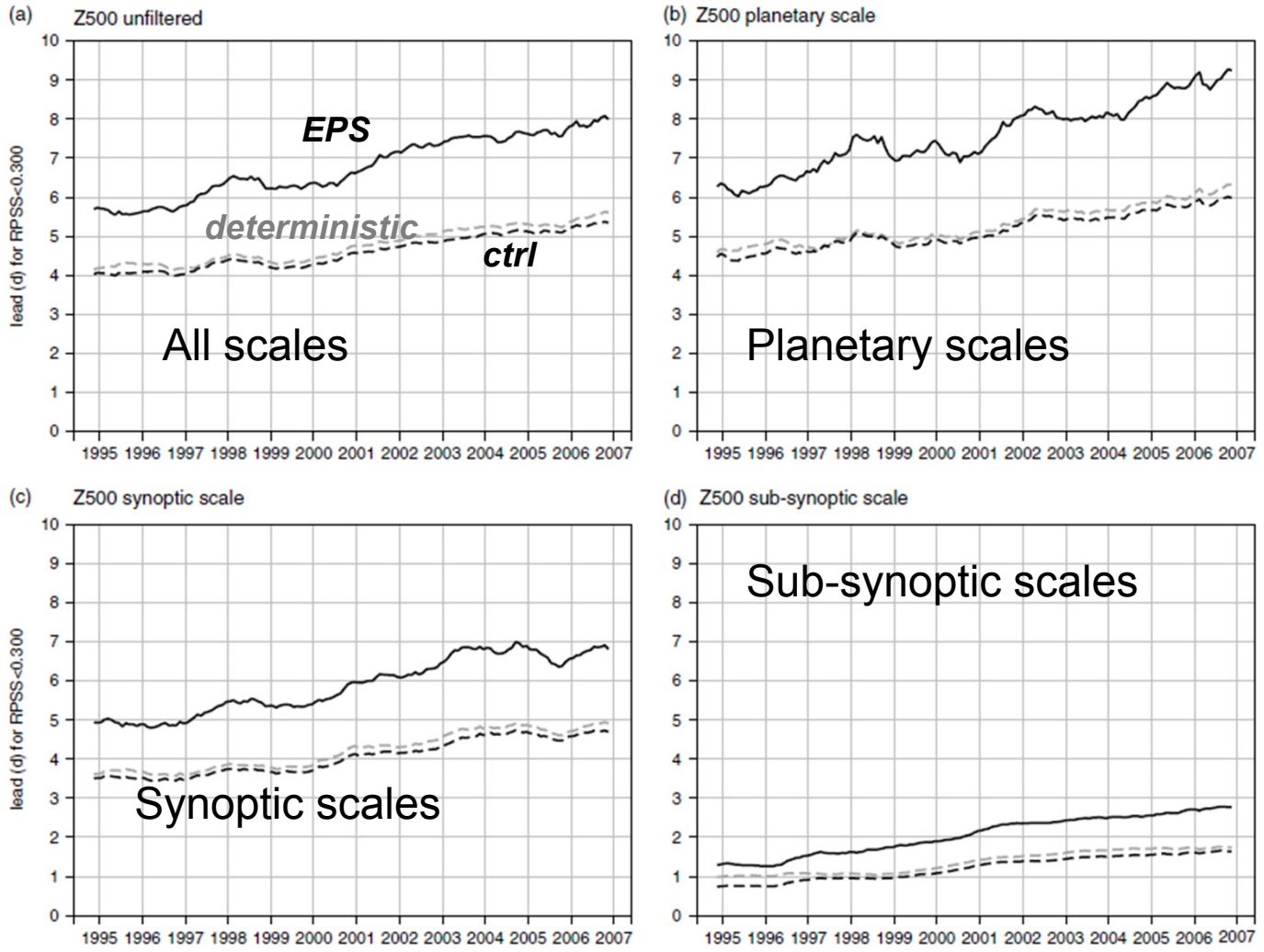

T. JUNG AND M. LEUTBECHER *Q. J. R. Meteorol. Soc.* **134**: 973–984 (2008)

Predictability as a function of the spatial extension of weather systems III

Spectra of mean-square 850hPa vorticity errors

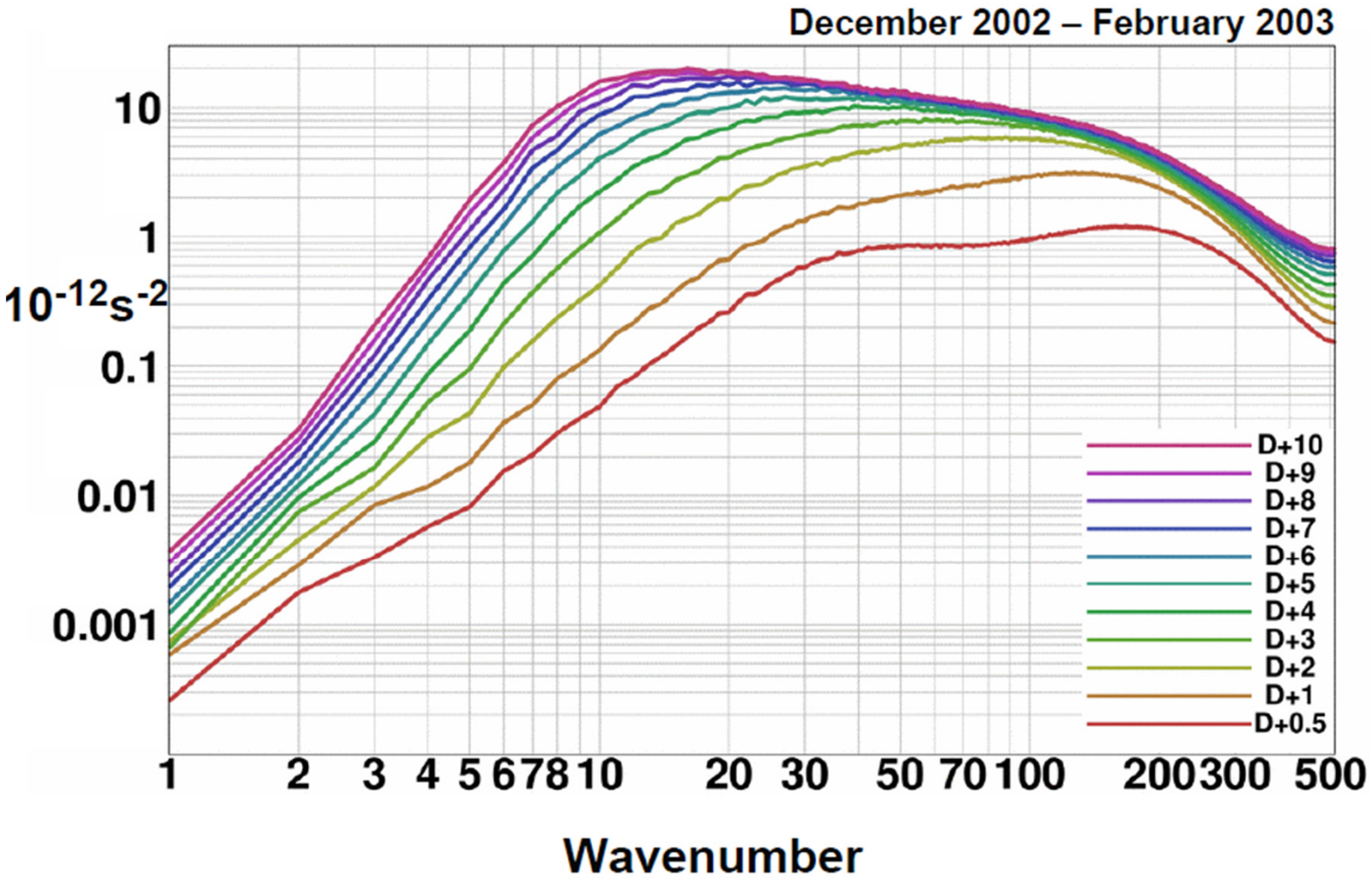

Courtesy: A. Simmons; ECMWF

The consensus forecast: Unpredictable components are filtered

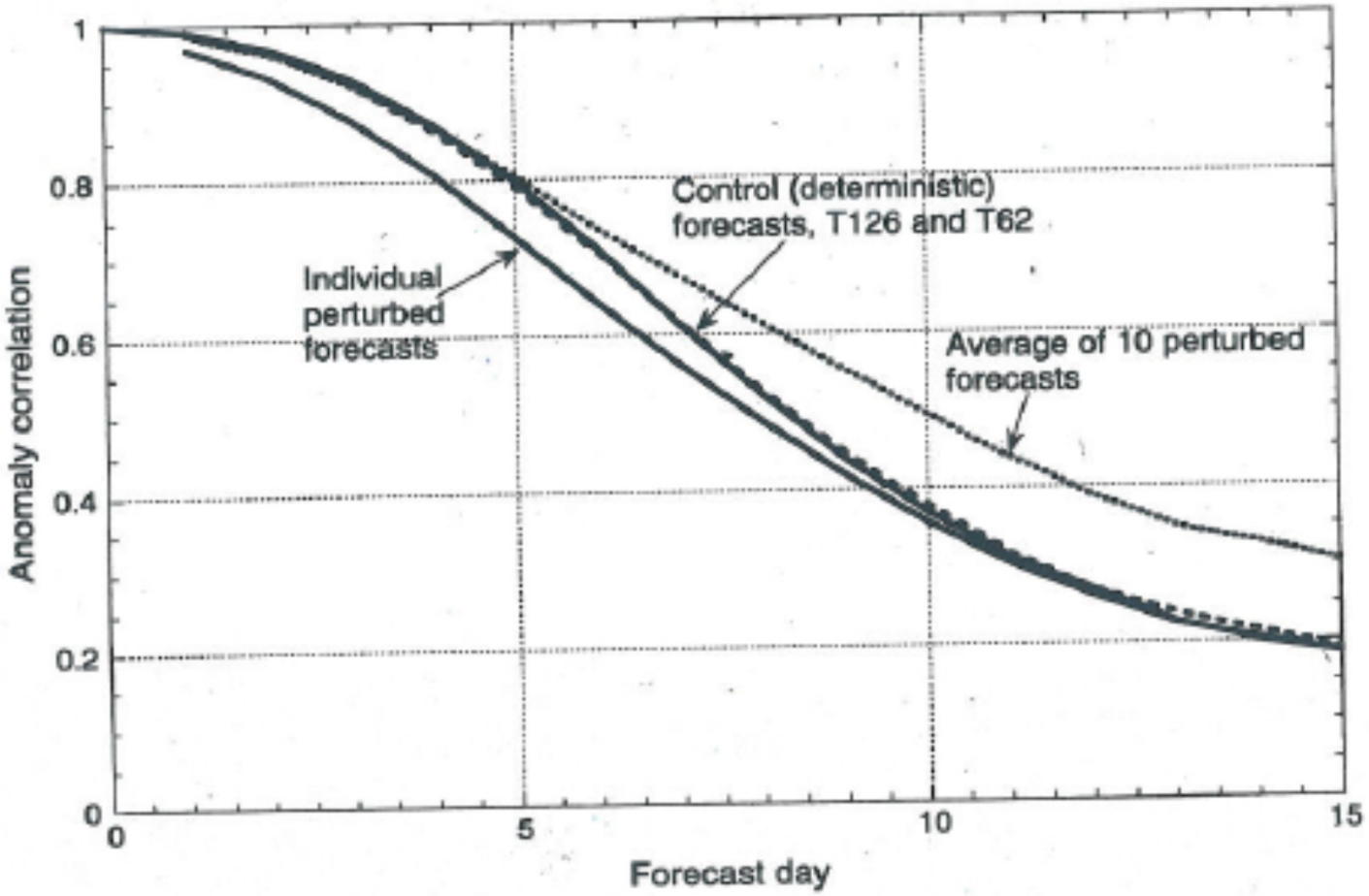

Winter 1997-98

Figure 1.7.1: Anomaly correlation of the ensembles during the winter of 1997–8 (controls, T_{126} and T_{62}, and ten perturbed ensemble forecasts). (Data courtesy Jae Schemm, of NCEP.)

In any case: to forecast extreme weather events categorically (either 100% or 0% certain) is overly optimistic.

”Regression towards the mean”:
when error-growth is non-linear, a majority of forecasts will tend towards maximum climatological occurrence

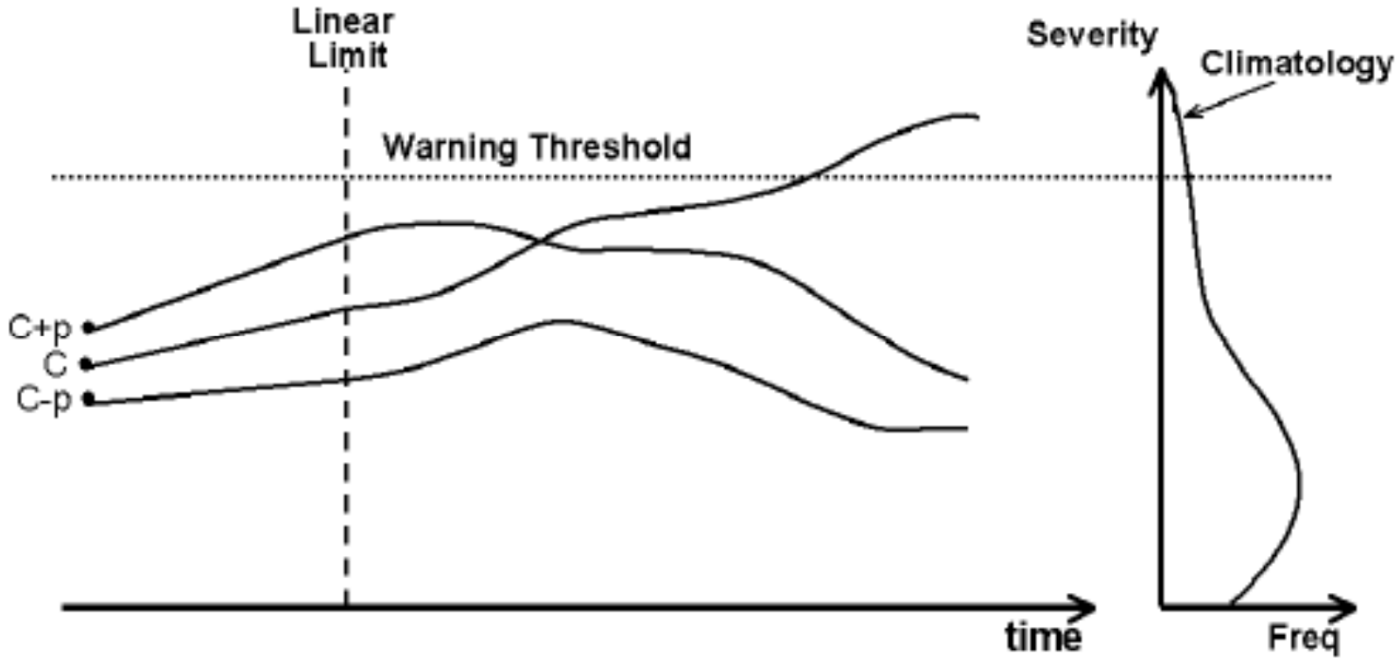

Probabilities

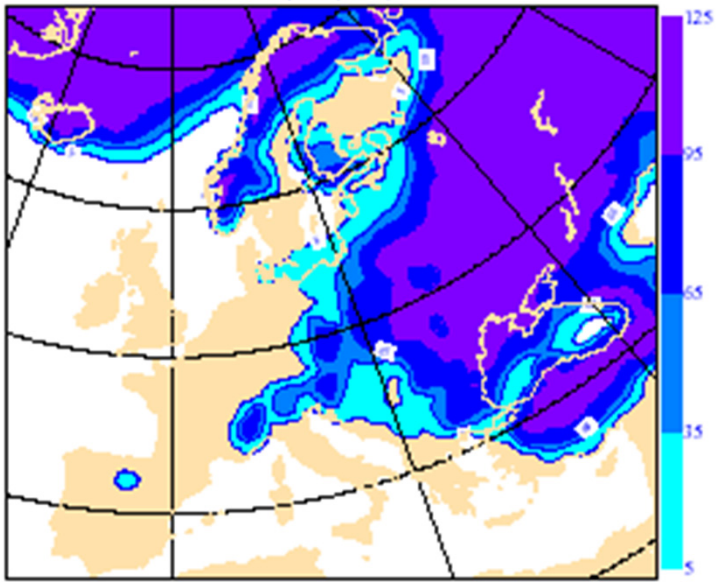

Prob T2m<0 C

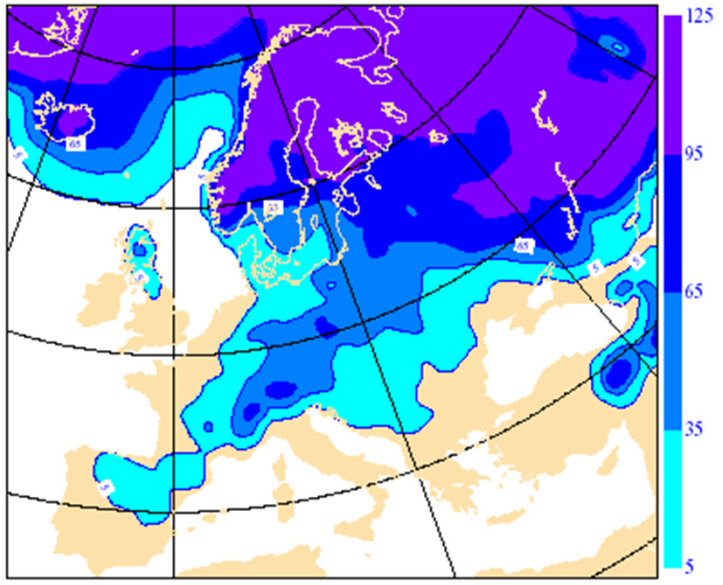

Val: 21.02.2004 12UT (+48)

Val: 24.02.2004 12 UT (+120)

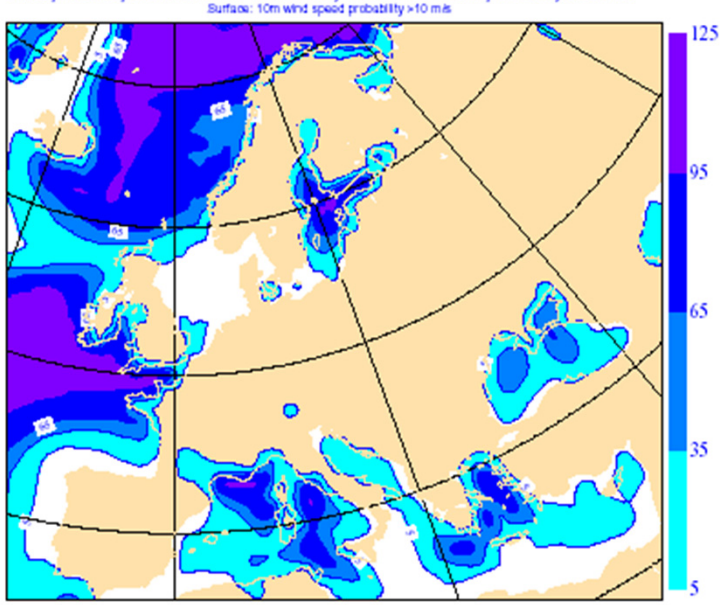

ff10m>10m/s

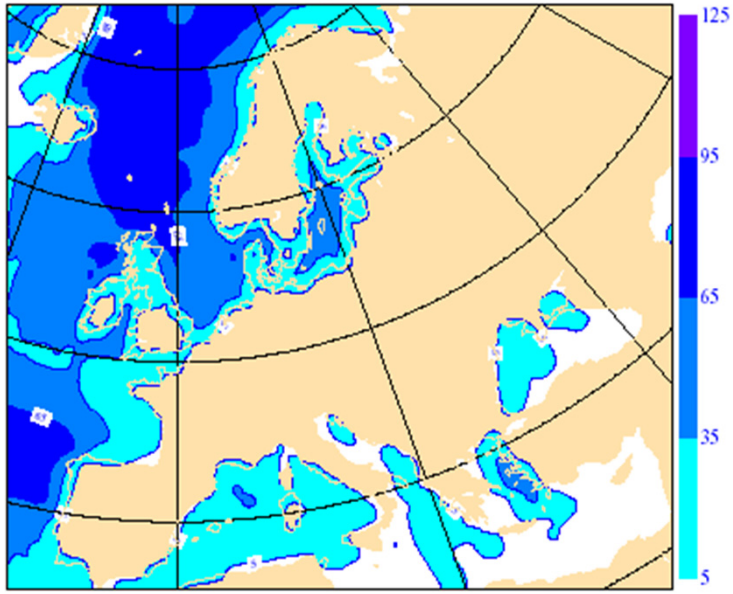

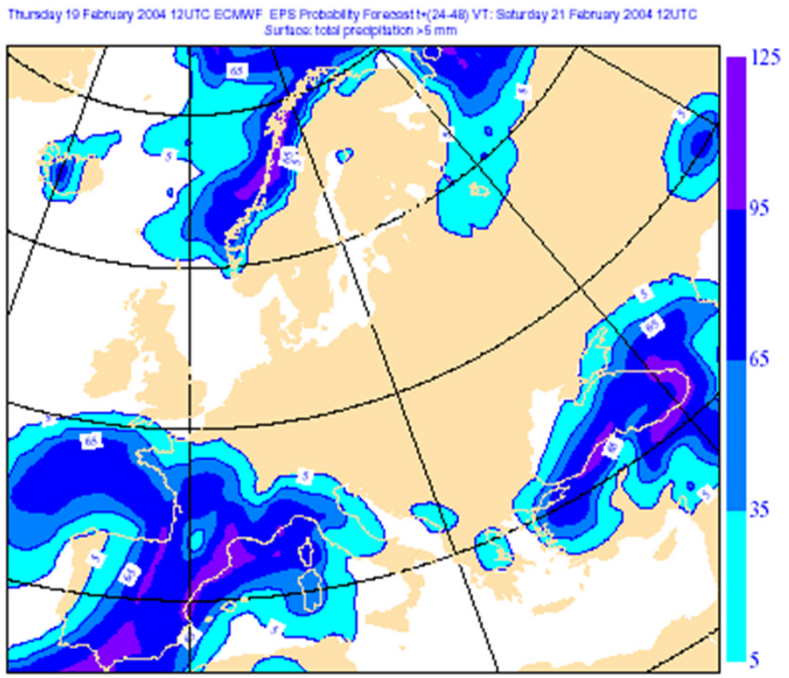

Prob
P>5 mm/24h

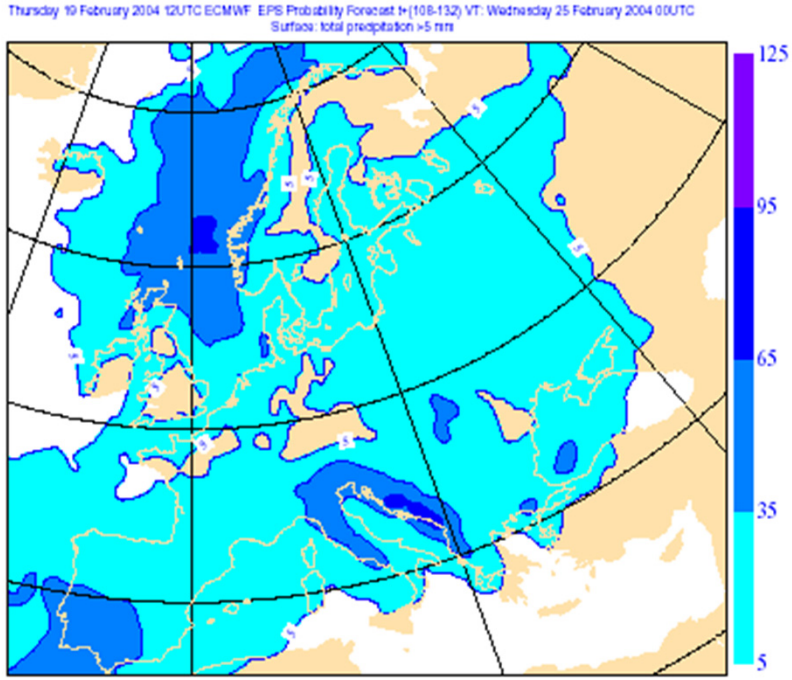

Val: 20.02.1995 12utc - 21.02.1995 12utc (+24-48)

Val: Tuesday 24.02.2004 0-24utc (+108-132)

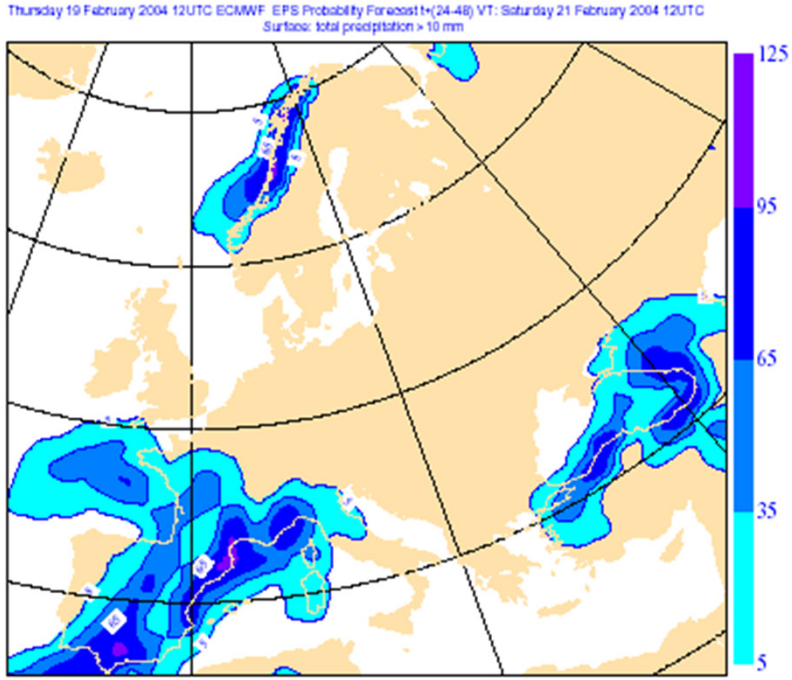

Prob
P>10 mm/24h

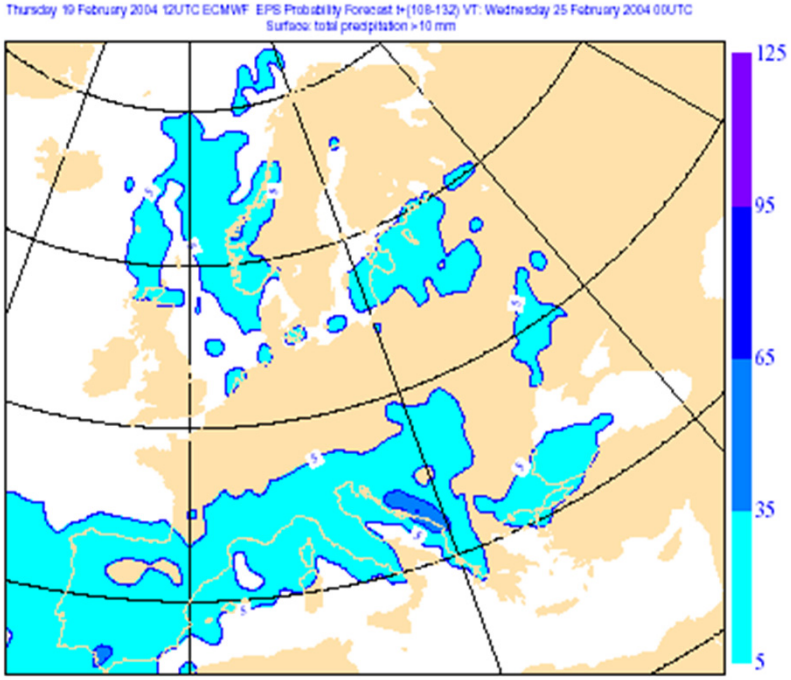

Distances in phase-space, inner products, and the adjoint

A distance between states in phase space can be the length of the inner product of a vector with itself. The vector, X, is then defined as the difference between the two state vectors, and:

$$\|X\| = \sqrt{\langle X, X \rangle}\,.$$

The adjoint to an operator L ***with respect to the inner product*** $\langle X, Y \rangle$ is denoted L^*, and is defined such that ***for any arbitrary vectors*** X ***and*** Y, $\langle LX, Y \rangle \equiv \langle X, L^*Y \rangle$. Note that in the text-book of Kalnay, the notation L^T (i.e. the transpose to L) is used for the adjoint, thus presuming real numbers and a standard Euclidian inner product. Here we continue to use the more general notation, L^*, of adjoints with respect to unspecified inner products.

The solution to the Tangent-Linear model is, as defined above: $\delta x(t) = L(t_0, t) \cdot \delta x_0$. The size of the perturbation is the distance between $x(t) + \delta x(t)$ and $x(t)$, hence:

$$\|\delta x(t)\|^2 = \langle \delta x(t), \delta x(t) \rangle = \langle L(t_0, t)\delta x_0, L(t_0, t)\delta x_0 \rangle = \langle L(t_0, t)^* L(t_0, t)\delta x_0, \delta x_0 \rangle\,;$$

which clearly demonstrates ***the importance of the combined operator*** $L(t_0, t)^* L(t_0, t)$.

Properties of the the adjoint

(1) Assume that the resolvent $L(t_0, t)$ can be split into K stepwise sub-intervals over time:

$$L(t_0, t) = L(t_{K-1}, t)L(t_{K-2}, t_{K-1}) \dots L(t_0, t_1) = L_{K-1}L_{K-2} \dots L_0$$

then

$$\begin{aligned}\langle L(t_0, t)\delta x_0, \delta x(t)\rangle &= \langle L_{K-1}L_{K-2} \dots L_0\delta x_0, \delta x(t)\rangle = \langle \delta x_0, L_0^* \dots L_{K-2}^* L_{K-1}^* \delta x(t)\rangle \\ &= \langle \delta x_0, L(t_0, t)^* \delta x(t)\rangle\end{aligned}$$

The adjoint operator $L(t_0, t)^*$ thus works backwards in time from t to t_0.

(2) It is also straightforward to show that: $L(t_0, t)^{**} = L(t_0, t)$ and that $L(t_0, t)^* L(t_0, t)$ is self-adjoint (or symmetric, Hermitian):

$$(L(t_0, t)^* L(t_0, t))^* = L(t_0, t)^* L(t_0, t)^{**} = L(t_0, t)^* L(t_0, t)$$

The eigenvalues of this particular self-adjoint operator are real and positive, and the eigenvectors are orthogonal with respect to this particular inner product.

Singular Vectors, SVs

The orthogonal eigenvectors to $\boldsymbol{L}(t_0,t)^*\boldsymbol{L}(t_0,t)$ with respect to the inner product, are $\boldsymbol{e}_i(t_0)$ with eigenvalues σ_i^2, for $i = 1,\ldots,N$, each fulfilling the equations:

$$\boldsymbol{L}(t_0,t)^*\boldsymbol{L}(t_0,t)\,\boldsymbol{e}_i(t_0) = \sigma_i^2\boldsymbol{e}_i(t_0) \text{ for } i = 1,\ldots,N.$$

If we define $\boldsymbol{L}(t_0,t)\boldsymbol{e}_i(t_0) = \boldsymbol{e}_i(t)$, i.e. the eigenvector evolved from t_0 to t, the norm evolves according to:

$$\|\boldsymbol{e}_i(t)\|^2 = \langle \boldsymbol{e}_i(t), \boldsymbol{e}_i(t)\rangle = \langle \boldsymbol{L}(t_0,t)\boldsymbol{e}_i(t_0), \boldsymbol{L}(t_0,t)\boldsymbol{e}_i(t_0)\rangle = \langle \boldsymbol{L}(t_0,t)^*\boldsymbol{L}(t_0,t)\boldsymbol{e}_i(t_0), \boldsymbol{e}_i(t_0)\rangle$$

$$= \sigma_i^2\|\boldsymbol{e}_i(t_0)\|^2$$

Notice that $\boldsymbol{e}_i(t_0)$ and $\boldsymbol{e}_i(t)$ can have different directions in the phase space.

Define:

- $\boldsymbol{e}_i(t_0)$ are the ***initial singular vectors*** to the propagator $\boldsymbol{L}(t_0,t)$ (**v** in Kalnay)
- $\boldsymbol{e}_i(t)$ are the ***evolved singular vectors*** to the propagator $\boldsymbol{L}(t_0,t)$ (**u** in Kalnay)
- σ_i are the ***singular values*** vectors to the propagator $\boldsymbol{L}(t_0,t)$.

Singular Vectors, SVs

The adjoint to the evolved singular vector produces the initial singular vectors in a similar way as the propagator to the initial singular vector produces the evolved:

$$\boldsymbol{L}(t_0,t)^* \boldsymbol{e}_i(t) = \boldsymbol{L}(t_0,t)^* \boldsymbol{L}(t_0,t)\, \boldsymbol{e}_i(t_0) = \sigma_i^2 \boldsymbol{e}_i(t_0)$$

From this, we also see that:

$$\boldsymbol{L}(t_0,t)\boldsymbol{L}(t_0,t)^* \boldsymbol{e}_i(t) = \sigma_i^2 \boldsymbol{L}(t_0,t)\, \boldsymbol{e}_i(t_0) = \sigma_i^2 \boldsymbol{e}_i(t)$$

Hence, the evolved singular vectors are eigenvectors to $\boldsymbol{L}(t_0,t)\boldsymbol{L}(t_0,t)^*$ with eigenvalues σ_i^2.

Now, assume that the initial singular vectors are normalized, i.e. $\|\boldsymbol{e}_i(t_0)\| = 1$ for all $i=1,..,N$.

We can use these singular vectors as an orthonormal basis for any vector in the phase space:

$\delta \boldsymbol{x}_0 = \sum_{i=1}^{N} \alpha_i\, \boldsymbol{e}_i(t_0)$; where $\alpha_i = \langle \delta \boldsymbol{x}_0, \boldsymbol{e}_i(t_0) \rangle$. It is straightforward to show that:

$$\|\boldsymbol{\delta x}(t)\|^2 = \langle \boldsymbol{\delta x}(t), \boldsymbol{\delta x}(t) \rangle = \langle \boldsymbol{L}(t_0,t)\boldsymbol{\delta x}_0, \boldsymbol{L}(t_0,t)\boldsymbol{\delta x}_0 \rangle = \sum_{i=1}^{N} \alpha_i^2\, \sigma_i^2$$

Singular Vectors, SVs

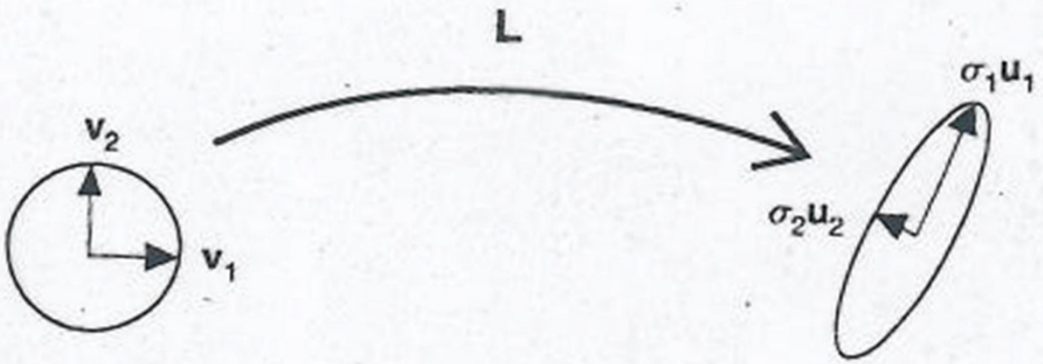

Figure 6.3.1: Schematic of the application of the tangent linear model to a sphere of perturbations of size 1 for a given interval (t_0, t_1).

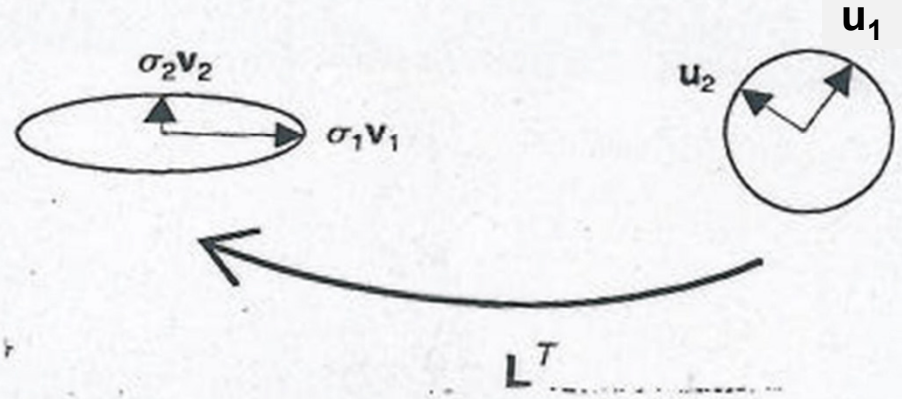

Figure 6.3.2: Schematic of the application of the adjoint of the tangent linear model to a sphere of perturbations of size 1 at the final time.

Singular Vectors, SVs

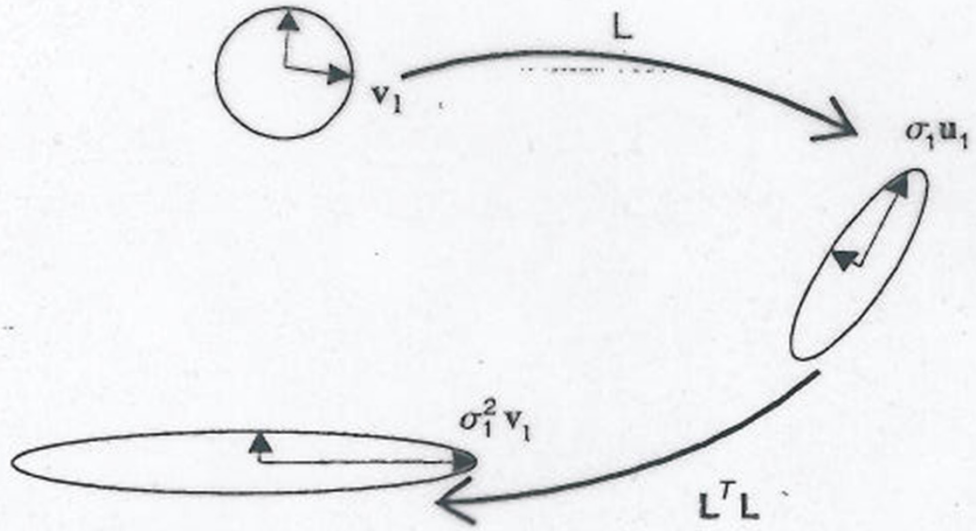

Figure 6.3.3: Schematic of the application of the tangent linear model forward in time followed by the adjoint of the tangent linear model to a sphere of perturbations of size 1 at the initial time.

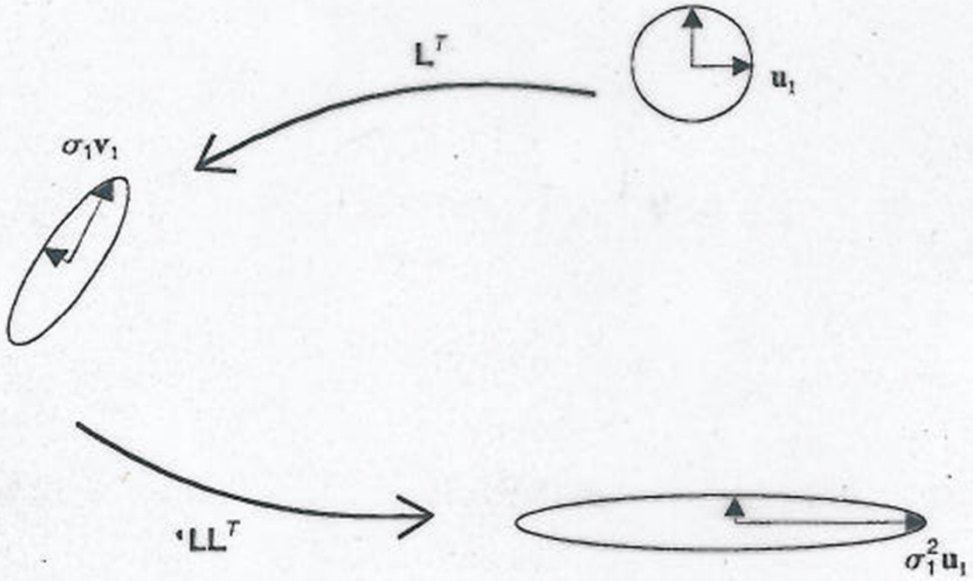

Figure 6.3.4: Schematic of the application of the adjoint of the tangent linear model backward in time followed by the tangent linear model forward to a sphere of perturbations of size 1 at the final time.

The Lorenz model
Singular Values

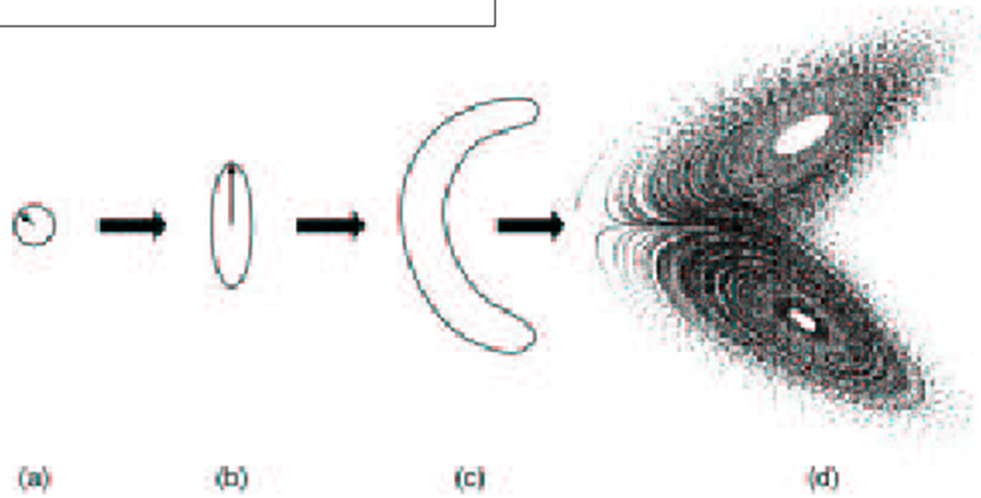

Figure 1: Schematic evolution of an isopleth of the probability density function (pdf) of initial and forecast error in N-dimensional phase space. (a) At initial time, (b) during the linearised stage of evolution. A (singular) vector pointing along the major axis of the pdf ellipsoid is shown in (b), and its pre-image at initial time is shown in (a). (c) The evolution of the isopleth during the nonlinear phase is shown in (c); there is still predictability, though the pdf is no longer Gaussian. (d) Total loss of predictability, occurring when the forecast pdf is indistinguishable from the attractor's invariant pdf.

6.3.4 Simple examples of singular vectors and eigenvectors

In order to get a more intuitive feeling of the relationship between singular vectors and Lyapunov vectors, we consider a simple linear model in two dimensions:

$$\begin{bmatrix} x_1(t+T) \\ x_2(t+T) \end{bmatrix} = \mathbf{M}_T[x(t)] = \begin{bmatrix} 2x_1(t) + 3x_2(t) + 7 \\ 0.5x_2(t) - 4 \end{bmatrix} \tag{6.3.39}$$

We compute the two-dimensional tangent linear model, constant in time:

$$\mathbf{L} = \begin{bmatrix} \frac{\partial M_1}{\partial x_1} & \frac{\partial M_1}{\partial x_2} \\ \frac{\partial M_2}{\partial x_1} & \frac{\partial M_2}{\partial x_2} \end{bmatrix} = \begin{bmatrix} 2 & 3 \\ 0 & 0.5 \end{bmatrix} \tag{6.3.40}$$

The propagation or evolution of any perturbation (difference between two solutions) over a time interval $(t, t+T)$ is given by

$$\delta\mathbf{x}(t+T) = \mathbf{L}\delta\mathbf{x}(t) \tag{6.3.41}$$

Note that the translation terms in (6.3.39) do not affect the perturbations. The eigenvectors of L (which for this simple constant tangent linear model are also the Lyapunov vectors) are proportional to

$$\mathbf{l}_1 = \begin{pmatrix} 1 \\ 0 \end{pmatrix} \qquad \mathbf{l}_2 = \begin{pmatrix} -2 \\ 1 \end{pmatrix}$$

corresponding to the eigenvalues $\lambda_1 = 2$, $\lambda_2 = 0.5$, respectively, which in this case are the two Lyapunov numbers (their logarithms are the Lyapunov exponents). If we normalize them, so that they have unit length, the Lyapunov vectors are

$$\mathbf{l}_1 = \begin{pmatrix} 1 \\ 0 \end{pmatrix} \qquad \mathbf{l}_2 = \begin{pmatrix} -0.89 \\ 0.45 \end{pmatrix} \tag{6.3.42}$$

The Lyapunov vectors are not orthogonal, they are separated by an angle of 153.4° (Fig. 6.3.6(a)). We will see that because they are not orthogonal it is possible to find linear combinations of the Lyapunov vectors that grow faster than the leading Lyapunov vector. We will also see that the leading Lyapunov vector is the attractor of the system, since repeated applications of $\mathbf{L}$ to any perturbation makes it evolve towards $\mathbf{l}_1$.

Singular Vectors, SVs,

Examples

Applying first $\mathbf{L}$ and then its transpose $\mathbf{L}^T$ we obtain the symmetric matrix

$$\mathbf{L}^T\mathbf{L} = \begin{bmatrix} 4 & 6 \\ 6 & 9.25 \end{bmatrix} \tag{6.3.43}$$

whose eigenvectors are the *initial singular vectors*, and whose eigenvalues are the squares of the singular values. The initial singular vectors (eigenvectors of $\mathbf{L}^T\mathbf{L}$) are

$$\mathbf{v}_1 = \begin{pmatrix} 0.55 \\ 0.84 \end{pmatrix} \mathbf{v}_2 = \begin{pmatrix} 0.84 \\ -0.55 \end{pmatrix} \tag{6.3.44}$$

with eigenvalues $\sigma_1^2 = 13.17$, $\sigma_2^2 = 0.076$. As indicated before, the *singular values* of $\mathbf{L}$ are the square roots of the eigenvalues of $\mathbf{L}^T\mathbf{L}$, i.e., $\sigma_1 = 3.63$, $\sigma_2 = 0.275$. Note that this implies that during the optimization period $(0, T)$ the leading singular vector grows almost twice as fast as the leading Lyapunov vector (3.63 vs. 2). The angle that the leading *initial singular vector* has with respect to the leading Lyapunov vector is 56.82°, whereas the second initial singular vector is perpendicular to the first one (Fig.6.3.6(a)).

The final or *evolved SVs at the end of the optimization period* $(0, T)$ are the eigenvectors of

$$\mathbf{L}\mathbf{L}^T = \begin{bmatrix} 13 & 1.5 \\ 1.5 & 0.25 \end{bmatrix} \tag{6.3.45}$$

and after normalization, they are

$$\mathbf{u}_1 = \begin{pmatrix} 0.99 \\ 0.12 \end{pmatrix} \qquad \mathbf{u}_2 = \begin{pmatrix} 0.12 \\ -0.99 \end{pmatrix} \tag{6.3.46}$$

Note again that the operators $\mathbf{L}^T\mathbf{L}$ and $\mathbf{L}\mathbf{L}^T$ are quite different, and the final singular vectors are different from the initial singular vectors, but they have the same singular values $\sigma_1^2 = 13.17$, $\sigma_2^2 = 0.076$.

Alternatively, the evolved singular vectors at the end of the optimization period can also be obtained by applying $\mathbf{L}$ to the initial singular vectors, which is computationally inexpensive. In this case,

$$\mathbf{u}_1(T) = \mathbf{L}\mathbf{v}_1(0) = \begin{bmatrix} 3.6 \\ 0.42 \end{bmatrix} \qquad \mathbf{u}_2(T) = \mathbf{L}\mathbf{v}_2(0) = \begin{bmatrix} 0.03 \\ -0.27 \end{bmatrix}$$

which is the same as (6.3.46) but without normalization.

The final leading singular vector has strongly rotated towards the leading Lyapunov vector: at the end of the optimization period the angle between the leading singular vector and the leading Lyapunov vector is only 6.6° (Fig. 6.3.6(b)), and because the singular vectors have been optimized for this period, the final singular vectors are still orthogonal.

Singular Vectors, SVs,

Examples

Singular Vectors, SVs, Examples

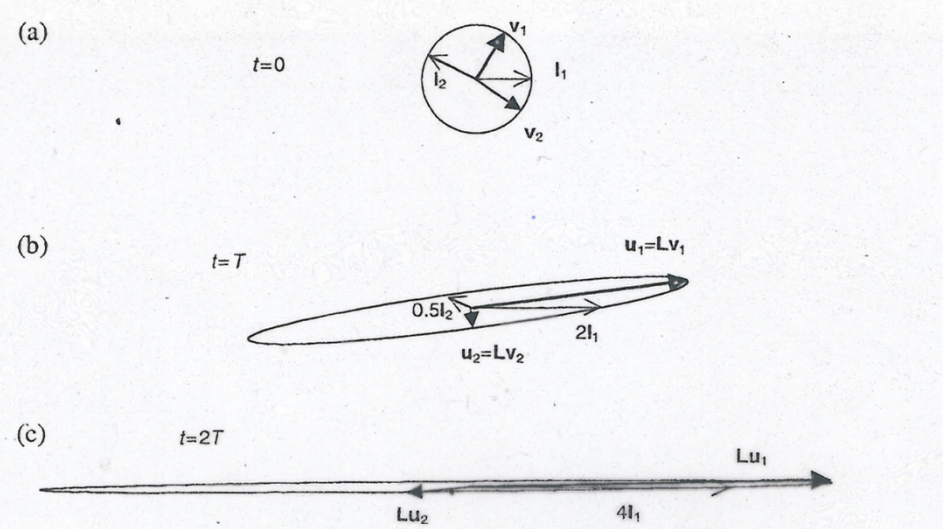

Figure 6.3.6: Schematic of the evolution of the two nonorthogonal Lyapunov vectors (thin arrows $\mathbf{l}_1$ and $\mathbf{l}_2$), and the corresponding two initial singular vectors (thick arrows $\mathbf{v}_1(0)$and $\mathbf{v}_2(0)$), optimized for the interval $(0, T)$, for the tangent linear model

$$\mathbf{L} = \begin{bmatrix} 2 & 3 \\ 0 & 0.5 \end{bmatrix}$$

with eigenvalues 2 and 0.5. (a) Time $t = 0$, showing the initial singular vectors $\mathbf{v}_1(0)$ and $\mathbf{v}_2(0)$, as well as the Lyapunov vectors $\mathbf{l}_1$ and $\mathbf{l}_2$. (b) Time $t = T$, evolved singular vectors, $\mathbf{u}_1(T) = \mathbf{L}\mathbf{v}_1(0)$, $\mathbf{u}_2(T) = \mathbf{L}\mathbf{v}_2(0)$ at the end of the optimization period; the Lyapunov vectors have grown by factors of 2 and 0.5 respectively, whereas the leading singular vector has grown by 3.63. The second evolved singular vector has grown by 0.275, and is still orthogonal to the first singular vector. (c) Time $t = 2T$. Beyond the optimization period T, the evolved singular vectors $\mathbf{u}_1(t + 2T) = \mathbf{L}\mathbf{u}_1(t + T)$, $\mathbf{u}_2(2T) = \mathbf{L}\mathbf{u}_2(T)$ are not orthogonal and they approach the leading Lyapunov vector with similar growth rates.

To obtain the evolution of the singular vectors *beyond the optimization period* $(0, T)$ we apply $\mathbf{L}$ again to the evolved singular vector valid at $t = T$ and obtain

$$\mathbf{u}_1(t + 2T) = \mathbf{L}\mathbf{u}_1(t + T) = \begin{bmatrix} 8.47 \\ 0.21 \end{bmatrix} \qquad \mathbf{u}_2(t + 2T) = \mathbf{L}\mathbf{u}_2(t + T) = \begin{bmatrix} -0.76 \\ -0.14 \end{bmatrix}$$

During the interval $(T, 2T)$ the leading singular vector grows by a factor of just 2.33, which is not very different from the growth rate of the leading Lyapunov vector. At the end of this second period (Fig. 6.3.6(c)) the angle with the leading Lyapunov vector is only 1.41°. The angle of the second evolved singular vector at time T, after applying the linear tangent model $\mathbf{L}$ and the leading Lyapunov vector is also quite small (10.24°), and because it was further away from the attractor, the second singular vector (whose original, transient, singular value was 0.5), grows by a factor of 2.79. This example shows how quickly *all perturbations, including all singular vectors, evolve towards the leading Lyapunov vector, which is the attractor of the system.* It is particularly noteworthy that during the optimization period $(0, T)$, the first singular vector grows very fast as it rotates towards the attractor, but once it gets close to the leading Lyapunov vector, its growth returns to the normal leading Lyapunov vector's growth.

Let us now choose as the tangent linear model another matrix

$$\mathbf{L} = \begin{bmatrix} 2 & 30 \\ 0 & 0.5 \end{bmatrix}$$

with the same eigenvalues 2 and 0.5, i.e., with eigenvectors (Lyapunov vectors) that still grow at a rate of $2/T$ and $0.5/T$ respectively. However, now the angle between the first and the second Lyapunov vector is 177°, i.e. the Lyapunov vectors are almost antiparallel. In this case, the first singular vector grows by a factor of over 30 during the optimization period, but beyond the optimization period it essentially continues evolving like the leading Lyapunov vector.

These results do not depend on the fact that one Lyapunov vector grows and the other decays. As a third example, we choose

$$\mathbf{L} = \begin{bmatrix} 2 & 3 \\ 0 & 1.5 \end{bmatrix}$$

with two Lyapunov vectors growing with rates $2/T$ and $1.5/T$. The Lyapunov vectors are almost parallel, with an angle of 170°, and the leading singular vector grows during the optimization period by a factor of 3.83. Applying the tangent linear model again to the evolved singular vectors we obtain that at time $2T$ the leading singular vector has grown by a factor of 2.9 and its angle with respect to the leading Lyapunov vector is 1°. Because it is not decaying, the second Lyapunov vector is also part of the attractor, but only those perturbations that are exactly parallel to it will remain parallel, all others will move towards the first Lyapunov vector.

Non-normality and final-time growth

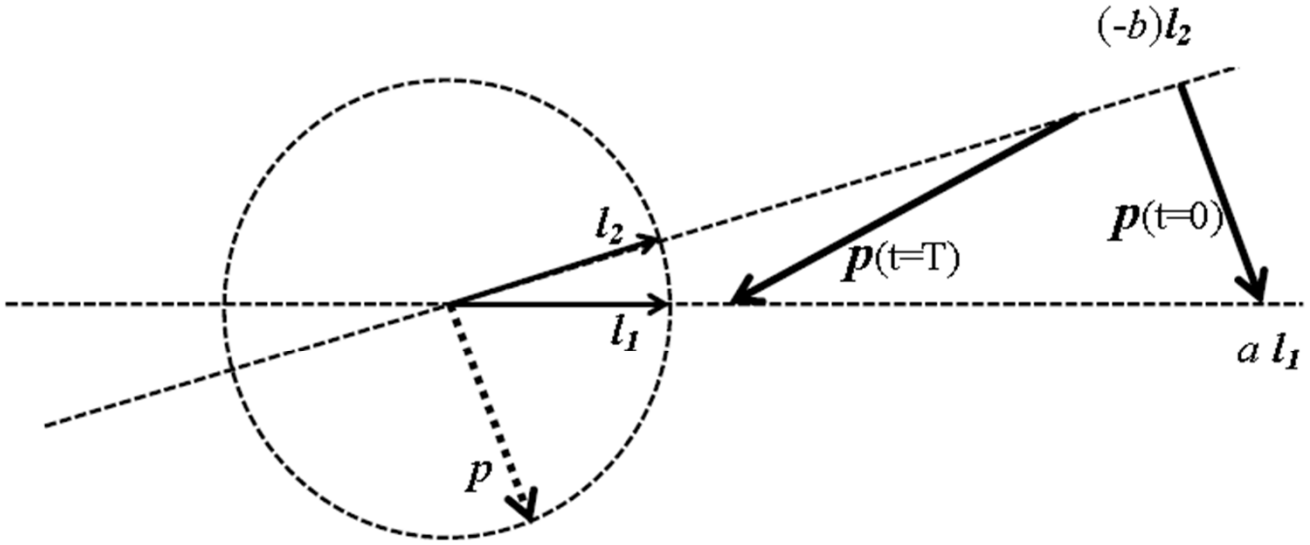

$$\frac{d}{dt}\boldsymbol{\delta x} = \boldsymbol{J}\,\boldsymbol{\delta x}$$

$$\boldsymbol{J}\,\boldsymbol{l_i} = -\mu_i \boldsymbol{l_i}\,; \qquad Normal\ modes = LLV$$

$$Assume\ stability:\ \mu_1 > 0\ and\ \mu_2 > 0$$

$$\boldsymbol{p} = a\boldsymbol{l_1} + b\boldsymbol{l_2}\ and\ \|\boldsymbol{p}\| = 1:$$

$$a\ is\ max\ when\ \boldsymbol{p}\cdot\boldsymbol{l_2} = \boldsymbol{0}$$

$$\frac{d}{dt}\boldsymbol{p} = a\frac{d}{dt}\boldsymbol{l_1} + b\frac{d}{dt}\boldsymbol{l_2} = -a\mu_1\boldsymbol{l_1} - b\mu_2\boldsymbol{l_2}$$

Initial perturbations

Operational ensemble prediction

Predictability varies with the weather situation

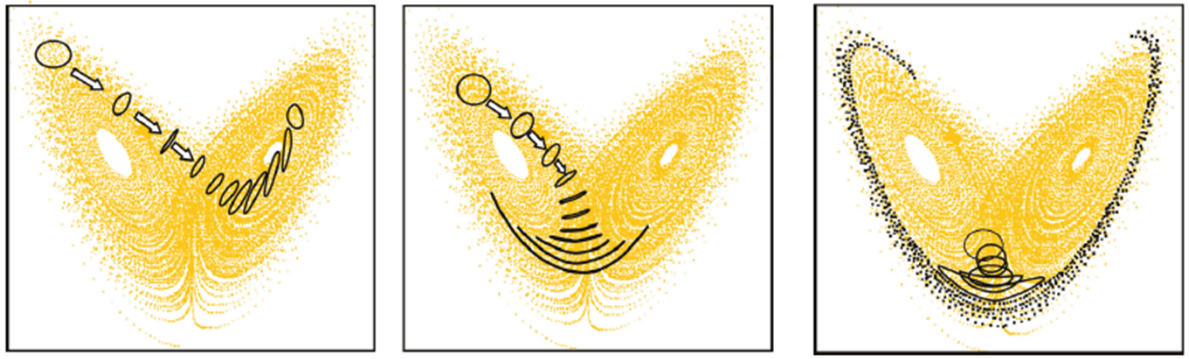

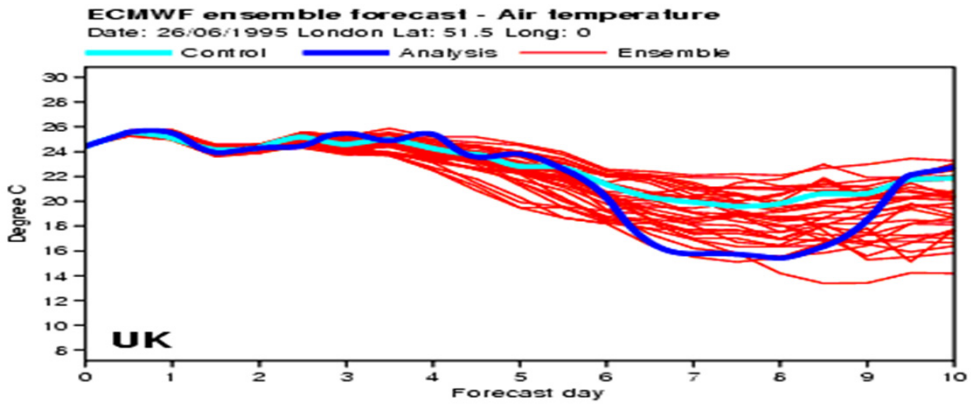

High predictability:
the ensemble mean is skillful

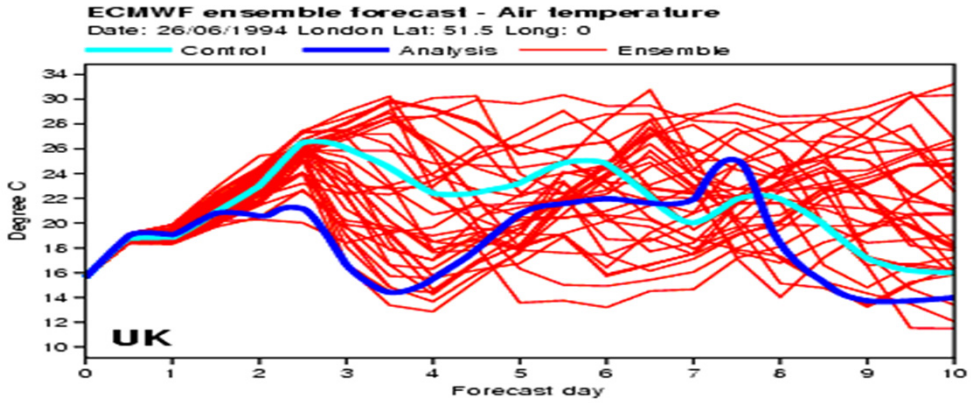

Low predictability:
low skill of ensemble mean

The «deterministic» and «stochastic» phases of atmospheric predictions.

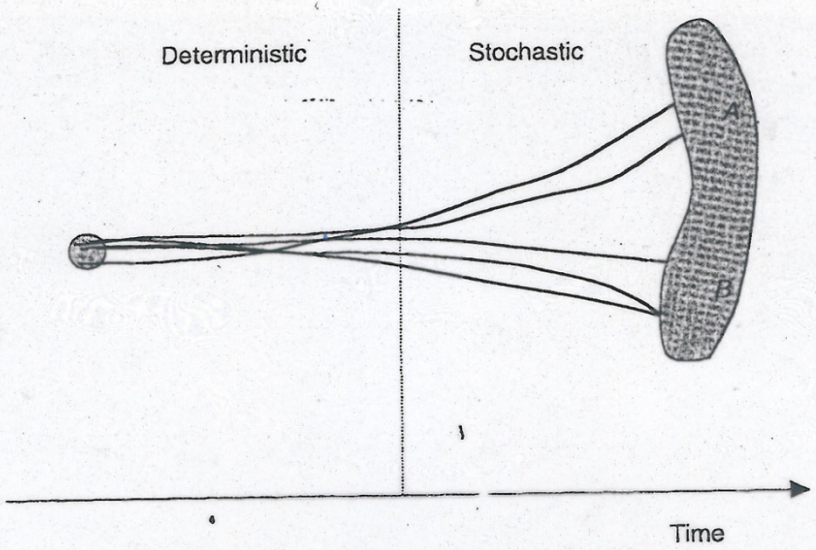

Figure 6.4.1: Schematic of ensemble prediction, with individual trajectories drawn for forecasts starting from a representative set of perturbed initial conditions within a circle representing the uncertainty of the initial conditions (ideally the analysis error covariance) and ending within the range of possible solutions. For the shorter range, the forecasts are close to each other, and they may be considered deterministic, but beyond a certain time, the equally probable forecasts are so different that they must be considered stochastic. The transition time is of the order of 2–3 days for the prediction of large-scale flow, but can be as short as a few hours for mesoscale phenomena like the prediction of individual storms. The transition time is shorter for strongly nonlinear parameters: even for large-scale flow, precipitation forecasts show significant divergence faster than the 500-hPa fields. The forecasts may be clustered into subsets *A* and *B*. (Adapted from Tracton and Kalnay, 1993.)

Good and bad ensemble systems

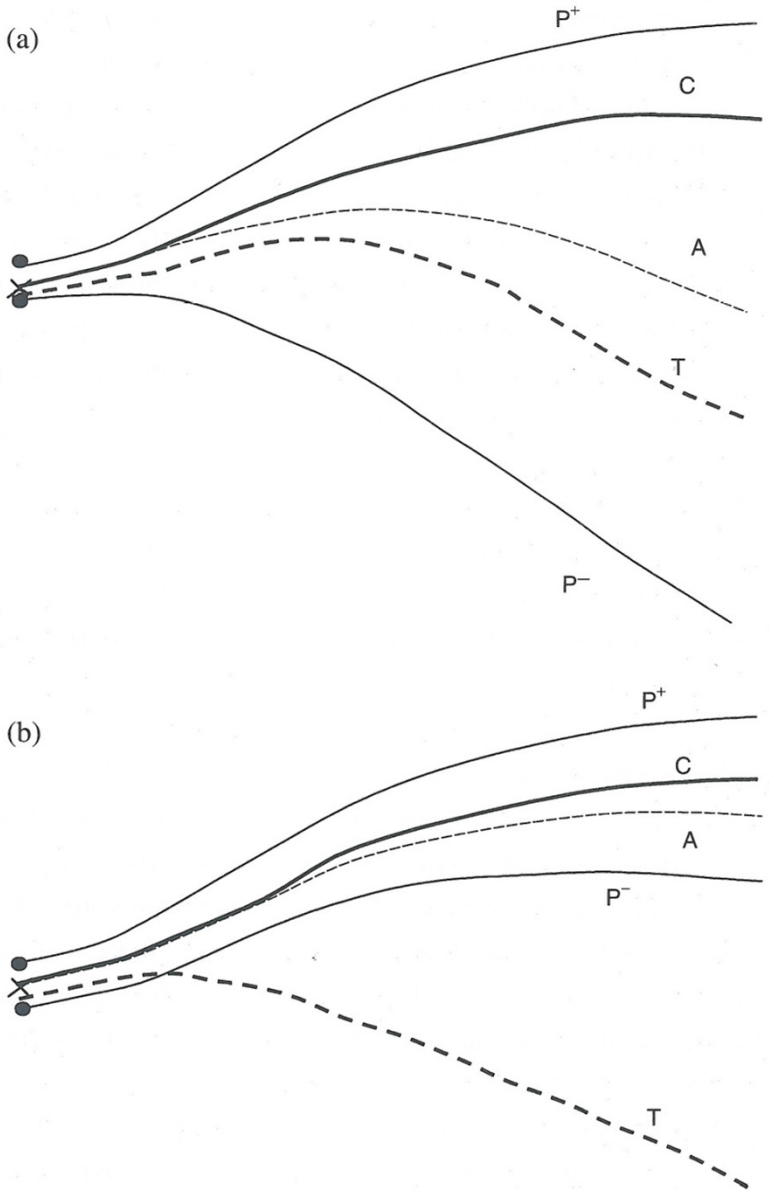

Figure 6.5.1: (a) Schematic of the components of a typical ensemble: (1) the control forecast (labeled C) which starts from the analysis (denoted by a cross), which is the best estimate of the true initial state of the atmosphere; (2) two perturbed ensemble forecasts (labeled P^+ and P^-) with initial perturbations added and subtracted from the control; (3) the ensemble average denoted A; and (4) the "true" evolution of the atmosphere labeled T. This is a "good" ensemble since the "truth" appears as a plausible member of the ensemble. Note that because of nonlinear saturation, the error of the ensemble member initially further away from the truth (in this case P^+) tends to grow more slowly than the error of the member initially closer to the truth. This results in a nonlinear filtering of the errors: the average of the ensemble members tends to be closer to the truth than the control forecast (Toth and Kalnay, 1997, also compare with Fig. 1.7.1). (b) Schematic of a "bad" ensemble in which the forecast errors are dominated by system errors (such as model deficiencies). In this case, the ensemble is not useful for forecasting, but it helps to identify the fact that forecast errors are probably due to the presence of systematic errors, rather than to the chaotic growth of errors in the initial conditions.

Initial-state perturbations; «monte carlo» and time-lagging.

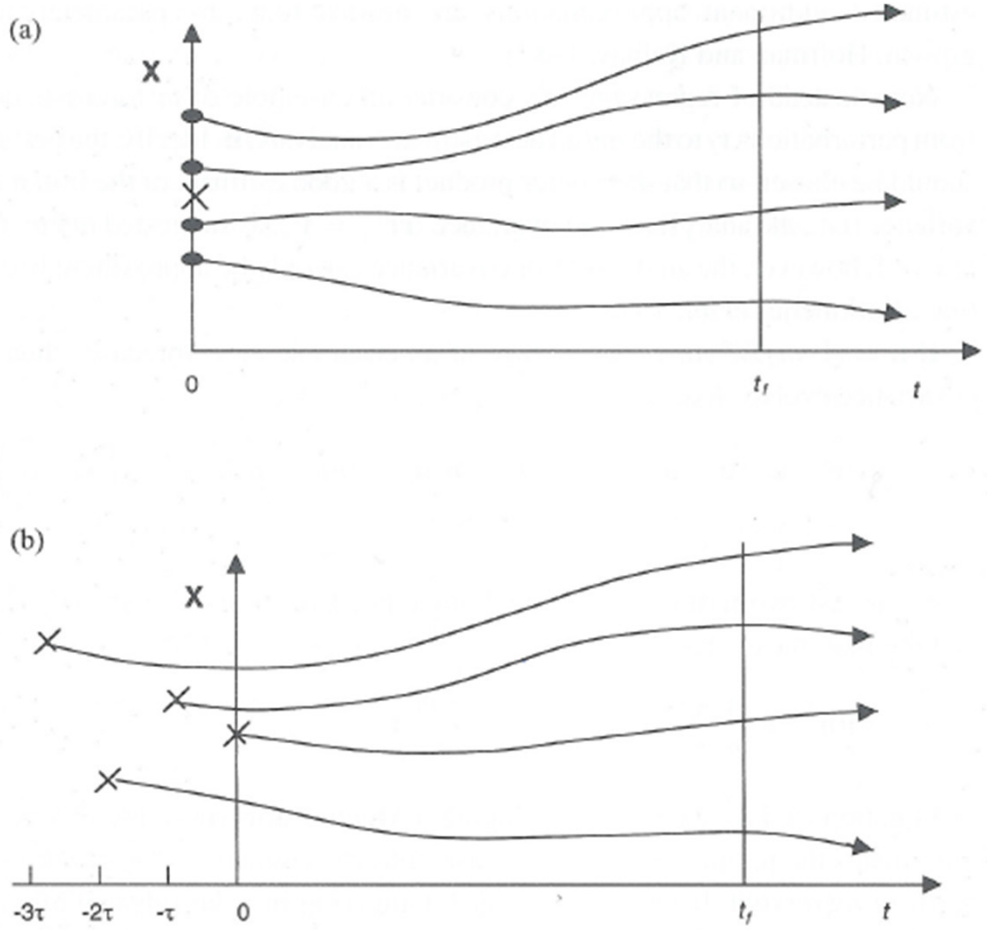

Figure 6.4.2: Schematic time evolutions of Monte Carlo forecasts (a) and lagged average forecasts (b). The abscissa is forecast time t, and the ordinate is the value of a forecast variable **X**. The crosses represent analyses obtained at time intervals τ, and the dots, randomly perturbed initial conditions; t_f is a particular forecast time. The initial "perturbation" for the lagged average forecast is the previous forecasts' error at the initial time. (Adapted from Hoffman and Kalnay, 1983.)

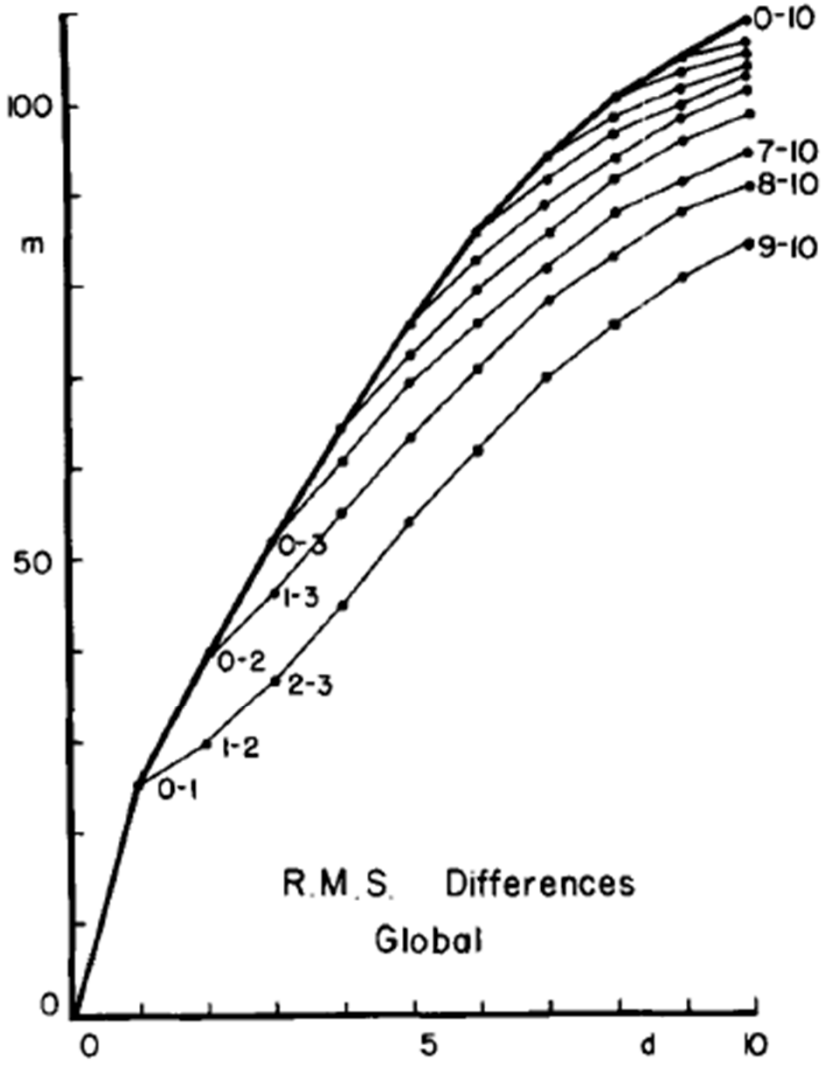

Fig. 1. Global root-mean-square 500-mb height differences E_{jk}, in meters, between j-day and k-day forecasts made by the ECMWF operational model for the same day, for $j < k$, plotted against k. Values of (j,k) are shown beside some of the points. Heavy curve connects values of E_{0k}. Thin curves connect values of E_{jk} for constant $k - j$.

Time-lagging

Lorenz (1982)

Heterogeneous distribution of initial-state uncertainty.

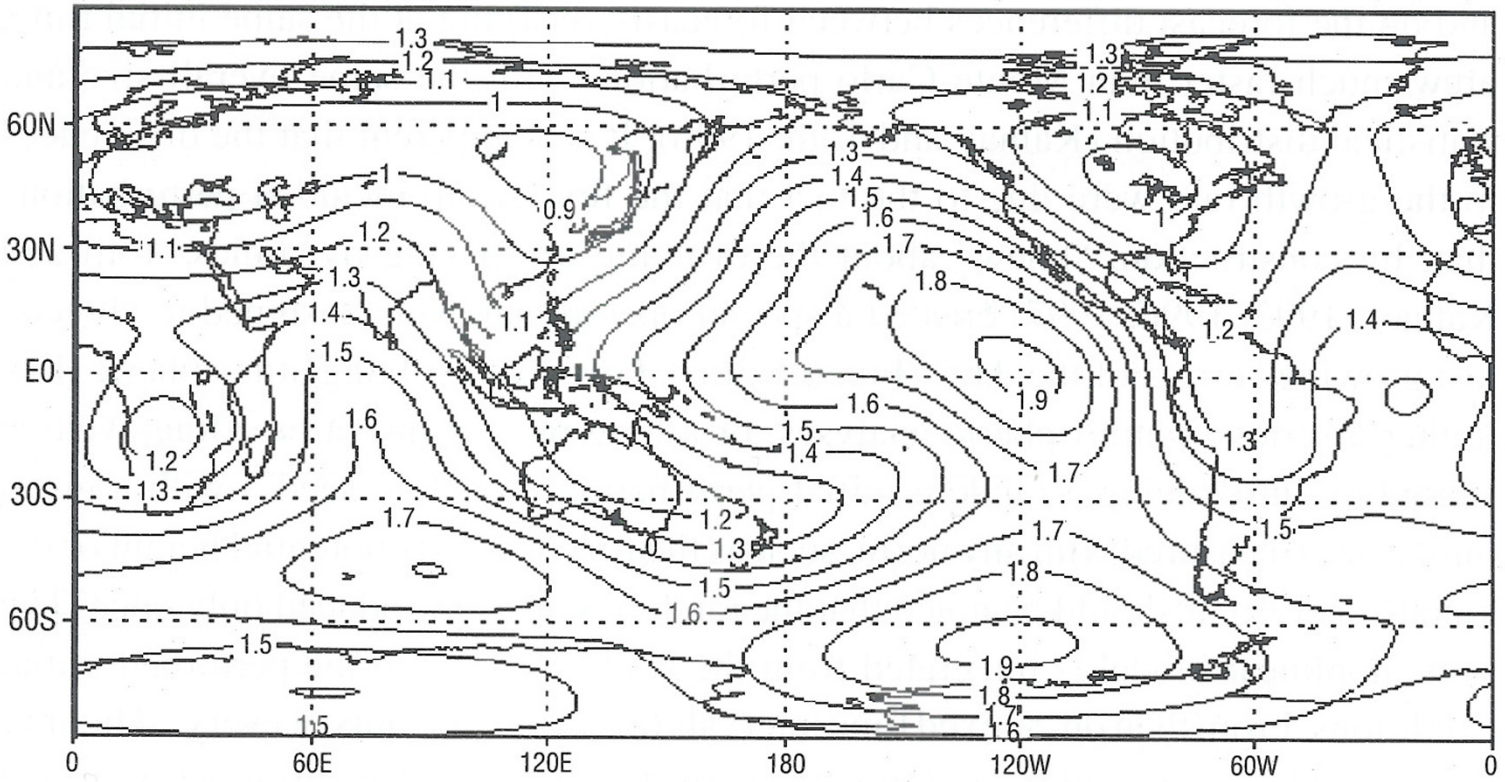

Figure 6.5.2: Estimation of the 500-hPa geopotential height analysis uncertainty obtained from running two independent analysis cycles, computing their rms difference, and using a filter to retain the planetary scales. The units are arbitrary. Note the minima over and downstream of rawinsonde-rich land regions and the maxima over the oceans (Courtesy I. Szunyogh, University of Maryland.)

Breeding

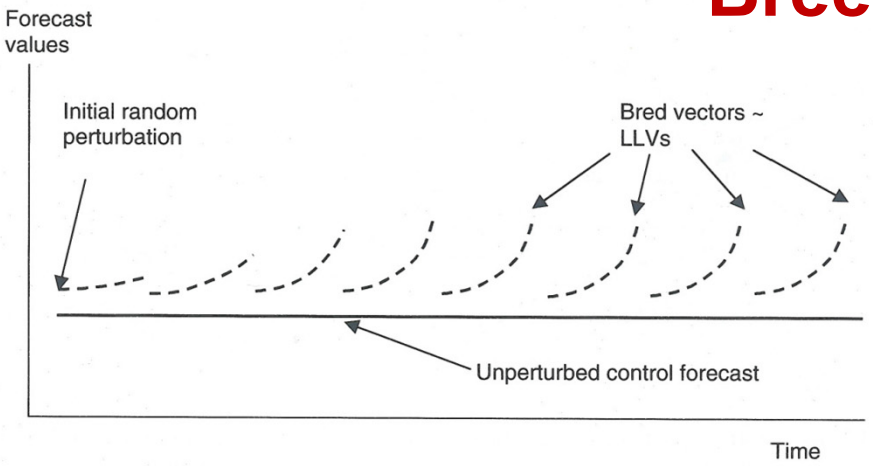

(a)

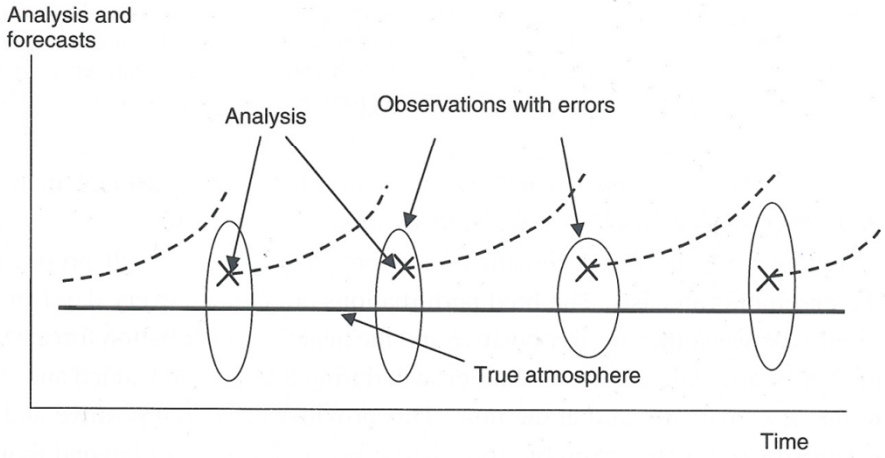

(b)

Figure 6.5.3: (a) Schematic of a breeding cycle run on an unperturbed (control) model integration. The initial growth after introducing a random initial perturbation is usually very small, but with time, the perturbation is more dominated by growing errors. The initial transient with slow growth lasts about 3–5 days. The difference of the complete perturbed (dashed line) and control (full line) forecasts is scaled back periodically (e.g., every 6 or every 24 hours) to the initial amplitude. The rescaling is done by dividing all the forecast differences by the same observed growth (typically about 1.5/day for mid-latitudes). In operational NWP, the unperturbed model integration is substituted by short-range control forecasts started from consecutive analysis fields. The breeding cycle is a nonlinear, finite-time, finite-amplitude generalization of the method used to obtain the leading Lyapunov vector. (Adapted from Kalnay and Toth, 1996.) (b) Schematic of the 6-h analysis cycle. Indicated on the vertical axis are differences between the true state of the atmosphere (or its observational measurements, burdened with observational errors). The difference between the forecast and the true atmosphere (or the observations) increases with time in the 6-h forecast because of the presence of growing errors in the analysis. (Adapted from Kalnay and Toth, 1996.)

Self-breeding

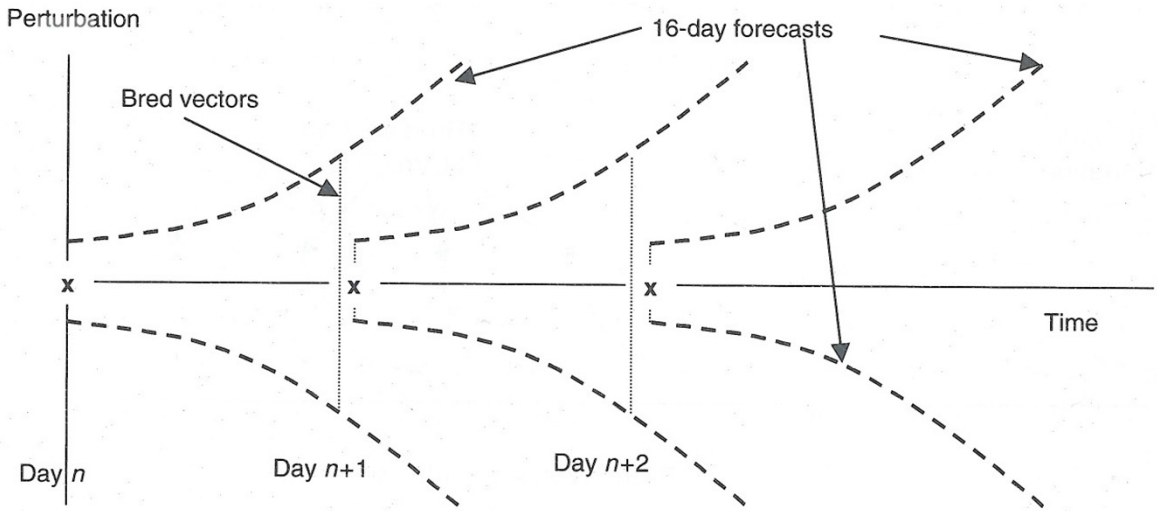

Figure 6.5.4: Schematic of a self-breeding pair of ensemble forecasts used at NCEP. Every day, the 1-day forecast from the negative perturbation is subtracted from the 1-day forecast from the positive perturbation. This difference is divided by 2, and then scaled down (by dividing all variables by the 1-day growth), so that difference is of the same size as the initial perturbation. The scaled difference is then added and subtracted from the new analysis, generating the initial conditions for the new pair of forecasts. This self-breeding is part of the extended ensemble forecast system, and does not require computer resources to generate initial perturbations beyond running the ensemble forecasts. (Adapted from Toth and Kalnay, 1997.)

Selective sampling: breeding vectors (NCEP)

At NCEP a different strategy based on perturbations growing fastest in the analysis cycles (bred vectors, BVs) was followed (now NCEP uses a different method called Ensemble Transformed with Rescaling, ETR, method). The breeding cycle was designed to mimic the analysis cycle.

Each BV was computed by (a) adding a random perturbation to the starting analysis, (b) evolving it for 24-hours (soon to 6), (c) rescaling it, and then repeat steps (b-c). BVs are grown non-linearly at full model resolution.

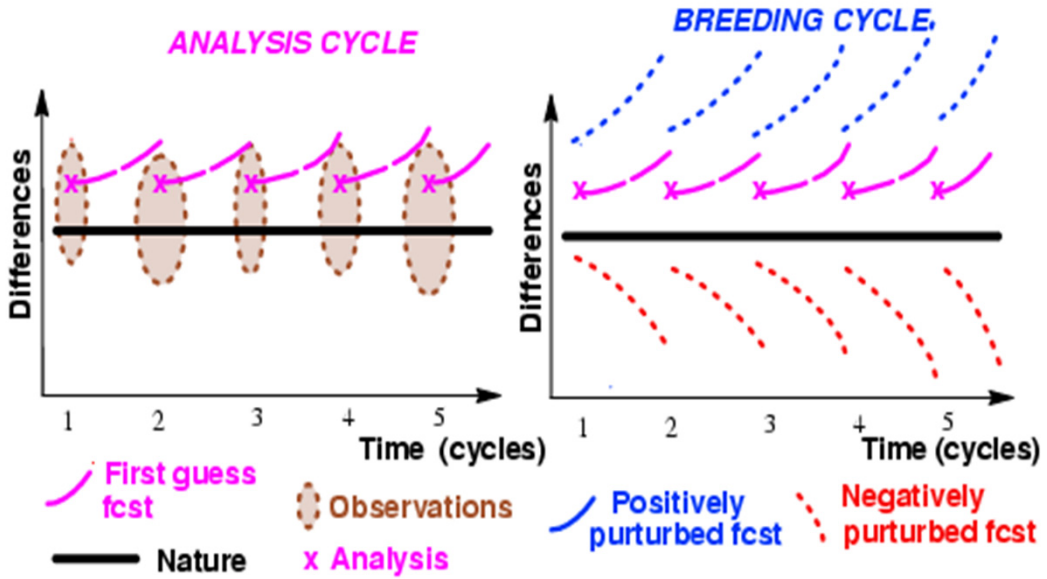

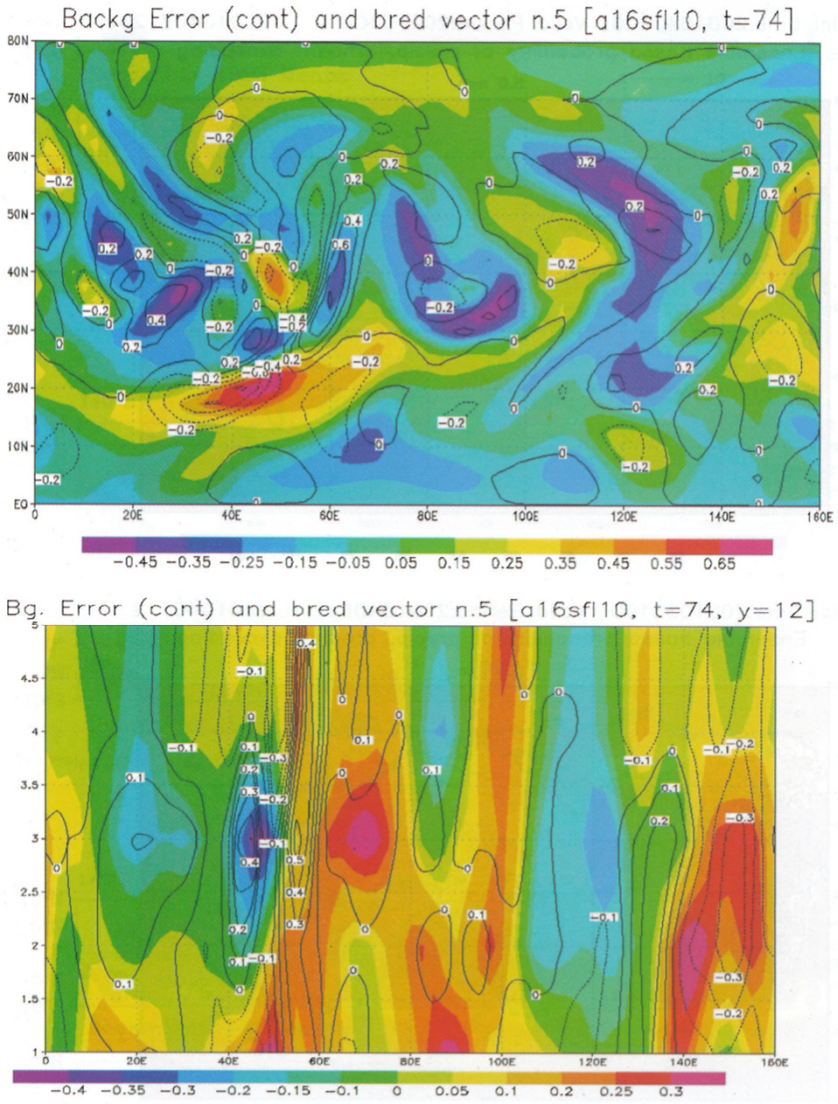

Plate 1 Comparison between the 12-h forecast error used as background (contours) and a randomly chosen bred vector for a data assimilation simulation system. The first image at the center level of the model. The second is a vertical cross-section (from Corazza et al, 2002).

Relation between Bred-vector amplitudes and forecast error.

Bred vector alignment and growing instability

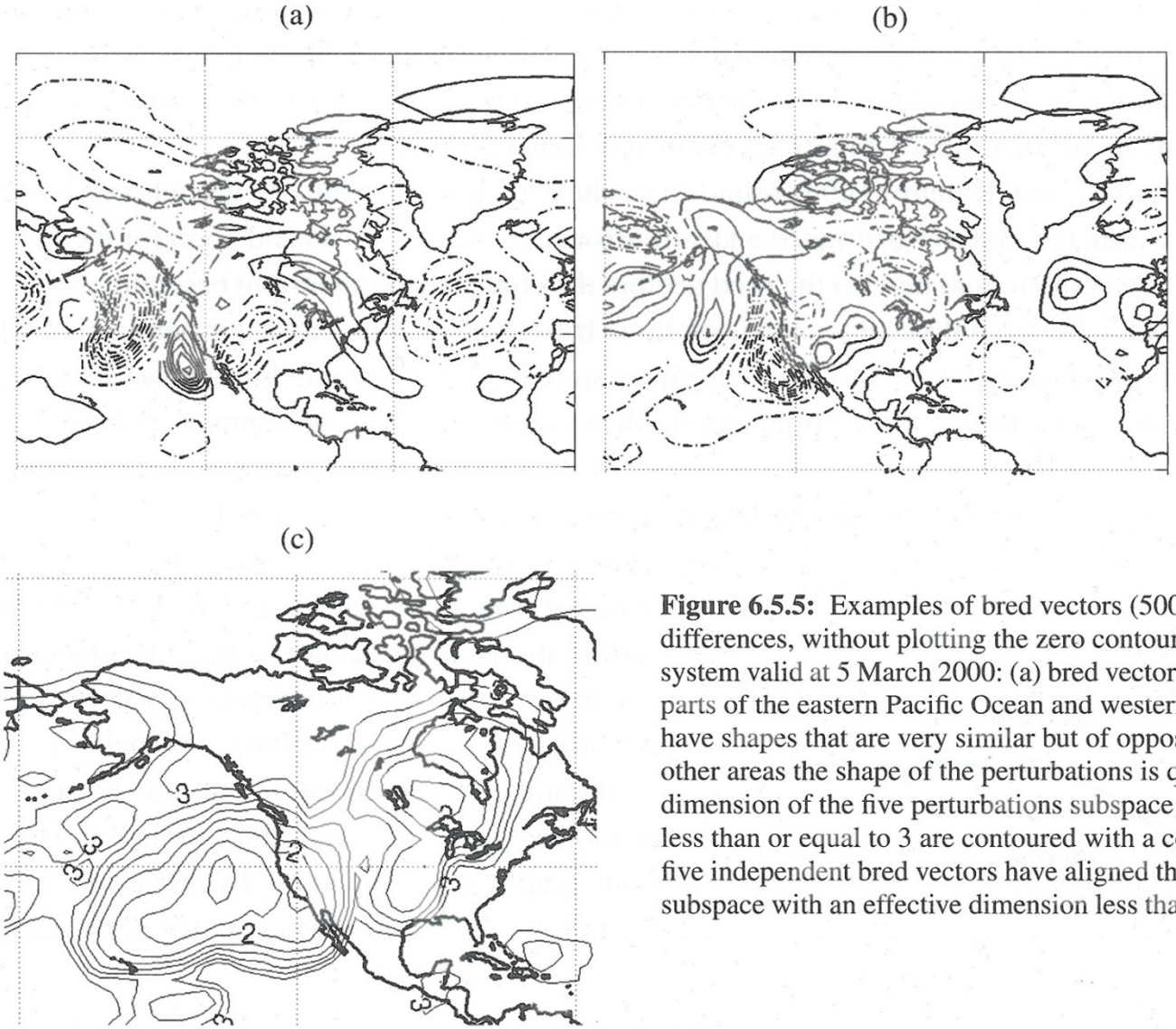

Figure 6.5.5: Examples of bred vectors (500-hPa geopotential height field differences, without plotting the zero contour) from the NCEP operational ensemble system valid at 5 March 2000: (a) bred vector 1; (b) bred vector 5. Note that over large parts of the eastern Pacific Ocean and western North America, the two perturbations have shapes that are very similar but of opposite signs and/or different amplitudes. In other areas the shape of the perturbations is quite different. (c) The bred-vector-local dimension of the five perturbations subspace (Patil *et al.*, 2001). Only dimensions less than or equal to 3 are contoured with a contour interval 0.25. In these areas the five independent bred vectors have aligned themselves into a locally low-dimensional subspace with an effective dimension less than or equal to 3. (Courtesy of D. J. Patil.)

Selecting modes of instability by choosing the size of initial state perturbations

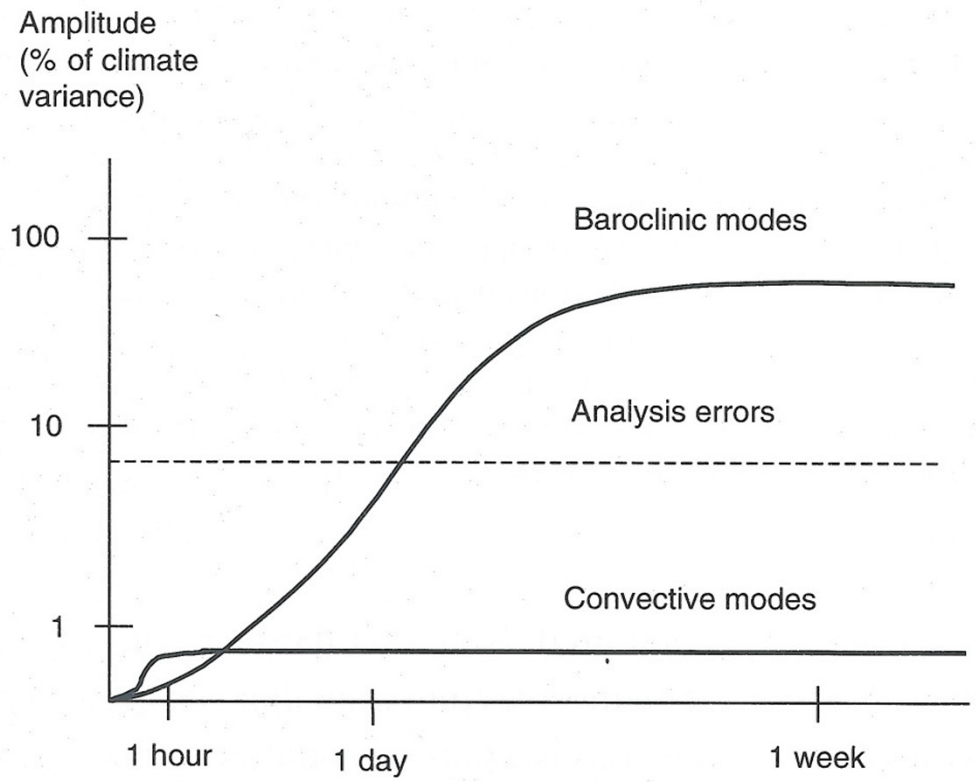

Figure 6.5.6: Schematic of the time evolution of the rms amplitude of high-energy baroclinic modes and low-energy convective modes. Note that although initially growing much faster than the baroclinic modes, convective modes saturate at a substantially lower level. These modes are therefore insignificant in the analysis/ensemble perturbation problem, since the errors in the analysis (dashed line) are much larger than the convective saturation level. (Adapted from Toth and Kalnay, 1993.)

SVs from more general inner products

Singular vectors can be defined as the result of

$$\langle \boldsymbol{\delta x}(t), \boldsymbol{\delta x}(t) \rangle_F = [\boldsymbol{PL\delta x}(0)]^T \boldsymbol{C_F PL\delta x}(0) = MAXIMUM,$$

with side condition $\langle \boldsymbol{\delta x}(0), \boldsymbol{\delta x}(0) \rangle_0 = [\boldsymbol{\delta x}(0)]^T \boldsymbol{C_0 \delta x}(0) = 1$

$\boldsymbol{C_0}$ and $\boldsymbol{C_F}$
positiv definit (having only positive eigenvalues), diagonal operators/matrices
$\boldsymbol{Px} = \boldsymbol{x}$ in all points inside a predefined target domain in physical space,

yields the eigenvalue problem:

$$[\boldsymbol{PL}]^T \boldsymbol{C_F PL\delta x}(0) = \sigma^2 \boldsymbol{C_0 \delta x}(0)$$

Scalar multiplication from left with $\boldsymbol{C_0^{-1/2}}$, and defining $\hat{\boldsymbol{e}}_\mathbf{0} \equiv \boldsymbol{C_0^{1/2}\delta x}(0)$, yields:

$$\hat{\boldsymbol{L}}^T \hat{\boldsymbol{L}}\, \hat{\boldsymbol{e}}_\mathbf{0} = [\, \boldsymbol{C_0^{-1/2} L^T P C_F P L C_0^{-1/2}}]\, \hat{\boldsymbol{e}}_\mathbf{0} = \sigma^2\, \hat{\boldsymbol{e}}_\mathbf{0}, \text{ where } \hat{\boldsymbol{L}} \equiv \boldsymbol{C_F^{1/2} P L C_0^{-1/2}}$$

$$\boldsymbol{e}(0) = \boldsymbol{C_0^{-1/2}} \hat{\boldsymbol{e}}_\mathbf{0}, \text{ and } \boldsymbol{e}(t) = \boldsymbol{L}(0,t)\boldsymbol{e}(0).$$

Practical procedures for generating SVs

When computing singular vectors and values, the matrices and operators are not explicitly calculated. Instead, an algorithm named *the Lanczos algorithm* is used. This algorithm devices

1) Assume a set of N initial perturbations at random or according to some assumption;
2) Transform this state by multiplying with coefficients as in $\boldsymbol{C_0^{-1/2}}$ and normalize w.r.t. the $\boldsymbol{C_0}$ inner product;
3) Integrate the TLM up to time t;
4) Transform the obtained state by multiplying with 0 or 1 of local projection P;
5) Transform this state by multiplying with coefficients as in $\boldsymbol{C_F}$;
6) Transform the obtained state by multiplying with 0 or 1 of local projection P;
7) Integrate the ADM back to time 0
8) Transform this state by multiplying with coefficients as in $\boldsymbol{C_0^{-1/2}}$ and normalize w.r.t. the $\boldsymbol{C_0}$ inner product;
9) Apply Lanczos and restart at 3) until satisfied with the accuracy of n SVs.
10) Transform the resulting n SVs with coefficients as in $\boldsymbol{C_0^{-1/2}}$.

Generating 50 alternative initial states for the ensemble

Let SV_i, $i=1,...25$ denote the SV-based preturbation fields, and $E_k = EDA_k - A_0$, k=1,…,10 denote the deviation from the control analysis by the EDA-based alternative analyses. The initial states for the n $(n=1,...,50)$ alternative ensemble forecasts are:

$$A_1=A_0+[SV_1+E_1];\ A_2=A_0-[SV_1+E_1];$$

$$\vdots$$

$$A_{19}=A_0+[SV_{10}+E_{10}];\ A_{20}=A_0-[SV_{10}+E_{10}];$$

$$A_{21}=A_0+[SV_{11}+E_1];\ A_{22}=A_0-[SV_{11}+E_1];$$

$$\vdots$$

$$A_{39}=A_0+[SV_{20}+E_{10}];\ A_{40}=A_0-[SV_{20}+E_{10}];$$

$$A_{41}=A_0+[SV_{21}+E_1];\ A_{42}=A_0-[SV_{21}+E_1];$$

$$\vdots$$

$$A_{49}=A_0+[SV_{25}+E_5];\ A_{50}=A_0-[SV_{25}+E_5];$$

Singular Vectors

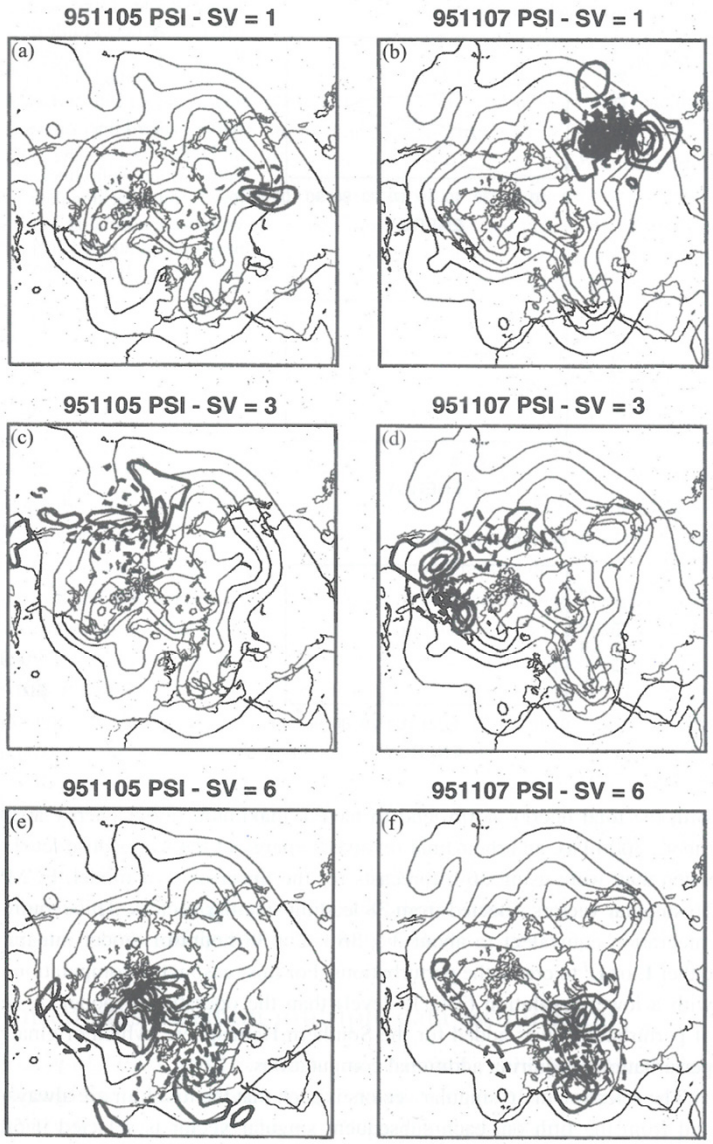

Figure 6.5.7: Singular vectors numbers 1 (top panels), 3 (middle panels), and 6 (bottom panels) at initial (left panels) and optimization time (right panels). Each panel shows the singular vector streamfunction at model level 11 (approximately 500 hPa), superimposed to the trajectory 500-hPa geopotential height field. Streamfunction contour interval is 0.5×10^{-8} m^2 s^{-1} for left panels and 20 times larger for the right panels; geopotential height contour interval is 80 m (from Buizza, 1997).

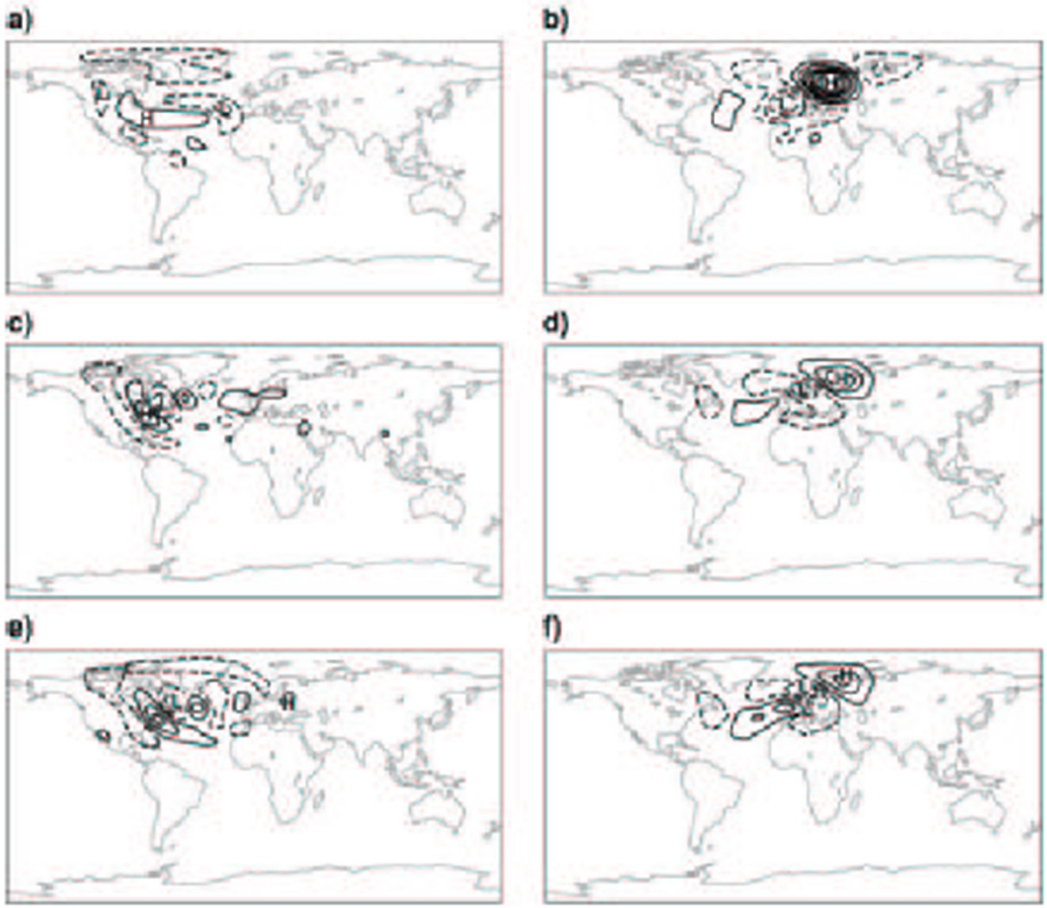

Figure 5: Streamfunction of the dominant singular atmospheric singular vector calculated using a primitive equation numerical weather prediction model for a 3-day trajectory portion made from initial conditions of 9 January 1993 at: (a) and (d) 200 hPa; (b) and (e) 700 hPa; (c) and (f) 850 hPa. The quantities in (a) - (c) are at initial time, in (d) - (f) at final time. The contour interval at optimisation time is 20 times larger than at initial time. From *Buizza and Palmer* (1995).

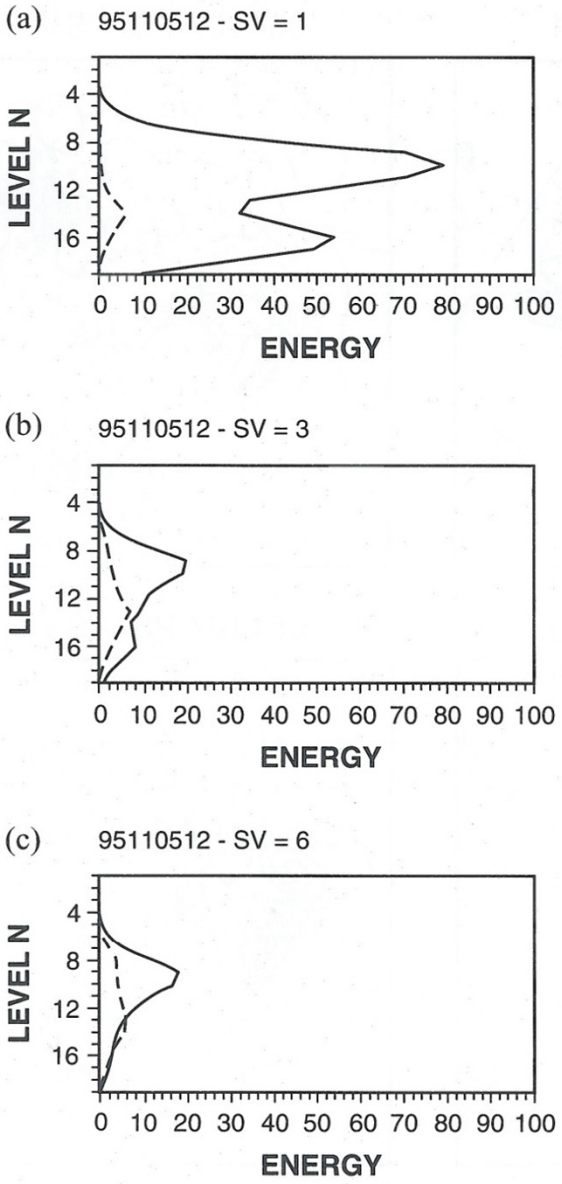

Figure 6.5.8: Total energy ($m^2\ s^{-2}$) vertical profile of the (a) first, (b) third, and (c) sixth singular vector of 5 November 1995, at the initial (dashed line, values multiplied by 100) and optimization (solid line) times. Note that singular vectors are normalized to have unit initial total energy norm. (From Buizza, 1997.)

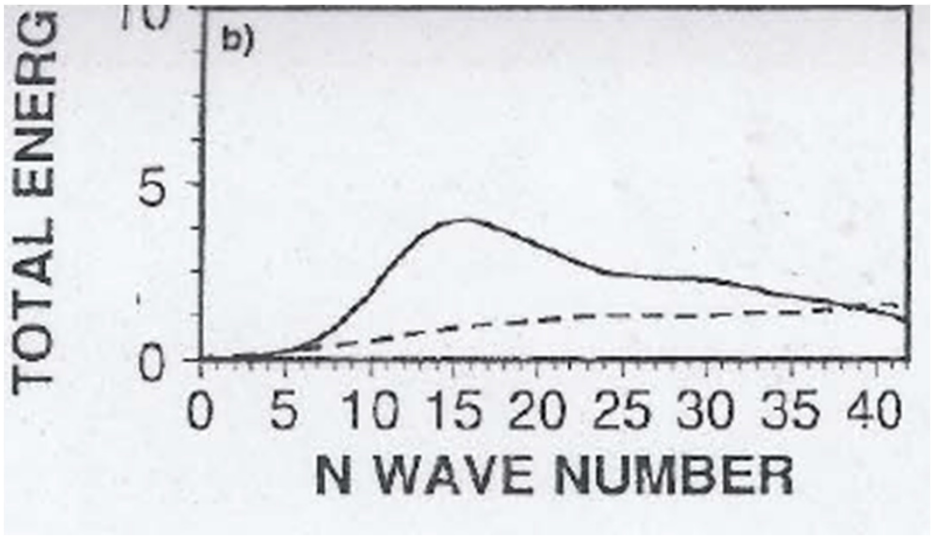

Upscale development
Of singular vectors

PALMER, T.N: PREDICTABILITY OF THE ATMOSPHERE AND OCEANS...

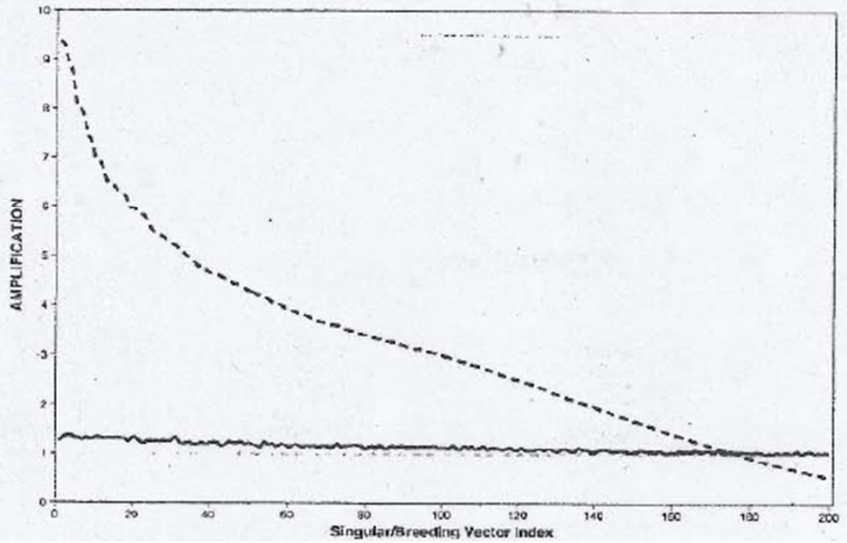

Amplification for
singular vectors
& bred vectors

Ensemble assimilation and prediction

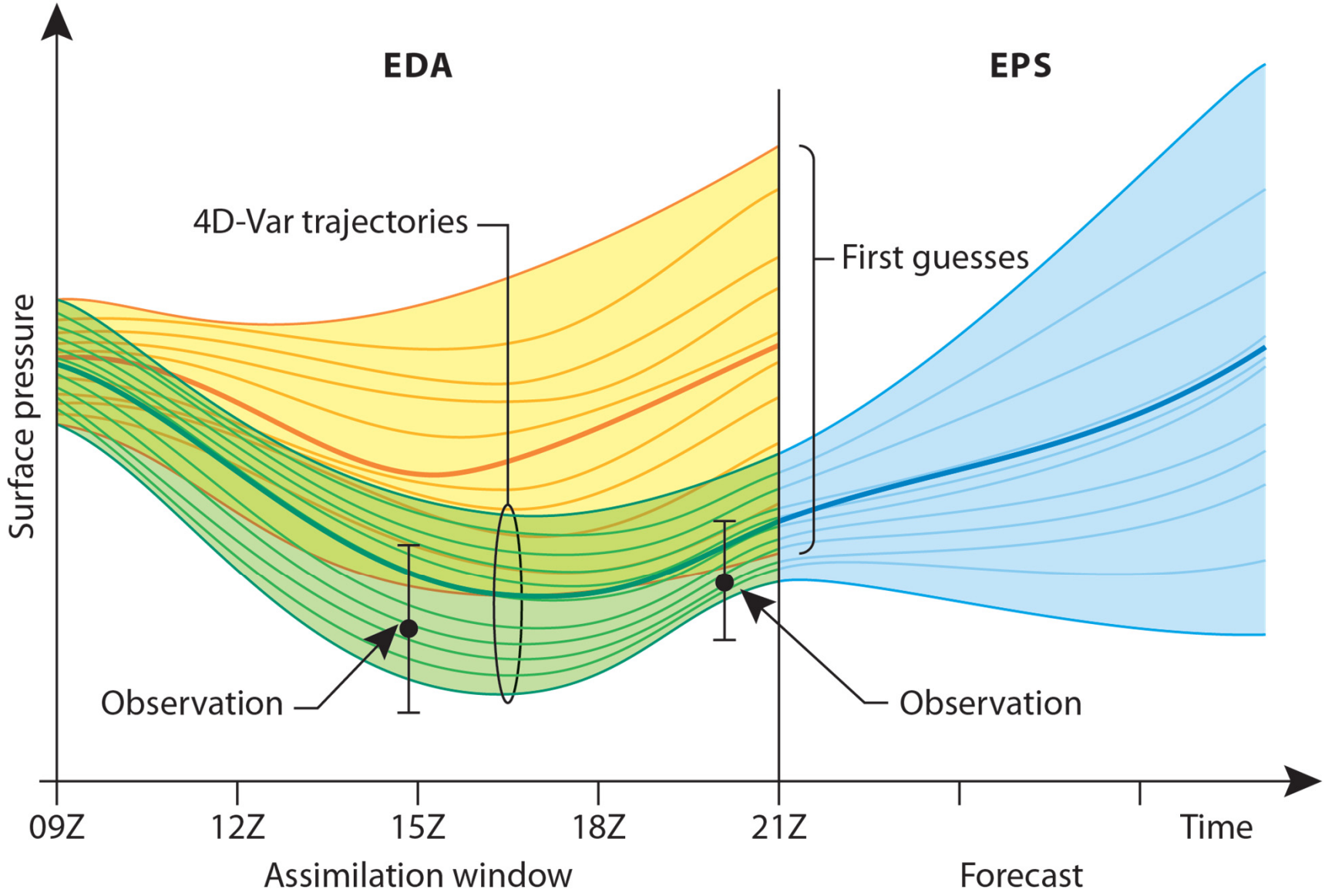

From Persson
Chapter 3

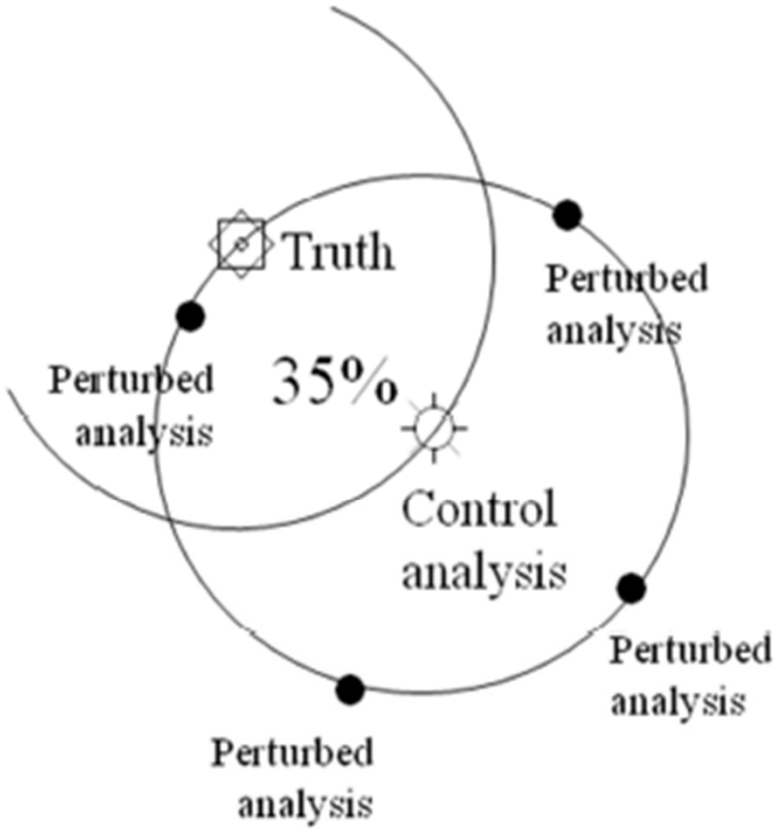

Figure 25: Although the perturbed analyses differ on average from the Control analysis as much as Control from the truth, for a specific gridpoint only 35% of the perturbed analyses are closer to the truth than the Control analysis.

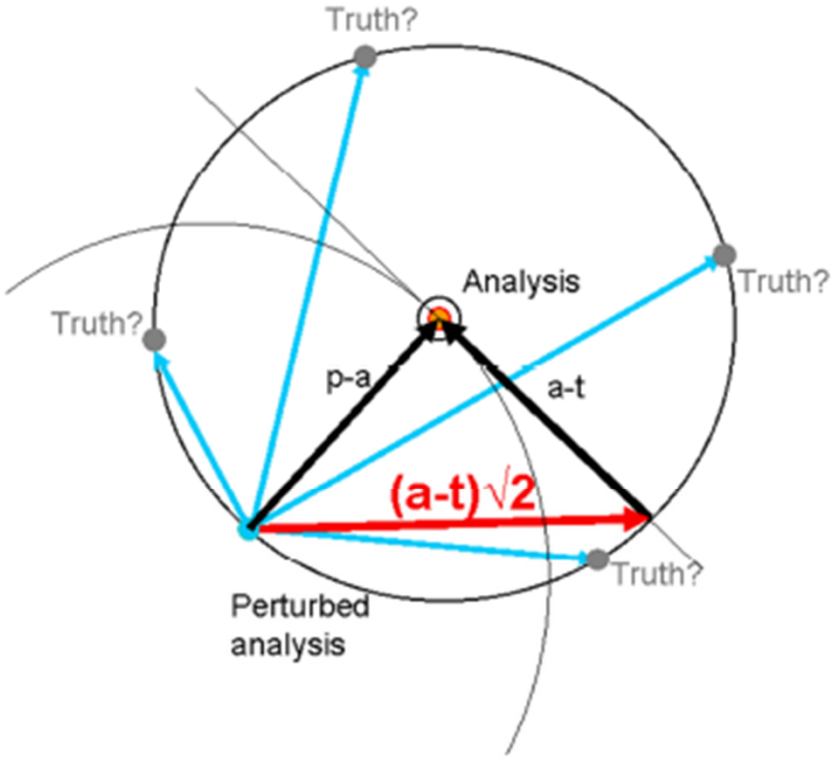

Figure 24: A schematic illustration of why the perturbations will, on average, be larger than the true Control analysis error. The analysis is known, as well as its average error, but not the true state of the atmosphere (which can be anywhere on the circle). Any perturbed analysis can be very close to the truth, but is in a majority of the cases much further away: on average the distance is the analysis error times $\sqrt{2}$

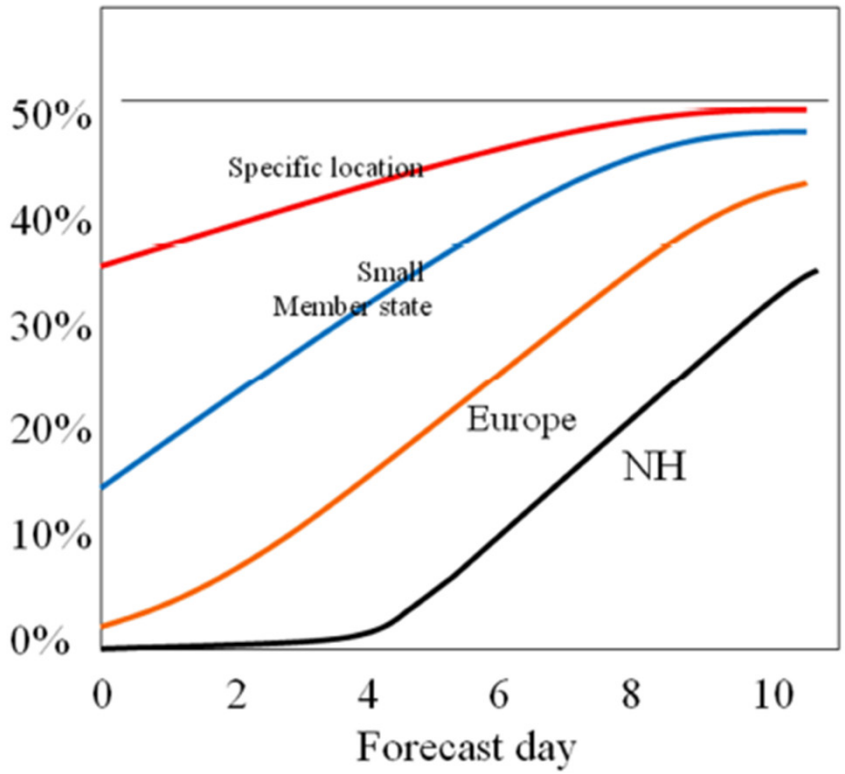

Figure 26: Schematic representation of the percentage of perturbed forecasts with lower RMSE than the Control forecast for regions of different sizes: northern hemiphere, Europe, a typical "small" Member State and a specific location. With increasing forecast range, fewer and fewer perturbed members are worse than the Control (from Palmer et al 2006).

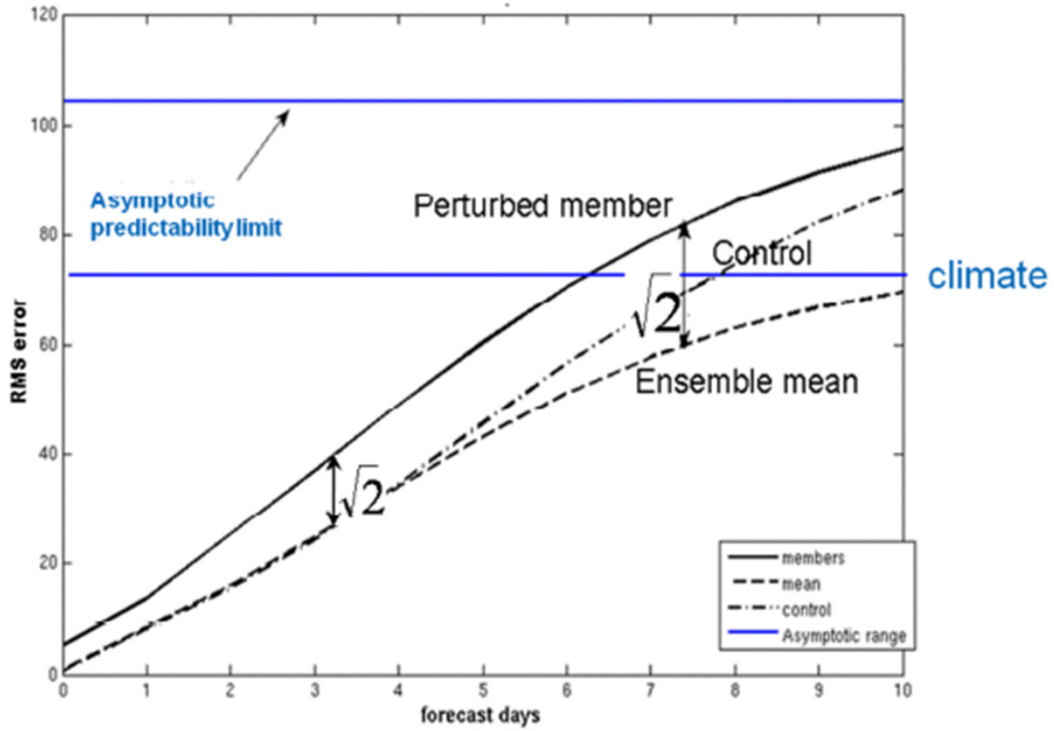

Figure 27: Schematic image of the RMS error of the ensemble members, ensemble mean and Control forecast as a function of lead-time. The asymptotic predictability limit is defined as the average difference between two randomly chosen atmospheric states. In a perfect ensemble system the RMS error of an average ensemble member is $\sqrt{2}$ times the error of the ensemble mean.

Extreme forecast index (EFI)

The EFI is an integral measure of the difference between the ensemble forecast (ENS) distribution and the model climate (M-climate) distribution.

This allows the abnormality of the forecast weather situation to be assessed without defining specific (space- and time-dependant) thresholds. The EFI takes values from -1 to +1. If all the ensemble members forecast values above the M-climate maximum, EFI = +1; if they all forecast values below the M-climate minimum, EFI = -1.

Experience suggests that EFI magnitudes of 0.5 - 0.8 (irrespective of sign) can be generally regarded as signifying that "unusual" weather is likely whilst magnitudes above 0.8 usually signify that "very unusual" weather is likely.

Although larger EFI values indicate that an extreme event is more likely, the values do not represent probabilities as such.

Model Climate (M-Climate)

For the calculation of EFI, M-climate is based on 9 consecutive semi-weekly re-forecast data sets (Mondays and Thursdays) consisting of 10+1 ensemble members, where the middle Monday or Thursday is the preceding Monday or Thursday closest to the actual ENS run date, **t**.

The resolution decreases with forecast range exactly as in the ENS. This procedure allows seasonal variations and model changes to be taken into account, as well as model drift.

Altogether **1980 re-forecast values are available for the M-climate computation** (20 years x 11 ENS members x 9 semi-weeks). The M-climate is updated semi-weekly on Mon- and Thursdays.

M-Climate= 9 semi-weekly, 11-member ENS, re-forcasts for previous 20 years

The figure shows an example when a Thursday is the closest, previous Mon- or Thursday

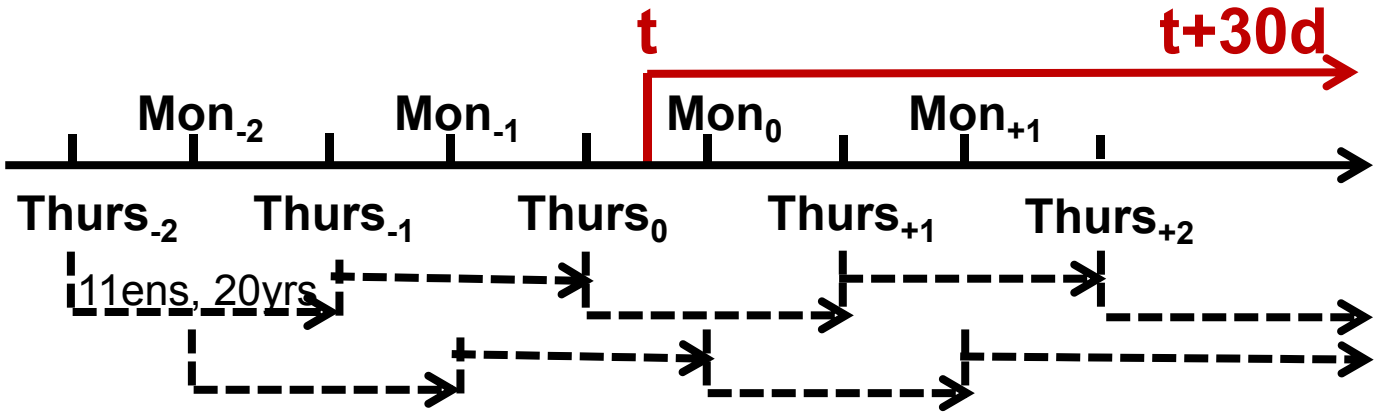

From Persson
Chapter 5

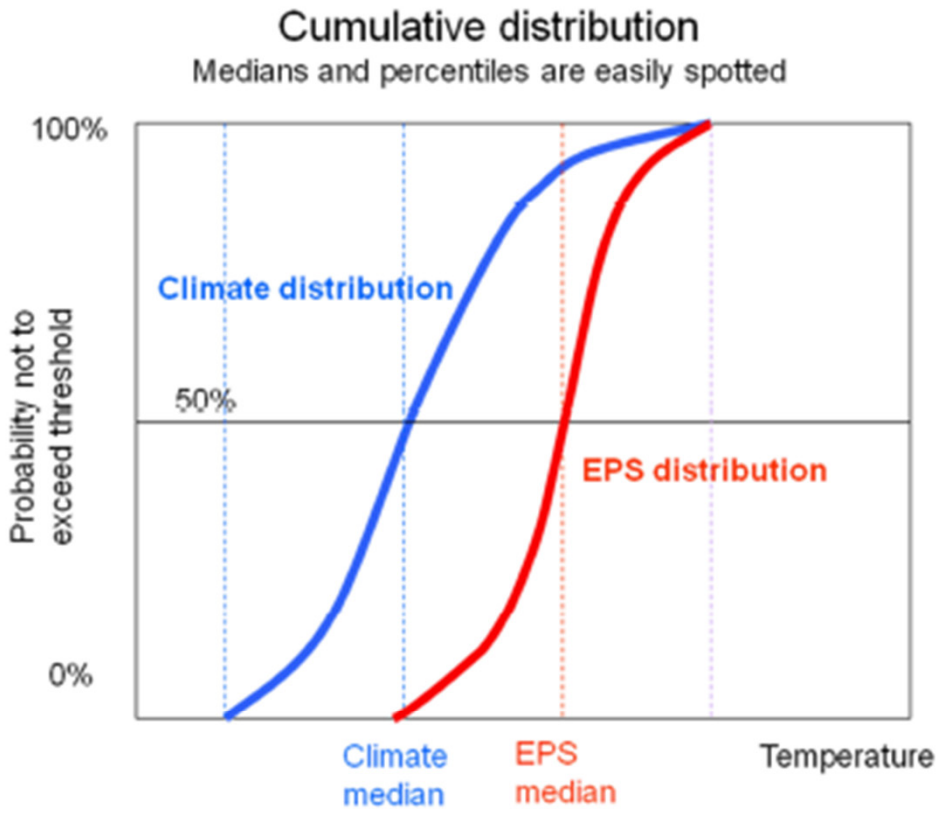

Figure 50: A schematic explanation of the principle behind the Extreme Forecast Index, measured by the area between the cumulative distribution functions (CDFs) of the M-Climate and the 50 EPS members. The steeper the slope of the CDF in an interval, the higher the probability in that interval.The EFI is, in this case, positive (red line to the right of the blue), indicating higher than normal probabilities of warm anomalies.

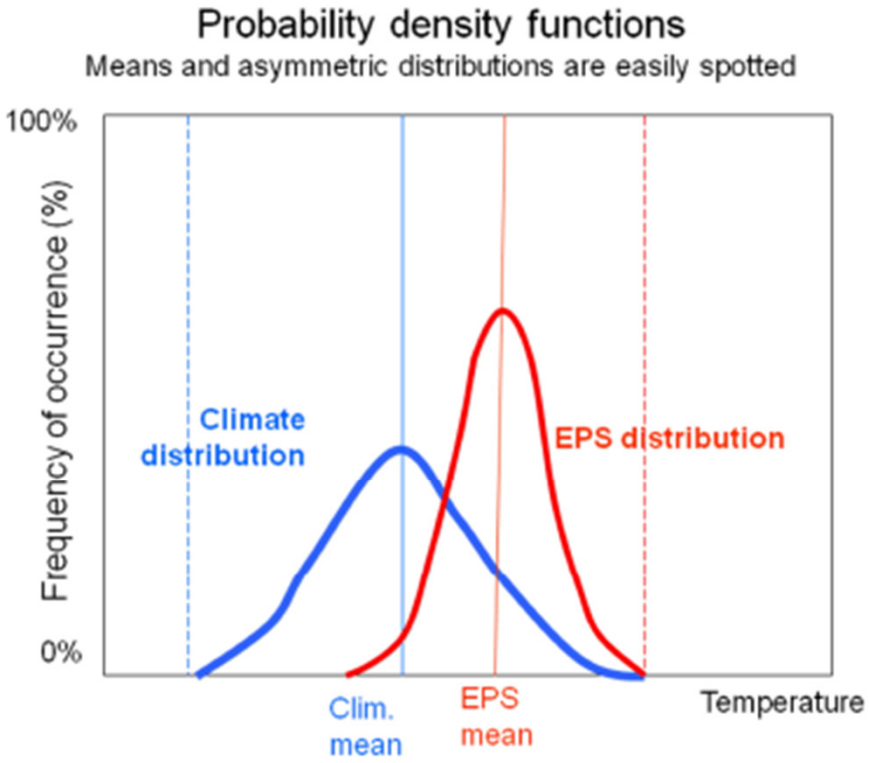

Figure 51: The temperature climatology (blue curve) and the EPS forecast distribution (red curve) presented as probability density functions corresponding to the CDF curves in Figure 50. The pdf is essentially the derivative of the CDF. The EPS pdf is to the right (red curve) of the M-climate pdf (blue curve), indicating that the EPS has higher than normal probabilities of warmer anomalies, consistent with the conclusions on positive EFI from Figure 50.

The Extreme Forecast Index is calculated according to the formula

$$EFI = \frac{2}{\pi}\int_0^1 \frac{p - F_f(p)}{\sqrt{p(1-p)}}\mathrm{dp}$$

where $F_f(p)$ denotes the proportion of EPS members lying below the p quantile of the climate

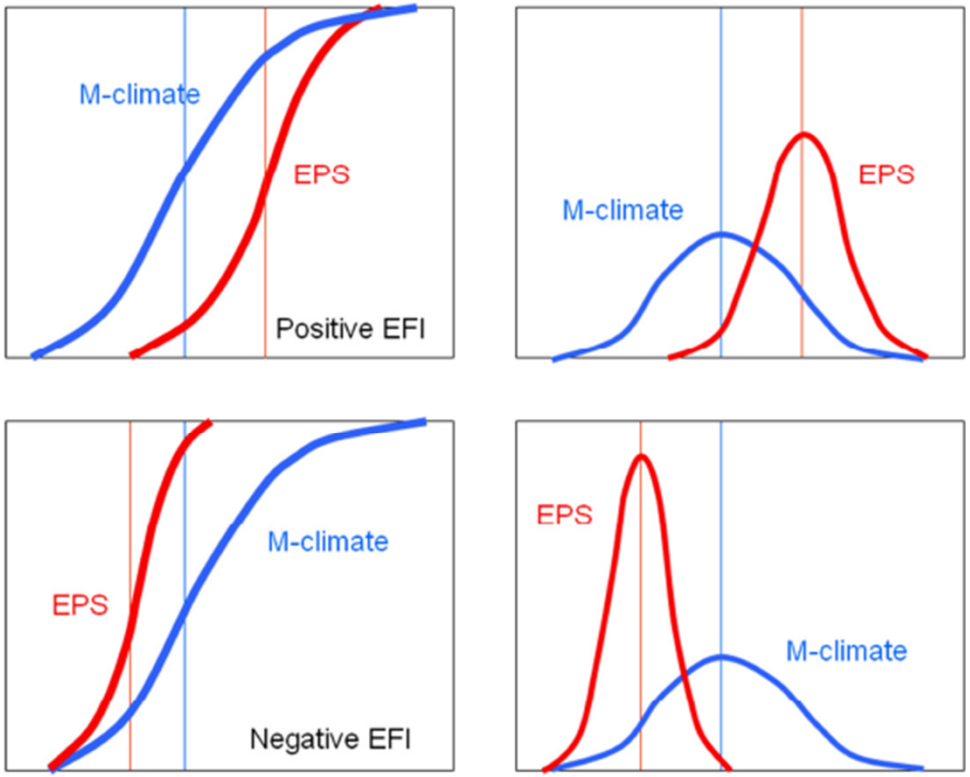

Figure 52: The EFI can have both negative and positive values: positive for positive anomalies (upper figures) and negative for negative anomalies (lower figures).

EFI and median T2 daily mean
Valid Saturday 20 - Sunday 21 Feb 00utc, 2016

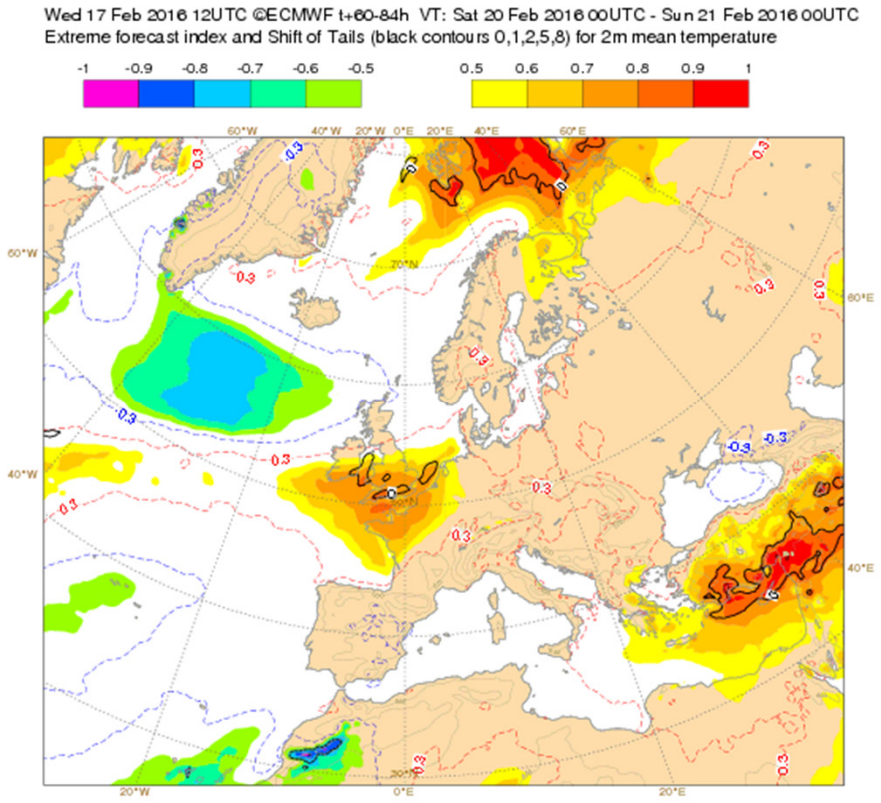

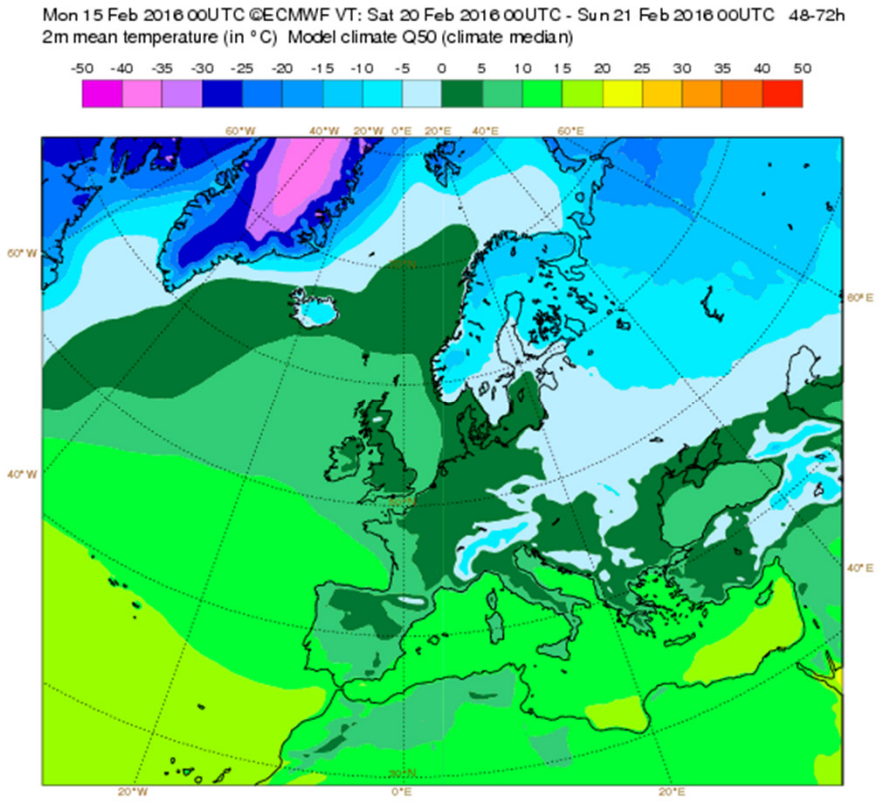

EFI and 99-percentile Precipitation
Valid Saturday 20 - Sunday 21 Feb. 00utc, 2016

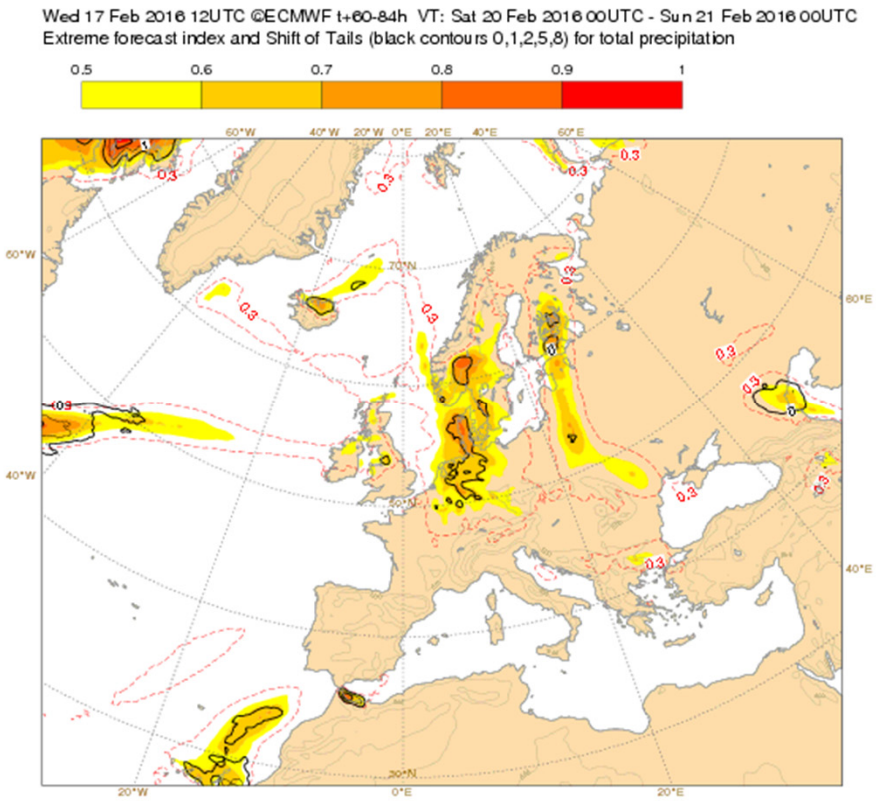

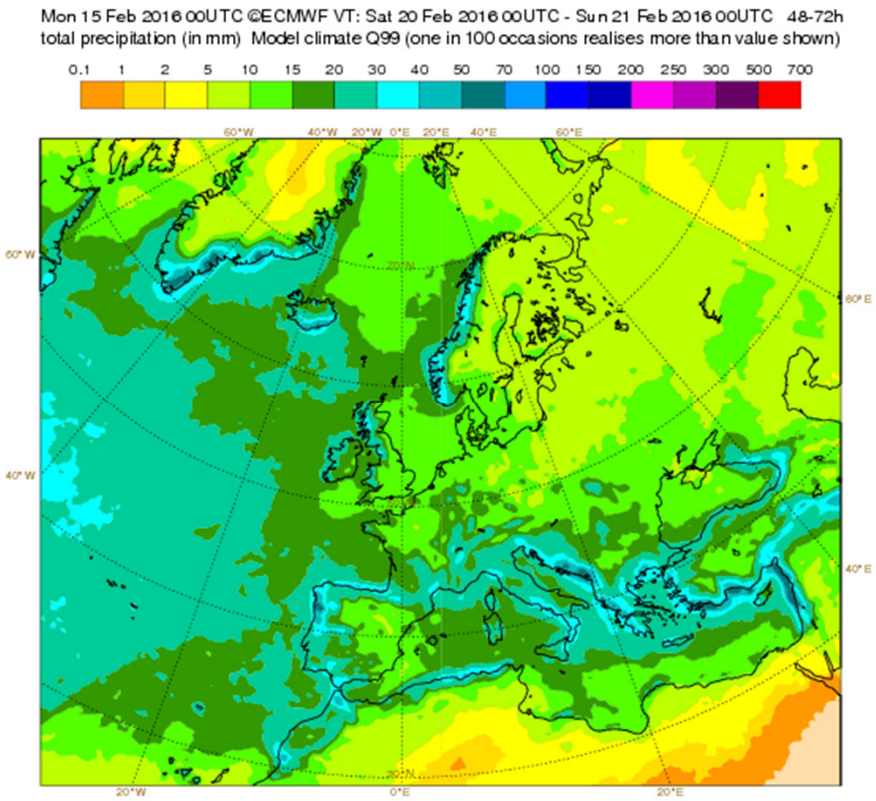

Error Growth

Kalnay, 6.6

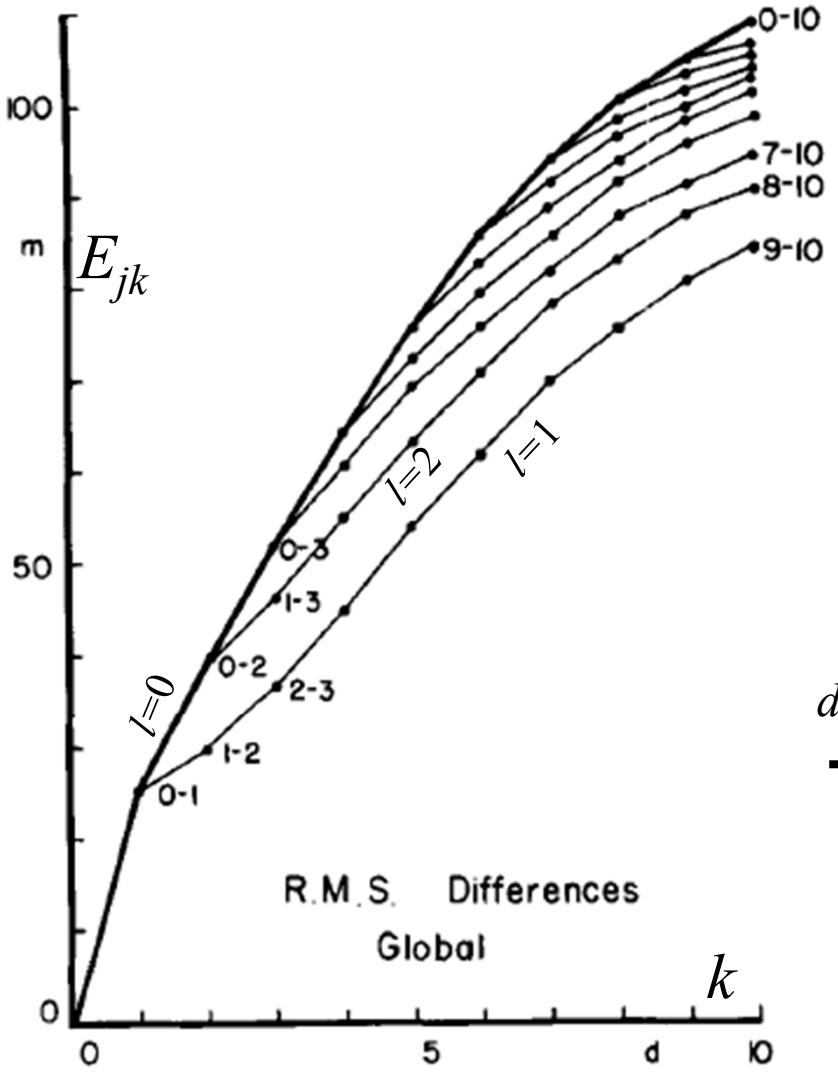

Fig. 1. Global root-mean-square 500-mb height differences E_{jk}, in meters, between j-day and k-day forecasts made by the ECMWF operational model for the same day, for $j < k$, plotted against k. Values of (j,k) are shown beside some of the points. Heavy curve connects values of E_{0k}. Thin curves connect values of E_{jk} for constant $k - j$.

Time-lagging
Lorenz (1982)

$$E_{jk} = \sqrt{\left\langle \left(f_j - f_k\right)^2 \right\rangle}$$

$$j = 0, \ldots, 10 - l;$$

$$k = l, \ldots, 10;$$

$$l = lagg\ interval\ (days) = k - j$$

$$f_j = j - days\ forecasts;$$

$$f_0 = a = analyses$$

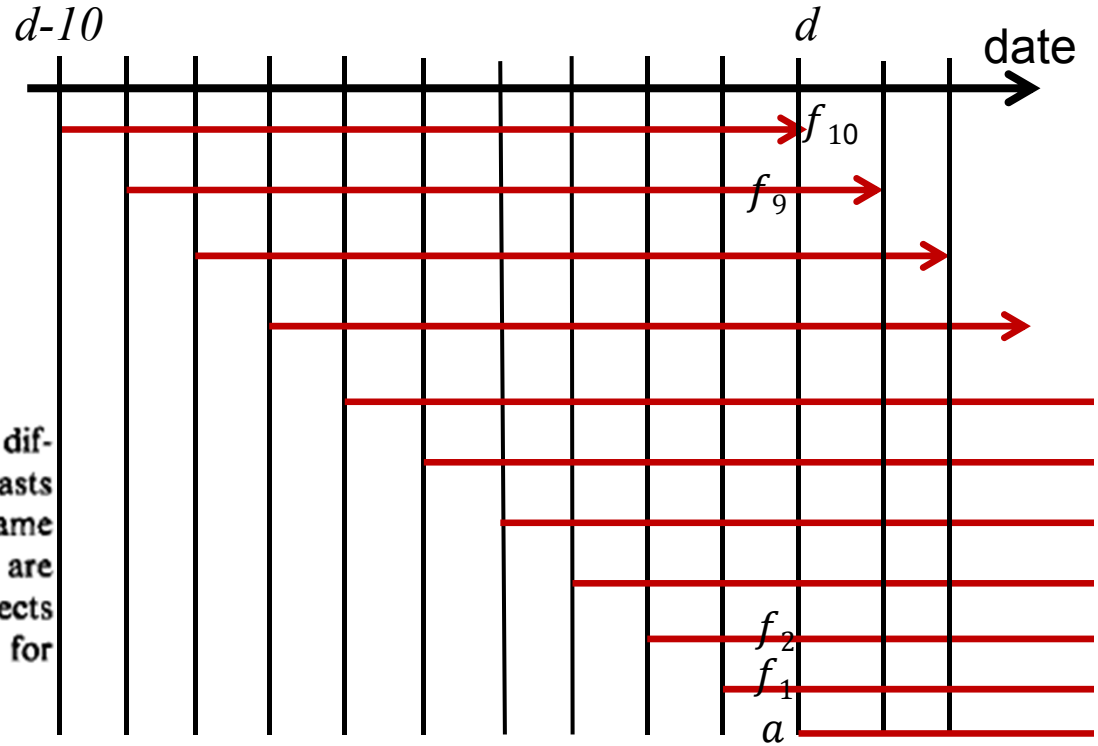

Representation of average model error

RMS-error: $E_j = \sqrt{\overline{(f_j - a)^2}} : \overline{((f_j - c) - (a - c))^2}$

$$= \overline{(f_j - c)^2} + \overline{(a - c)^2} - 2\overline{(f_j - c)(a - c)}$$

$$= (A_j)^2 + (A_a)^2 - 2\ \overline{(f_j - c)(a - c)}$$

With increasing forecast length t: $\overline{(f_i - c)(a - c)} \to 0$

➔ So that for increasing t: $E_j \to \sqrt{(A_j)^2 + (A_a)^2}$

And for a bias-free model: $E_j \to \sqrt{2}\, A_a$

Error growth-model (Lorenz, 1982):

$$\frac{\partial E}{\partial t} = \alpha E \left(1 - \frac{E}{E_\infty} \right)$$

$(\ln 2)/\alpha_{\cdot} = t_d \qquad E_\infty = \sqrt{2} A_a$

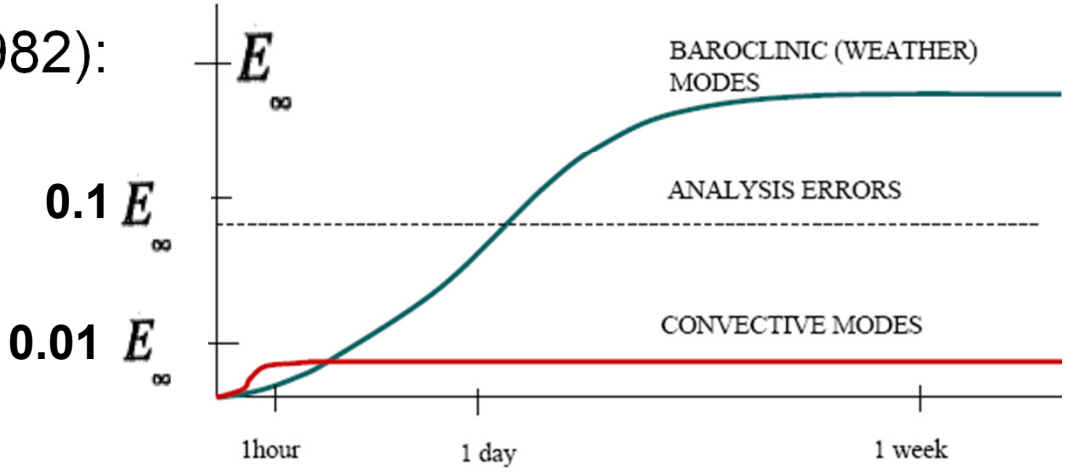

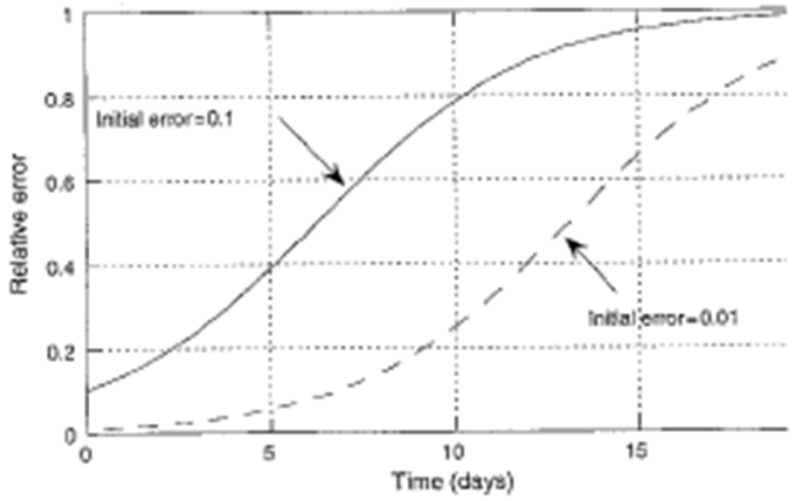

Figure 6.6.1: Time evolution of the rms forecast error divided by the squa twice the climatological variance. It assumes that the forecast error growth the logistic equation (6.6.1), and that the growth rate of small errors is abou 0.35/day, corresponding to a doubling of small errors in 2 days. Analysis er initial conditions are estimated to be about 10% or less, but not smaller tha

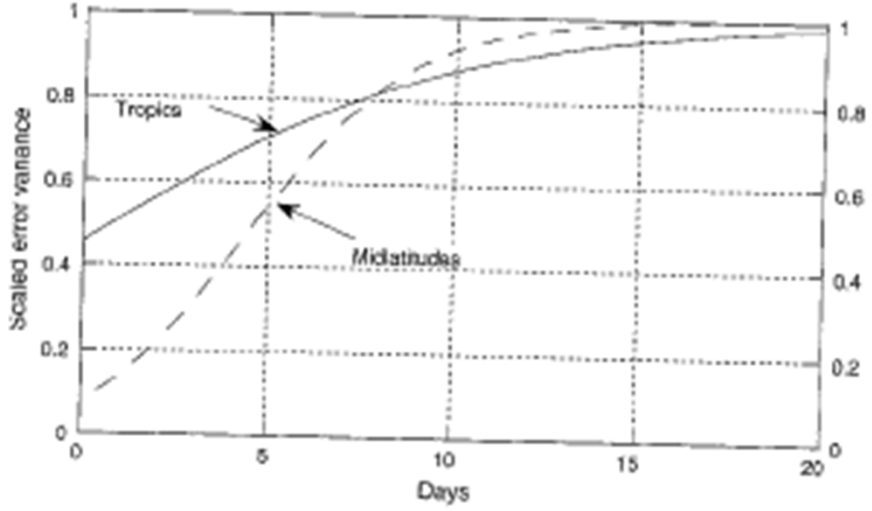

Figure 6.6.2: Parameterization of scaled forecast error variance in the presence of model deficiencies with values of the growth rate due to model deficiencies s and to instabilities b appropriate for mid-latitudes ($(b = 0.4, s = 0.05)$ and the tropics $b = 0.1, s = 0.1$). (From Reynolds *et al.*, 1994.)

Lagged forecasts, 1981 and 2001

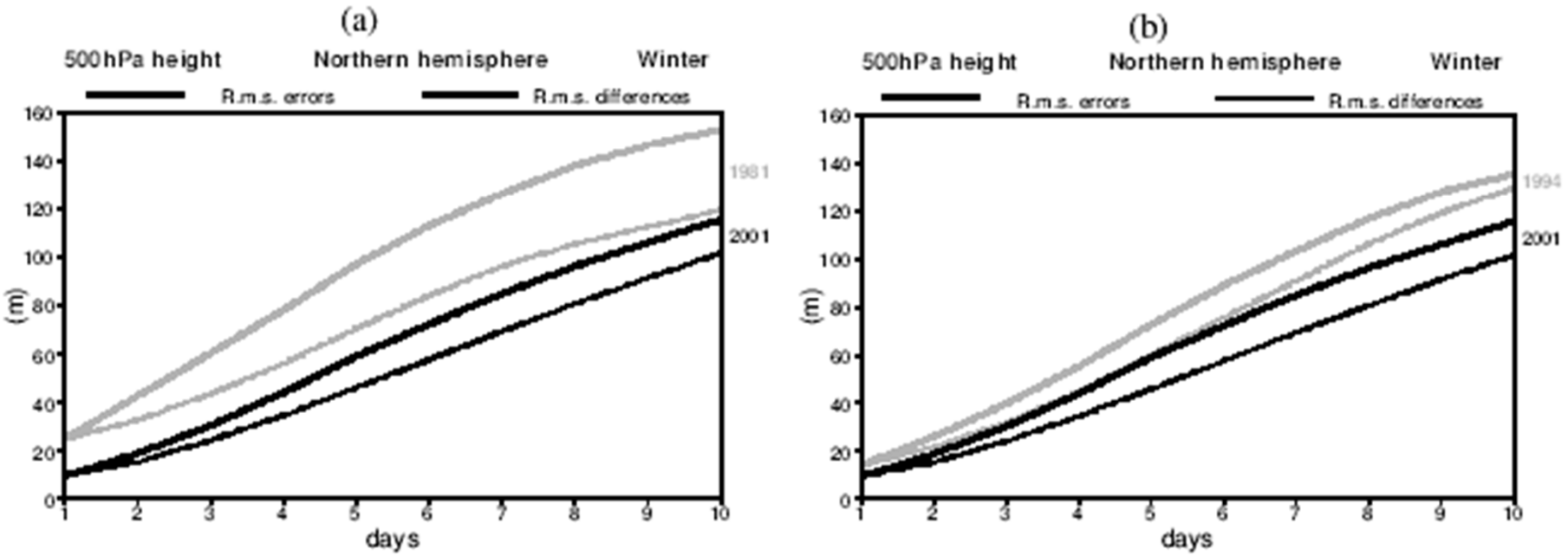

Figure 6. (a) R.m.s 500 hPa height forecast errors (solid) and differences between successive forecasts verifying at the same time (dashed) as functions of the forecast range, computed over the extratropical northern hemisphere, and shown for the winters of 1981 (grey) and 2001 (black). (b) As (a) but for the winters of 1994 (grey) and 2001 (black).

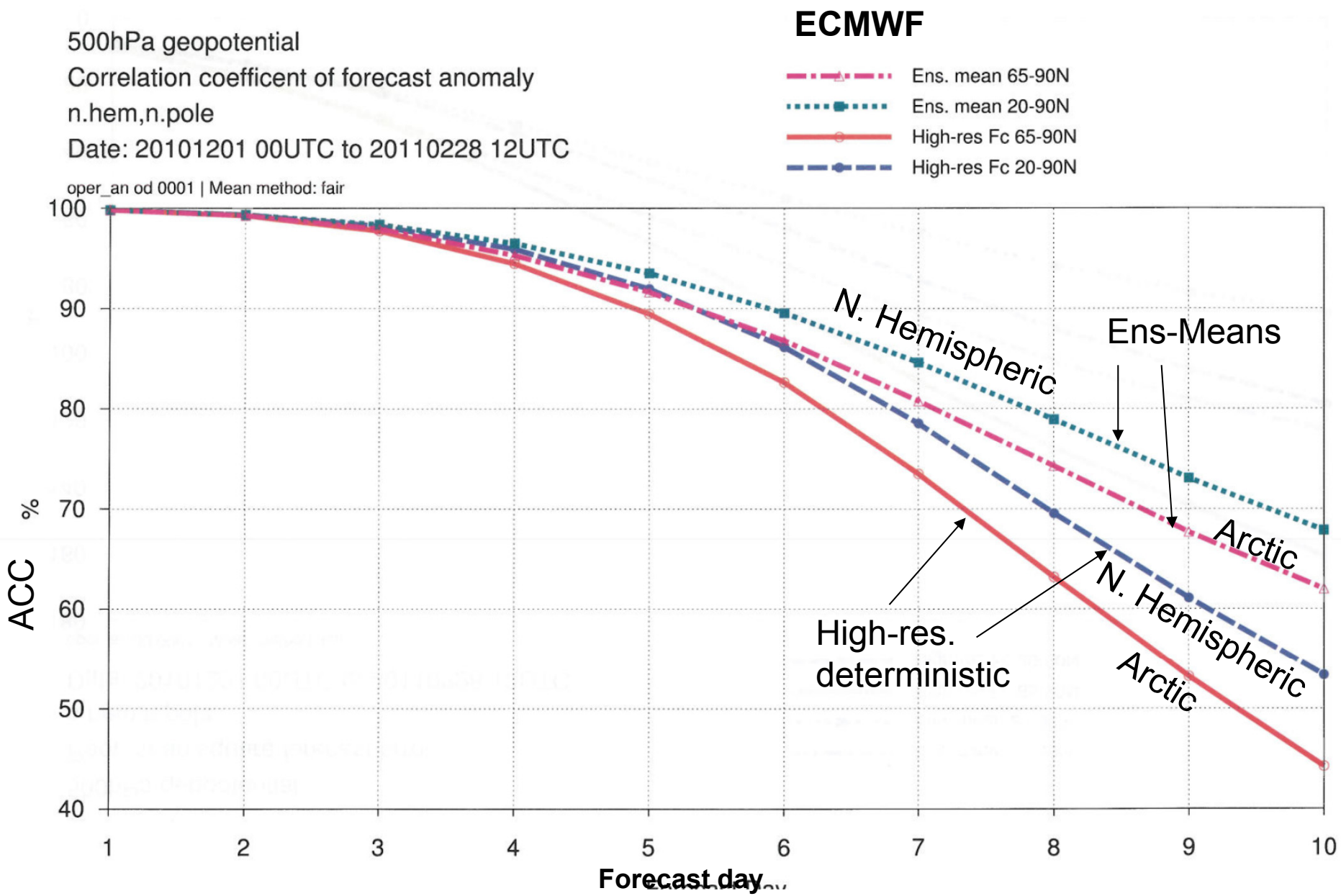

Martin Leutbecher, ECMWF, private communication

Data Assimilation

Kalnay, Ch 5
+ a few notes

$$z(x, y) = a_{00} + a_{10}x + a_{01}y + a_{20}x^2 + a_{11}xy + a_{02}y^2 \tag{5.1.1}$$

The six coefficients were determined by minimizing the mean square difference between the polynomial and observations close to the grid point (within *a radius of influence of the grid point*):

$$\min_{a_{ij}} E = \min_{a_{ij}} \sum_{k=1}^{K_z} p_k \left(z_k^o - z(x_k, y_k)\right)^2 + \sum_{k=1}^{K_v} q_k \left\{ \left[u_k^o - u_g(x_k, y_k)\right]^2 + \left[v_k^o - v_g(x_k, y_k)\right]^2 \right\} \tag{5.1.2}$$

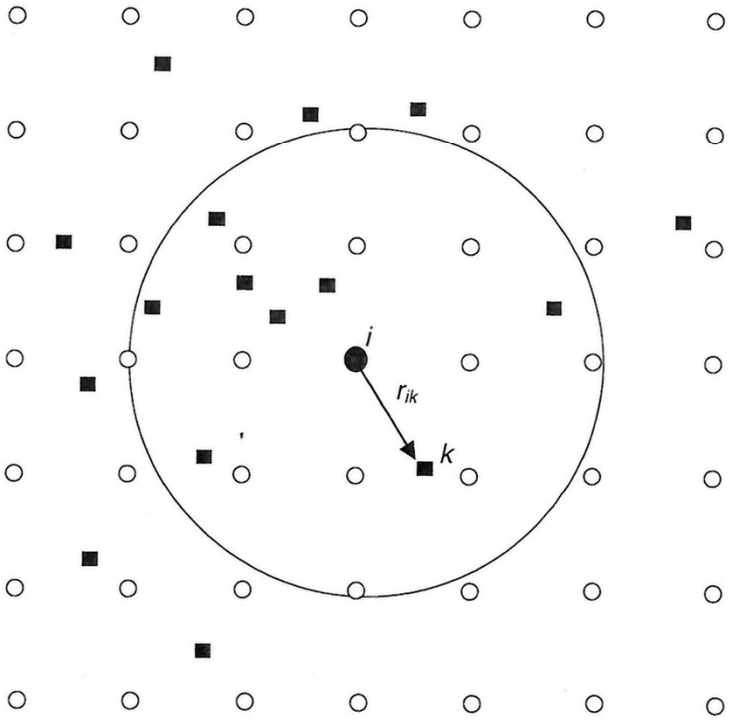

Figure 5.1.1: Schematic of grid points (circles), irregularly distributed observations (squares), and a radius of influence around a grid point i marked with a black circle. In 4DDA, the grid-point analysis is a combination of the forecast at the grid point (first guess) and the observational increments (observation minus first guess) computed at the observational points k. In certain analysis schemes, like SCM, only observations within the radius of influence, indicated by a circle, affect the analysis at the black grid point.

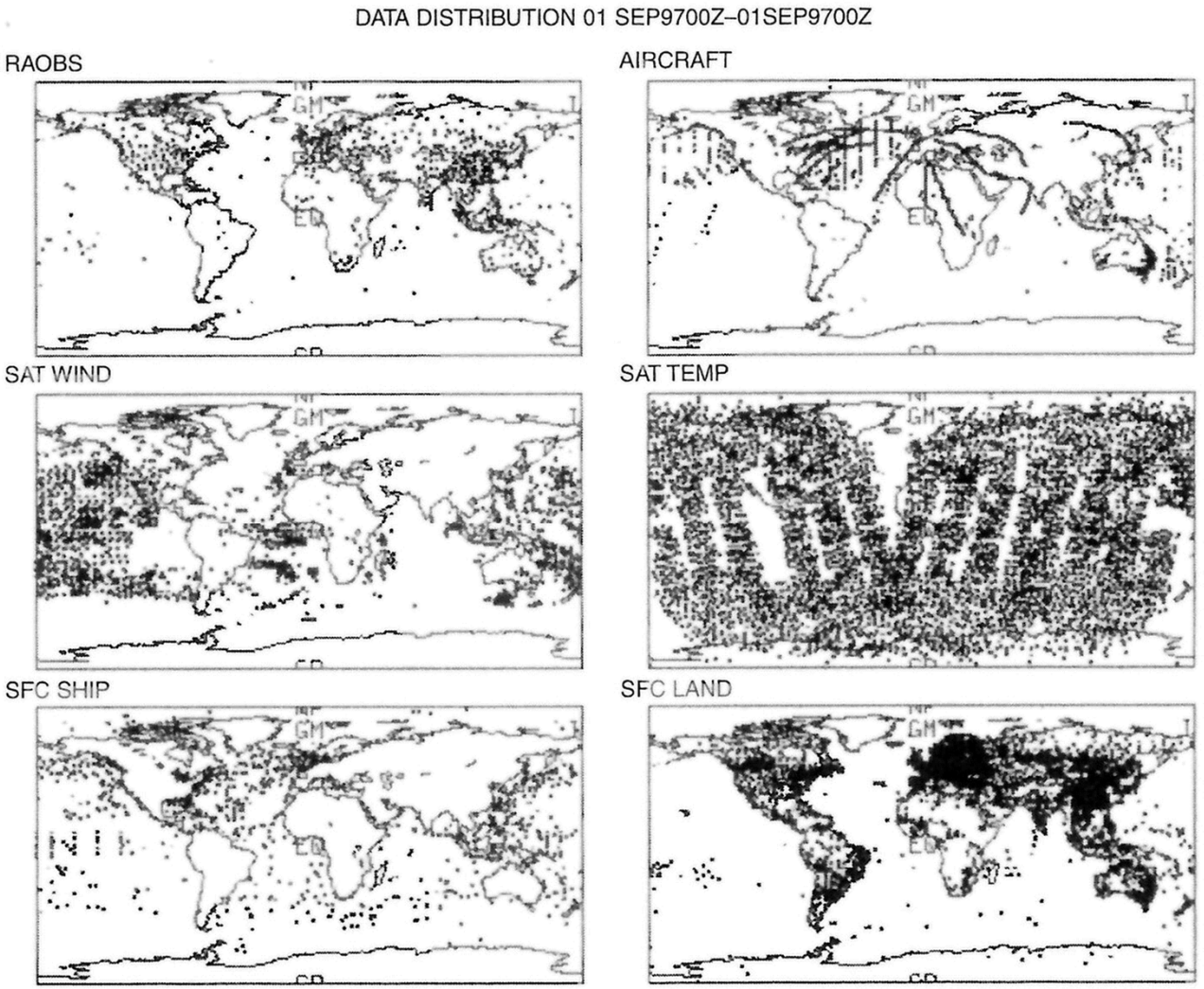

Figure 1.4.1: Typical distribution of observations in a ±3-h window.

The observing system

- Conventional observations
  - Surface
  - Profile - radiosonde and aircraft
  - WMO - coordinates observation routines and data exchange globally, EUCOS in Europe
- Remote sensing observations
  - Satellite
  - Agencies: EUMETSAT, ESA, NOAA/NASA
  - Ground based radars, "wind profilers"

- ECMWF model now: 30 mill. obs. available for assimilation per day. (State vector dimension ~10^8)

Conventional observation types used in data assimilation

Surface
- Synop (manual and automated) and ship (over land mainly pressure is assimilated)
- Buoys on ocean

Profile and upper air
- Radiosondes (TEMPs and PILOTs)
- Aircraft (AIREP and AMDAR)

Not all observation types are easy or even possible to assimilate in NWP (like clouds, visibility, …)

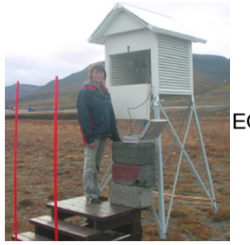

Synop+ship+metar

ECMWF Data Coverage (All obs DA) - Synop-Ship-Metar
10/Mar/2015; 00 UTC
Total number of obs = 64116

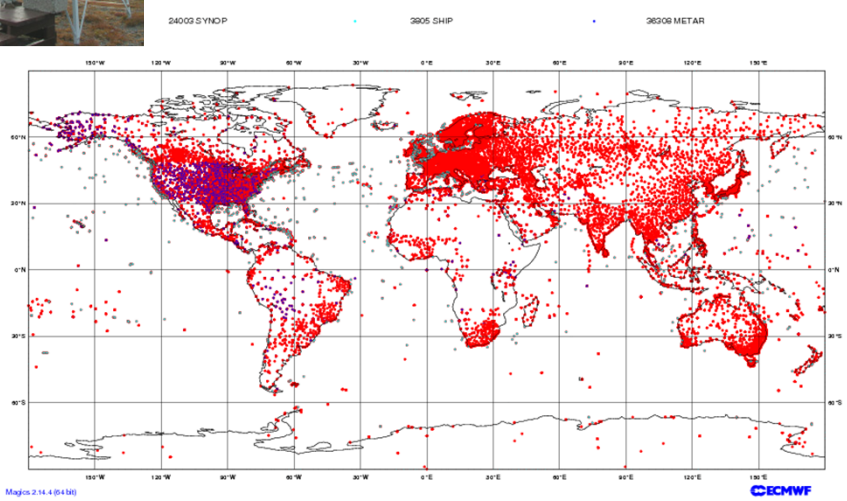

Radiosondes

ECMWF Data Coverage (All obs DA) - Temp
10/Mar/2015; 00 UTC
Total number of obs = 606

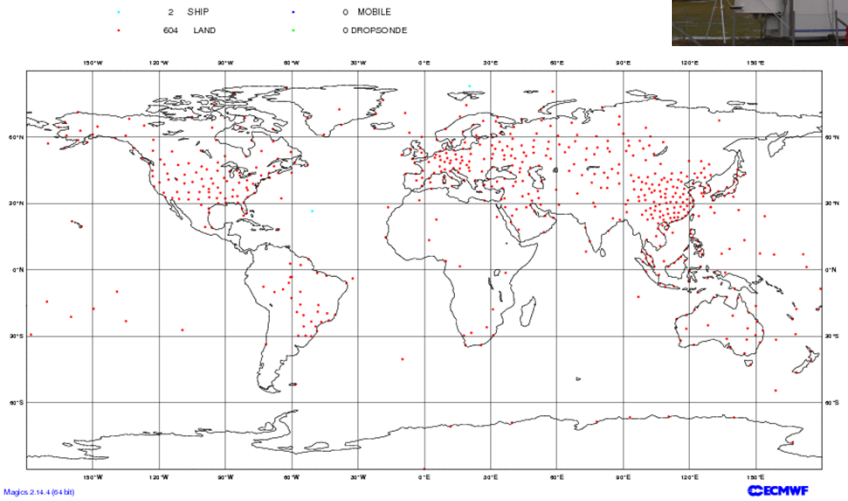

Drifting buoys

ECMWF Data Coverage (All obs DA) - Buoy
10/Mar/2015; 00 UTC
Total number of obs = 8601

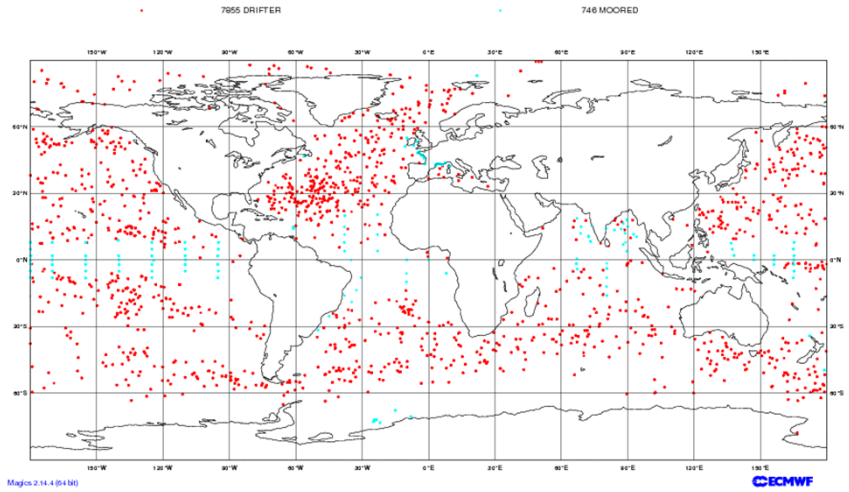

aircraft

ECMWF Data Coverage (All obs DA) - Aircraft
10/Mar/2015; 00 UTC
Total number of obs = 190101

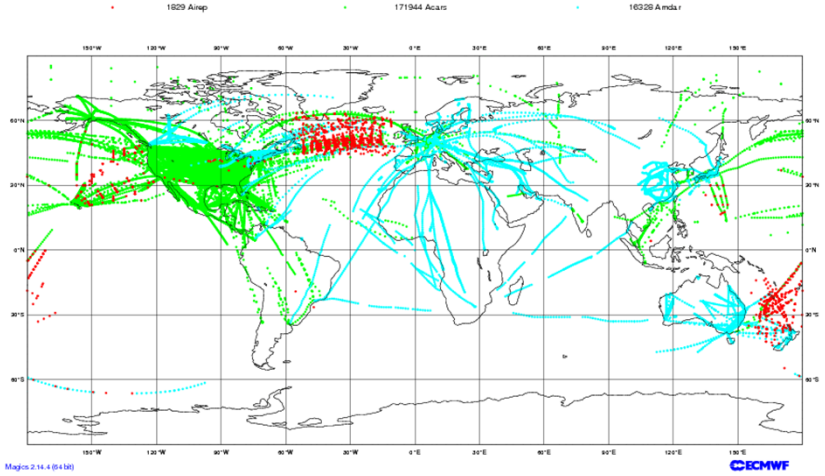

Satellite observations – divided into several groups

Passive (Top of Atmosphere radiances emitted from a surface-atmosphere column):

- Microwave
  - Profiling instruments: AMSU
  - Imaging instruments: SSM/I
- Infrared
  - Profiling instruments: HIRS, AIRS, IASI, CrIS
  - Imaging instruments: AVHRR, MODIS,
    - Atmospheric Motion Vectors

Active (RADAR, LIDAR, radio-signals):

- Scatterometer (ocean surface winds from radar)
- GPS (ground based from geodetic stations, radio occultation)

Microwaves

AMSU-B

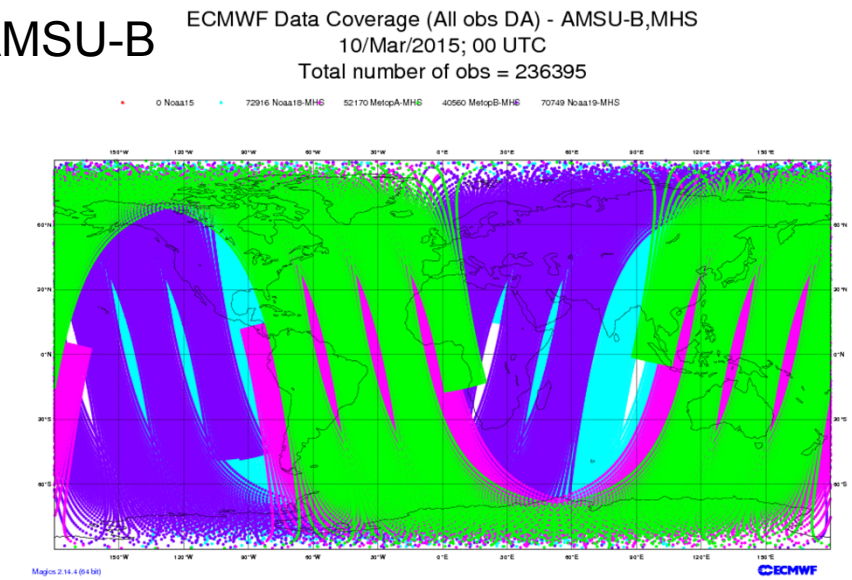

AMSU-A

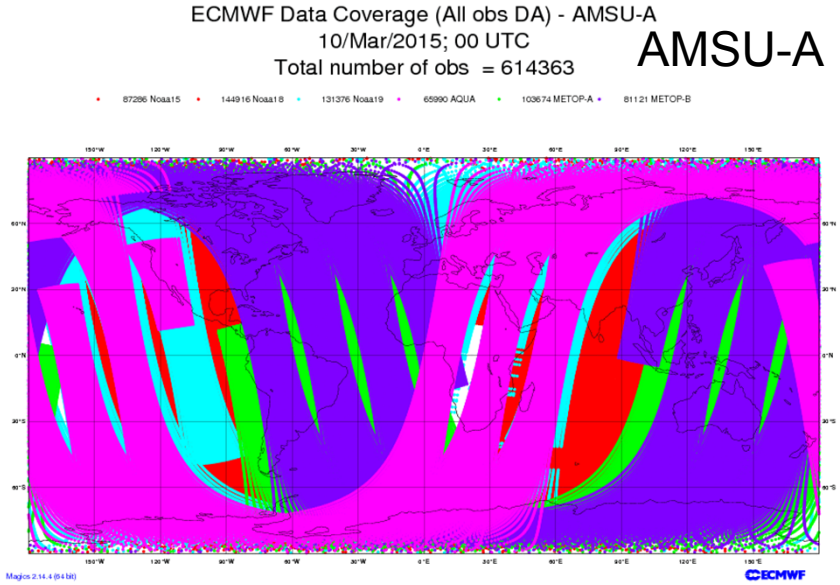

IASI

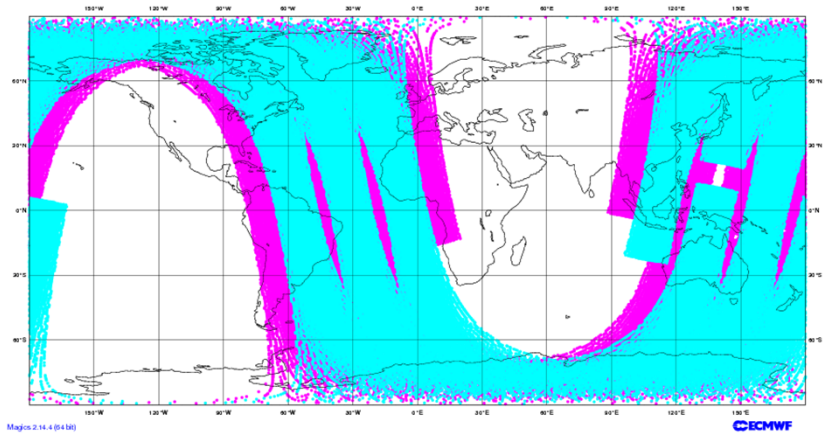

ECMWF Data Coverage (All obs DA) - Ground Based GPS
10/Mar/2015; 00 UTC
Total number of obs = 59552

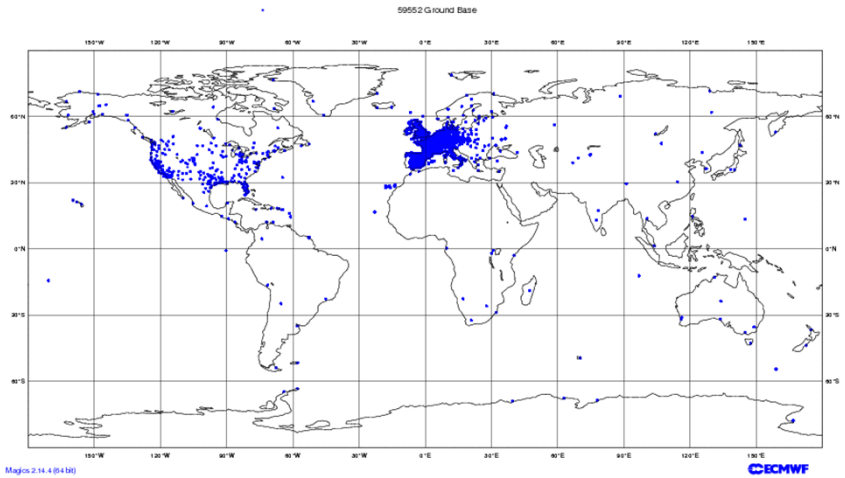

GPS radiooccultation

Scatterometer

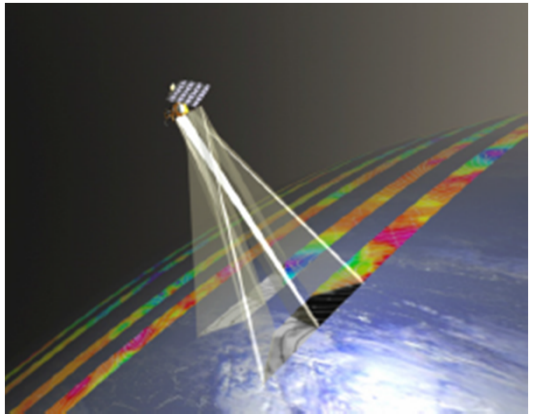

ECMWF Data Coverage (All obs DA) - SCAT
10/Mar/2015; 00 UTC
Total number of obs = 489574

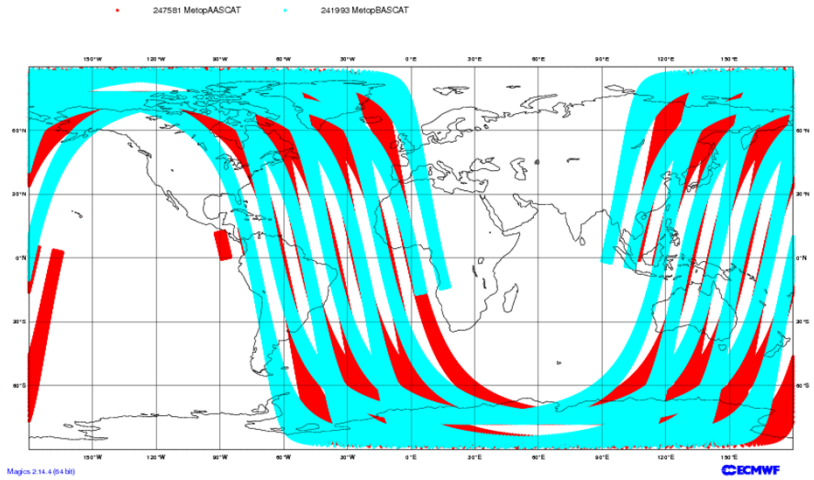

VIS

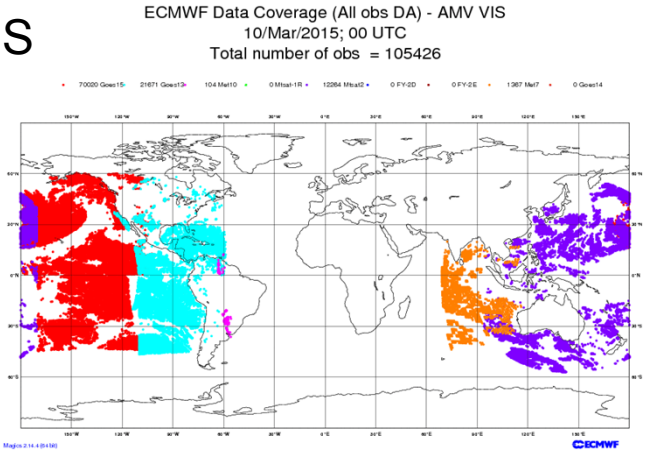

AMV= Atmospheric Motion Vectors

+ radiances

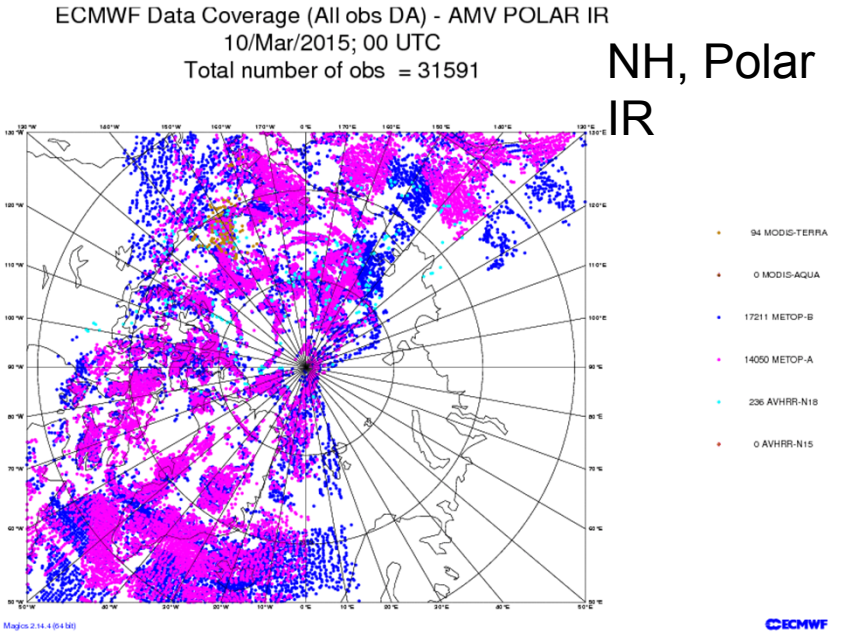

NH, Polar IR

IR

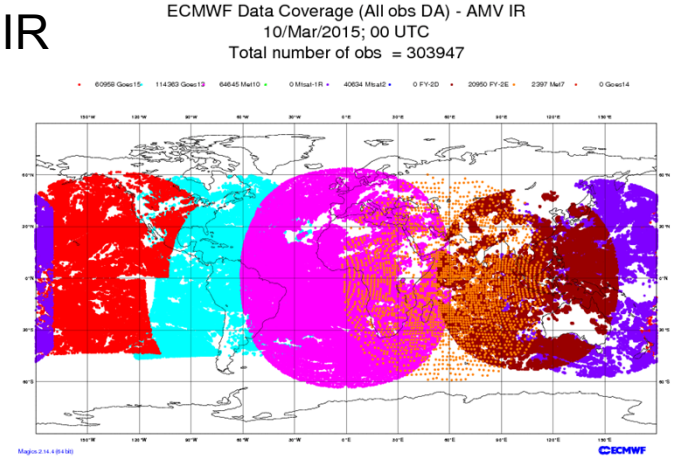

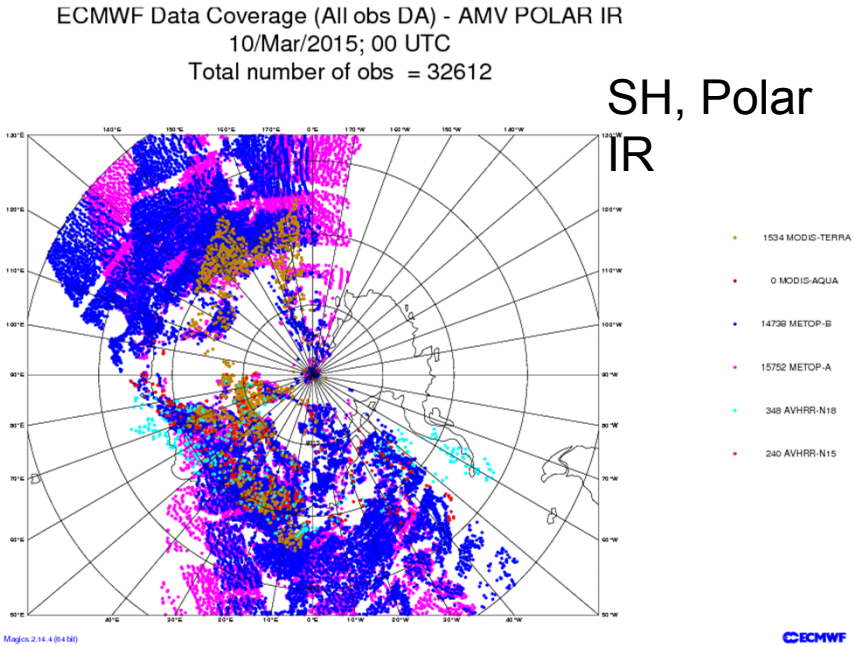

SH, Polar IR

WVap

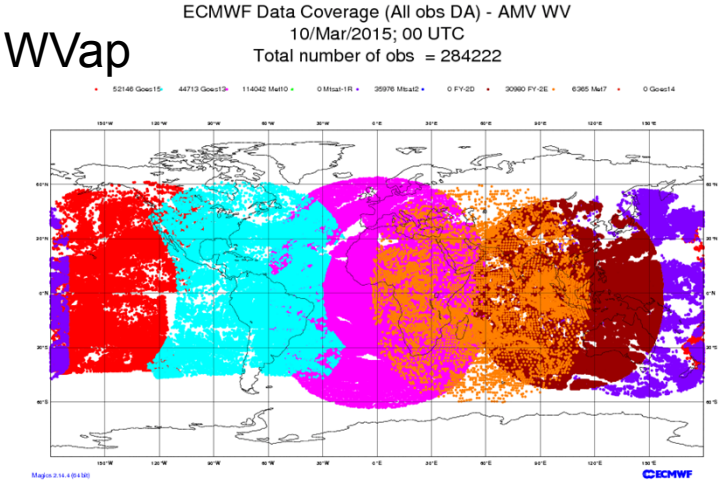

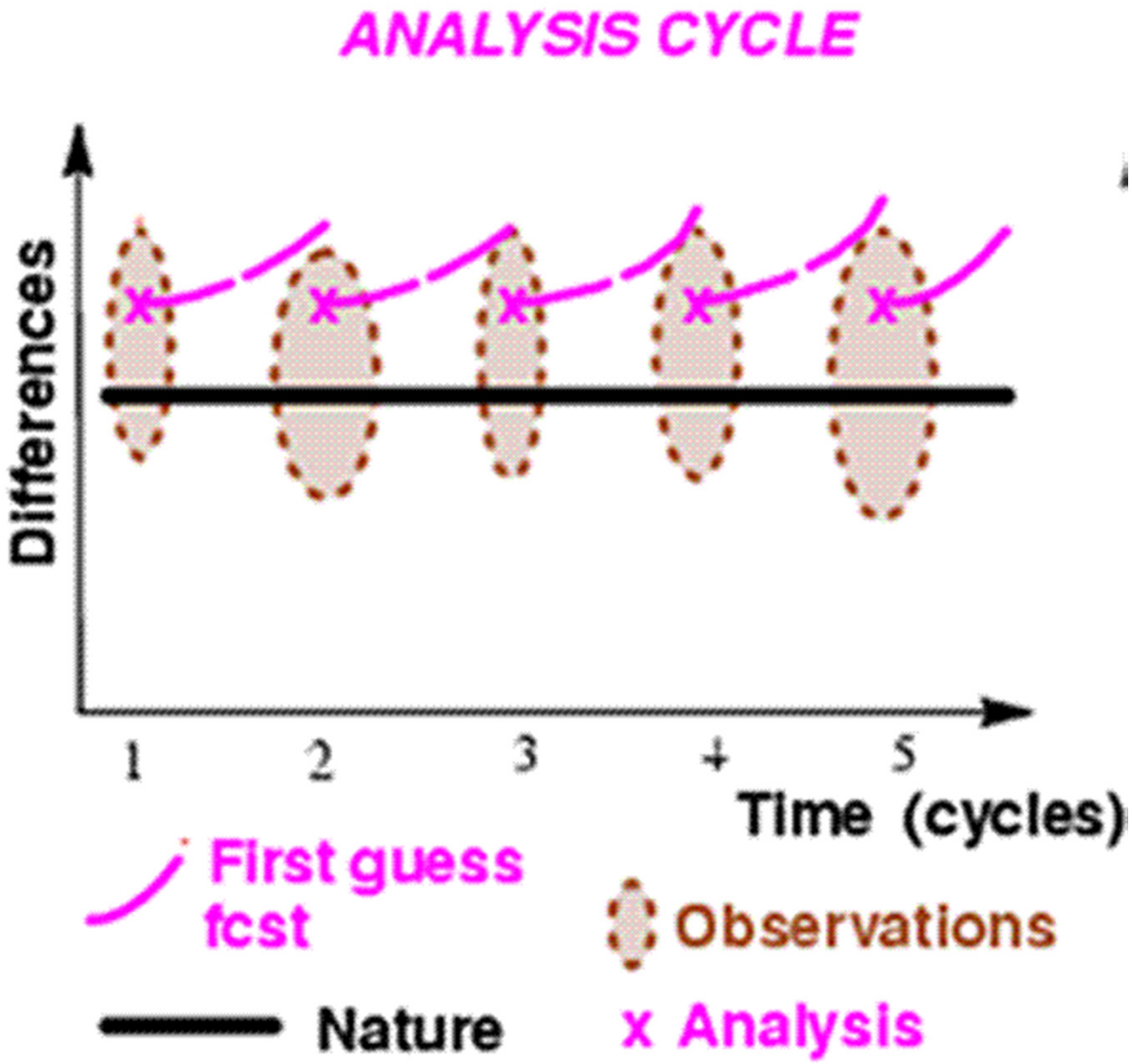
ANALYSIS CYCLE
Differences
1
2
3
4
5
Time (cycles)
First guess fcst
Observations
Nature
x Analysis

Increase in assimilated satellitte data (number of sensors) at ECMWF

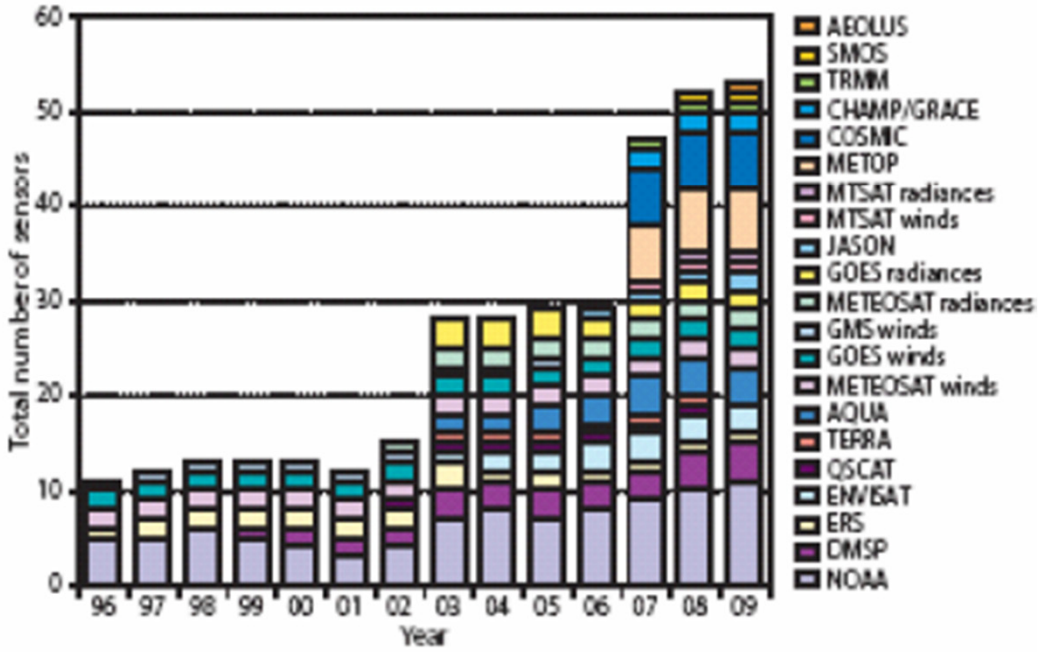

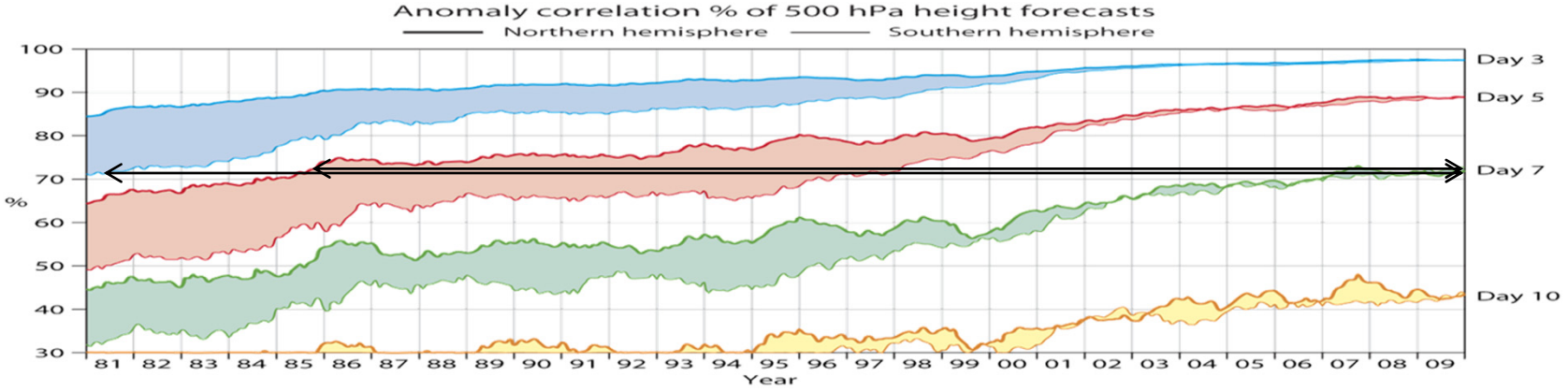

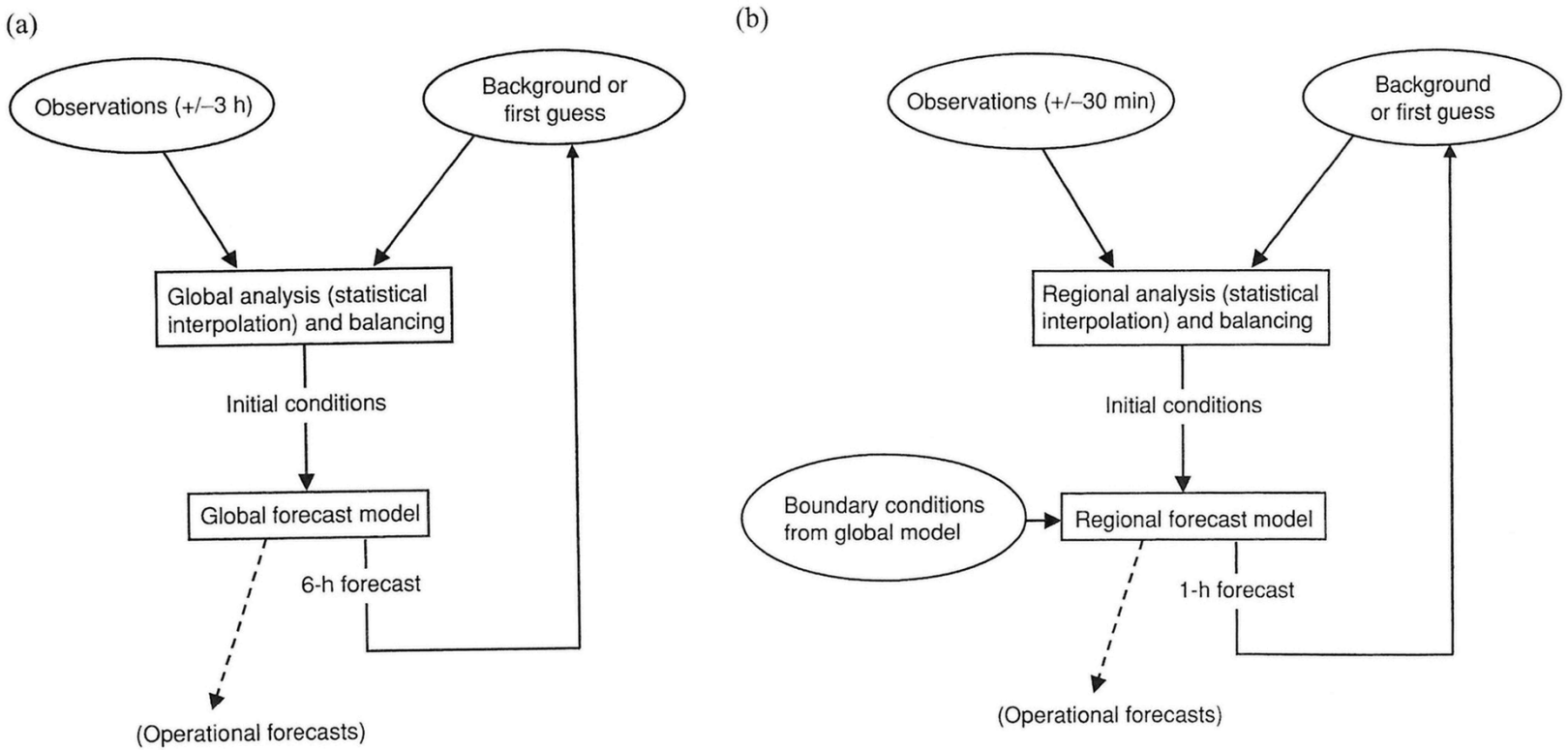

Figure 5.1.2: (a) Typical global 6-h analysis cycle performed at 00, 06, 12, and 18 UTC. The observations should be valid for the same time as the first guess. In the global analysis this has usually meant the rawinsondes are launched mostly at the main observing times (00 and 12 UTC), and satellite data are lumped into windows centered at the main observing times. The observations can be direct observations of variables used by the model, or indirect observations of geophysical parameters, such as radiances, that depend on the variables used in the model. (b) Typical regional analysis cycle. The main difference with the global cycle is that boundary conditions coming from global forecasts are an additional requirement for the regional forecasts.

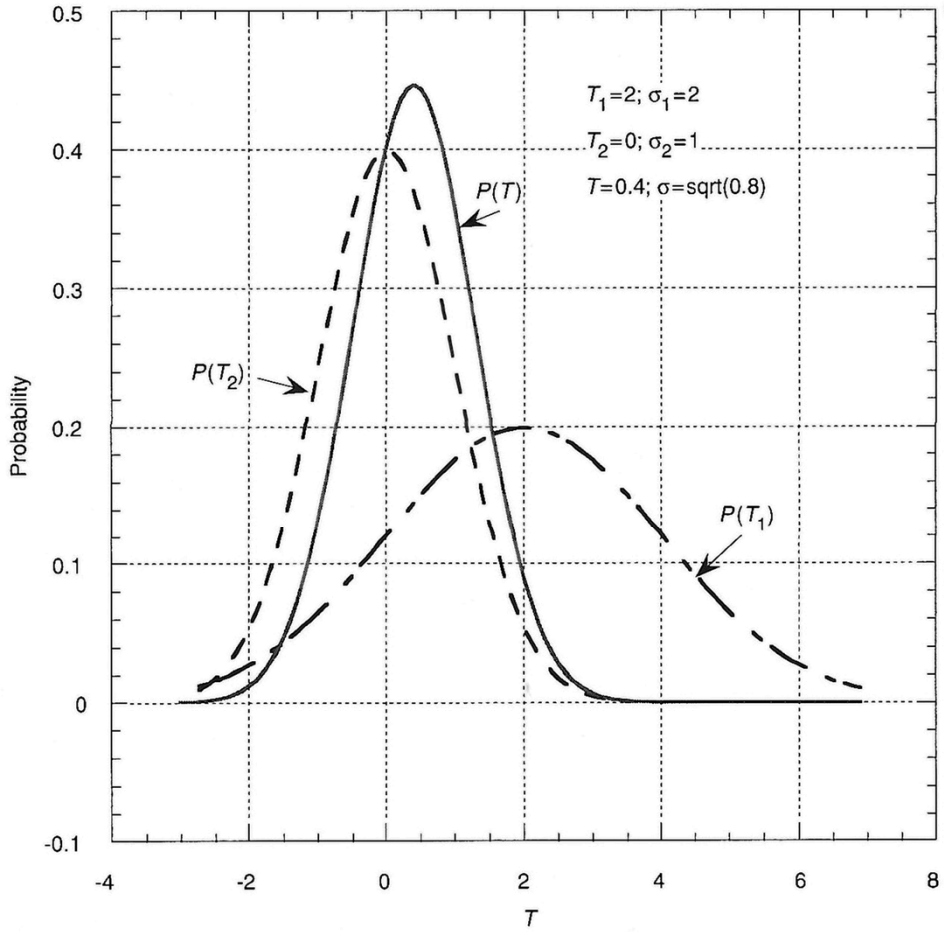

Figure 5.3.1: Illustration of the properties of the probability distribution of the analysis T, given observations T_1 and T_2, using either the least squares approach or the Bayesian approach (after Purser, 1984).

$$T_a = T_b + W(T_o - T_b) \tag{5.3.15}$$

where $(T_o - T_b)$ is defined as the *observational "innovation"* , i.e., the new information brought by the observation. It is also known as the *observational increment* (with respect to the background); W is the optimal weight, given by

$$W = \sigma_b^2(\sigma_b^2 + \sigma_o^2)^{-1} \qquad = \sigma_o^{-2}(\sigma_o^{-2} + \sigma_b^{-2})^{-1} \tag{5.3.16}$$

and the analysis error variance is, as before,

$$\sigma_a^2 = (\sigma_b^{-2} + \sigma_o^{-2})^{-1} \tag{5.3.17}$$

The analysis variance can in turn be written as $\sigma_a^2 = \sigma_b^2\sigma_o^2/(\sigma_b^2 + \sigma_o^2)$, or

$$\sigma_a^2 = (1 - W)\sigma_b^2 \tag{5.3.18}$$

1 parameter

For convenience, we repeat the basic equations of OI, and express in words their interpretation, which is similar to that for a scalar least square problem from the last section:

$$\mathbf{x}_a = \mathbf{x}_b + \mathbf{W}[\mathbf{y}_o - H(\mathbf{x}_b)] = \mathbf{x}_b + \mathbf{W}\mathbf{d} \tag{5.4.1}$$

$$\mathbf{W} = \mathbf{B}\mathbf{H}^T(\mathbf{R} + \mathbf{H}\mathbf{B}\mathbf{H}^T)^{-1} \tag{5.4.19a}$$

We will see in Section 5.5 (where we derive the variational approach or 3D-Var) that the weight matrix (5.4.19) can be written in an alternative equivalent form as

$$\mathbf{W} = (\mathbf{B}^{-1} + \mathbf{H}^T\mathbf{R}^{-1}\mathbf{H})^{-1}\mathbf{H}^T\mathbf{R}^{-1} \tag{5.4.19b}$$

(see (5.5.11) in Section 5.5)

$$\mathbf{P}_a = (\mathbf{I}_n - \mathbf{W}\mathbf{H})\mathbf{B} \tag{5.4.20}$$

where the subscript n is a reminder that the identity matrix is in the analysis or model space.

$$\mathbf{P}_a^{-1} = \mathbf{B}^{-1} + \mathbf{H}^T\mathbf{R}^{-1}\mathbf{H} \tag{5.4.22}$$

Equation (5.4.22) says: "The analysis precision, defined as the inverse of the analysis error covariance, is the sum of the background precision and the observation precision projected onto the model space."

Multi-parameter

N= model phase-space dim

P= obs phase-space dim

3DVar and 4DVar

simple presentation

Based on notes by A. Persson and F. Grizzini, ECMWF 2007

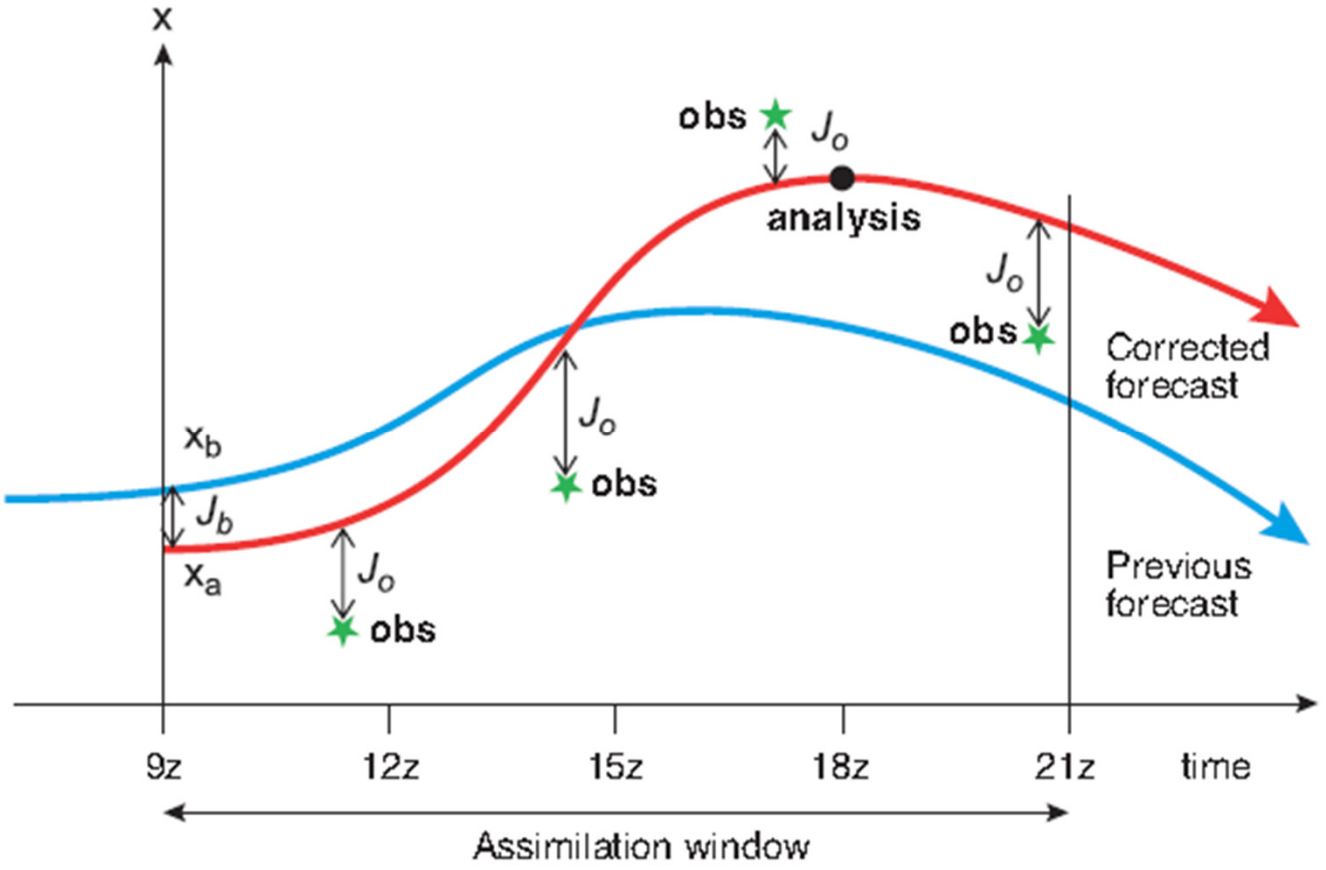

The analysis, A, defined by least-squares assumption

(Equations from Persson & Grazzini vs. Kalnay)

observation (O)
background field value (F)
accuracies σ_O and σ_B

$$A = O\frac{\sigma_B^2}{\sigma^2{}_B + \sigma^2{}_O} + F\frac{\sigma_O^2}{\sigma^2{}_B + \sigma^2{}_O}$$

Equivalent to combining (5.3.15) and (5.3.16) in Kalnay *($A=T_a$; $F=T_b$; $O=T_o$):*

$$T_a = \sigma_b^2(\sigma_o^2 + \sigma_b^2)^{-1}\, T_o + \sigma_o^2(\sigma_o^2 + \sigma_b^2)^{-1} T_b$$

Variational form:

For any atmospheric state S, define:

$$J(S) = \frac{1}{2}\left[\frac{(F-S)^2}{\sigma_B^2} + \frac{(O-S)^2}{\sigma_O^2}\right]$$

"cost function" J(S)

From (5.3.12) in Kalnay, where *T (=S)* is any state:

$$J(S) = \frac{1}{2}\left[\frac{(T_b-S)^2}{\sigma_b^2} + \frac{(T_o-S)^2}{\sigma_o^2}\right]$$

Find the value of S which minimizes J(S):
$\delta J/\delta S = 0$ for S = A

Generalize to three spatial dimensions and multiple variables.

First: write an alternative formula for *J(S)* for one variable:

$$J(S) = \frac{1}{2}\left[(F-S)\frac{1}{\sigma_B^2}(F-S) + (O-S)\frac{1}{\sigma_O^2}(O-S)\right]$$

Then: Let Y = generalized observation (e.g. an indirect variable);
H(S) = conversion of model state S to generalised obs-variable

$$J(S) = \frac{1}{2}\left[(F-S)\frac{1}{\sigma_F^2}(F-S) + (Y-H(S))\frac{1}{\sigma_O^2}(Y-H(S))\right]$$

Finally: three spatial dimansions and many variables simultaneously
→ Transform to formula for state vectors in phase space.

$$J(\mathbf{S}) = \frac{1}{2}[(\mathbf{F}-\mathbf{S})^T\mathbf{B}^{-1}(\mathbf{F}-\mathbf{S}) + (\mathbf{Y}-\mathbf{H}(\mathbf{S}))^T\mathbf{R}^{-1}(\mathbf{Y}-\mathbf{H}(\mathbf{S}))]$$

where: **Y, F, S** and **H(S)** are vectors; **B** and **R** are error covariance matrices

Minimize *J* → **3DVar** solution

In 3DVar:

Observations taken over the assimilation window

are implemented at the analysis time in the midde of the window

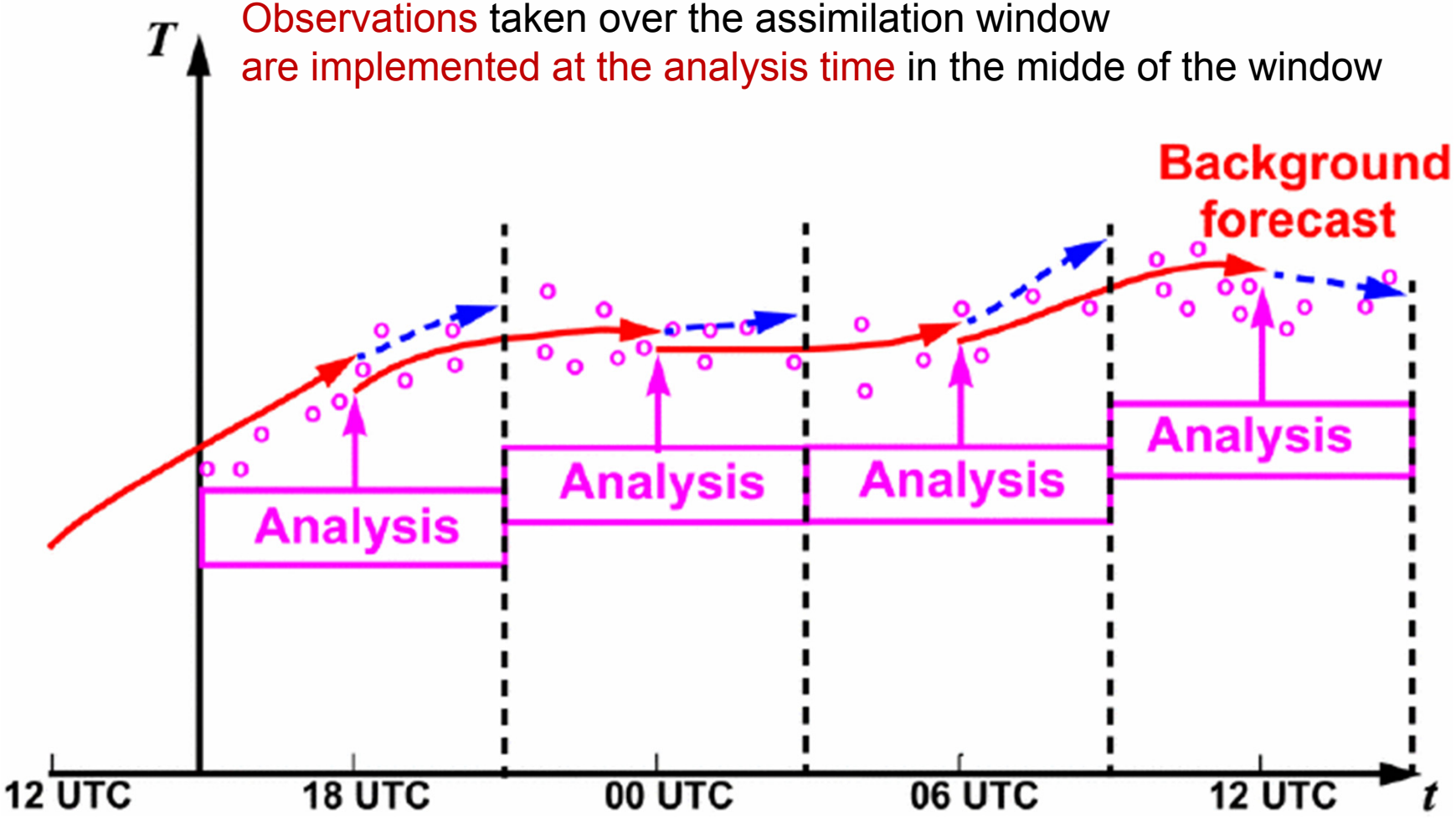

Six-hourly 3D analysis

Thanks to Adrian Simmons ECMWF

Generalization to include time explicitely →**4DVar**

Observations are used at the times they are taken

Find a state **S** (= **A**) which developes from timestep no. 0 to timestep N, and minimizes:

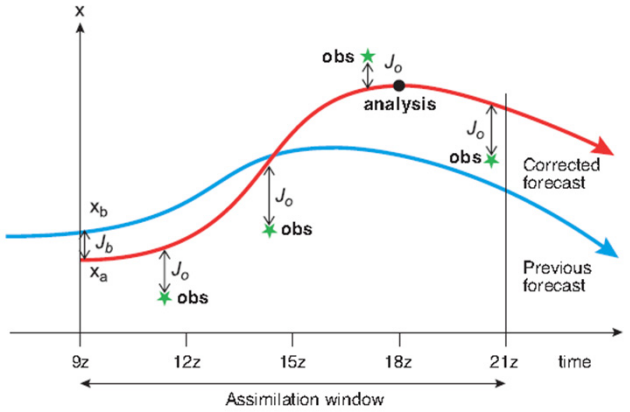

$$J(\mathbf{S}) = \frac{1}{2}[(\mathbf{F}_0 - \mathbf{S}_0)^T \mathbf{B}_0^{-1}(\mathbf{F}_0 - \mathbf{S}_0) + \sum_{n=1}^{N} ((\mathbf{Y}_n - \mathbf{H}\mathbf{M}_n(\mathbf{S}_0))^T)\mathbf{R}_n^{-1}(\mathbf{Y}_n - \mathbf{H}\mathbf{M}_n(\mathbf{S}_0))$$

$\mathbf{M_n}$ = the modelled value at any timelevel n within the assimilation window from n=0 to N.

The first term: the difference between the first guess and the initial state determines only partly the size of J.

The second term: the Σ–term, sums up all the differences between the evolving forecast and the *n* number of observations of varying kind.

Four Dimensional variational data assimilation (4D-Var)

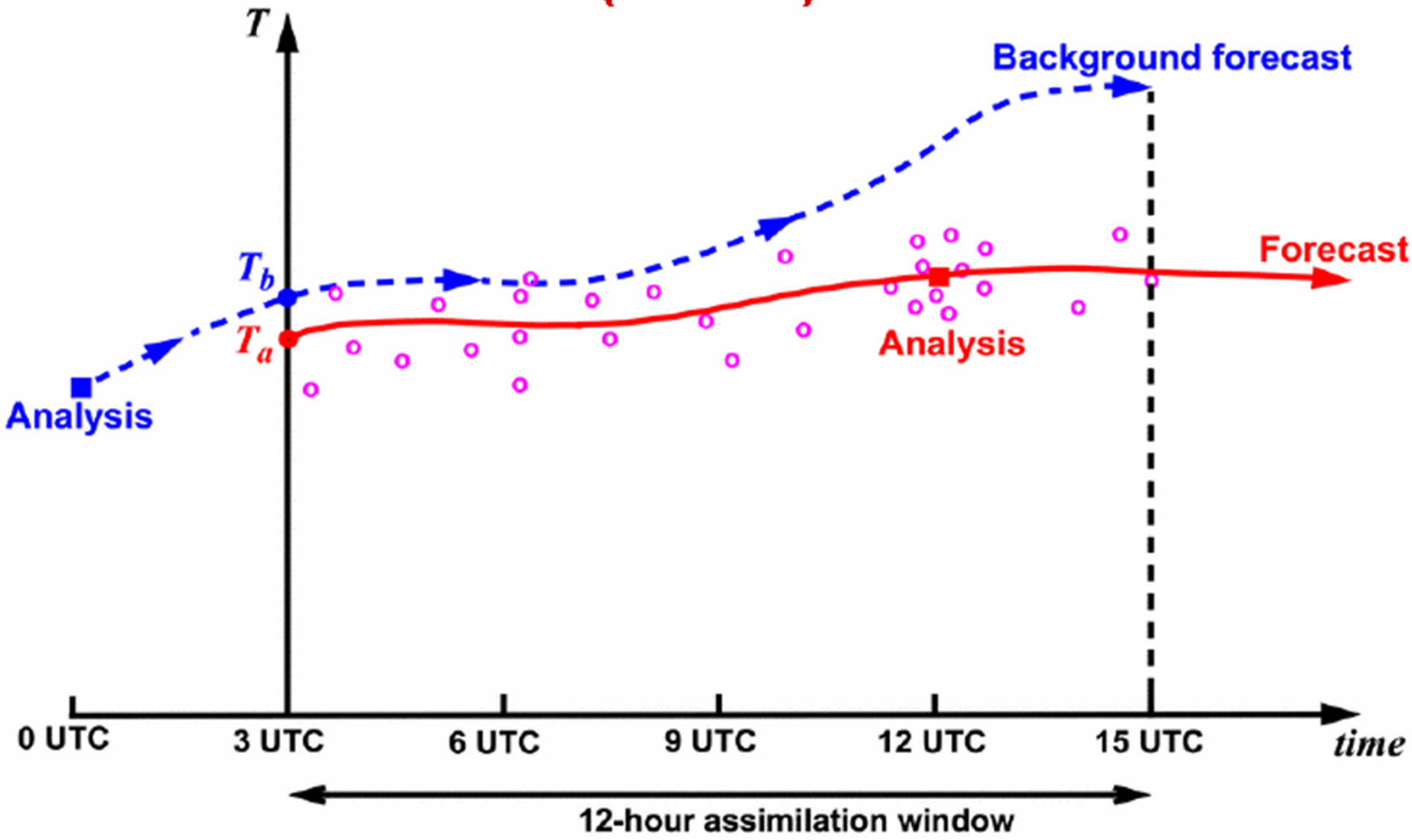

Thanks to Adrian Simmons ECMWF

Extended and Long Range

MJO: Madden-Julian Oscilation

The largest element of ***intraseasonal (30–90 day)*** variability in the tropical atmosphere is characterized by an eastward progression of large regions of both enhanced and suppressed tropical rainfall, observed mainly over the Indian and Pacific Ocean.

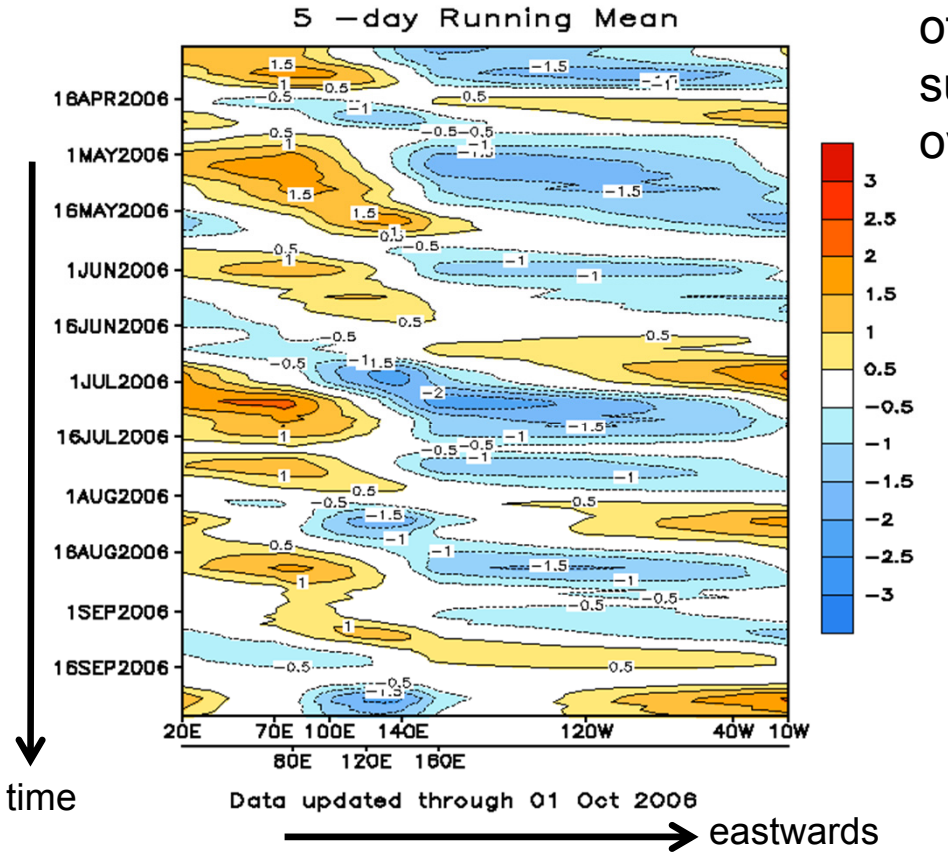

A [Hovmöller diagram] of the 5-day running mean of [outgoing longwave radiation] showing the MJO. Time increases from top to bottom in the figure, so contours that are oriented from upper-left to lower-right represent movement from west to east.

Speculation being researched:

Potential connections between MJO and NAO.
And potential source of intraseasonal predictability in N-Atlantic and Europe

ENSO:
El Niño, Southern Oscilation

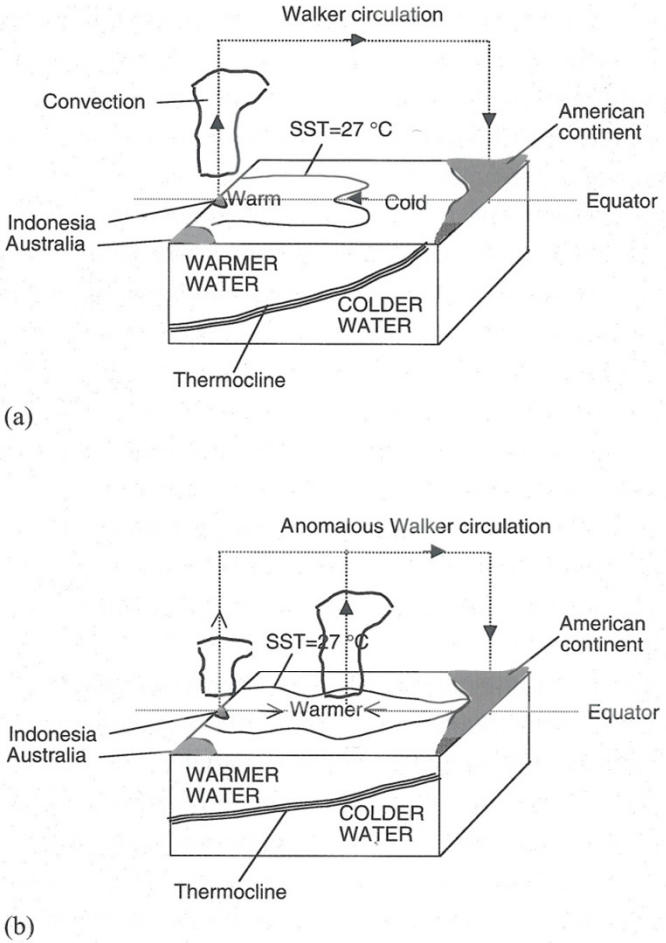

Figure 6.7.1: Schematic of the coupling of the ocean and atmosphere in the tropical Pacific: (a) normal conditions; (b) El Niño conditions.

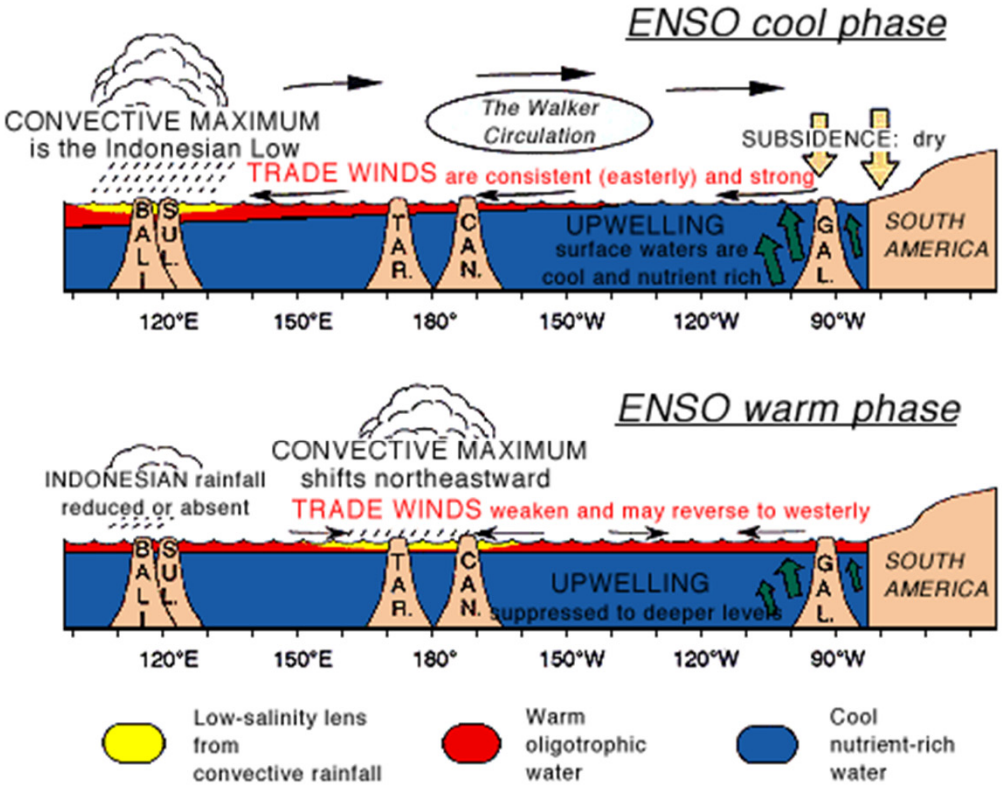

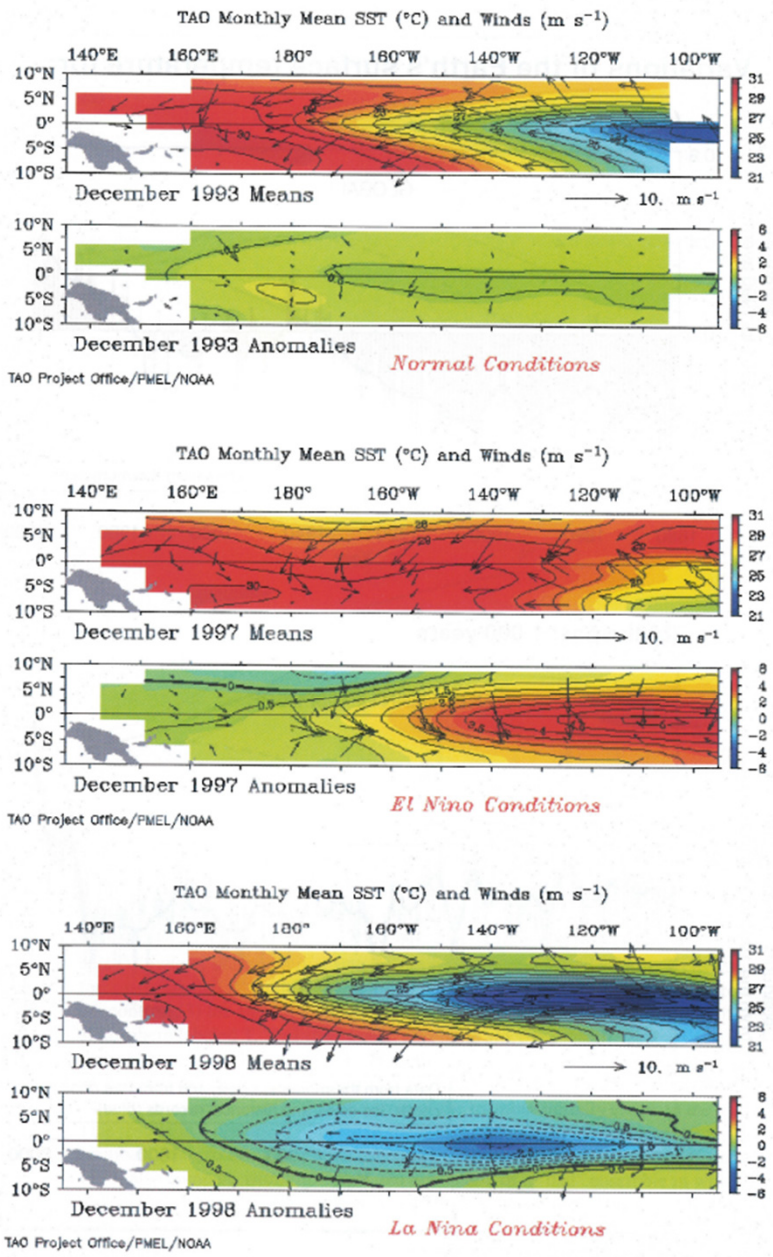

Plate 3 Equatorial Pacific SST and surface winds from TOGA TAO buoys during December 1993 (considered to be normal), December 1997 (during El Niño) and December 1998 (during La Niña). The top panels shows the fields and the bottom panels the anomalies. Courtesy of NOAA/PMEL.

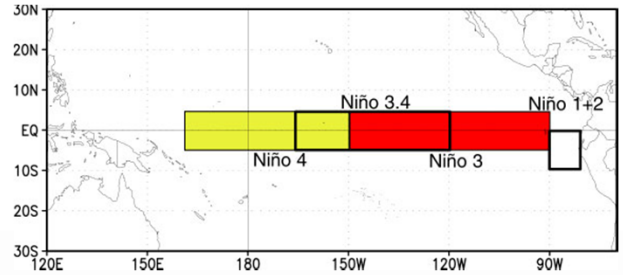

SST Anomaly in Nino 3.4 Region (5N-5S,120-170W)

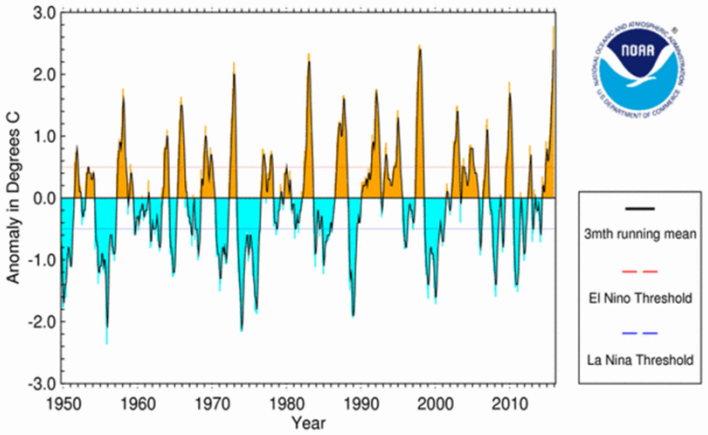

National Climatic Data Center / NESDIS / NOAA

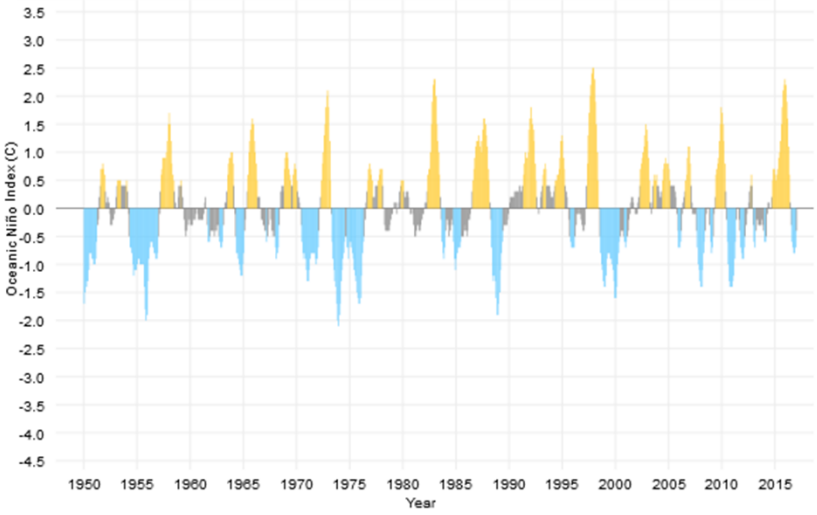

ENSO correlations

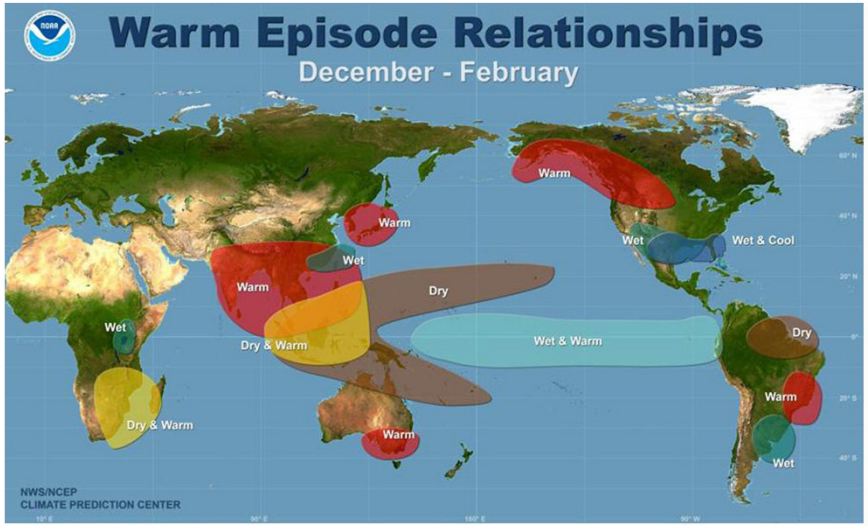

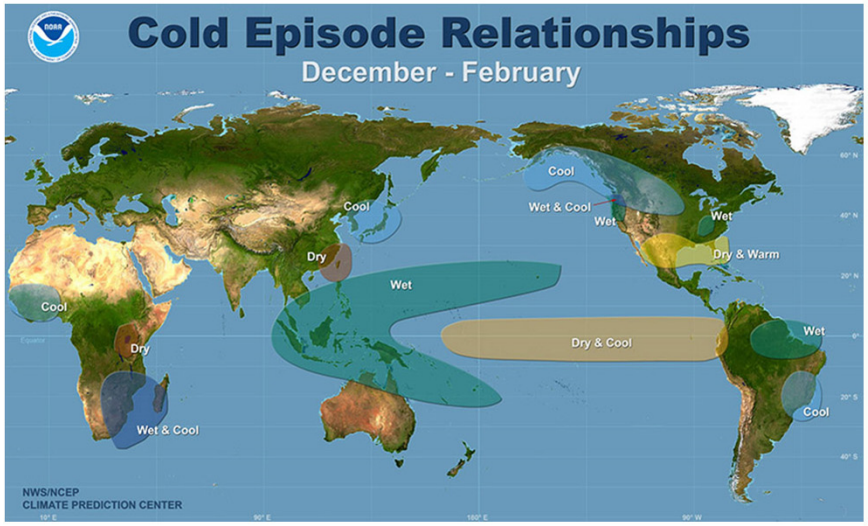

PNA Teleconnection pattern

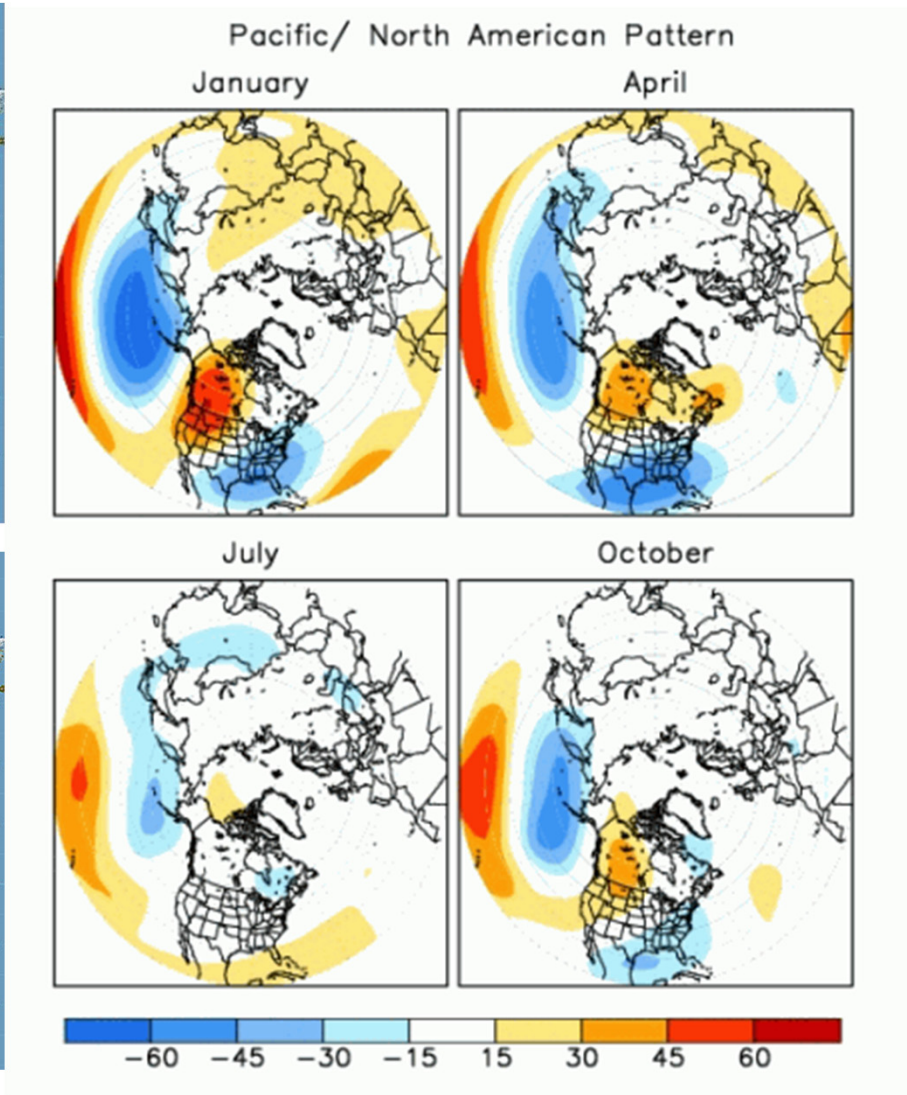

Anomalies in geopotential height (m); 500hPa for positive pattern index

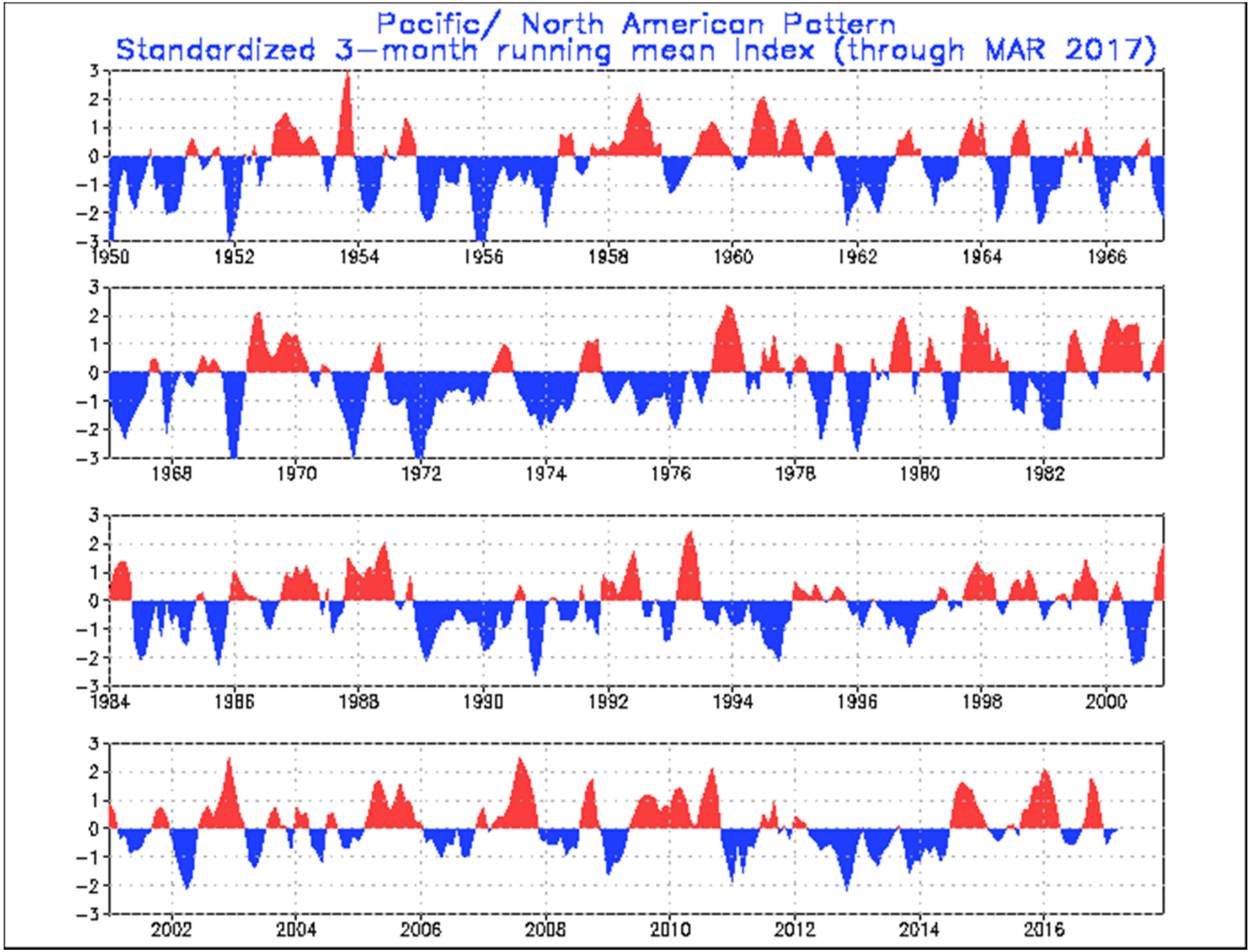
Pacific/ North American Pattern
Standardized 3-month running mean Index (through MAR 2017)
3
2
1
0
−1
−2
−3
1950
1952
1954
1956
1958
1960
1962
1964
1966
1968
1970
1972
1974
1976
1978
1980
1982
1984
1986
1988
1990
1992
1994
1996
1998
2000
2002
2004
2006
2008
2010
2012
2014
2016

NAO Teleconnection pattern

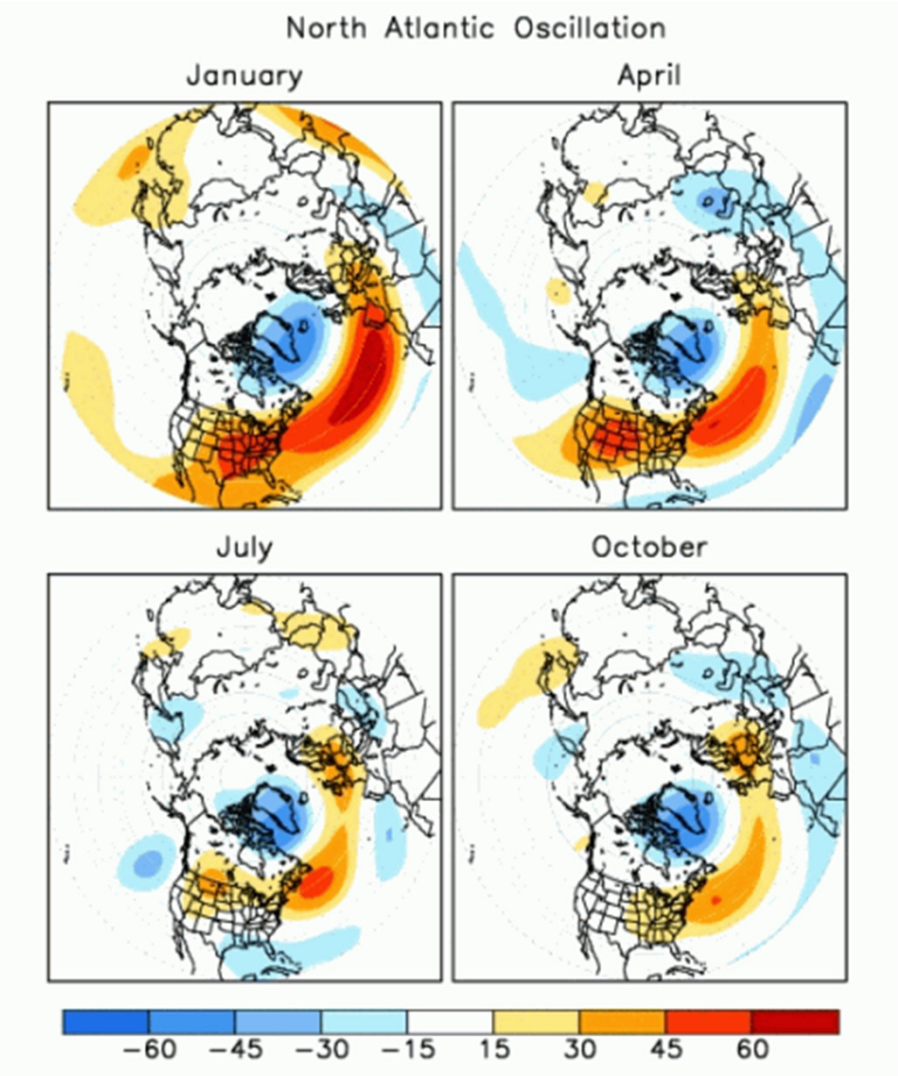

Anomalies in geopotential height (m); 500hPa for positive pattern index

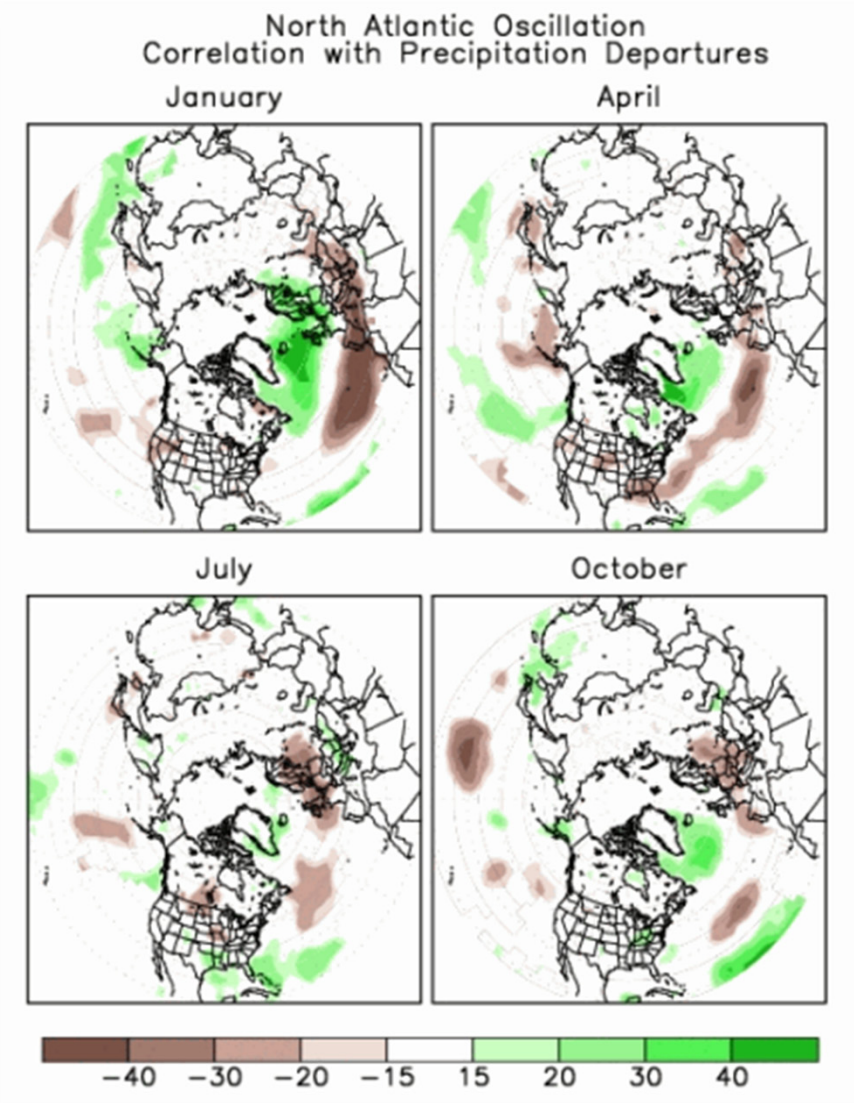

Correlation (%)

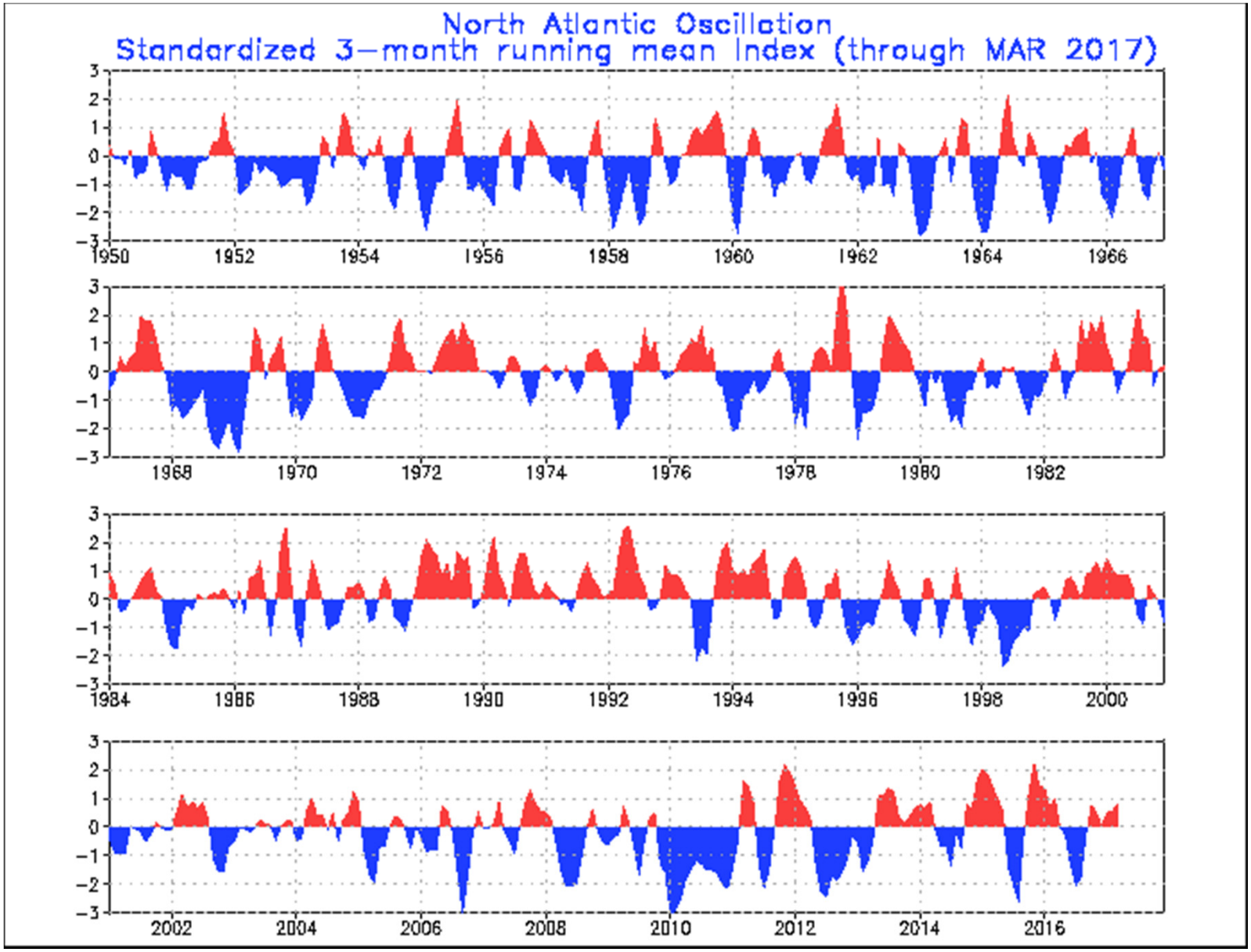
North Atlantic Oscillation
Standardized 3-month running mean Index (through MAR 2017)
3
2
1
0
−1
−2
−3
1950
1952
1954
1956
1958
1960
1962
1964
1966
1968
1970
1972
1974
1976
1978
1980
1982
1984
1986
1988
1990
1992
1994
1996
1998
2000
2002
2004
2006
2008
2010
2012
2014
2016

Monthly Forecasts, ECMWF

Twice a week (Monday and Thursday at 00Z),
the coupled model is integrated forward to make a
32 day forecast with 51 different initial conditions,
in order to create a 51-member ensemble.
Full coupling is applied between the ocean and atmosphere from the start of the forecast (day 0). **Initial atmospheric perturbations**: as for the medium-range (EDA+SVs). **Initial ocean perturbations**: wind stress perturbations are differences between different wind stress analyses. 5 ocean assimilations (1 control and 4 perturbed) are produced by picking 2 from the set of wind stress perturbations for each month of data assimilation and add and subtract to the analyzed wind stress.

Because of model errors, a drift occurs in the coupled system. This model drift is evaluated by integrating the coupled model up to day 46 with 11 different initial conditions at the same day and month as the real time forecast, but over the past 20 years. This is further extended by using a one-week window about the actual date. Thus, the climate ensemble is of size 11(ens.memb.) x 20(years) x 3(dates) = 660.

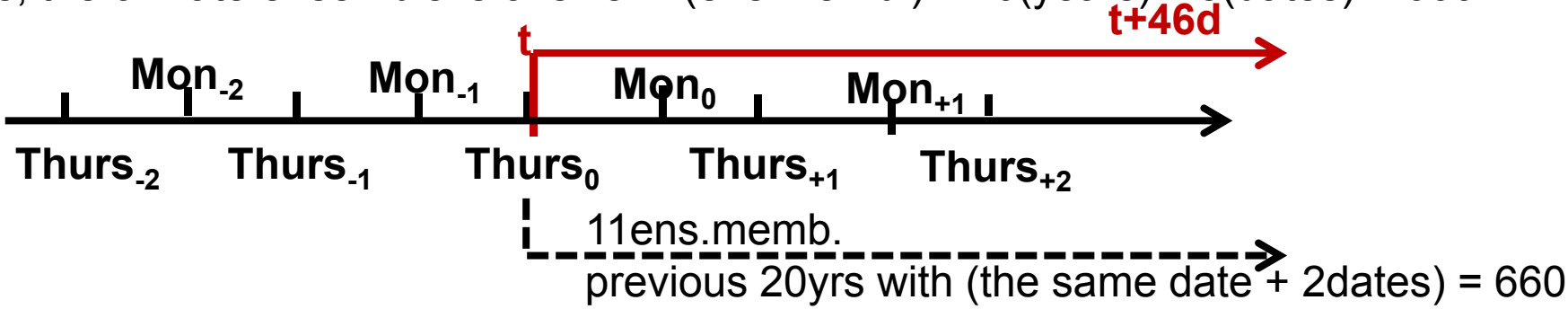

Temp & Prec anom, week 1 & 2

starting from Monday 28. March 2016

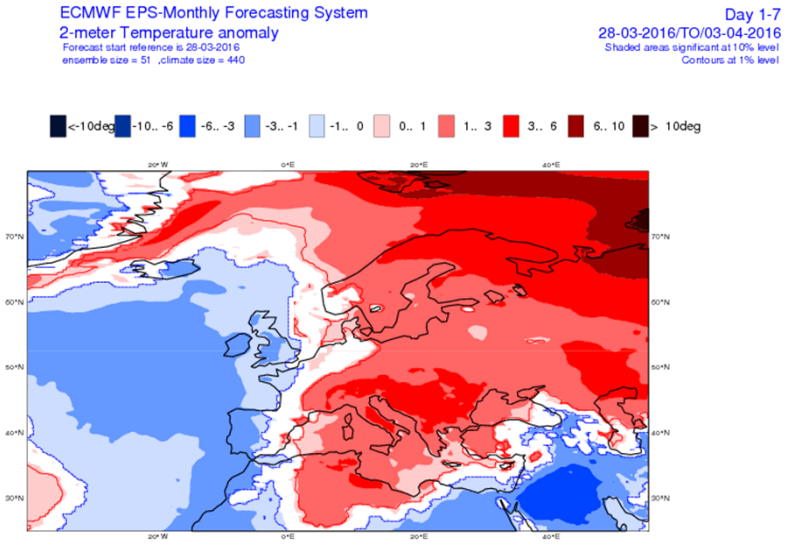

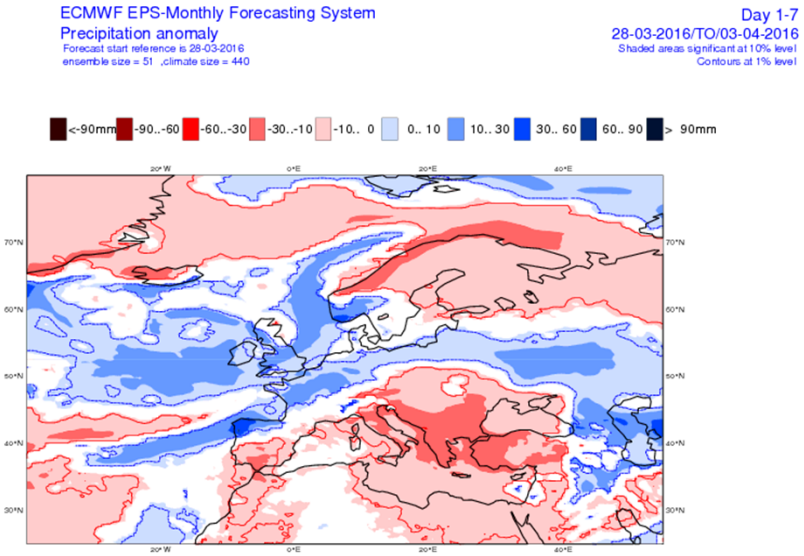

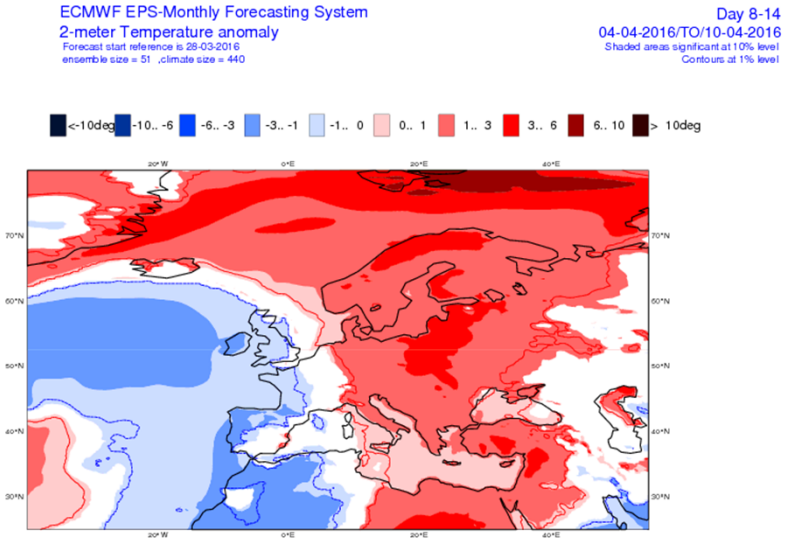

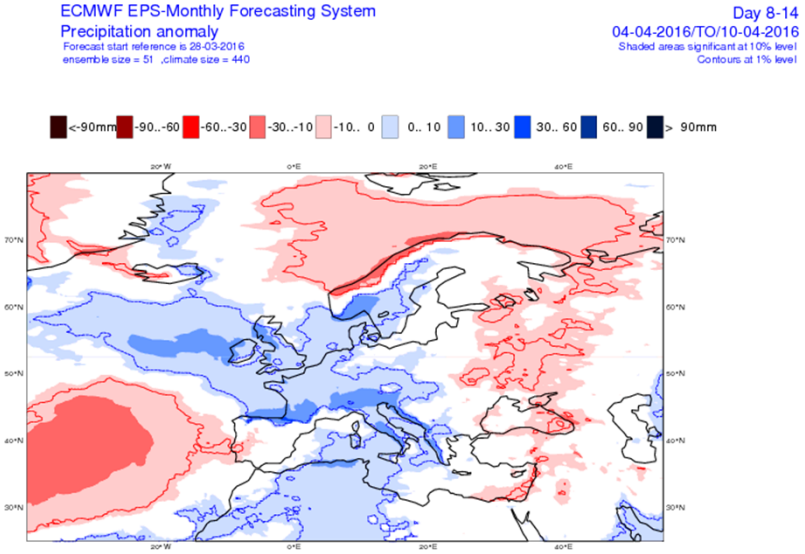

Temp & Prec anom, week 3 & 4

starting from Monday 28. March 2016

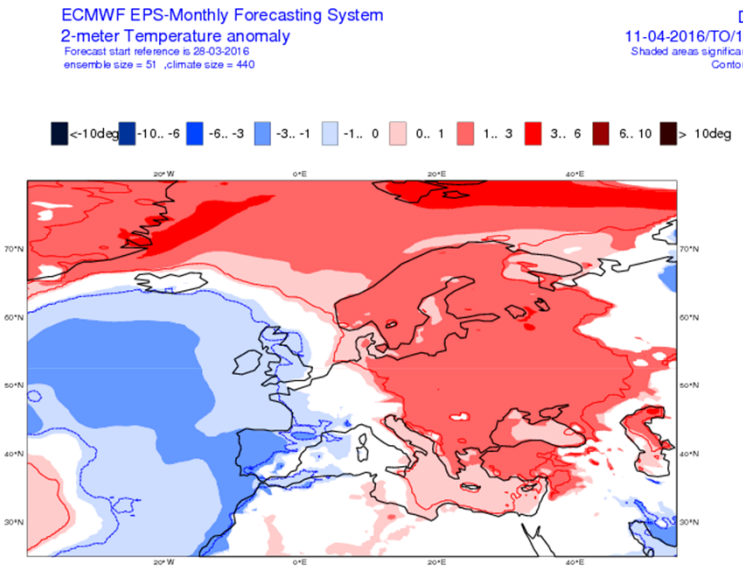

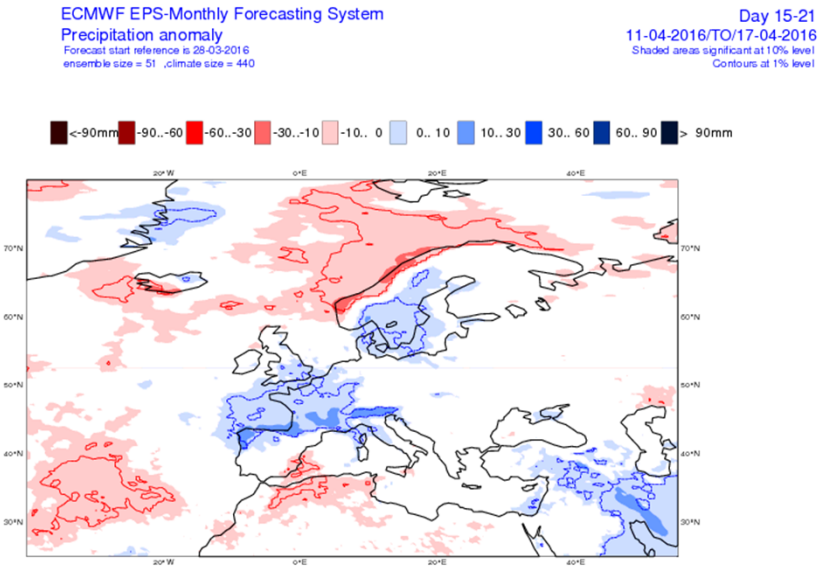

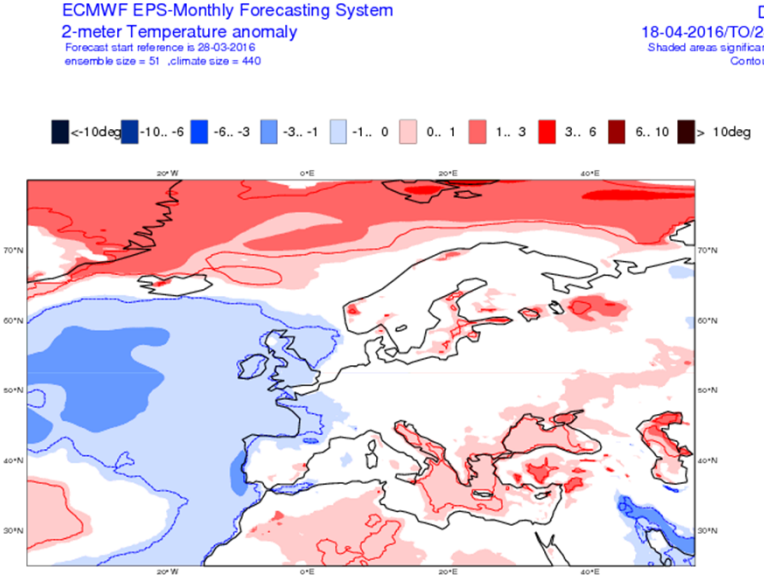

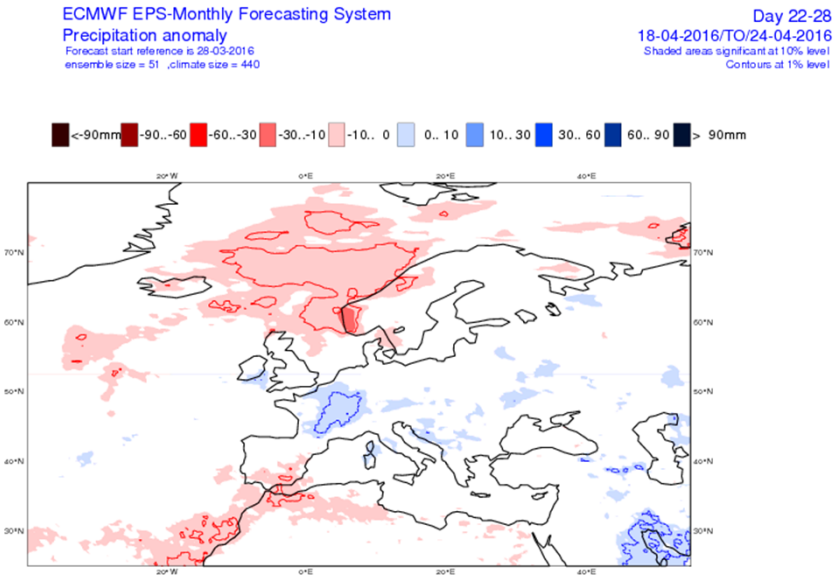

Z_500 anom, week 1, 2, 3 & 4

Weekly-mean 500hPa geopotential anomaly for the ensemble mean.
Contour intervals of 2dam (zero line not shown).
starting from 28. March 2016

Day 1-7: Mon 20160328- Sun 20160403

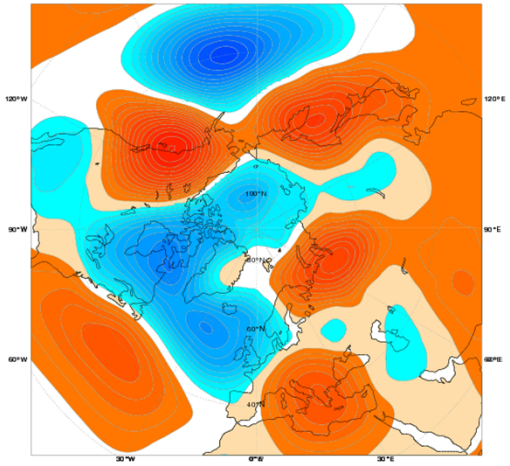

Day 8-14: Mon 20160404- Sun 20160410

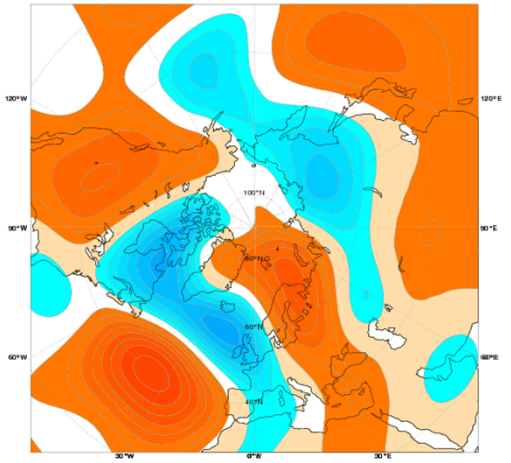

Day 15-21: Mon 20160411- Sun 20160417

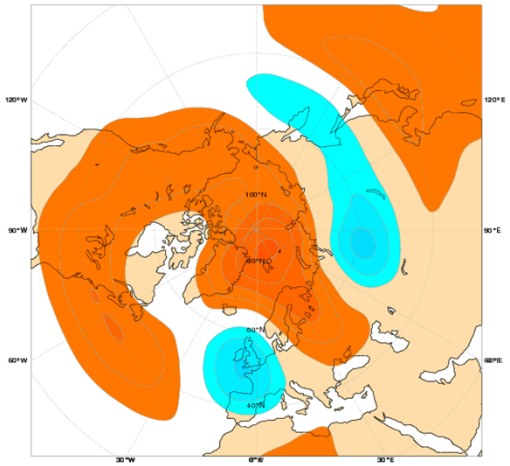

Day 22-28: Mon 20160418- Sun 20160424

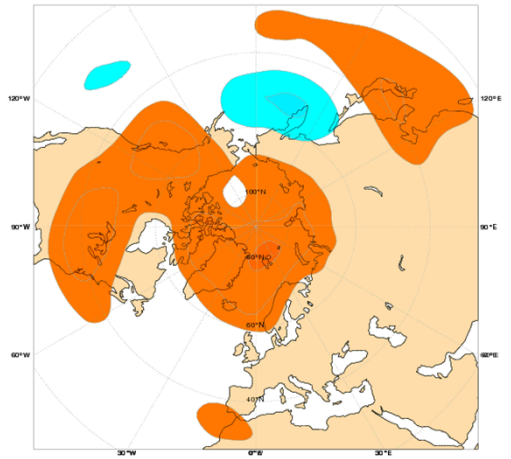

The plumes show the daily evolution of the ensemble forecast distribution, binned in 12.5% intervals (shading) together with the median (solid line).

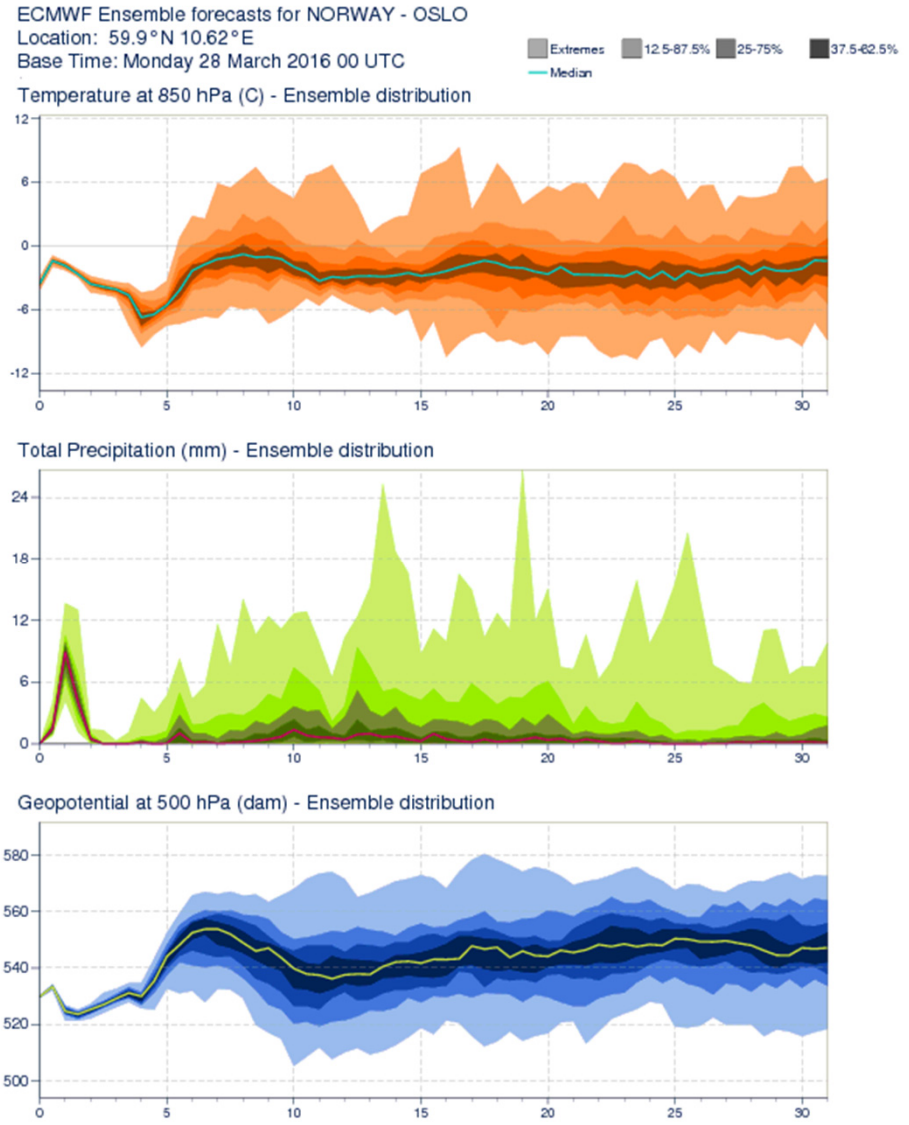

starting from 28. March 2016

Seasonal Forecasts, ECMWF

The seasonal forecasts consist of a **51 member ensemble** using a coarser-resolution version of the atmospheric model. The ensemble is **constructed by combining the 5-member ensemble ocean analysis with SST perturbations and the activation of stochastic physics.**
The forecasts have an **initial date of the 1st of each month, and run for 7 months**. Forecast data and products are released at 12Z UTC on a specific day of the month. For System 4, this is the 7th.

Model-climate for bias-correction & anomaly-evaluation
A set of **re-forecasts** are made starting on the **1st of every month for the years 1981-2010**. They are identical to the real-time forecasts in every way, except that the individual date ensemble size is only 15 rather than 51.
The **total re-forecast ensemble size is thus: 15x30 = 450**.

An annual-range (13 months) forecast is made **four times per year**, with start dates the **1st February, 1st May, 1st August and 1st November,** run as an extension of the seasonal forecasts, and are made using the same model but with a smaller ensemble size. Both re-forecasts and real-time forecasts and have an **ensemble size of 15.**
The annual range forecasts are designed primarily to give an outlook for El Nino. They have an experimental rather than operational status.

Nino_3-4 Plumes

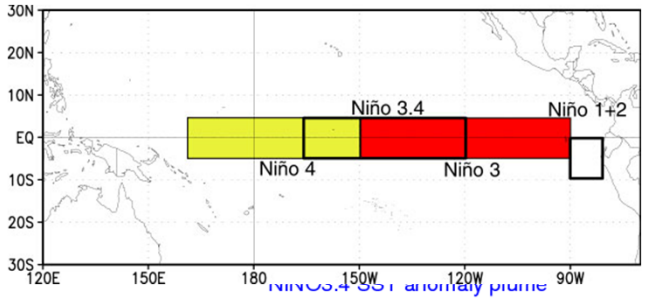

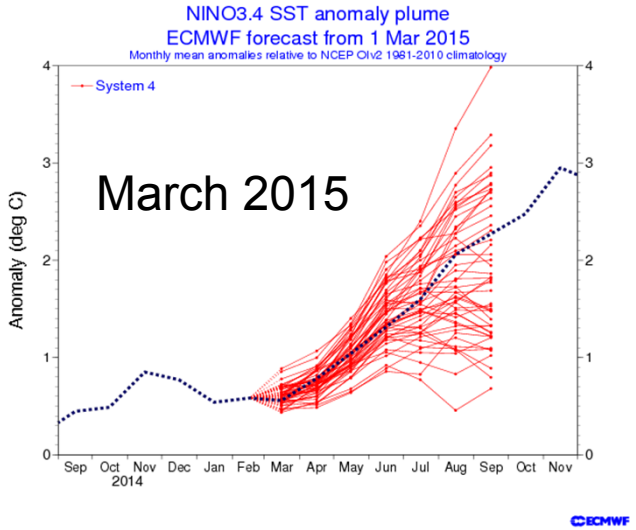

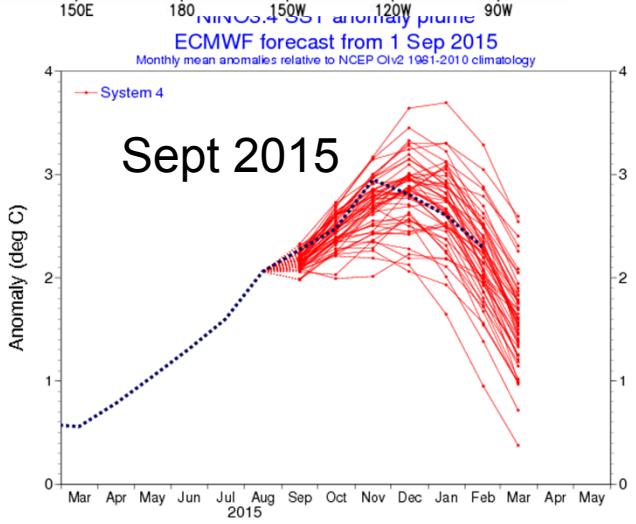

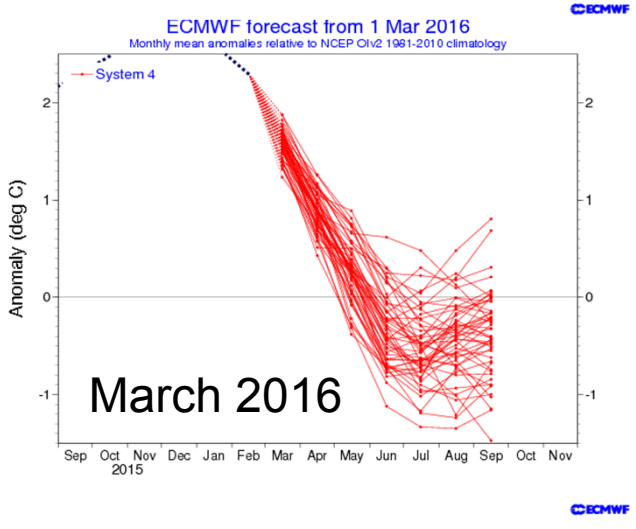

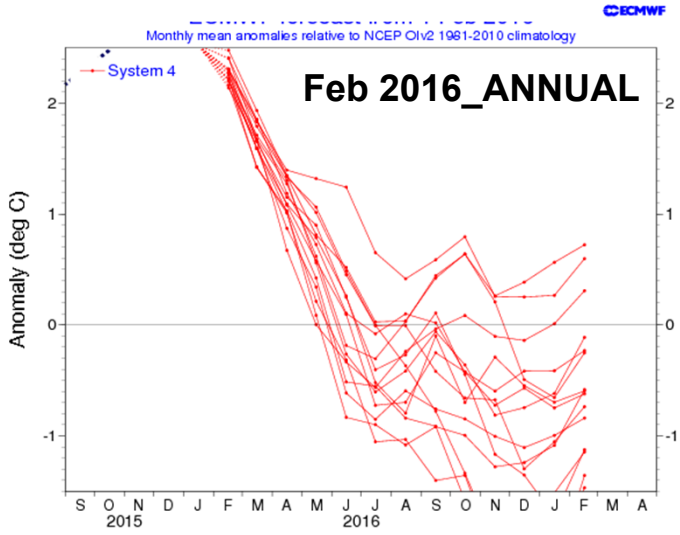

The limits of the purple/grey whiskers and yellow band correspond to the 5th and 95th percentiles, those of the purple/grey box and orange band to the lower and upper tercile, while the median is represented by the line within the purple/grey box and orange band.

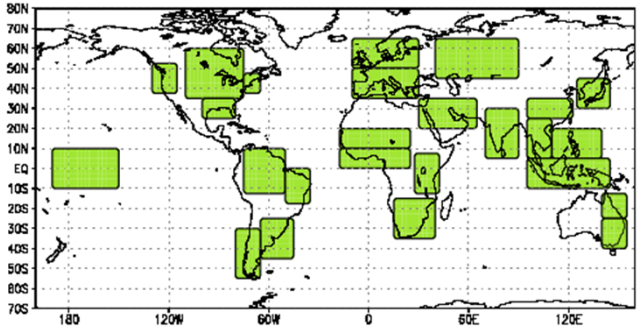

NAO

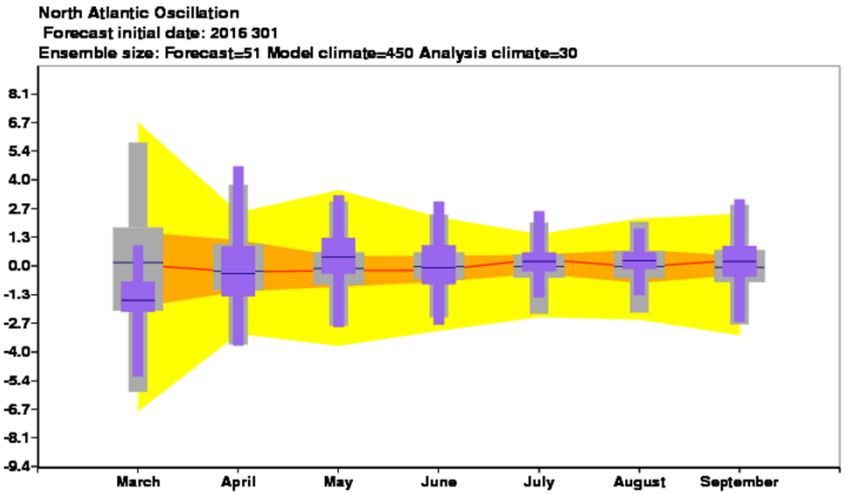

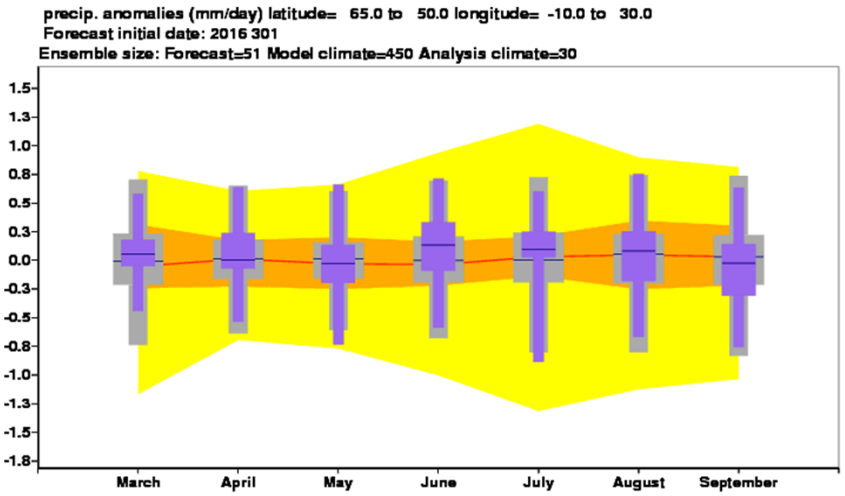

Northern Europe precip anomaly

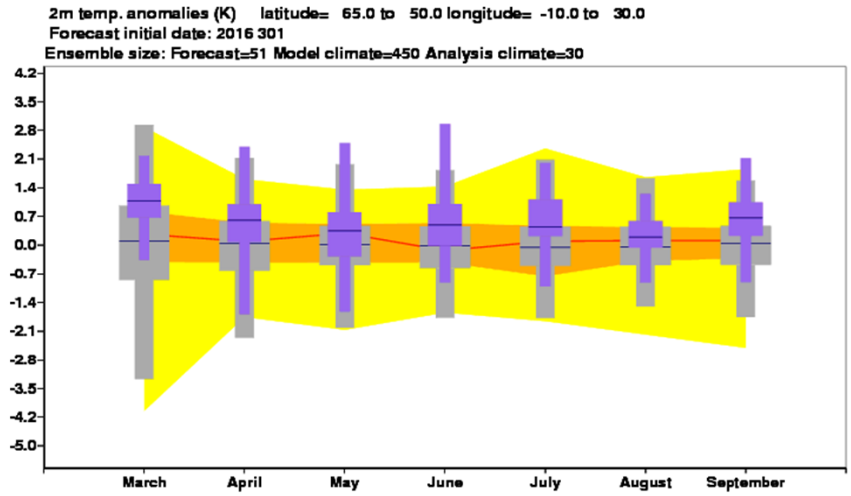

Northern Europe Temp anomaly

Prob relative to upper and lower terciles, JJA 2016
T2m and Precip

T2 <lower

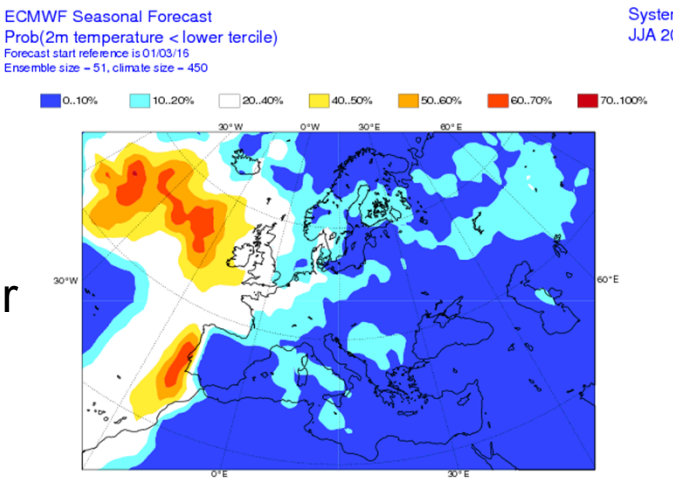

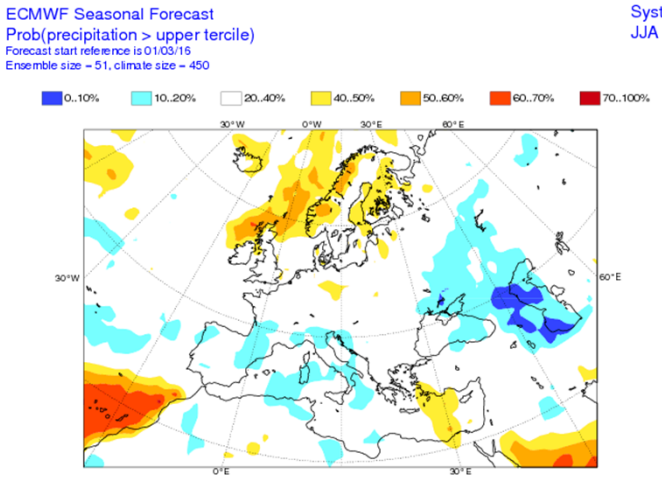

Prec >upper

T2 >upper

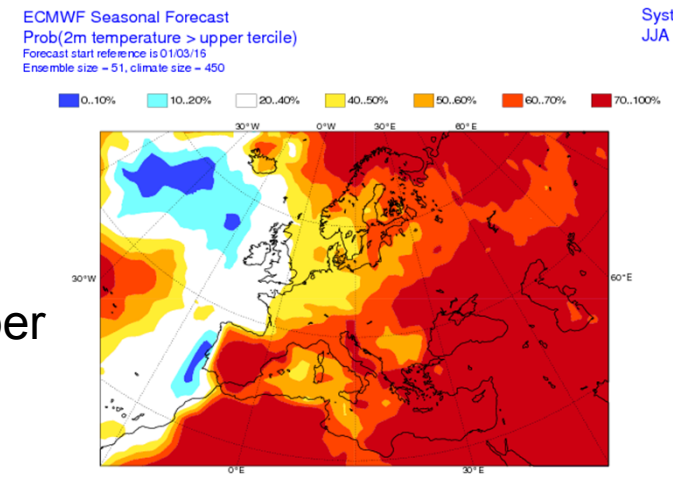

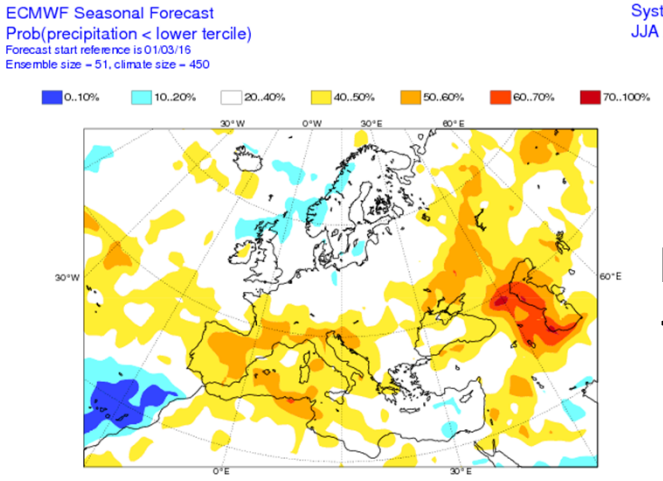

Prec <lower

From Predictions to Projections

(Decadal Climate Predictions)

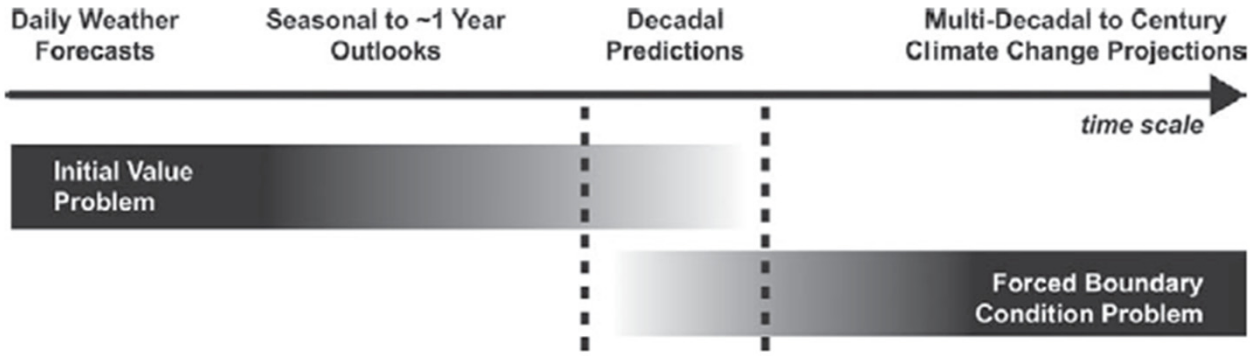

FIG. 2. Schematic illustrating progression from initial value problems with daily weather forecasts at one end, and multidecadal to century projections as a forced boundary condition problem at the other, with seasonal and decadal prediction in between.

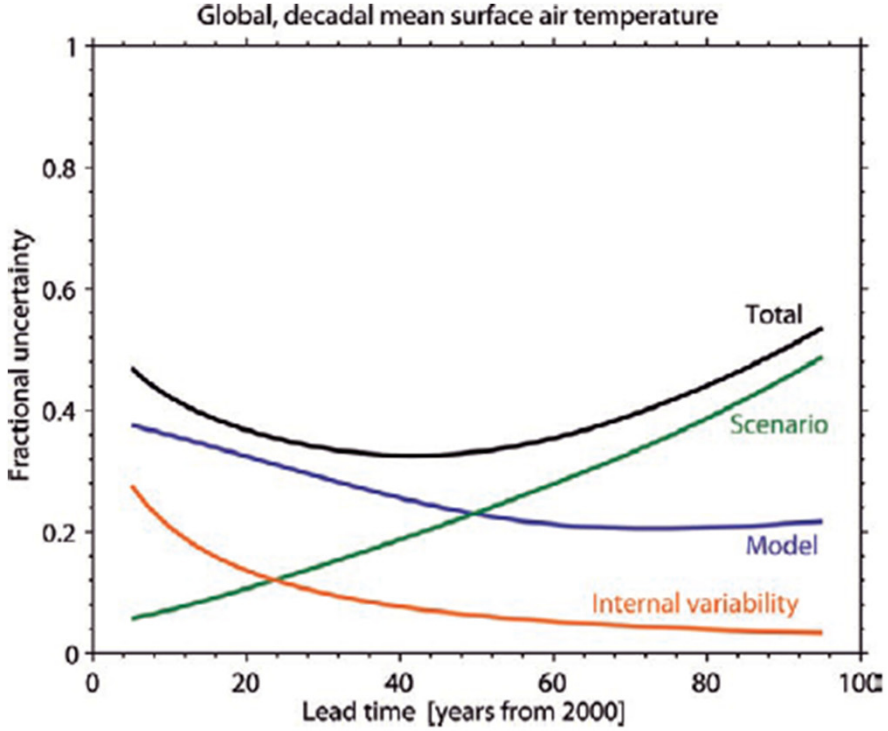

from uncertainties in the forced response, and also from unpredictable aspects of internal variability, on those time and space scales (Barnett et al. 2008). On continental scales, the observed response to external

FIG. 3. The relative importance of different sources of uncertainty in IPCC GCM projections of decadal-mean global-mean surface air temperature in the twenty-first century is shown by the fractional uncertainty (i.e., the prediction uncertainy divided by the expected mean change, relative to the 1971–2000 mean). Model uncertainty is the dominant source of uncertainty for lead times up to 50 yr, with internal variability being important for the first decade or so. Scenario uncertainty becomes important at multidecadal lead times (from Hawkins and Sutton 2009a).

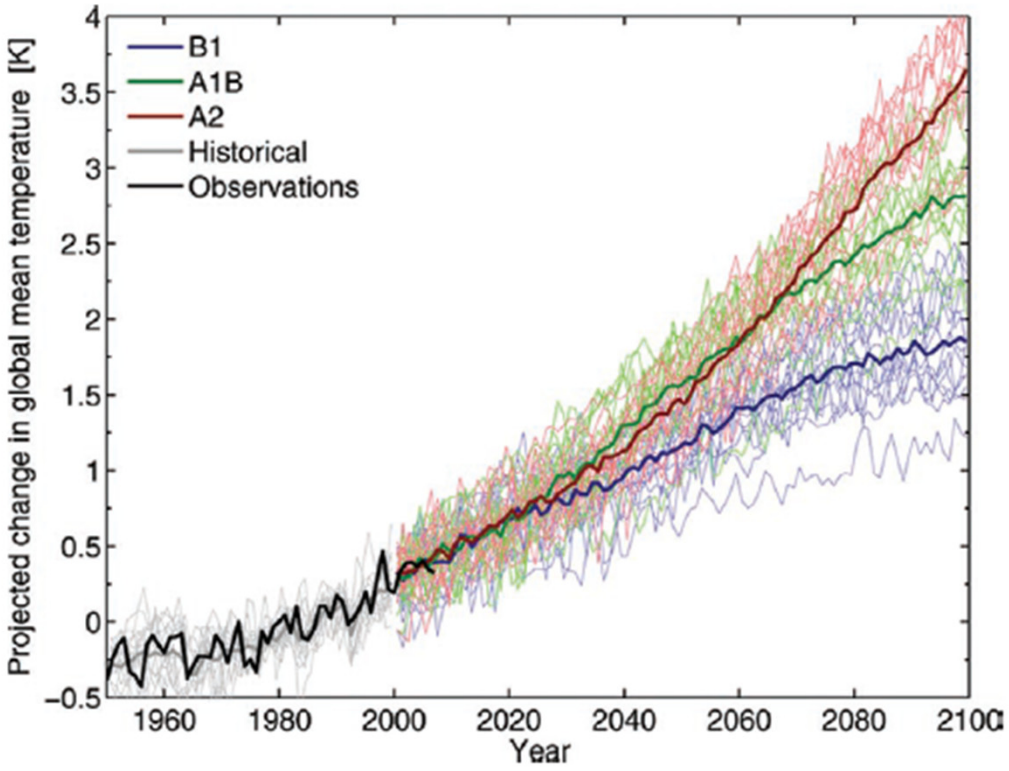

FIG. 1. Global mean, annual mean, surface air temperature predictions from 15 different global climate models under three different emission scenarios from 2000 to 2100 (thin lines): SRES A2 (red), A1B (green), and B1 (blue), designated as high-, medium-, and low-emissions paths, respectively. The same models forced with historical forcings are shown as the thin gray lines, and the observed global mean temperatures from 1950 to 2007 (Brohan et al. 2006) are shown as the thick black line. The multimodel mean for each emissions scenario is shown with thick colored lines demonstrating how uncertainty in future emissions gives rise to uncertainty in climate predictions. The different scenarios give nearly identical predictions until around 2025, demonstrating the delayed effect of future emissions. Each model has a different response to climate forcings, as seen by the spread in results for one particular scenario (or color). The internal (interannual) variability can be seen superimposed on the trend for any one individual prediction. All temperatures are shown as anomalies from the 1971–2000 mean.

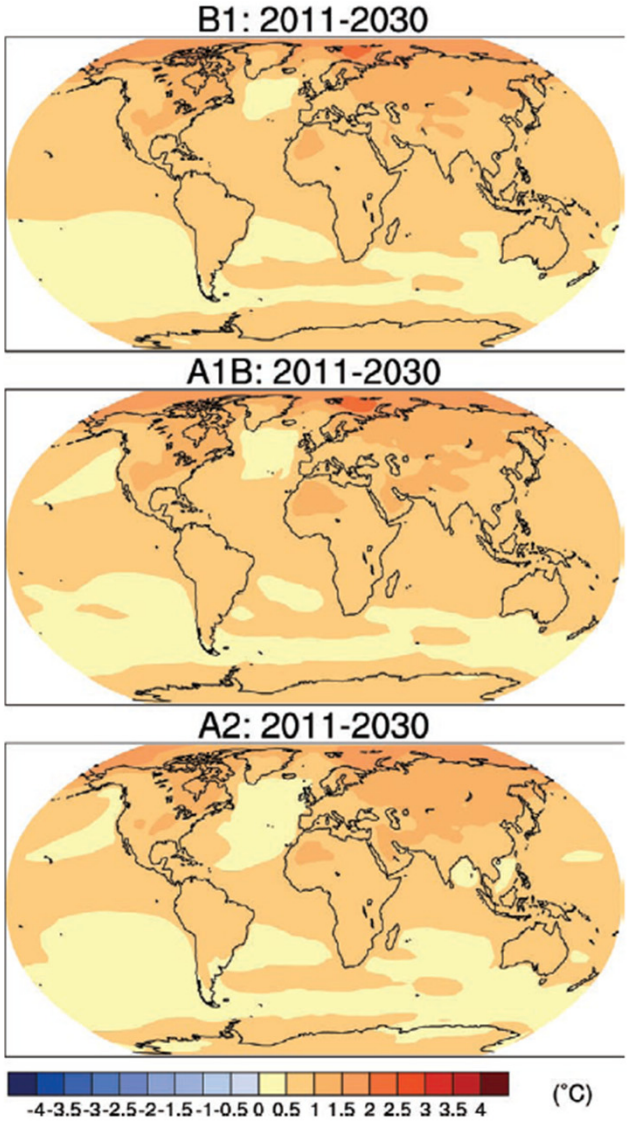

Fig. 1. Near-term surface air temperature anomalies from CMIP3 multimodel projections, 2011–30 minus 1980–99 (°C), for the (top) low, (middle) medium, and (bottom) high emission scenarios from IPCC AR4 (Figure: from *Climate change 2007: The Physical Science Basis*. Working Group I Contribution to the Fourth Assessment Report of the Intergovernmental Panel on Climate Change, Fig. 10.8, Cambridge University Press).

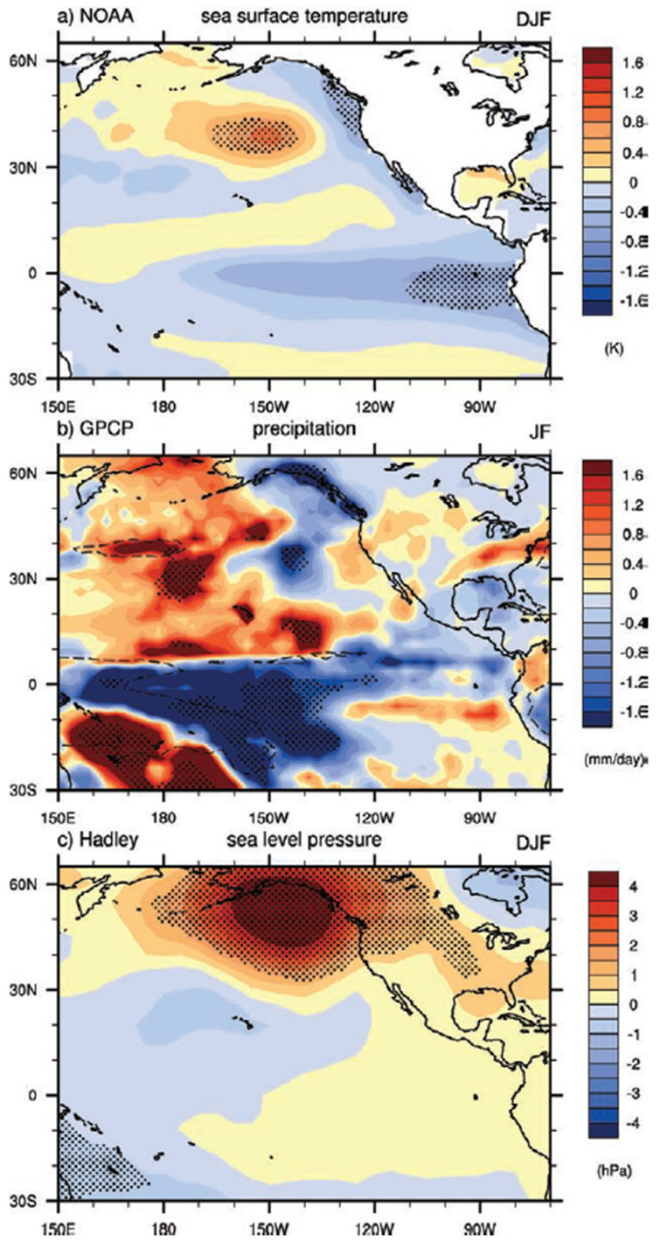

Pacific decadal potential predictability Linked to solar forcing periodicity

FIG. 5. (a) The average anomalies of sea surface temperature in 11 solar peak years (°C), computed relative to all other years, Dec–Feb, from the NOAA Extended Reconstructed Sea Surface Temperature dataset; (b) the average tropical rainfall anomalies [Global Precipitation Climatology Project (GPCP) gridded precipitation dataset] in the solar peak years starting in the late 1970s (mm day^{-1}), Jan–Feb, in comparison to all other years. Dashed line is the 6 mm day^{-1} contour from the long-term mean climatology; (c) same as (a), but for the average anomalies of sea level pressure (Hadley Centre sea level pressure dataset) in 11 solar peaks (hPa), Dec–Feb. Shading indicates significance at or above the 95% level, indicating the relative magnitude of the anomalies compared to the noise (Meehl et al. 2008).

Pacific decadal potential predictability
Linked to internal variability (PDO / IPO)

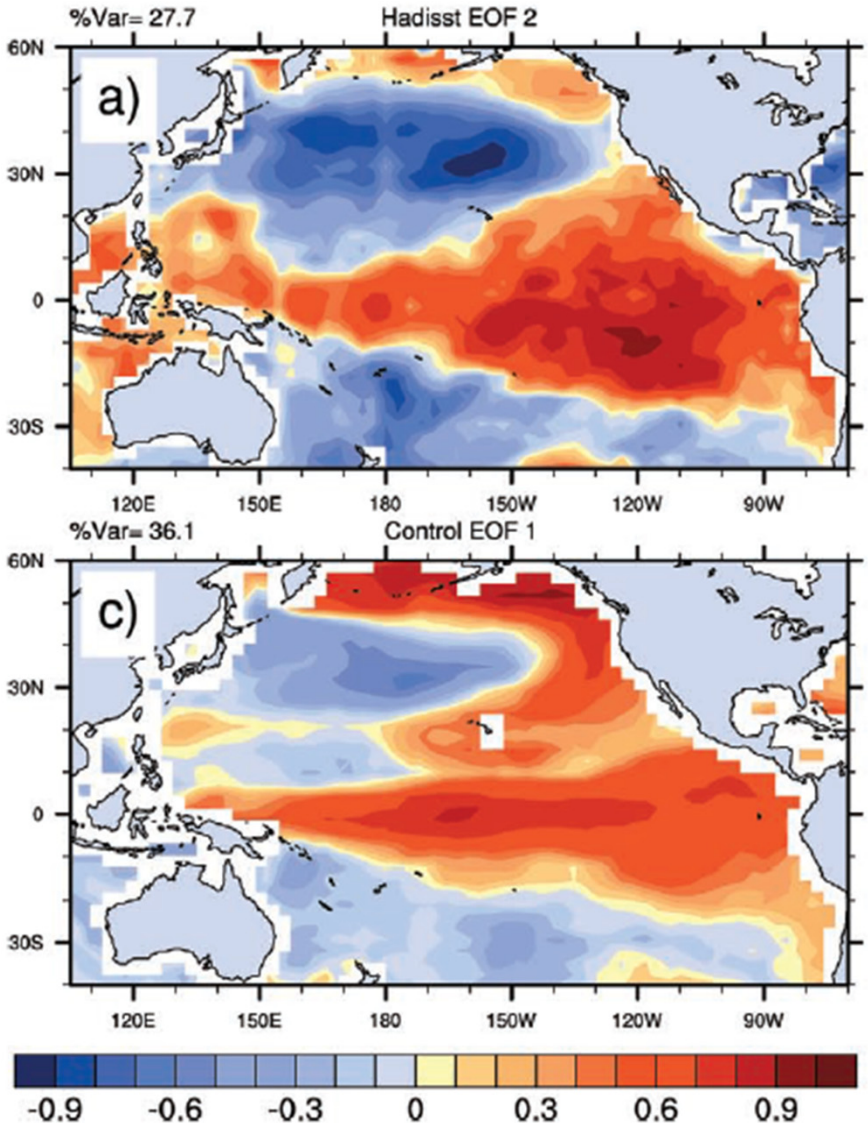

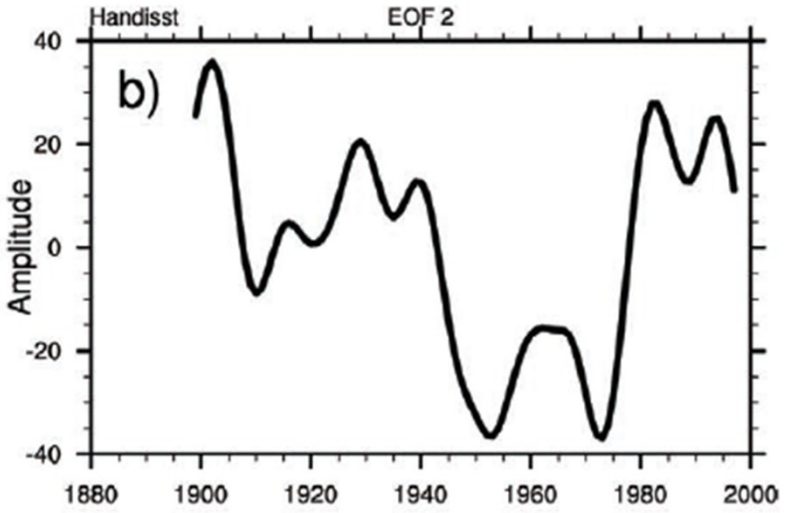

FIG. 6. (a) The second EOF (the first EOF is the trend) of 13-yr low-pass-filtered non-detrended observed SSTs for the period of 1890–2006, (b) PC time series for second EOF, (c) the first EOF of 13-yr low-pass-filtered SSTs from a 300-yr period of an unforced model control run (Meehl et al. 2009a). Units for panels (a) and (c) are arbitrary, PC time series is in °C.

Colman 2006). The PDO and IPO are usually characterized by a low-pass-filtered SST EOF pattern that has an "El Niño–like" character,

PDO

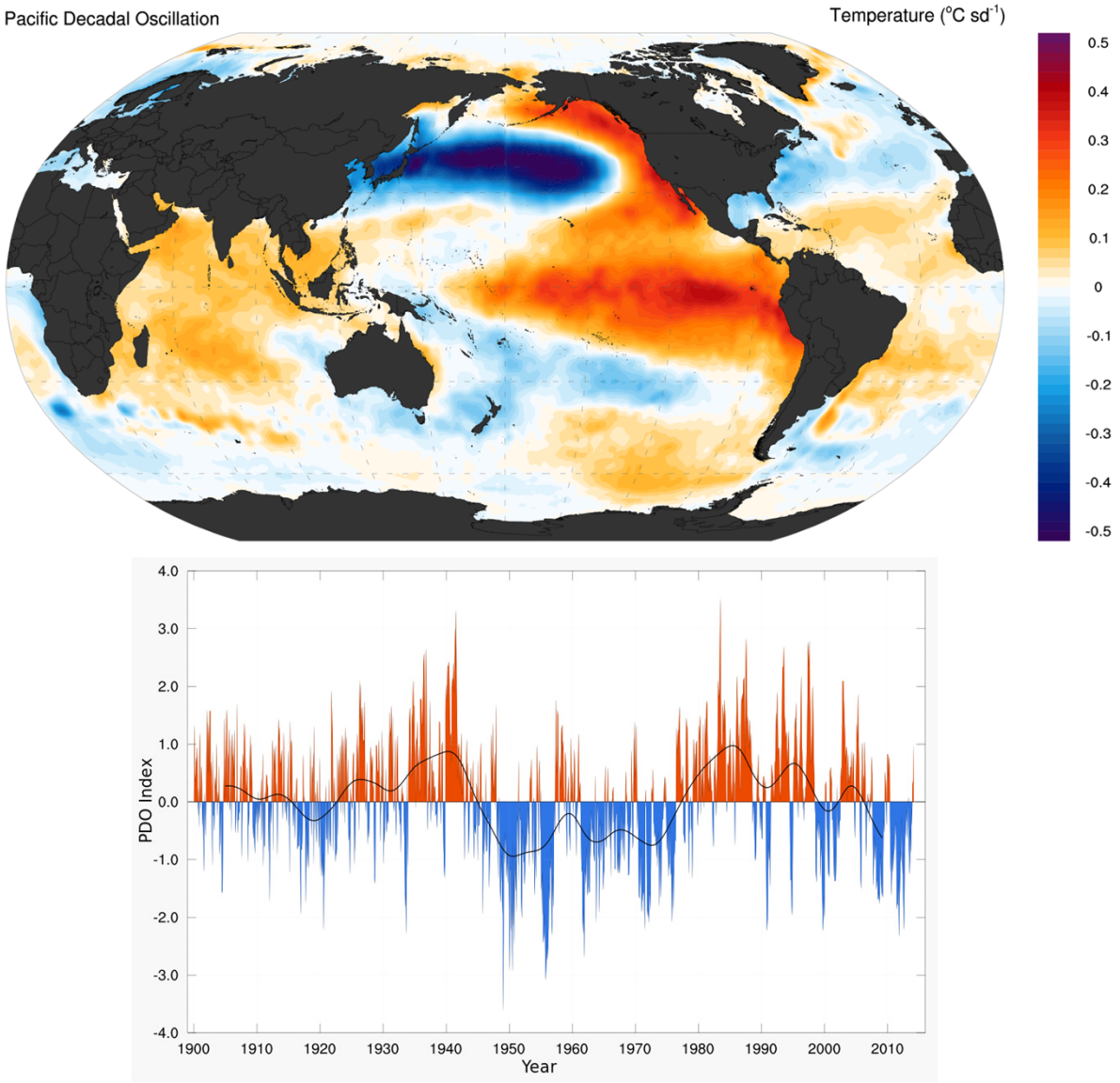
Pacific Decadal Oscillation
Temperature (°C sd-1)
0.5
0.4
0.3
0.2
0.1
0
-0.1
-0.2
-0.3
-0.4
-0.5
PDO Index
4.0
3.0
2.0
1.0
0.0
-1.0
-2.0
-3.0
-4.0
1900
1910
1920
1930
1940
1950
1960
1970
1980
1990
2000
2010
Year

AMO: Atlantic Multidecadal Oscilation
Potential decadal predictability?

*Schlesinger, M. E. (1994). "An oscillation in the global climate system of period 65-70 years". Nature **367** (6465): 723–726. doi:10.1038/367723a0*

Atlantic Multidecadal Oscillation index computed as the linearly detrended North Atlantic sea surface temperature anomalies 1856-2013.

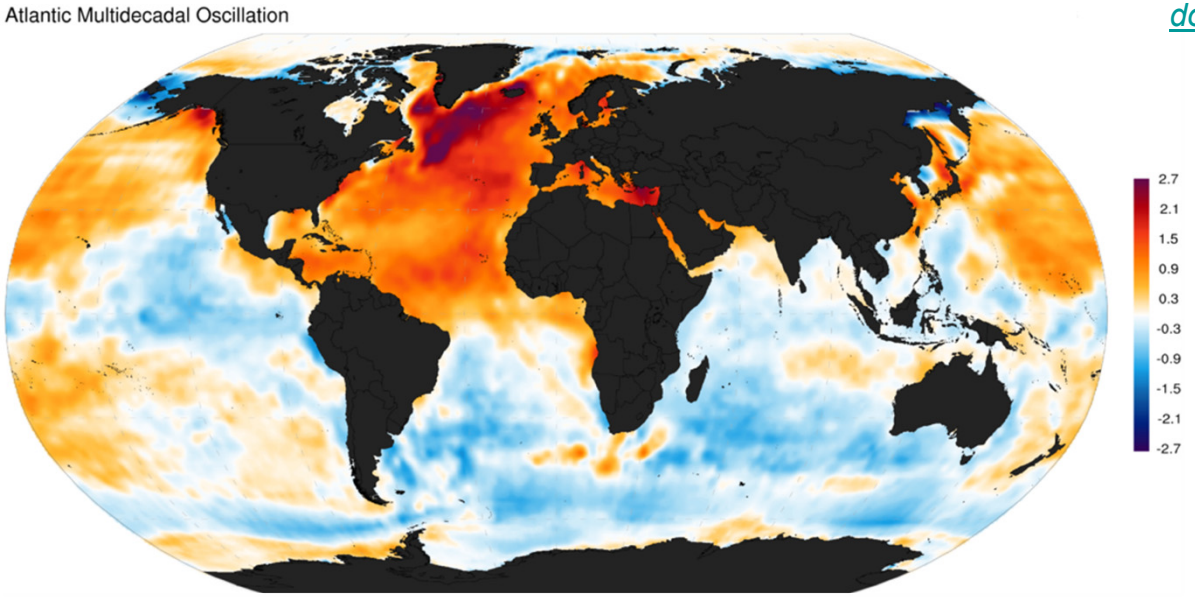

Monthly values for the AMO index, 1856 -2013

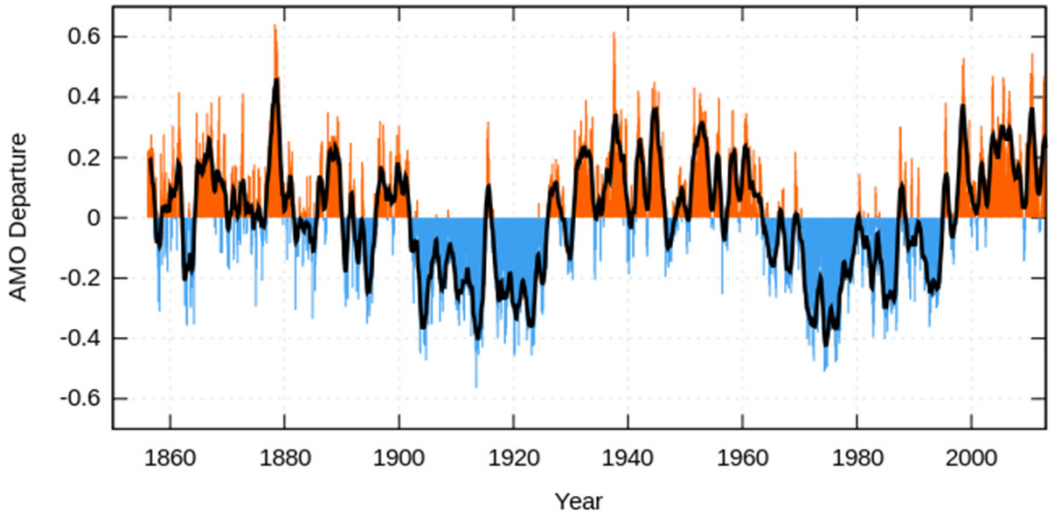

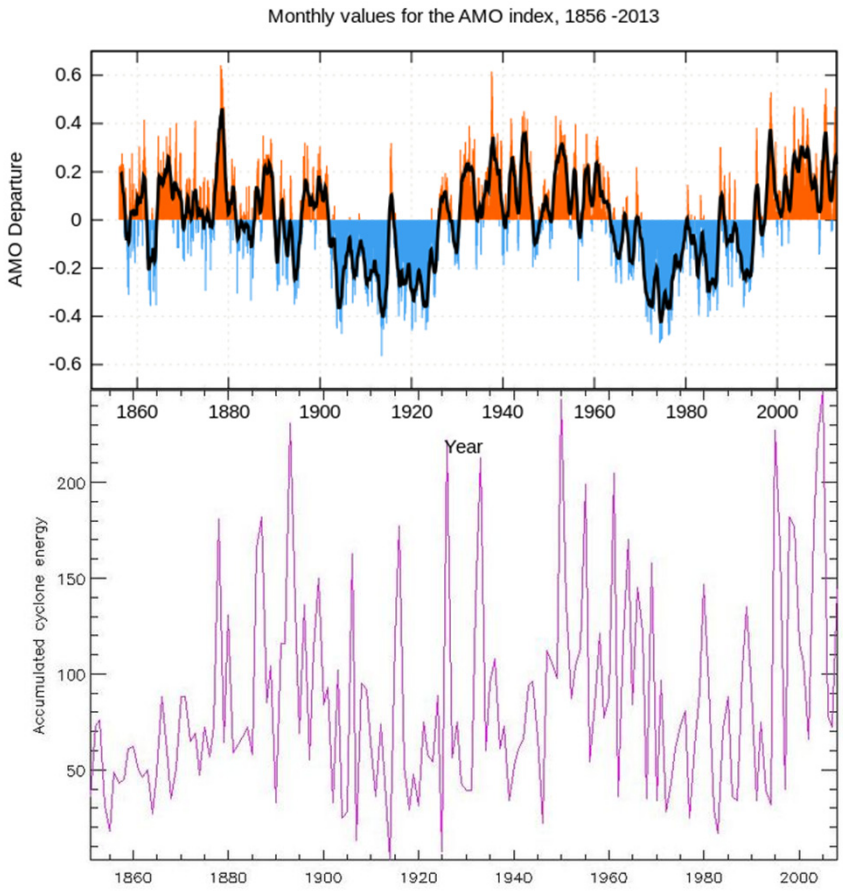

AMO and Atlantic Hurricanes

The number of tropical storms that can mature into severe hurricanes is much greater during warm phases of the AMO than during cool phases, at least twice as many. *(Re.: NOAA)*
The hurricane activity index is highly correlated with the Atlantic multi-decadal oscillation. The AMO alternately obscures and exaggerates the global increase in temperatures due to human-induced global warming.[*Chylek, P. & Lesins, G. (2008). "Multidecadal variability of Atlantic hurricane activity: 1851–2007". Journal of Geophysical Research* ***113***: D22106. doi:10.1029/2008JD010036

The recent AMO increased the average number of Atlantic hurricanes and named storms from 6 to 12, when it began in 1995. This phase may have ended in 2012.

North Atlantic Ocean sensitivity to initial perturbations

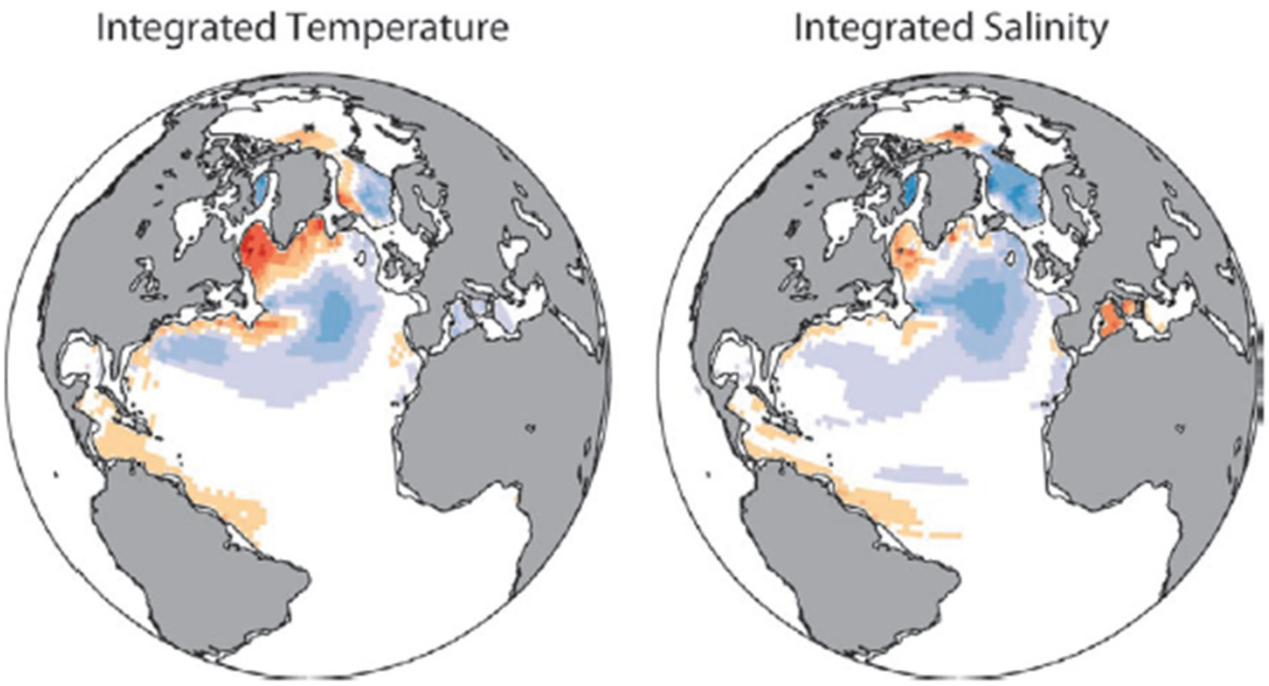

FIG. 7. An optimal perturbation for the Atlantic domain from the HadCM3 model, using a linear inverse modeling approach (from Hawkins and Sutton 2009b). The panels show integrated (left) temperature (in K) and (right) salinity (in PSU) multiplied by five from the surface to a depth of 1,800 m. The colored regions indicate where the ocean is sensitive to small anomalies, and are thus the optimal regions for initial condition perturbations and for targeted observations to improve forecast skill. The color scale is the same in both panels and is arbitrary. White regions represent small anomalies of either sign.

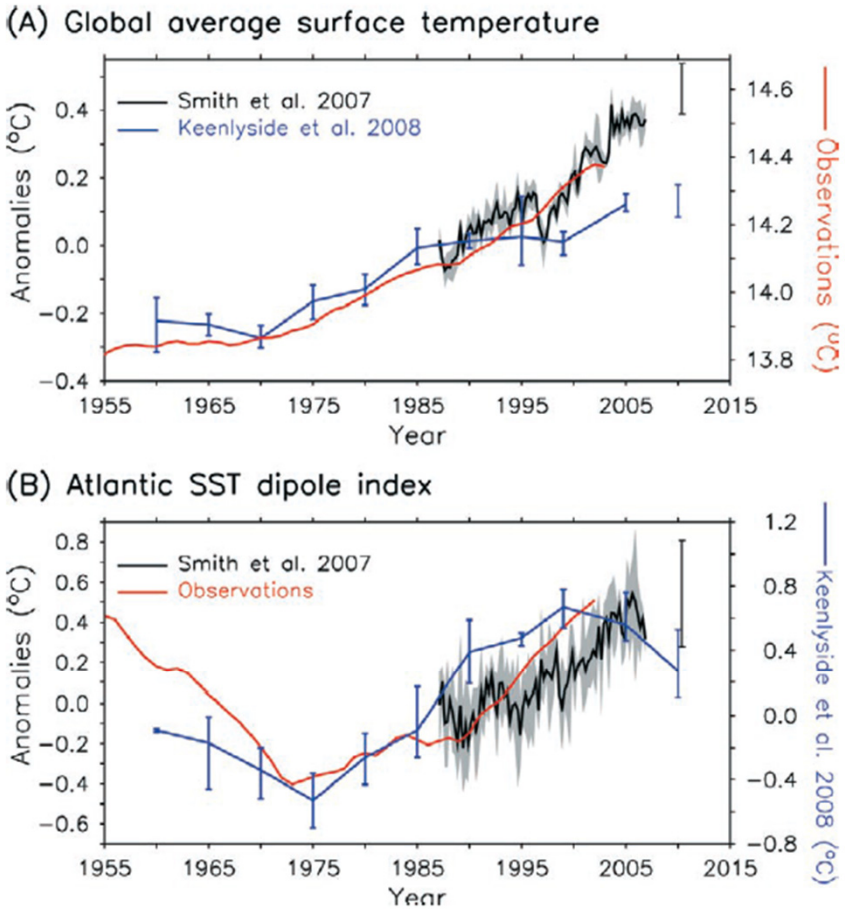

FIG. 8. Decadal prediction examples. Observed and hindcast values of (a) 10-yr mean global mean surface temperature and (b) an Atlantic SST dipole index. The latter is a proxy for MOC fluctations and is defined as the average SST difference for 60°–10°W, 40°–60°N minus 50°–0°W, 40°–60°S. Hindcasts begin in 1982 (1955) in Smith et al. (2007) and Keenlyside et al. (2008), with a four (three) member forecast every season (5 yr); shading (error) indicates the ensemble range. The error bars centered on 2010 represent actual forecasts for the period of 2005–15. Hindcasts for Smith et al. (2007) and Keenlyside et al. (2008) are adjusted to have the observed means over the 1979–2001 (1955–2005) period. Note the different axis used in (b) for Keenlyside et al. (2008). Observations are from HadISST 1.1 and HadCRU3.

Examples of decadal predictions.

Recent efforts at decadal prediction, with the similar strategy: Initialize a global climate model from observations and reanalyses and run it forward 10 yr, while accounting for changes in external forcing (natural and anthropogenic).

Smith et al. (2007) showed that global-mean temperature could be predicted out to a decade in advance (Fig. 8a), with more skill than obtained when only external radiative forcing changes are accounted for.

Keenlyside et al. (2008) demonstrated that SST variations associated with the Atlantic MOC could be predicted a decade in advance, but because of an overly strong MOC signal, their strength was overestimated (Fig. 8b). Ten-year averaged global surface temperature variations were also predictable (Fig. 8a), but with marginally less skill than that obtained from radiative forcing only.

In both studies forecasts were made for the next 10 yr (Fig. 8b), and **in both cases natural internal variability was found to temporarily offset anthropogenic global warming**.
The offset was largest in Keenlyside et al. (2008), whose results suggest a temporary lull in global warming for the next decade; however, the simplicity of the scheme employed needs to be kept in mind. The results of both studies highlight the impact ofinternal variability.

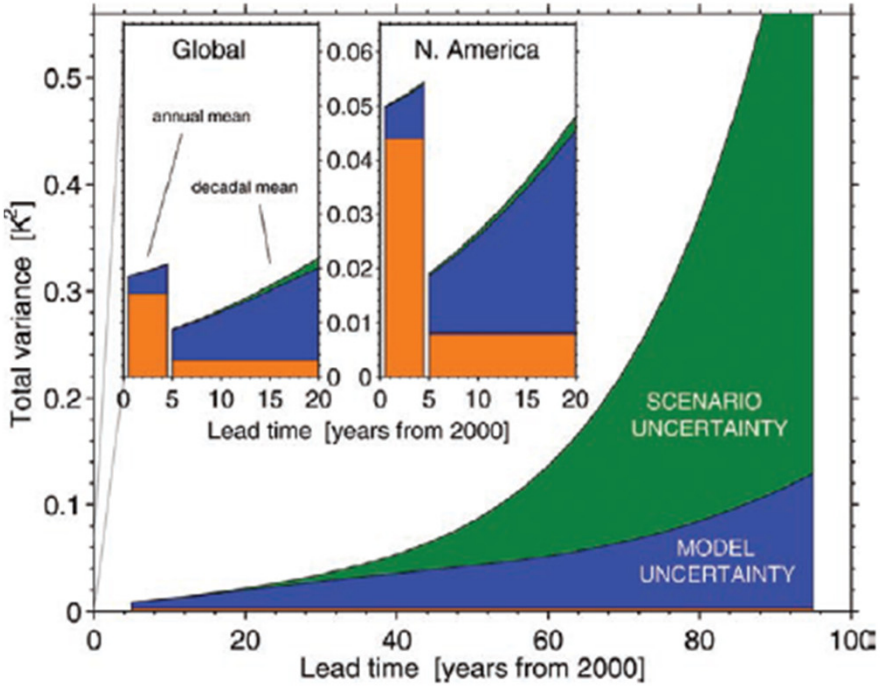

FIG. 2. The relative importance of the three sources of uncertainty changes significantly with region, forecast lead time, and the amount of any temporal meaning applied. Main panel: Total variance for the global-mean, decadal mean surface air temperature predictions, split into the three sources of uncertainty. Insets: As in the main panel, but only for lead times less than 20 yr for (left) the global mean and (right) a North American mean. The orange regions represent the internal variability component. For lead times shorter than 5 yr we plot the results using annual mean data to highlight how the internal variability component is vastly reduced when considering decadal mean data. The uncertainty in the regional prediction is larger than for a global mean.

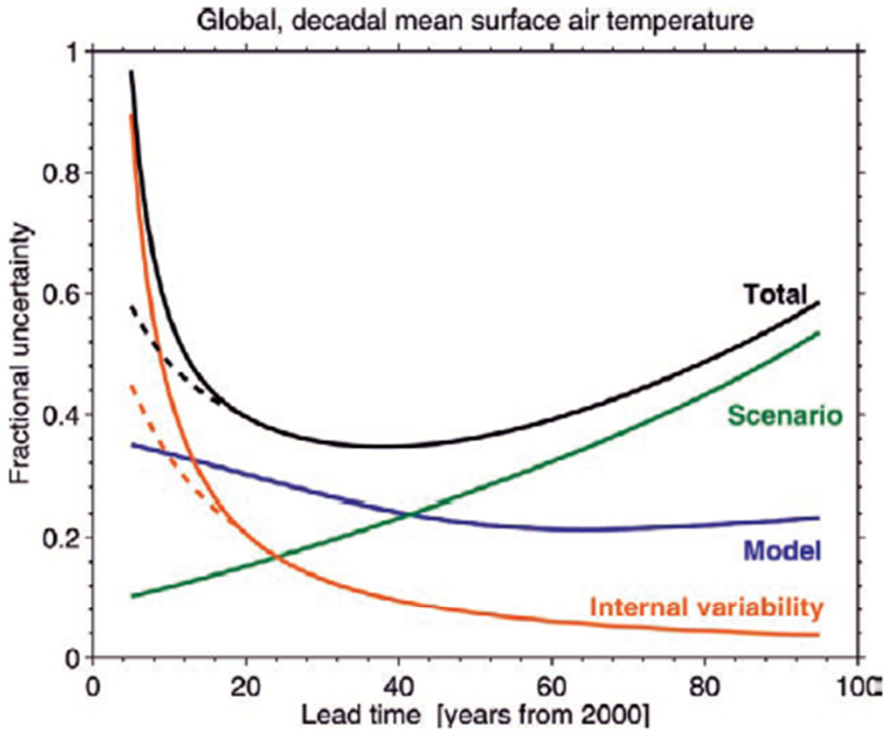

FIG. 3. The relative importance of each source of uncertainty in decadal mean surface air temperature predictions is shown by the fractional uncertainty (the 90% confidence level divided by the mean prediction), for the global mean, relative to the warming since the year 2000 (i.e., a lead of zero years). The dashed lines indicate reductions in internal variability, and hence total uncertainty, that may be possible through proper initialization of the predictions through assimilation of ocean observations (Smith et al. 2007).

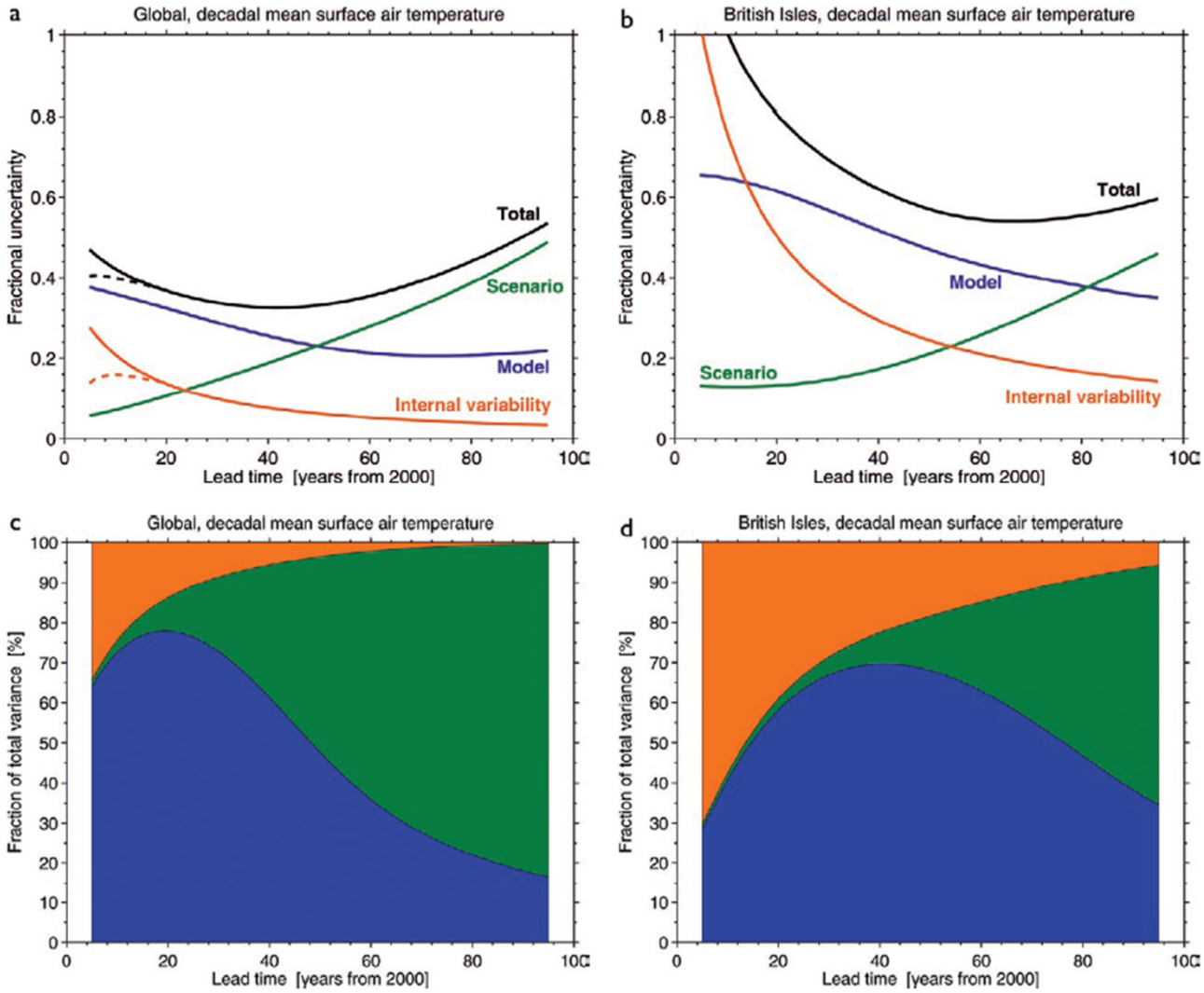

FIG. 4. The relative importance of each source of uncertainty in decadal mean surface temperature projections is shown by the fractional uncertainty (the 90% confidence level divided by the mean prediction) for (a) the global mean, relative to the warming from the 1971–2000 mean, and (b) the British Isles mean, relative to the warming from the 1971–2000 mean. The importance of model uncertainty is clearly visible for all policy-relevant timescales. Internal variability grows in importance for the smaller region. Scenario uncertainty only becomes important at multidecadal lead times. The dashed lines in (a) indicate reductions in internal variability, and hence total uncertainty, that may be possible through proper initialization of the predictions through assimilation of ocean observations (Smith et al. 2007). The fraction of total variance in decadal mean surface air temperature predictions explained by the three components of total uncertainty is shown for (c) a global mean and (d) a British Isles mean. Green regions represent scenario uncertainty, blue regions represent model uncertainty, and orange regions represent the internal variability component. As the size of the region is reduced, the relative importance of internal variability increases.

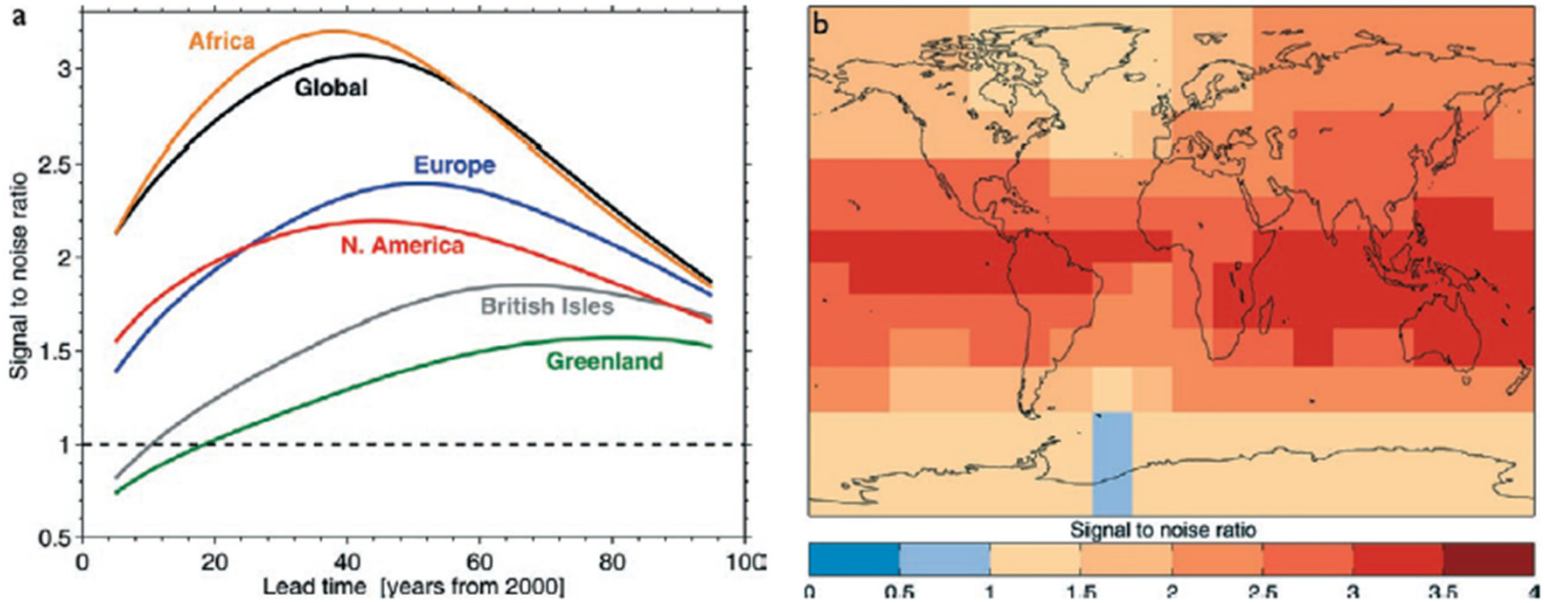

FIG. 5. (a) Signal-to-noise ratio for decadal mean surface air temperature predictions for different regions as labeled (90% confidence levels). The time of the highest S/N is when climate forecasts give most "added value," and this varies with the region as shown. Smaller regions generally have lower signal-to-noise ratios, but Africa does better than a global mean due to its location in the tropics where model uncertainty and internal variability are smaller than average. Greenland has a particularly low signal-to-noise ratio due to uncertainty in high-latitude climate feedbacks. (b) Maps of S/N indicate which regions have more confident predictions. This example shows this ratio for predictions of the fourth decade ahead (90% confidence levels). The tropical regions stand out as having high S/N, whereas Atlantic longitudes have reduced S/N values, perhaps due to uncertainty in the response of the Atlantic Ocean thermohaline circulation to radiative forcings.

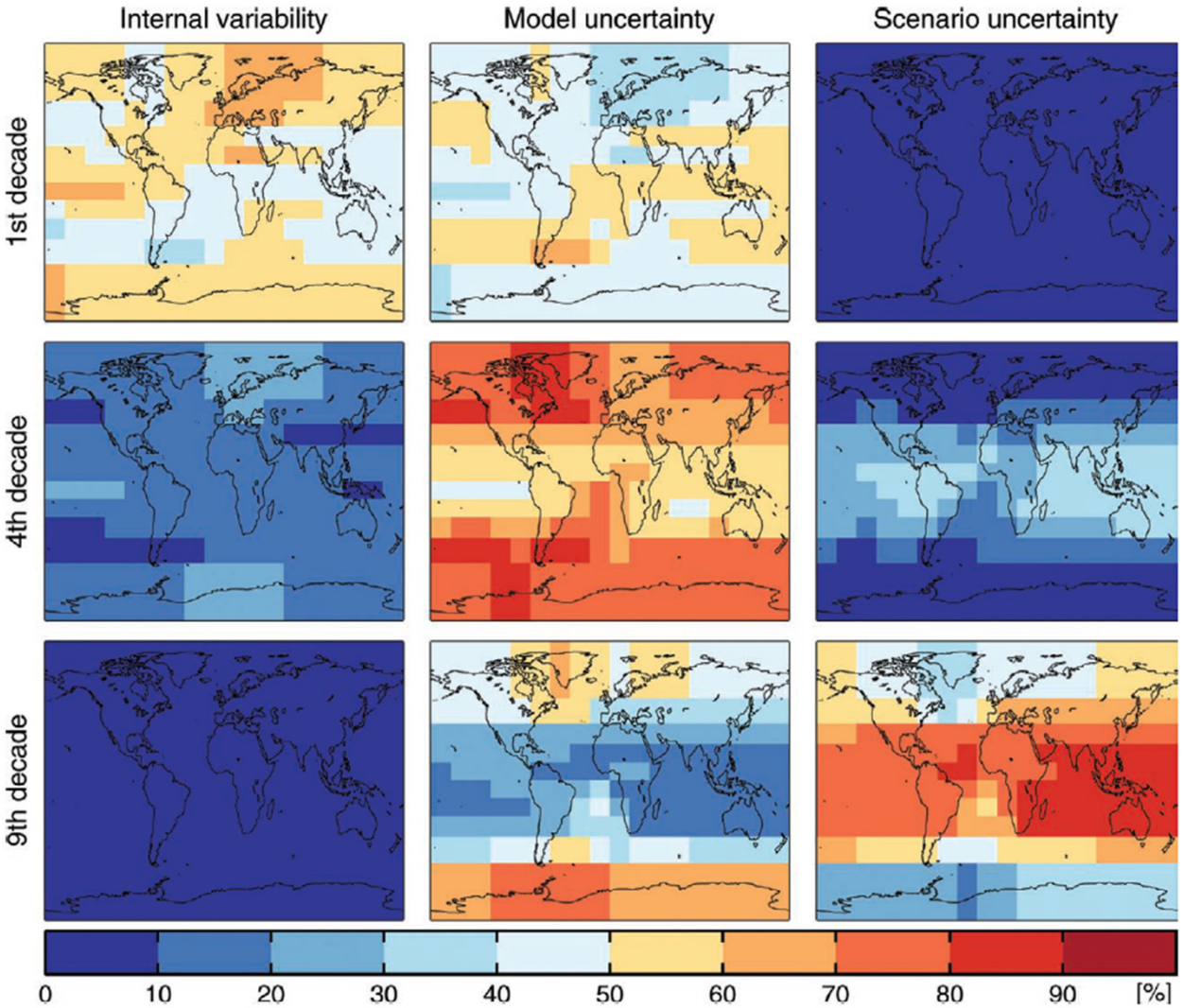

FIG. 6. Maps of the sources of uncertainty for decadal mean surface temperature for various lead times give information on where any reduction in uncertainty will have the most benefit. The columns show the total variance explained by (left) internal variability, (middle) model uncertainty, and (right) scenario uncertainty for predictions of the (top) first, (middle) fourth, and (bottom) ninth decade. It should be noted that (i) even on regional scales, the uncertainty due to internal variability is only a significant component for lead times up to a decade or two, (ii) the largest differences between models occur at high latitudes where climate feedbacks are particularly important, and (iii) even by the end of the century, the emissions scenario is less important than model uncertainty for the high latitudes but dominates in the tropics.

Met Office

Latest Decadal Forecast: 2014-2018

NB: Produced in January 2014

The forecast being described here is from **the experimental decadal prediction system using the latest Met Office climate model, HadGEM3,** developed as part of the Hadley Centre Climate Programme. This system is at the cutting edge of research in understanding, simulating and predicting decadal variability.

It is only feasible to run the forecast out **for the next 5 years.**
Furthermore, **the number of ensemble members (10)** is substantially less than that used in the Met Office seasonal forecasting system (42). For these reasons **the following results should not be over-interpreted.**

The **decadal forecast produced in January 2014, for the 5-year period 2014-2018**, is shown in Figure 1 as the set of dark blue lines, each representing an individual forecast from the 10-member ensemble. For comparison last year's forecast (from January 2012) is shown in light blue lines.

The **baseline 30-year mean climatology** against which the forecast anomalies have been expressed, **is1981-2010**, in line with WMO recommendations and other forecast products.

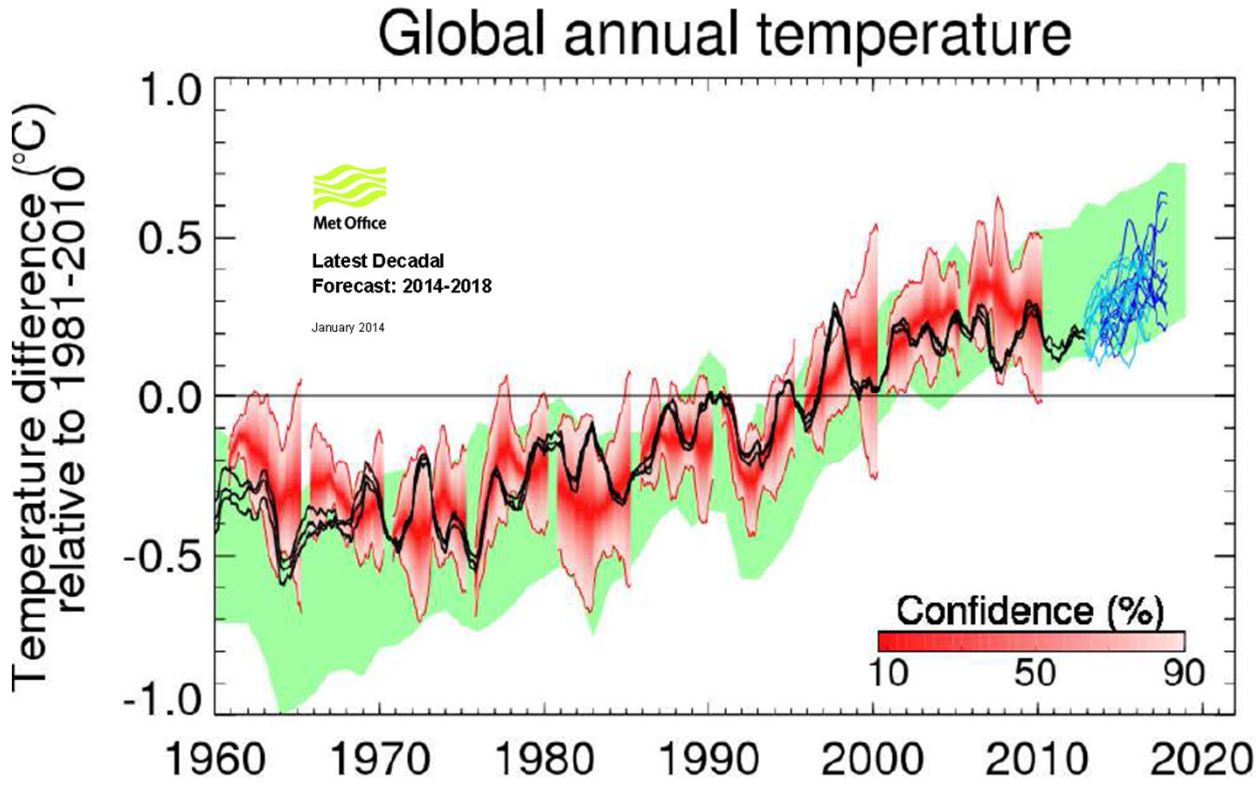

Figure 1: Global annual temperature record since 1960 and the latest ensemble of forecasts from the Met Office decadal prediction system produced in January 2014. The ***dark blue lines*** show the evolution of the 10 individual forecasts from this year's forecast starting from November 2013 and the pale blue lines the equivalent for last year's forecast. All data are rolling annual mean values.

The gap between the black curves and blue curves arises because the last observed value represents the period November 2012 to October 2013 whereas the first forecast period is November 2013 to October 2014.

The thin black curves show the observed annual-mean time-series from 3 independent datasets. Previous predictions starting from November 1960, 1965,..., 2005 are ***shown in red***, and 22 Coupled Model Intercomparison Project phase 5 (CMIP5) model simulations that have not been initialized with observations are ***shown in green***. In both cases, the shading represents the probable range, such that the observations are expected to lie within the shading 90% of the time.

All temperatures are represented as anomalies from the 1981-2010 mean.

Decadal forecast; Forecast issued in January 2016.

Met Office

- **Averaged over the five-year period 2016-2020**,
  - enhanced warming over land, and at high northern latitudes;
  - some indication of continued cool conditions in the Southern Ocean,
  - relatively cool conditions in the North Atlantic sub-polar gyre.
  - global average temperature is expected to remain high;
  - Likely between 0.28°C and 0.77°C above the (1981-2010) average.
    - (an anomaly of +0.44 ± 0.1 °C observed in 2015)
  - consistent with high levels of **greenhouse gases** and **big changes** currently underway in the climate system

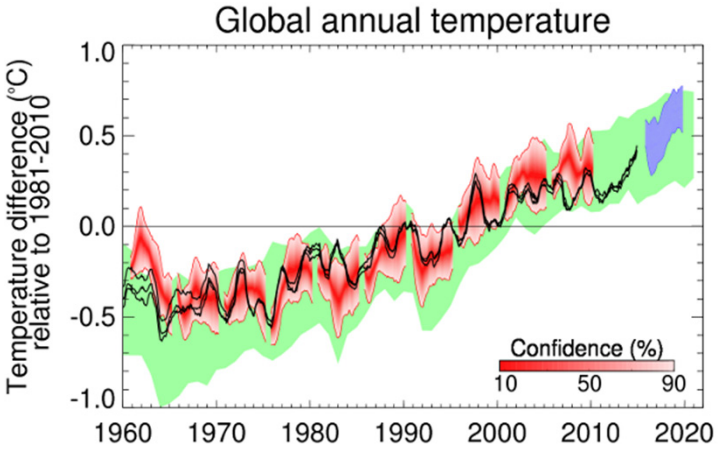

Observed (black, from Met Office Hadley Centre, GISS and NCDC) and **predicted** (blue) from November 2015 global average annual surface temperature difference relative to 1981-2010. **Previous predictions** starting from November 1960, 1965, ..., 2005 in red, and **22 simulations from CMIP5** in green.

Observations are expected to lie within the shading 90% of the time. Moving 12-month mean values.

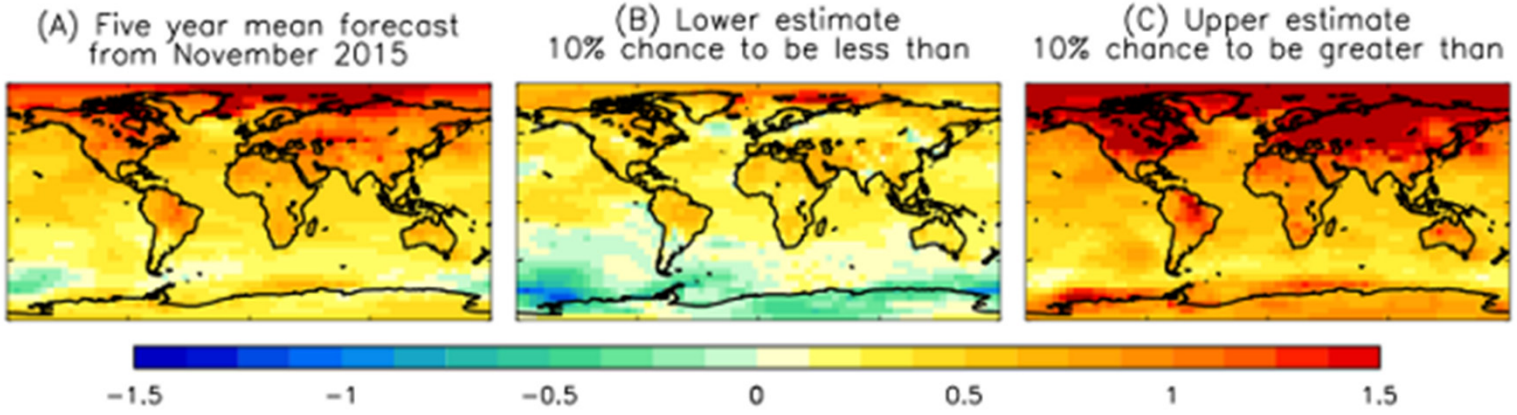

Big Changes Underway in the Climate System?

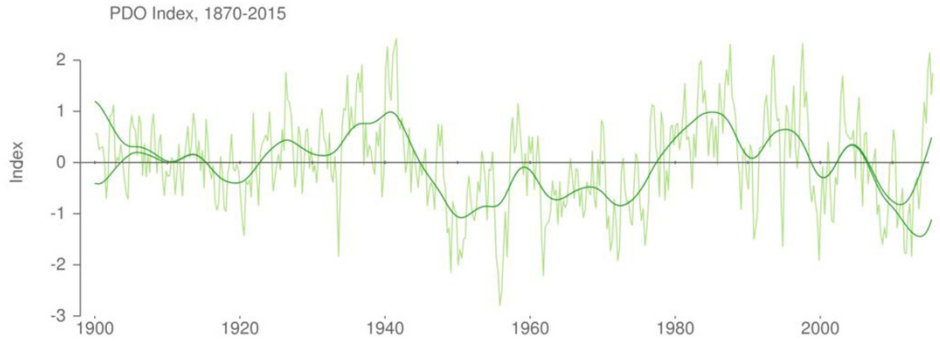

Pacific Decadal Oscillation. Three-month averages of the monthly PDO index of Zhang et al. (1997) from 1900 to 2015. The same series after smoothing to retain decadal and longer variations is overlaid. The pair of curves at each end illustrate large uncertainty due to lack of data before and after the series.

***The current developments** in the worldwide pattern of sea surface temperatures are consistent with an **emerging positive shift in the PDO**, but it is too early to be confident that this will outlast the current El Niño.*

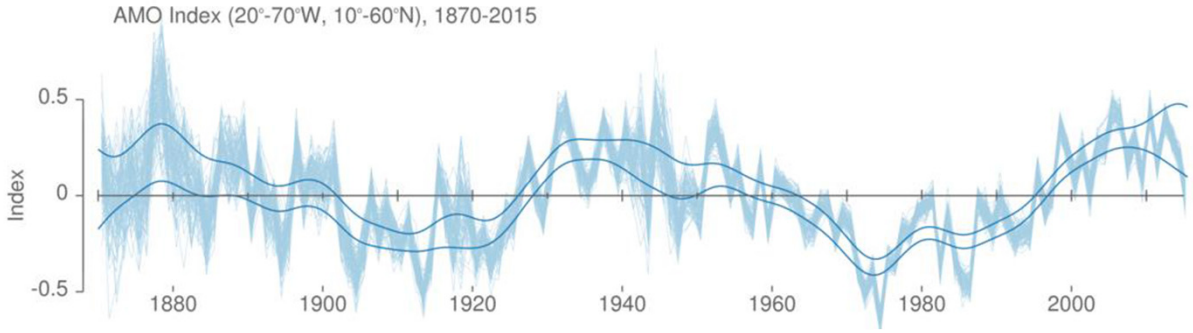

Atlantic Multidecadal Oscillation. Values are annual average, area average North Atlantic sea surface temperature with the long-term linear warming trend removed (˚C), derived from the HadSST3 dataset (Kennedy et al., 2011a,b). The spread of values is a measure of the uncertainty arising from sampling and measurement errors. The solid lines show the low frequency AMO component.

The current trends suggest that the chances of a shift in the next few years have increased. However, it is not certain that there will be a shift towards cooler Atlantic conditions over the next few years. Temporary cooling has occurred in the past without leading to a sustained AMO shift.

Climate projections

Procedures for Climate projections

CMIP: Coupled Model Intercomparison Project (WMO-activity)
CMIP5 →production for IPCC AR5 (2013)
CMIP6 →production for IPCC AR6 (ongoing, scheduled for 2022)

Purpose:
Calculate all possible states that can be realized in the climate system
for a predefined set of externally defined governing conditions.
I.e.: **a prediction of the second kind**, for which the actual intial state is irrelevant

MIPs = more than
20 projects with specified
purpose experiments

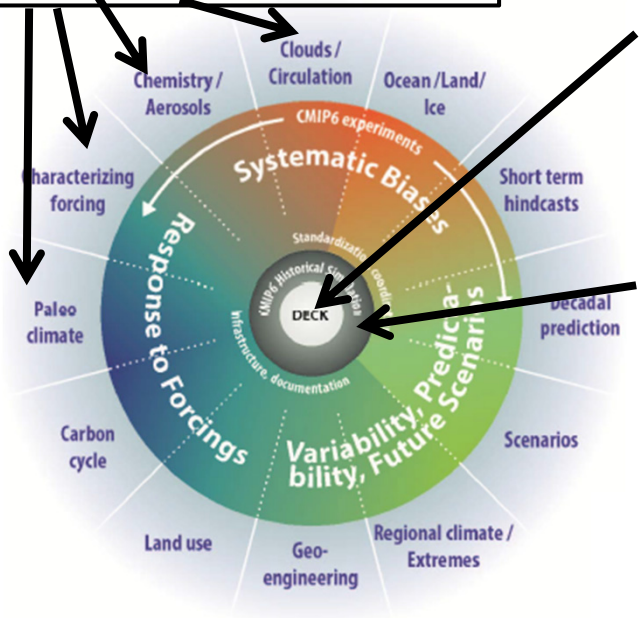

Note: The themes in the outer circle of the figure might be slightly revised at the end of the MIP endorsement process

Qualifying a model for CMIP6 participation: CMIP DECK and CMIP6 Historical Simulation

DECK (entry card for CMIP)
(Diagnostic, Evaluation and Characterization of Klima)
i. AMIP simulation (~1979-2014) (pure Atmospheric Model)
ii. Pre-industrial control simulation (1850 conditions)
iii. 1%/yr CO2 increase until 4 times CO2 at 1850, then kept constant)
iv. Abrupt 4xCO2 run (4 times CO2 at 1850=

CMIP6-Hist: Historical Simulation: entry card for CMIP6

v. Historical simulation using re-constructed forcing for (1850-2014)

MIPs: Model Intercomparison Projecys designed for specific purposes
A wide range of process-experimental runs, diagnostic attribution runs, and climate projection runs, including detection and attributuin and future projections based on scenarioes. Also paleoclimate runs and decadal prediction runs are included as MIPs.

A simplified description of basic procedures for climate projections

Stepwise procedure:

- Start from a state of the climate system as close as possible to 1850 conditions
  - There are available data from previous model runs, e.g. for CMIP5
- Provide boundary data as close as possible to 1850 conditions
  - land-surface, solar activity, atmospheric composition, earth's orbit etc.
- Start a ***multi-century spin-up run:*** run the model to achieve an average energy equilibrium at the top of the atmosphere and a long-term, stable climate;
  - normally several re-starts are needed with parameters adjusted (model tuning)
  - up to a few thousand model years may be required to reach a stable equilibrium
- ***PI-Control:*** after spin-up, run >500 years for pre-industrial (PI) 1850. (CMIP-DECK)
- ***Historical:*** At the same time: a historical run from 1850 to present day with driving external conditions given (CMIP6-Hist);
- ***Ensemble:*** Several additional historical runs started from indep. states in the PI-Control.
  - ***Used for model validation***
- **Attribution runs:** One selected ensemble member for the historical period is re-run with single contributions to forcing (aerosols only; GHG only, Natural only)
- **Future Projections based on scenarioes.** Future scenarios for societal development, energy demand, is used to estimate future development of land-use, GHG-emissions, and aerosol emissions. Different pathways is estimated to produce a radiative forcing at the top of the atmosphere; Representative Concentration Pathways (RCP) by 2100 tompared to 1850. The historical runs are extended to 2100 (or 2300) using the RCPs. RCPn, n=2.6, 4.5, 6.0 or 8.5 W/m^2 .

Observational basis for a changing climate

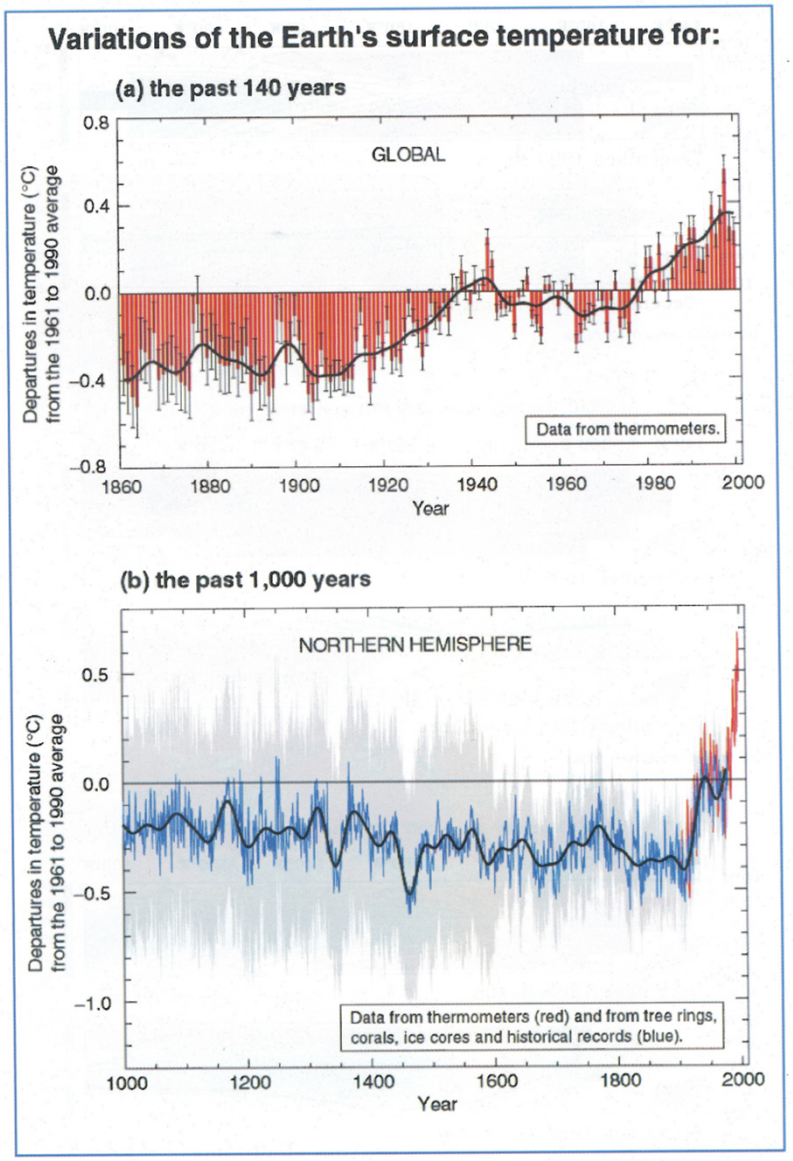

Plate 4 Variation of the surface temperature over: (a) the last 140 years and (b) the last millennium. In (a) the red bars represent the annual average for the globe based on thermometer data, and the whiskers the 95% confidence range, including uncertainties due to coverage, biases and urbanization. The black line is a 10-year moving average. In (b) the blue line represents proxy data. Adapted from IPCC (2002).

Sources of uncertainty in model-calculated climate projectionsand interpretation of observations

Variations vs. change

1. Random, natural climate variability (”chaos”)
2. Uncertain external forcing (natural and anthropogenic)
3. Uncertain quality of climate models (”known unknowns”)
4. All other unknown contributions (”unknown unknowns”)

Major challenge

1. Climate change implies non-stationary statistics
   - time-averages cannot represent the full climate statistics
2. Time-scale of changes (”trends”) overlap with time-scale of natural climate variability

The ”hockey-stick”

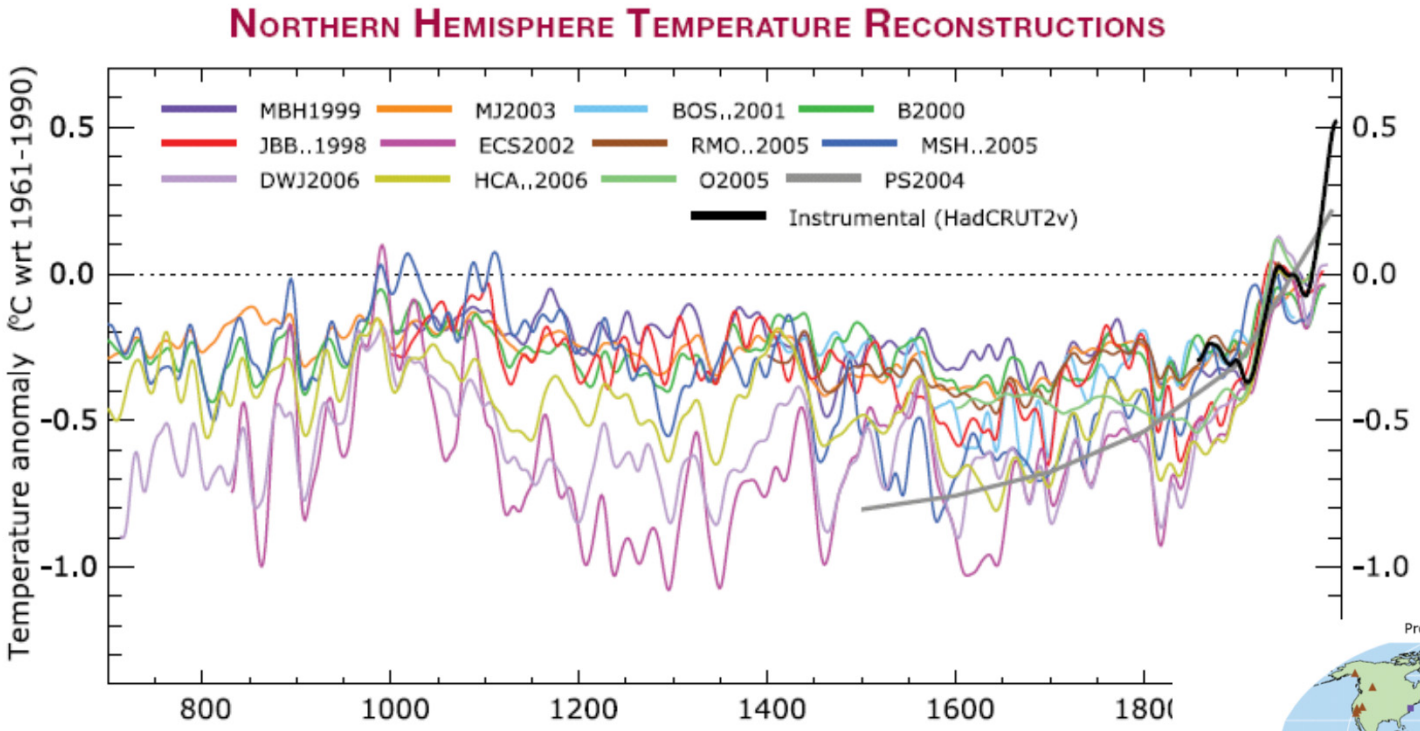

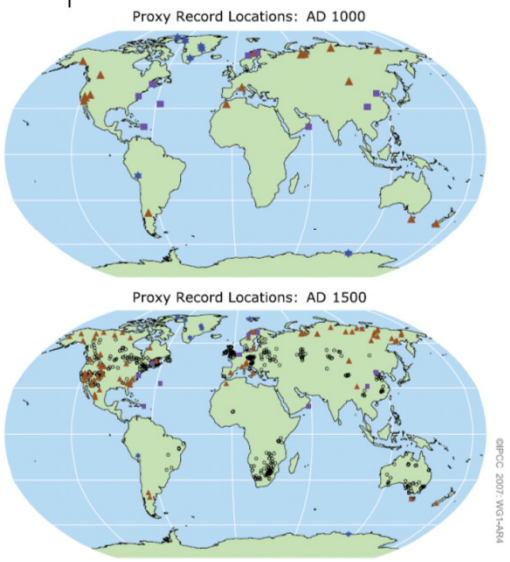

Figure TS.20. *(Top) Records of Northern Hemisphere temperature variation during the last 1300 years with 12 reconstructions using multiple climate proxy records shown in colour and instrumental records shown in black. (Middle and Bottom) Locations of temperature-sensitive proxy records with data back to AD 1000 and AD 1500 (tree rings: brown triangles; boreholes: black circles; ice core/ice boreholes: blue stars; other records including low-resolution records: purple squares). Data sources are given in Table 6.1, Figure 6.10 and are discussed in Chapter 6. (Figures 6.10 and 6.11)*

Continental air warmes faster than marine air

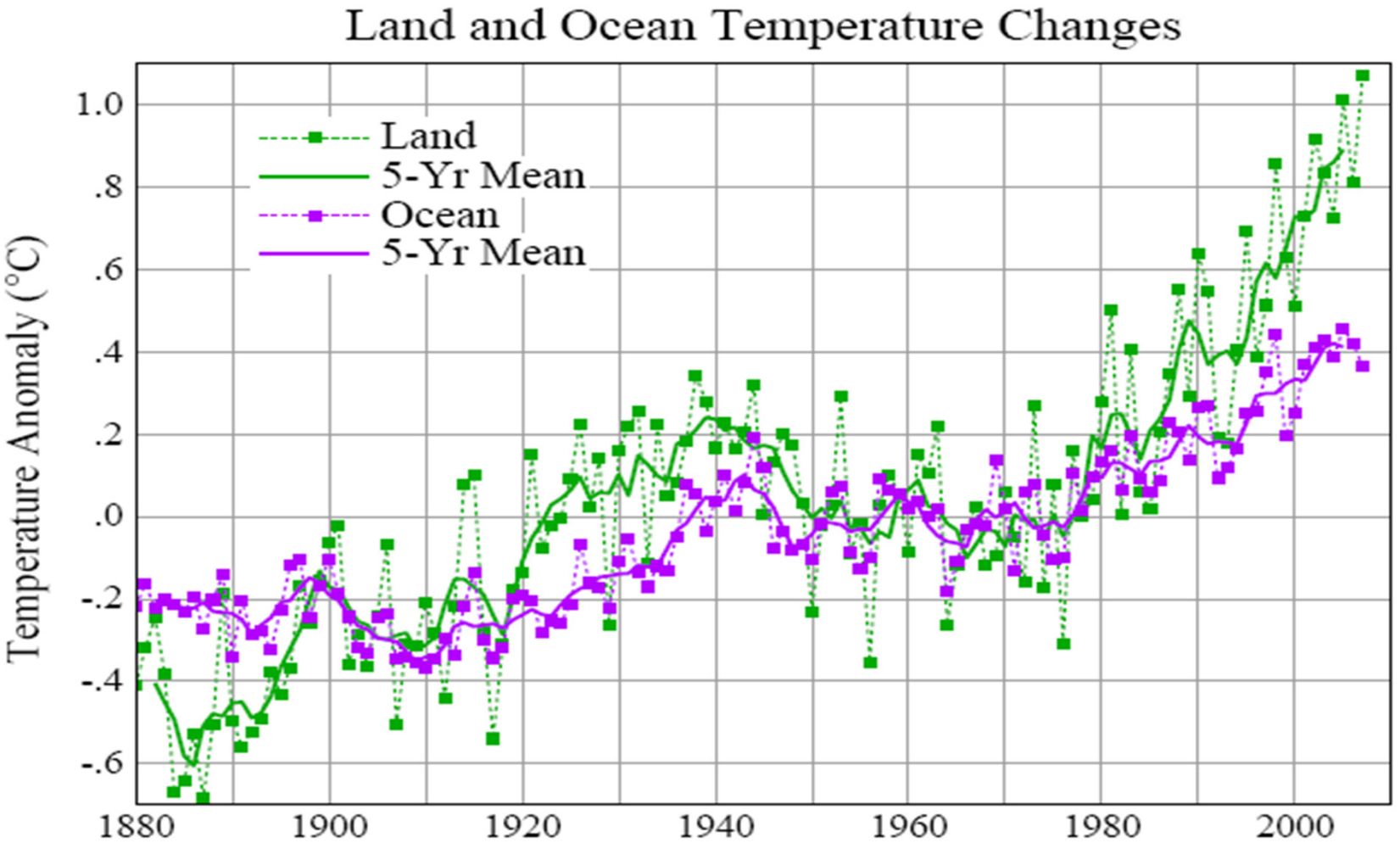

Updated to include 2015 (NASA/NOAA)

"Since 1880, Earth's average surface temperature has warmed by about 0.8 Celsius. The majority of that warming has occurred in the past three decades."

"Earth's 2015 surface temperatures were the warmest since modern record keeping began in 1880"

according to independent analyses by NASA's Goddard Institute for Space Studies and NOAA's National Centers for Environmental Information.

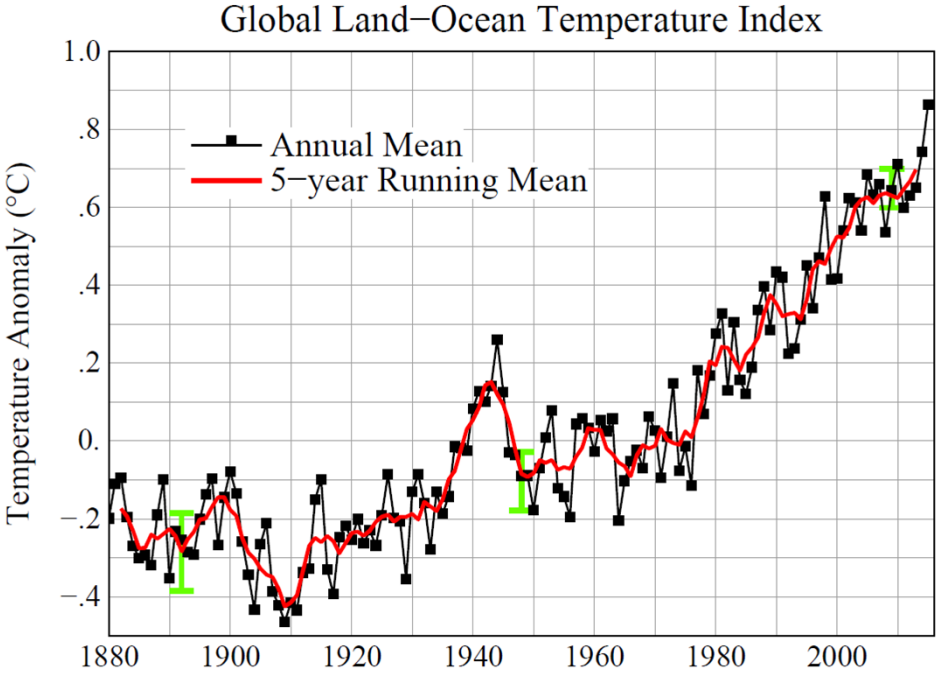

Climate Research Unit (CRU), Univ of East-Anglia, UK

The time series shows the combined global land and marine surface temperature record from 1850 to 2015. This year was the equal warmest on record. This record uses the latest analysis, referred to as HadCRUT.

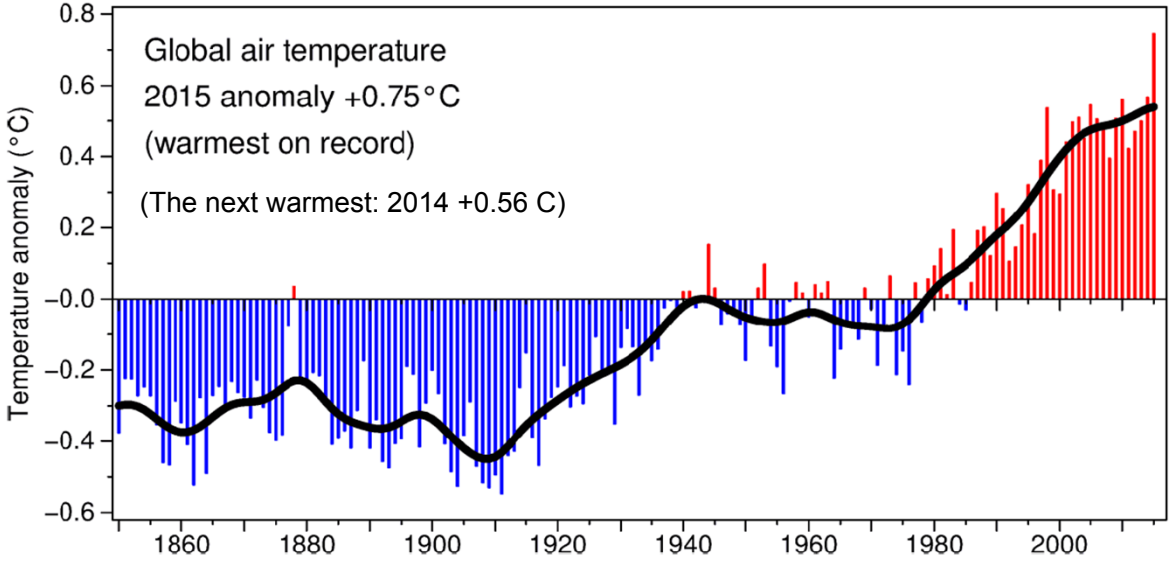

Morice, C.P., Kennedy, J.J., Rayner, N.A. and Jones, P.D., (2012). Journal of Geophysical Research,117, D08101,doi:10.1029/2011JD017187

2015 was the warmest year since modern record-keeping began in 1880, according to a new analysis by **NASA's Goddard Institute for Space Studies**. The record-breaking year continues a long-term warming trend — 15 of the 16 warmest years on record have now occurred since 2001. (Credit: NSA/GSFC/Scientific Visualization Studio)

Globally-averaged temperatures in 2015 shattered the previous mark set in 2014 by 0.23 degrees Fahrenheit (0.13 Celsius). Only once before, in 1998, has the new record been greater than the old record by this much.

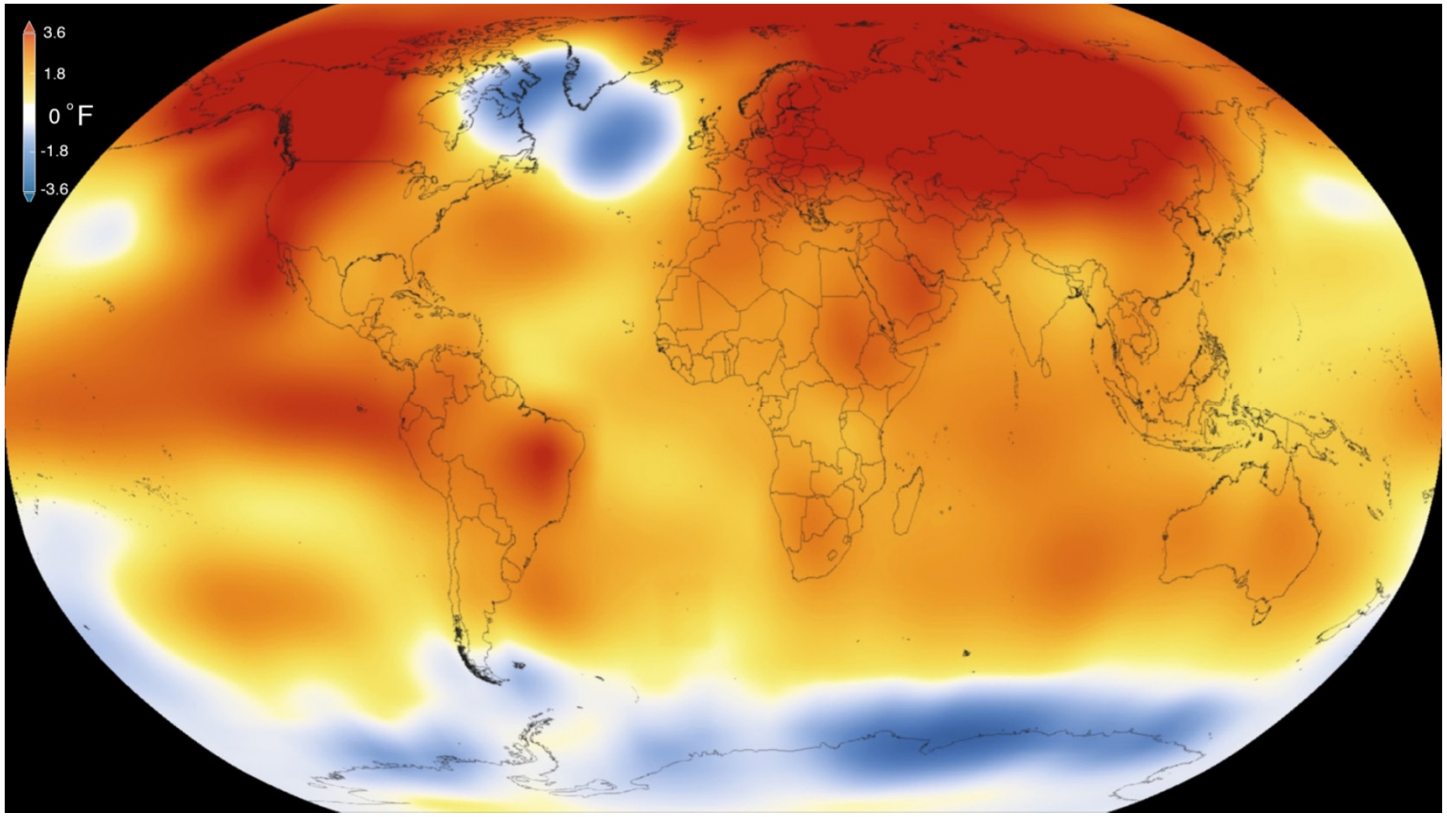

Order of annual global mean Ts anomalies

2015 Versus the Warmest Years

annual temperature departures ranked coolest to warmest using a common 1951-80 base period

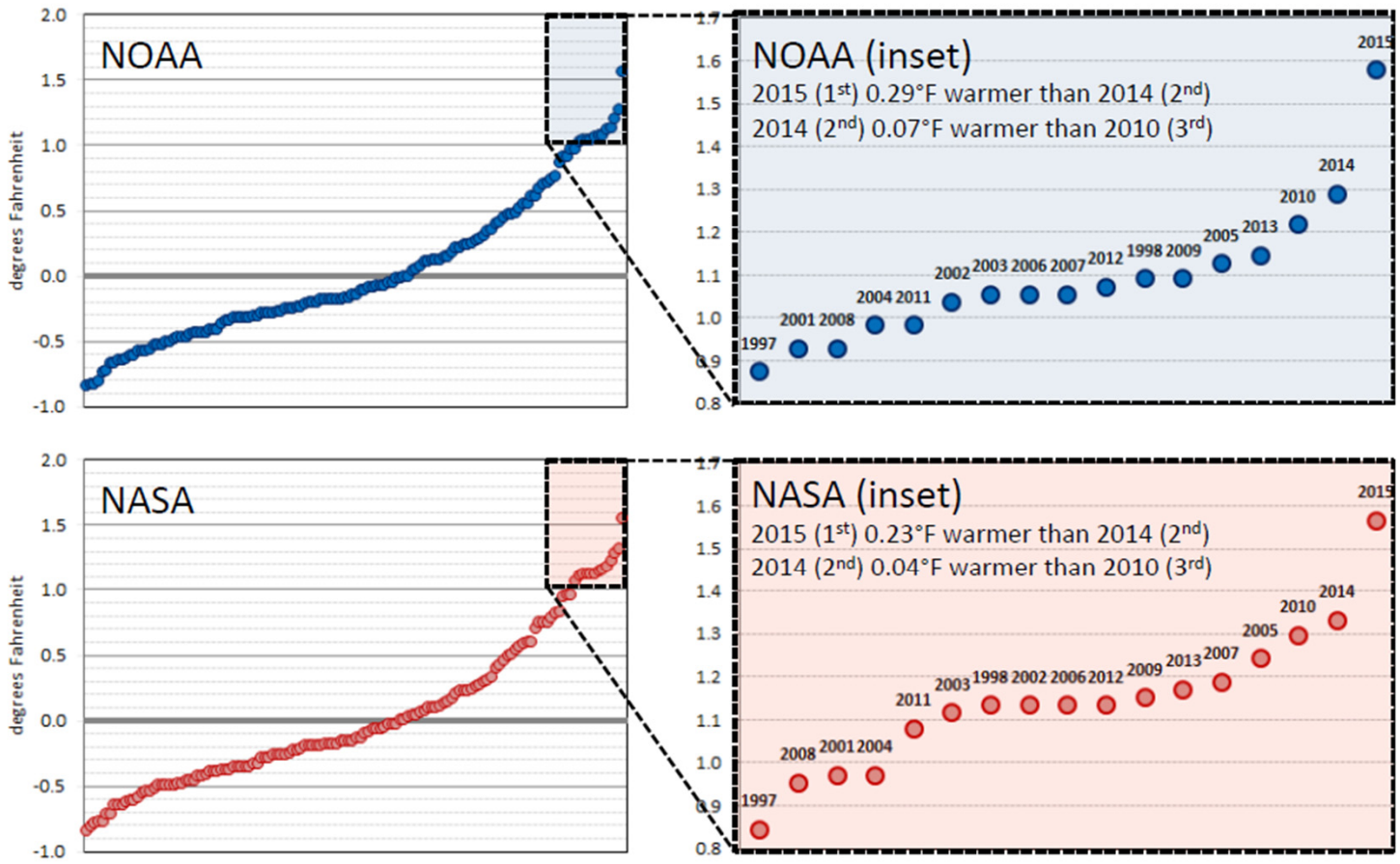

Monthly (NOAA) **global Ts-anomalies** (rel.1951-80) **during El Niño, La Niña, ENSO neutral** (Nino3.4 index)

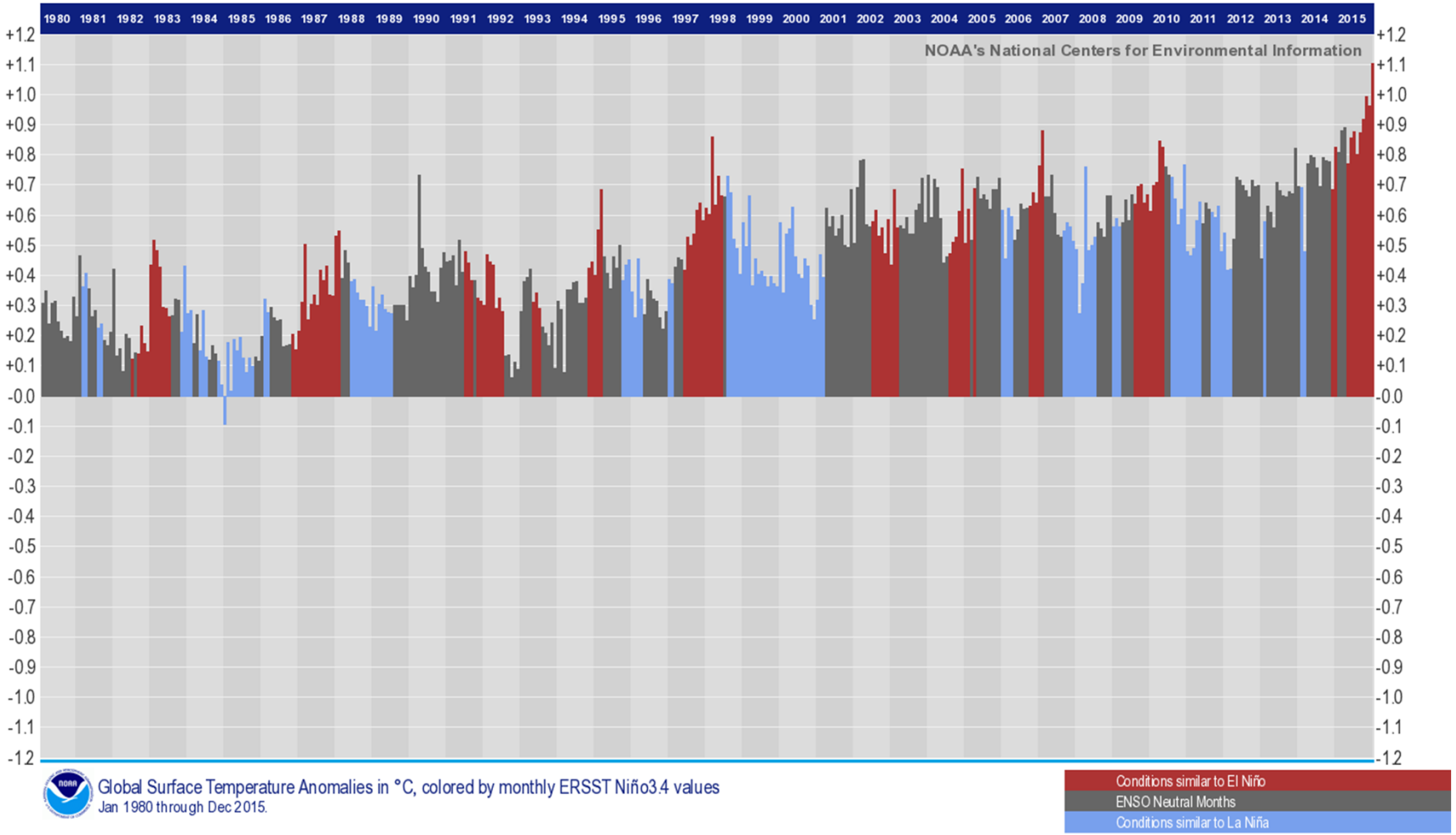

Variations above ground

IPCC

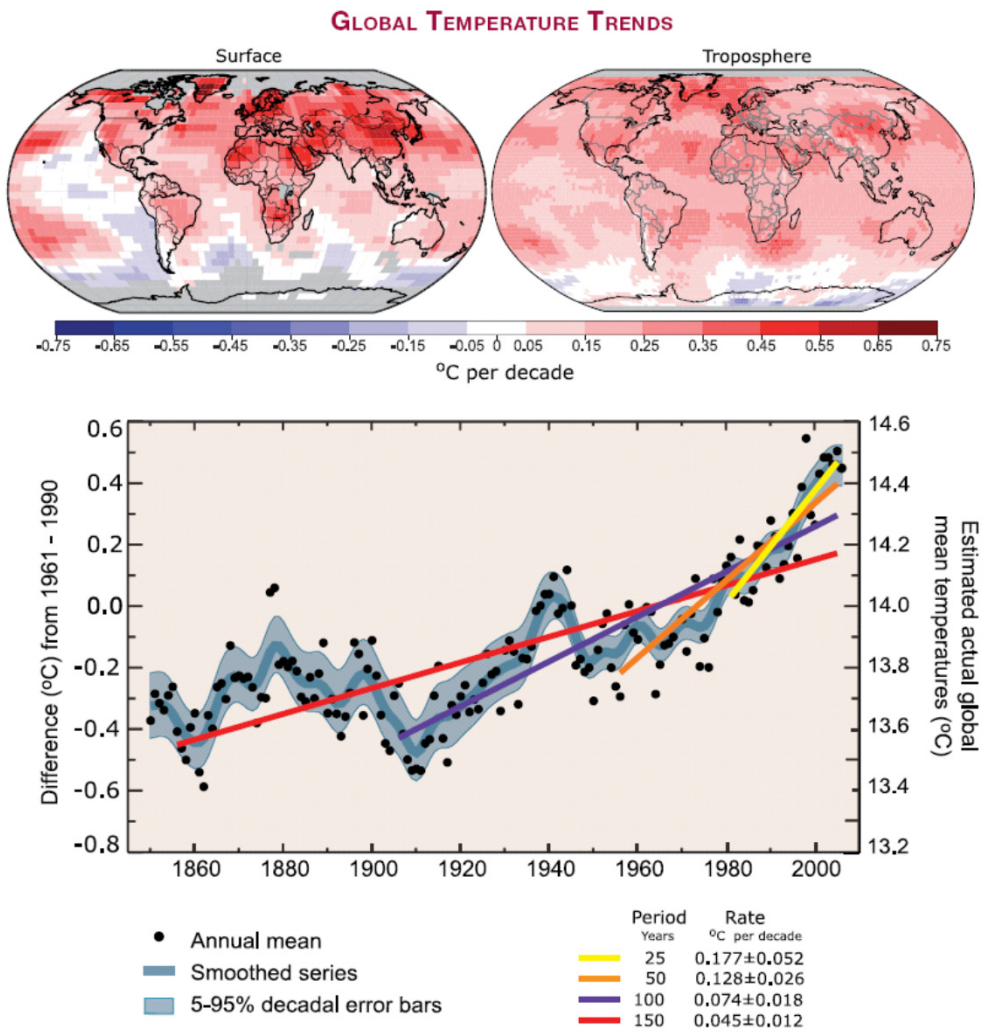

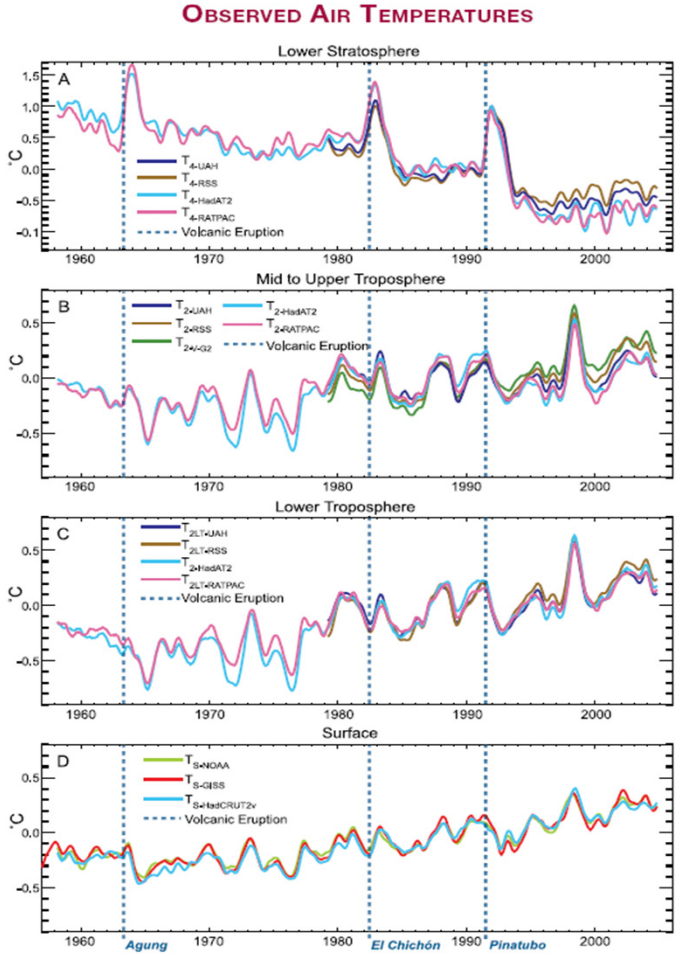

Figure TS.7. *Observed surface (D) and upper air temperatures for the lower troposphere (C), mid- to upper troposphere (B) and lower stratosphere (A), shown as monthly mean anomalies relative to the period 1979 to 1997 smoothed with a seven-month running mean filter. Dashed lines indicate the times of major volcanic eruptions. {Figure 3.17}*

Can models explain observed changes since 1900? IPCC

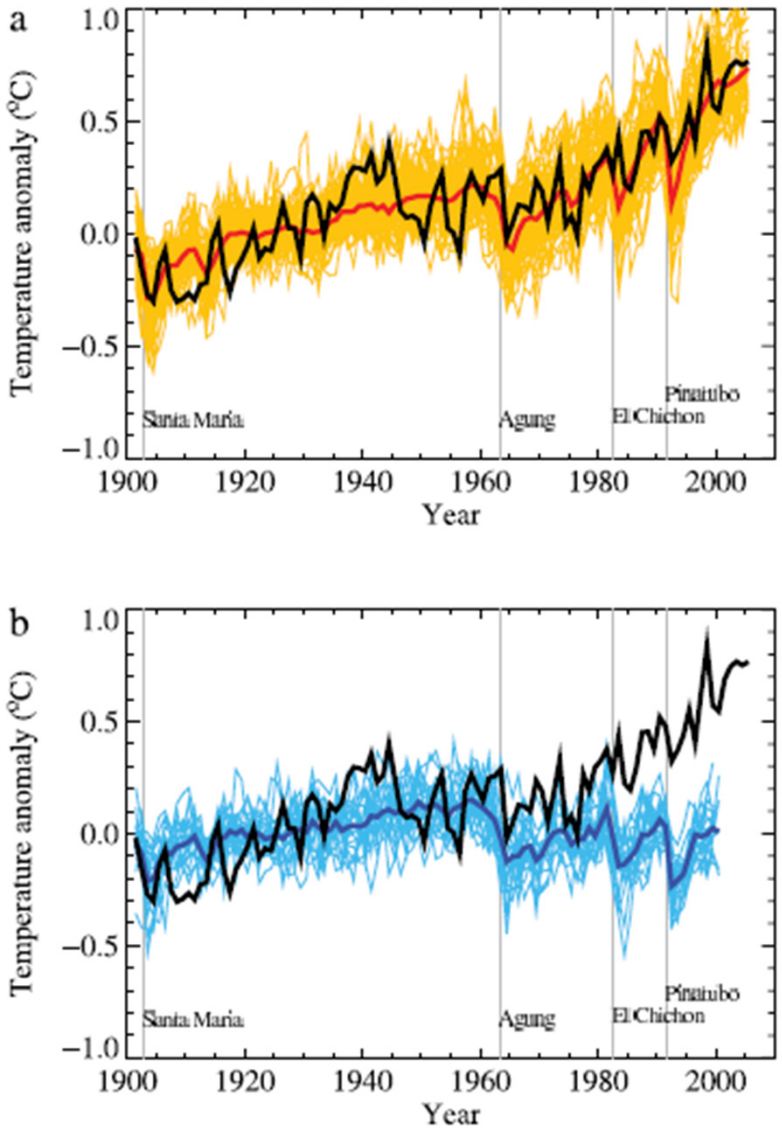

Figure 9.5. *Comparison between global mean surface temperature anomalies (°C) from observations (black) and AOGCM simulations forced with (a) both anthropogenic and natural forcings and (b) natural forcings only. All data are shown as global mean temperature anomalies relative to the period 1901 to 1950, as observed (black, Hadley Centre/Climatic Research Unit gridded surface temperature data set (HadCRUT3); Brohan et al., 2006) and, in (a) as obtained from 58 simulations produced by 14 models with both anthropogenic and natural forcings. The multi-model ensemble mean is shown as a thick red curve and individual simulations are shown as thin yellow curves. Vertical grey lines indicate the timing of major volcanic events. Those simulations that ended before 2005 were extended to 2005 by using the first few years of the IPCC Special Report on Emission Scenarios (SRES) A1B scenario simulations that continued from the respective 20th-century simulations, where available. The simulated global mean temperature anomalies in (b) are from 19 simulations produced by five models with natural forcings only. The multi-model ensemble mean is shown as a thick blue curve and individual simulations are shown as thin blue curves. Simulations are selected that do not exhibit excessive drift in their control simulations (no more than 0.2°C per century). Each simulation was sampled so that coverage corresponds to that of the observations. Further details of the models included and the methodology for producing this figure are given in the Supplementary Material, Appendix 9.C. After Stott et al. (2006b).*

Can models explain observed changes since 1900? IPCC

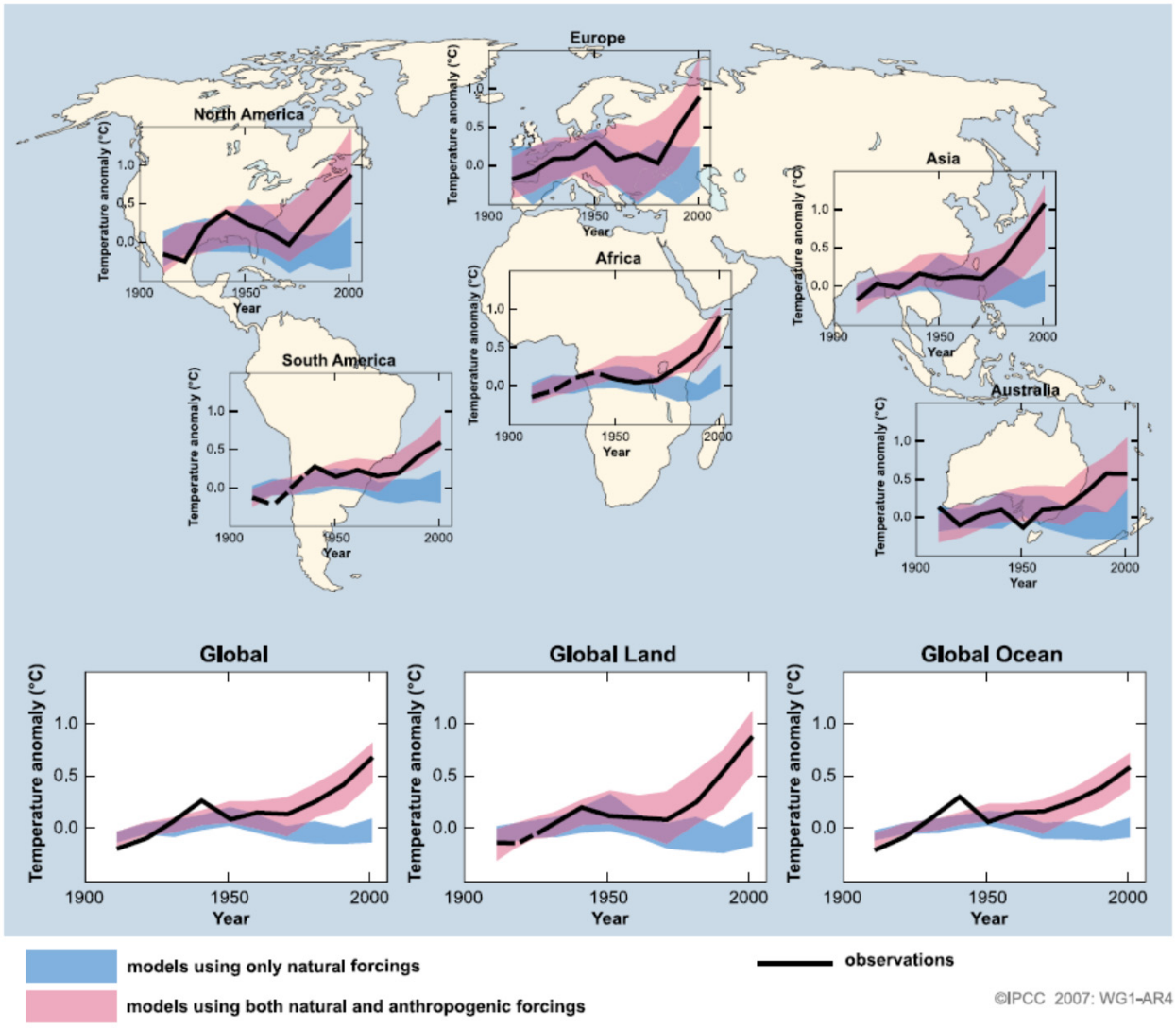

Climate development in the 21st century? Projection of surface air temperature IPCC

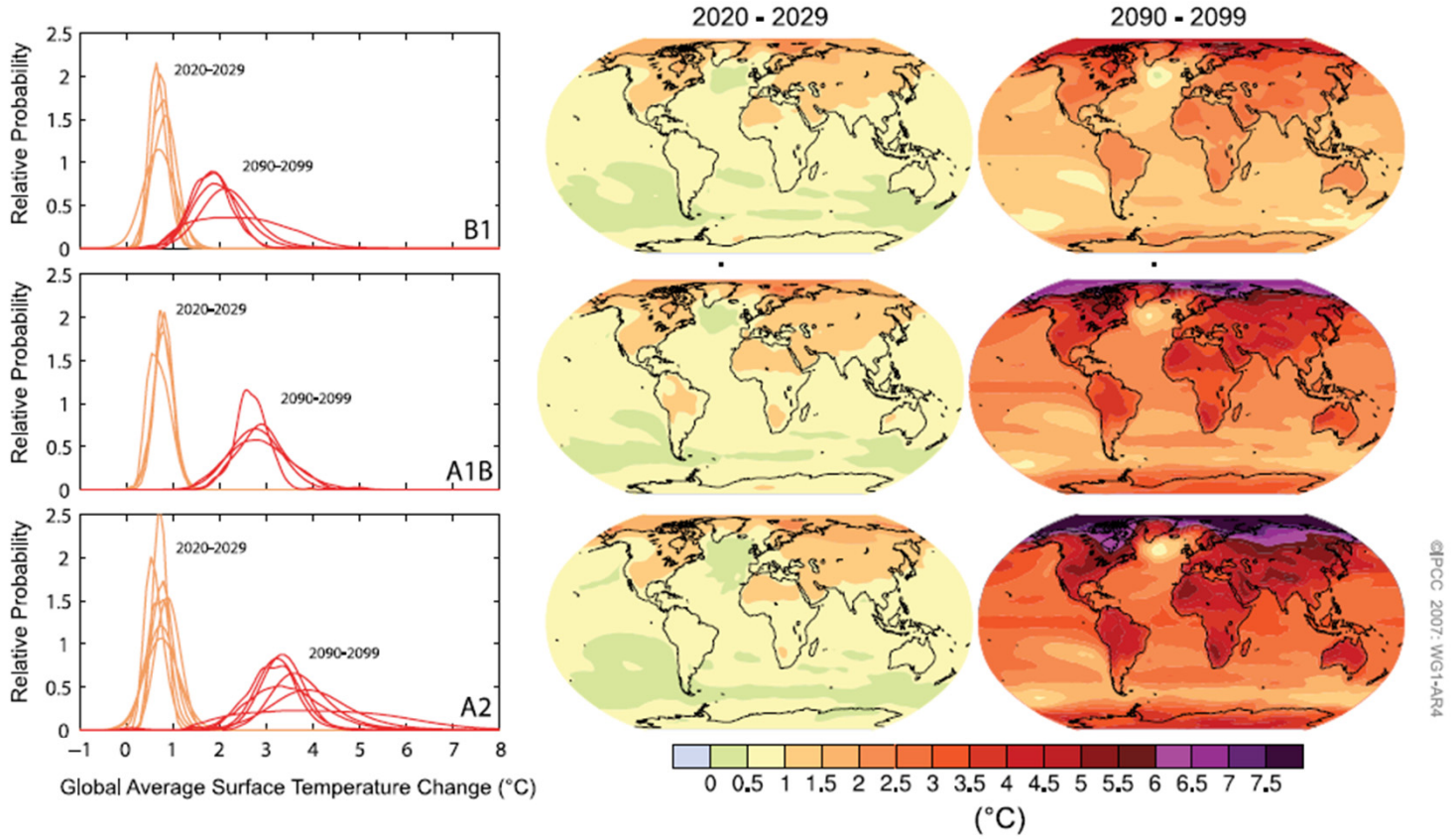

Figure SPM.6. *Projected surface temperature changes for the early and late 21st century relative to the period 1980–1999. The central and right panels show the AOGCM multi-model average projections for the B1 (top), A1B (middle) and A2 (bottom) SRES scenarios averaged over the decades 2020– 2029 (centre) and 2090–2099 (right). The left panels show corresponding uncertainties as the relative probabilities of estimated global average warming from several different AOGCM and Earth System Model of Intermediate Complexity studies for the same periods. Some studies present results only for a subset of the SRES scenarios, or for various model versions. Therefore the difference in the number of curves shown in the left-hand panels is due only to differences in the availability of results. {Figures 10.8 and 10.28}*

Climate development in the 21st century?
Projection of precipitation change IPCC

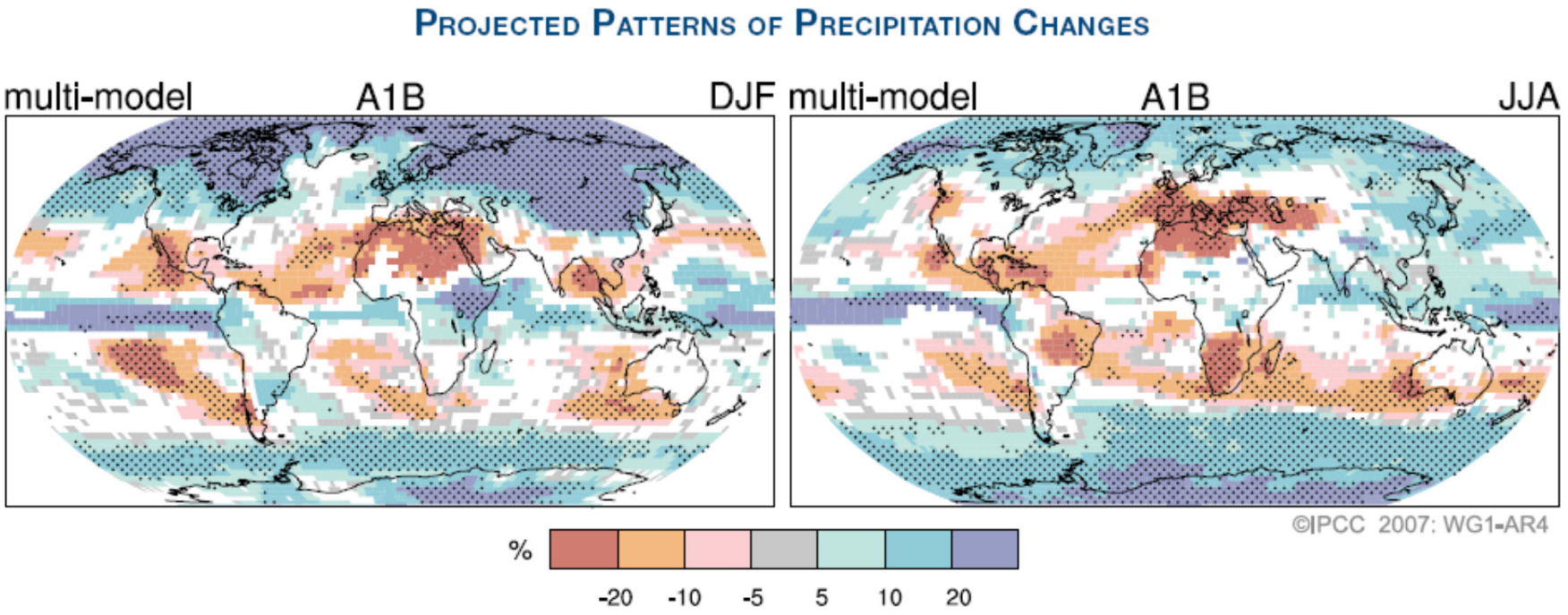

Figure SPM.7. *Relative changes in precipitation (in percent) for the period 2090–2099, relative to 1980–1999. Values are multi-model averages based on the SRES A1B scenario for December to February (left) and June to August (right). White areas are where less than 66% of the models agree in the sign of the change and stippled areas are where more than 90% of the models agree in the sign of the change. {Figure 10.9}*

Climate change and prefered regimes

Lorenz' 3-parameter model

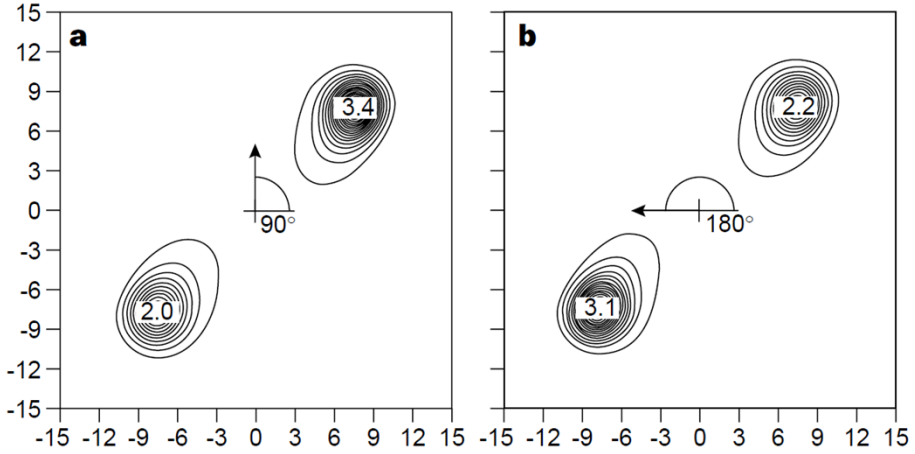

Figure 1 Response of a nonlinear chaotic model to imposed forcing. Illustrated is

Sensitivity vs. Response:
A (weak) forcing may not change regime patterns, but may change the relative occurrence of them.

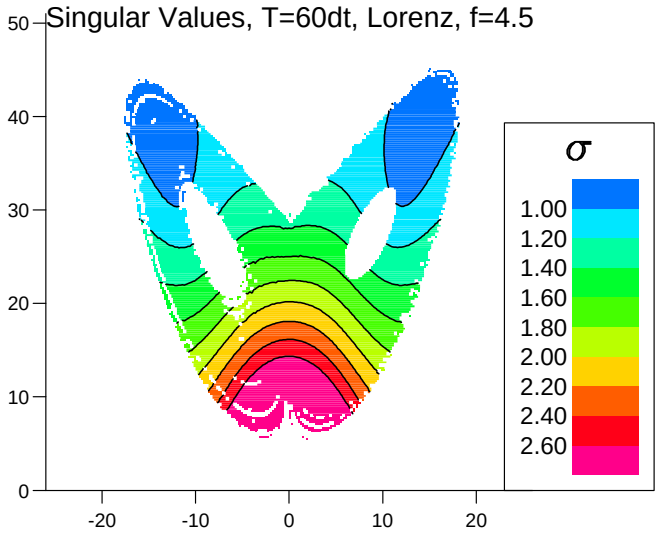

Transient realization with periodic forcing.

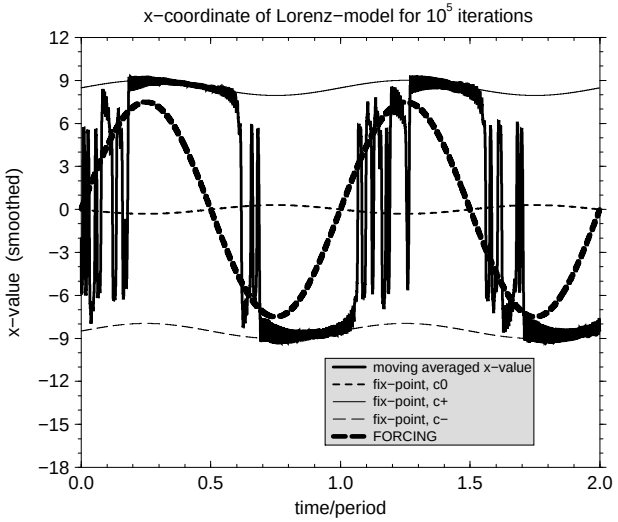

forcing - response

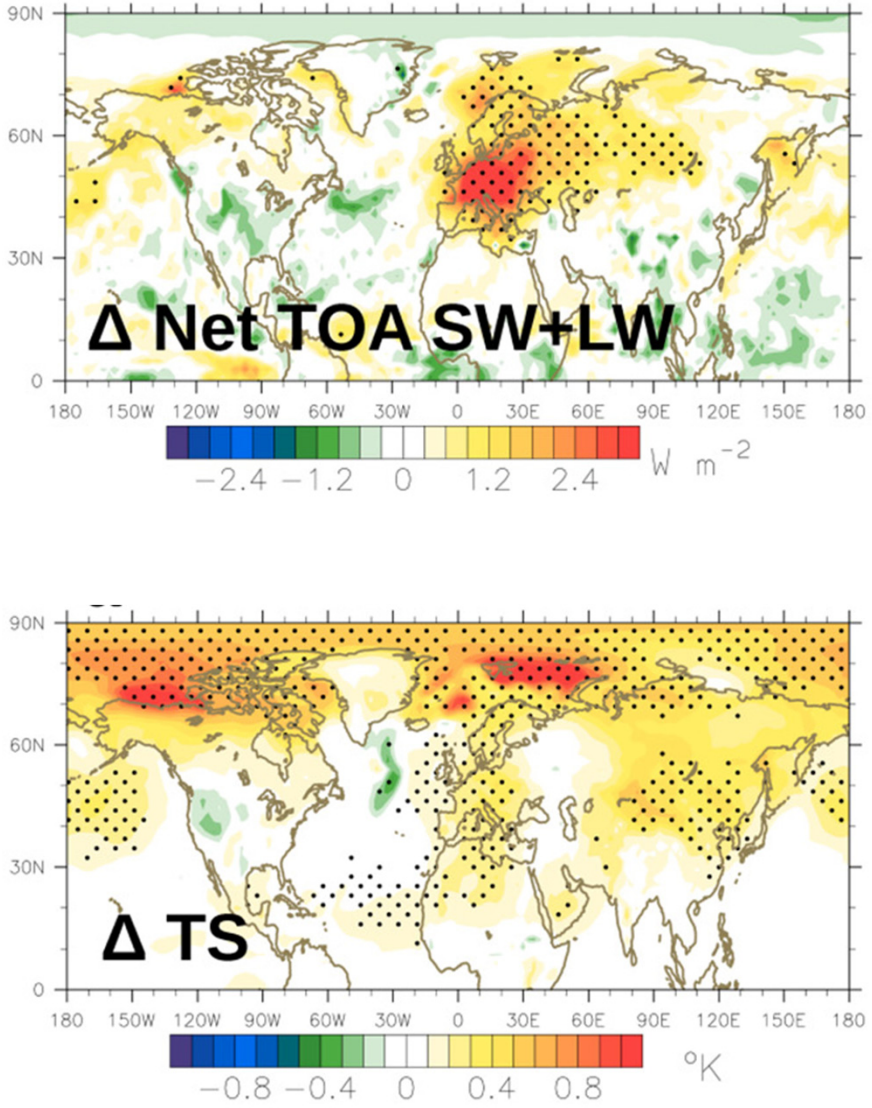

Example:

Amplification of Arctic warming by past air pollution reductions in Europe

JC. Acosta Navarro, V. Varma, I. Riipinen, Ø. Seland, A. Kirkevåg, H. Struthers,T. Iversen, H-C. Hansson, A. Ekman

Nature Geosciences, March 15th, 2016.

Regional change in temperature when $\Delta T_{glob} = +2\,^{\circ}\,C$

Notice the much larger temperature increase in the Arctic

(° C, RCP8.5)

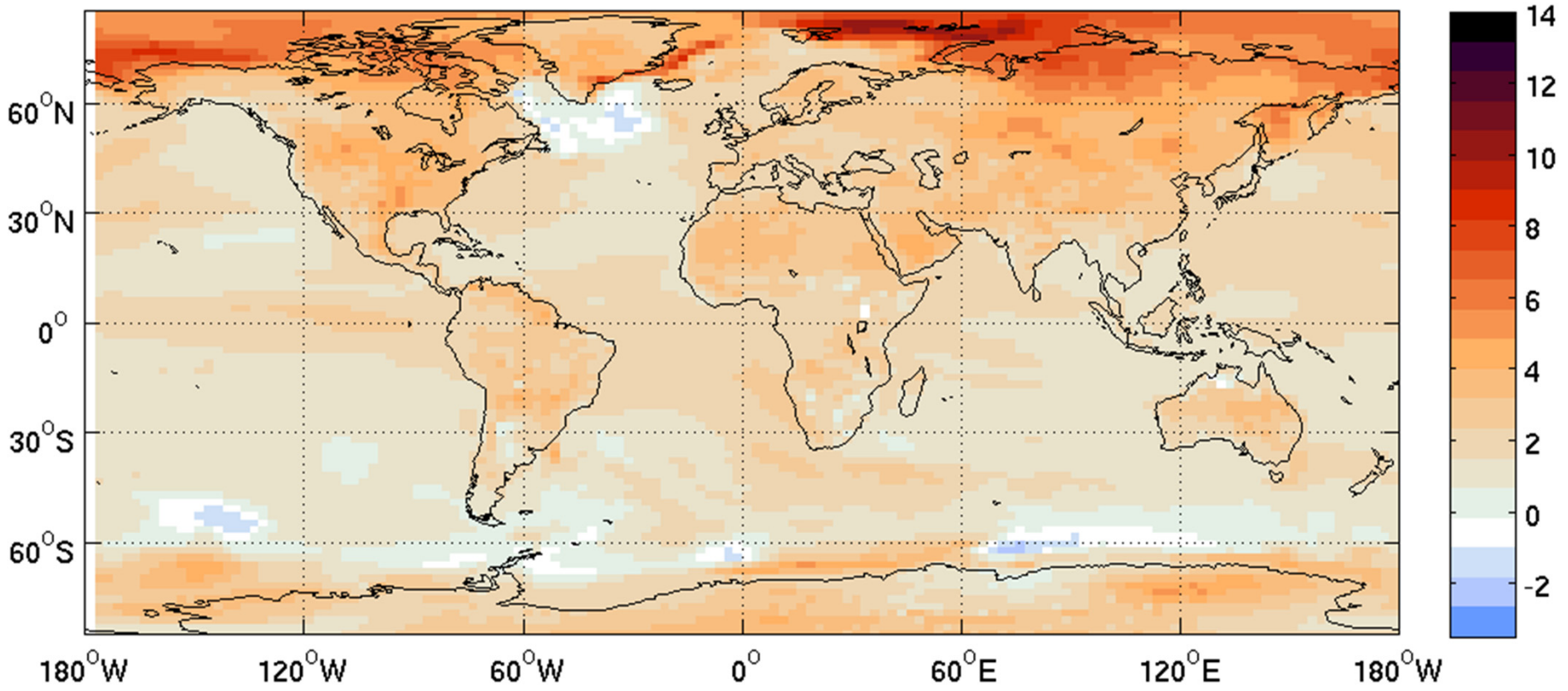

Helge Drange, UiB:

Estimated probability for global Ts-decrease over 10 years, from 17 global climate models

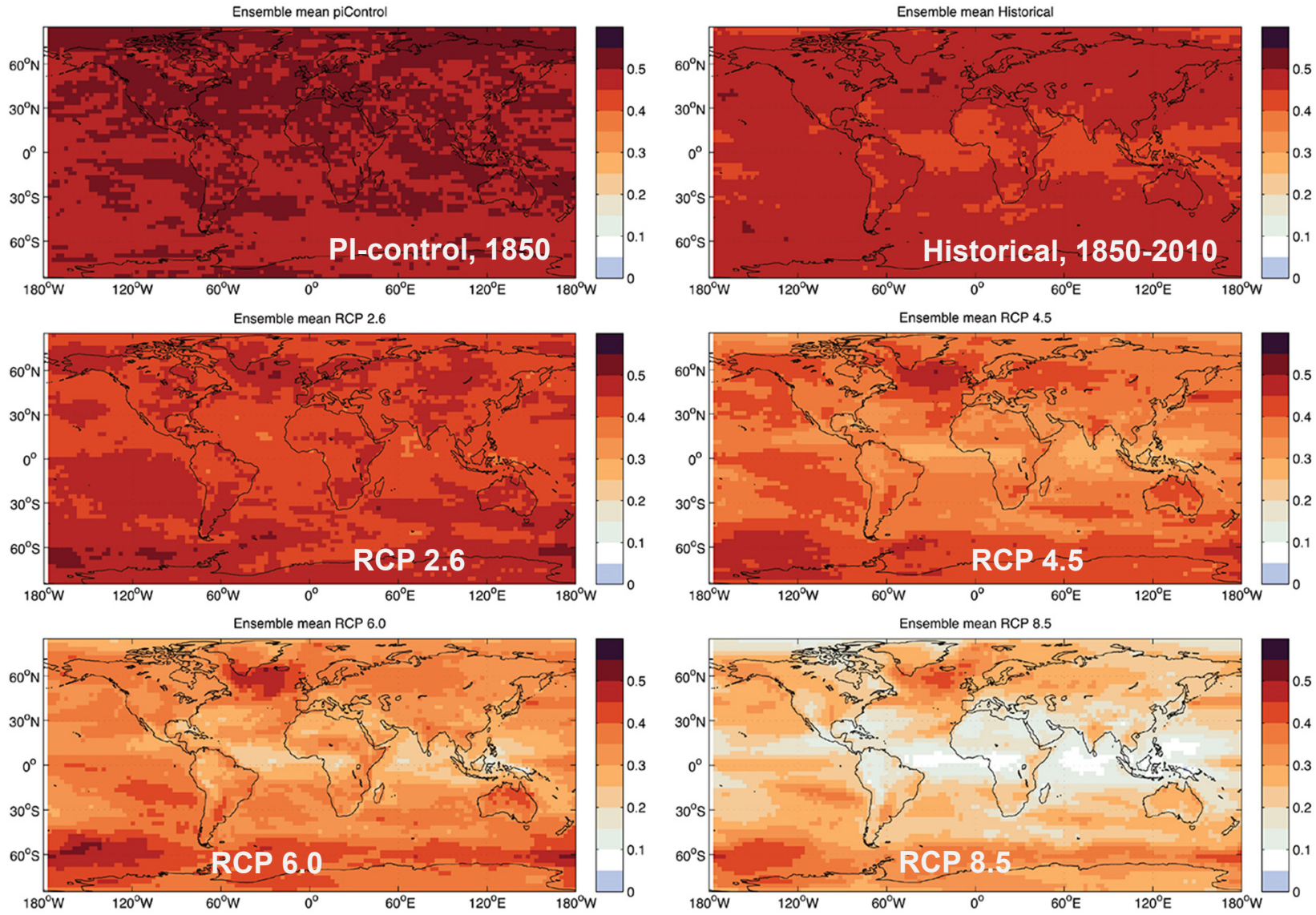

Helge Drange, UiB:

Verifying probabilistic forecasts

Renate Hagedorn

Objective of diagnostic/verification tools

Assessing the *goodness* of a forecast system involves determining skill and value of forecasts

A forecast has skill if it predicts the observed conditions well according to some objective or subjective criteria.

A forecast has value if it helps the user to make better decisions than without knowledge of the forecast.

- Forecasts with poor skill can be valuable (e.g. location mismatch)
- Forecasts with high skill can be of little value (e.g. blue sky desert)

- Characteristics of a forecast system:
  - **Consistency***: Do the observations statistically belong to the distributions of the forecast ensembles? (consistent degree of ensemble dispersion)
  - **Reliability**: Can I trust the probabilities to mean what they say?
  - **Sharpness**: How much do the forecasts differ from the climatological mean probabilities of the event?
  - **Resolution**: How much do the forecasts differ from the climatological mean probabilities of the event, and the systems gets it right?
  - **Skill**: Are the forecasts better than my reference system (chance, climatology, persistence,…)?

---

* Note that terms like consistency, reliability etc. are not always well defined in verification theory and can be used with different meanings in other contexts

- Characteristics of a forecast system:
  - **Consistency**: Do the observations statistically belong to the distributions of the forecast ensembles? (consistent degree of ensemble dispersion)

    Rank Histogram
  - **Reliability**: Can I trust the probabilities to mean what they say?
  - **Sharpness**: How much do the forecasts differ from the climatological mean probabilities of the event?
  - **Resolution**: How much do the forecasts differ from the climatological mean probabilities of the even, and the systems gets it right?

    Reliability Diagram
  - **Skill**: Are the forecasts better than my reference system (chance, climatology, persistence,…)?

    Brier Skill Score

Rank Histogram

- Rank Histograms asses whether the ensemble spread is consistent with the assumption that the observations are statistically just another member of the forecast distribution
  - Check whether observations are equally distributed amongst predicted ensemble
  - Sort ensemble members in increasing order and determine where the observation lies with respect to the ensemble members

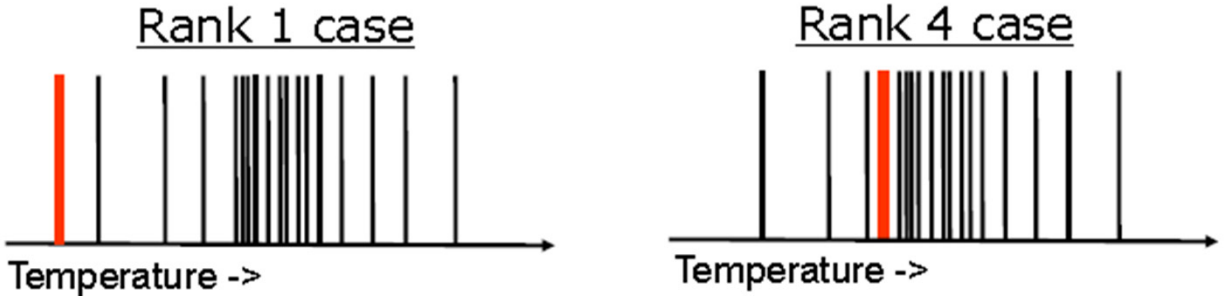

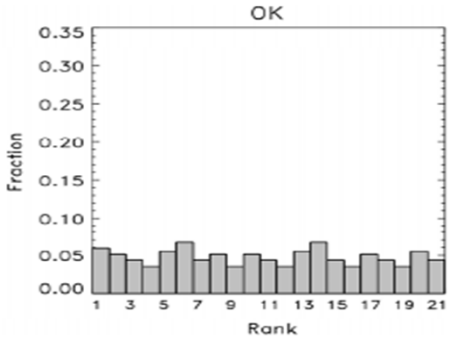

OBS is indistinguishable from any other ensemble member

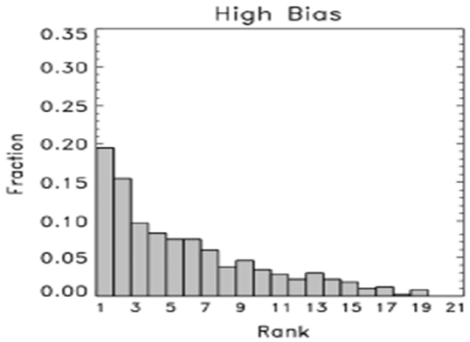

OBS is too often below the ensemble members (biased forecast)

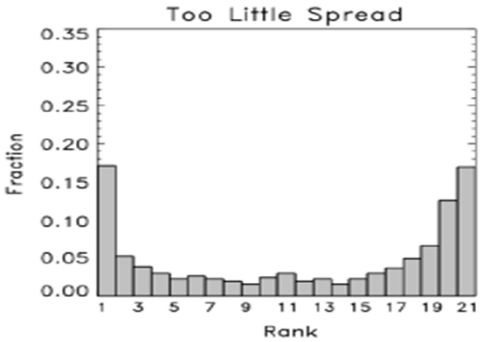

OBS is too often outside the ensemble spread

Reliability

- A forecast system is reliable if:
  - statistically the predicted probabilities agree with the observed frequencies, i.e.
  - taking all cases in which the event is predicted to occur with a probability of x%, that event should occur exactly in x% of these cases; not more and not less.
- A reliability diagram displays whether a forecast system is reliable (unbiased) or produces over-confident / under-confident probability forecasts
- A reliability diagram also gives information on the resolution (and sharpness) of a forecast system

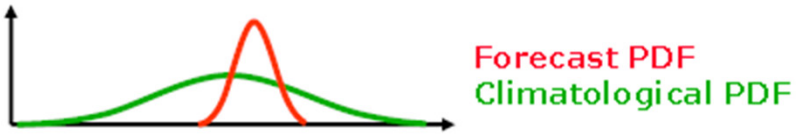

Reliability Diagram

Take a sample of probabilistic forecasts:
e.g. 30 days x 2200 GP = 66000 forecasts
How often was event (T > 25) forecasted with X probability?

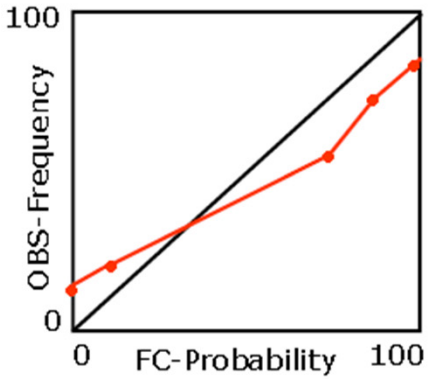

FC Prob.	# FC	"perfect FC" OBS-Freq.	"real" OBS-Freq.
100%	8000	8000 (100%)	7200 (90%)
90%	5000	4500 (90%)	4000 (80%)
80%	4500	3600 (80%)	3000 (66%)
....	....	....	....
....	....	....	....
....	....	....	....
10%	5500	550 (10%)	800 (15%)
0%	7000	0 (0%)	700 (10%)

over-confident model

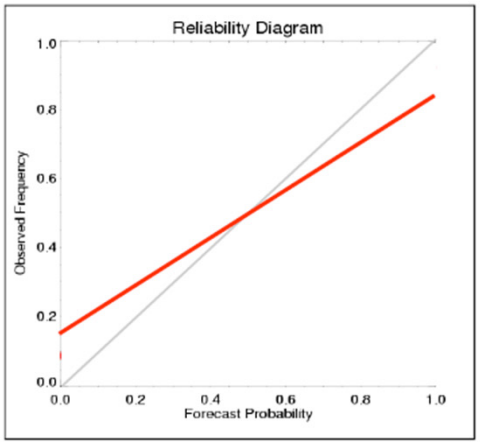

perfect model

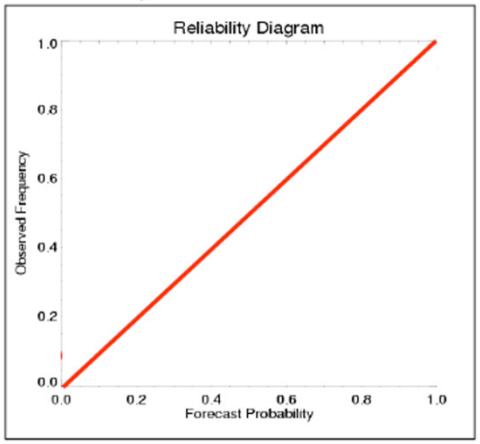

under-confident model

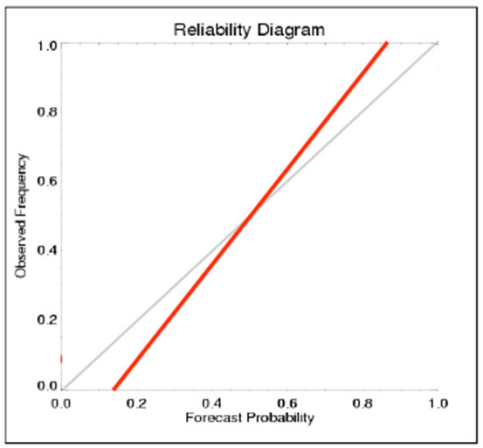

Brier Score

- The Brier score is a measure of the accuracy of probability forecasts
- Considering *N* forecast – observation pairs the BS is defined as:

$$BS = \frac{1}{N}\sum_{n=1}^{N}(p_n - o_n)^2$$

with *p*: forecast probability (fraction of members predicting event)
o: observed outcome (1 if event occurs; 0 if event does not occur)

- BS varies from 0 (perfect deterministic forecasts) to 1 (perfectly wrong!)
- BS corresponds to RMS error for deterministic forecasts

Brier Skill Score

- Skill scores are used to compare the performance of forecasts with that of a reference forecast such as climatology or persistence
- Constructed so that perfect FC takes value 1 and reference FC = 0

$$\text{Skill score} = \frac{\text{score of current FC} - \text{score for ref FC}}{\text{score for perfect FC} - \text{score for ref FC}}$$

$$BSS = 1 - \frac{BS}{BS_c}$$

- positive (negative) BSS ➢ better (worse) than reference

Components of the Brier Score

$$REL = \frac{1}{N}\sum_{i=1}^{I} n_i (f_i - o_i)^2$$

$$RES = \frac{1}{N}\sum_{i=1}^{I} n_i (o_i - c\ )^2$$

$$UNC = c(1-c\ )$$

N = total number of cases
I = number of probability bins
n_i = number of cases in probability bin i
f_i = forecast probability in probability bin I
o_i = frequency of event being observed when forecasted with f_i
c = frequency of event being observed in whole sample

- Reliability: forecast probability vs. observed relative frequencies
- Resolution: ability to issue reliable forecasts close to 0% or 100%
- Uncertainty: variance of observations frequency in sample

Brier Score = Reliability – Resolution + Uncertainty

Reliability diagram

Reliability score (the smaller, the better)
Resolution score (the bigger, the better)

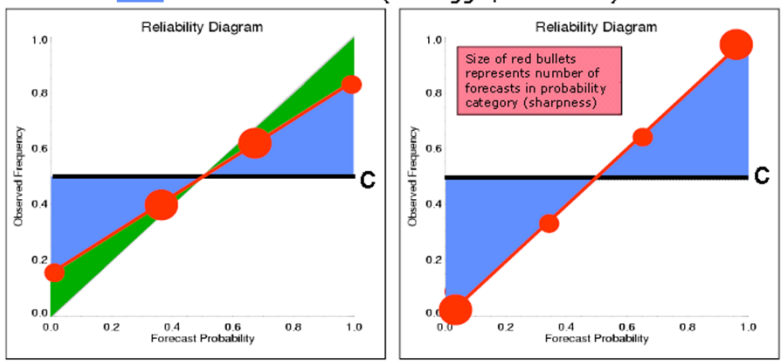

Poor resolution

Good resolution

Ranked Probability Score

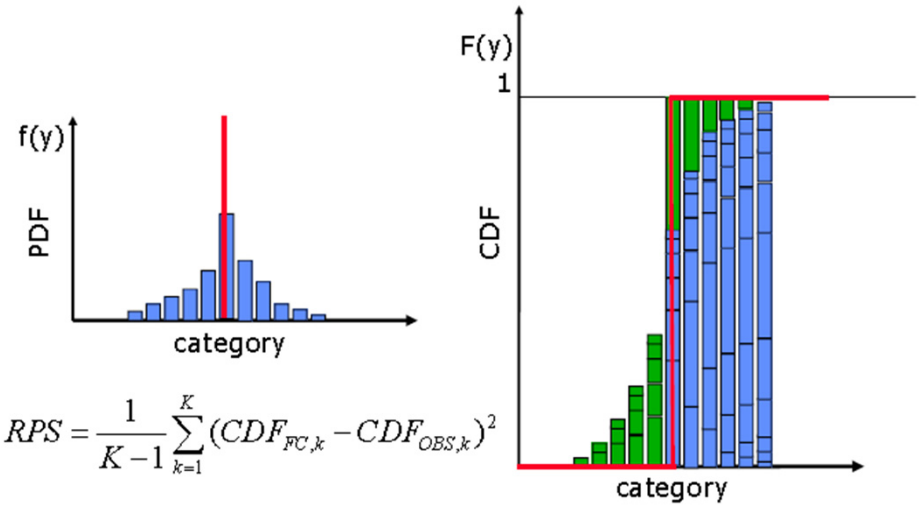

$$RPS = \frac{1}{K-1}\sum_{k=1}^{K}(CDF_{FC,k} - CDF_{OBS,k})^2$$

- Measures the quadratic distance between forecast and verification probabilities for several probability categories *k*
- Emphasizes accuracy by penalizing large errors more than "near misses"
- Rewards sharp forecast if it is accurate
- It is the average Brier score across the range of the variable

$$RPS = \frac{1}{K-1}\sum_{k=1}^{K} BS_k$$

- Ranked Probability Skill Score (RPSS) is a measure for skill relative to a reference forecast

$$RPSS = 1 - \frac{RPS}{RPS_c}$$

Benefits for different users - decision making

- A user (or "decision maker") is sensitive to a specific weather event
- The user has a choice of two actions:
  - do nothing and risk a potential loss L if weather event occurs
  - take preventative action at a cost C to protect against loss L
- Decision-making depends on available information:
  - no FC information: either always take action or never take action
  - deterministic FC: act when adverse weather predicted
  - probability FC: act when probability of specific event exceeds a certain threshold **(this threshold depends on the user)**
- Value V of a forecast:
  - savings made by using the forecast, normalized so that
    - V = 1 for perfect forecast
    - V = 0 for forecast not better than climatology

Ref: D. Richardson, 2000, QJRMS

Decision making: the cost-loss model

Potential costs		Event occurs	
		Yes	No
Action taken	Yes	C	C
	No	L	0

Fraction of occurences		Event occurs	
		Yes	No
Event forecast	Yes	a	b
	No	c	d
		$\bar{o}$	1-$\bar{o}$

- Climate information – expense: $E_C = \min(C, \bar{o}L)$
- Perfect forecast – expense: $E_P = \bar{o}C$
- Always use forecast – expense: $E_F = aC + bC + cL$
- Value: $$V = \frac{\text{saving from using forecast}}{\text{saving from perfect forecast}} = \frac{E_C - E_F}{E_C - E_P}$$

Decision making: the cost-loss model

$$V = \frac{\text{saving from using forecast}}{\text{saving from perfect forecast}} = \frac{E_C - E_F}{E_C - E_P}$$

$$= \frac{\min(C, \bar{o}L) - (aC + bC + cL)}{\min(C, \bar{o}L) - \bar{o}C}$$

$$= \frac{\min(\alpha, \bar{o}) - F(1-\bar{o})\alpha + H\bar{o}(1-\alpha) - \bar{o}}{\min(\alpha, \bar{o}) - \bar{o}\alpha}$$

with: α = C/L
H = a/(a+c)
F = b/(b+d)
$\bar{o}$ = a+c

- For given weather event and FC system: $\bar{o}$, H and F are fixed
- value depends on C/L
- max if: C/L = $\bar{o}$
- V_{max} = H-F

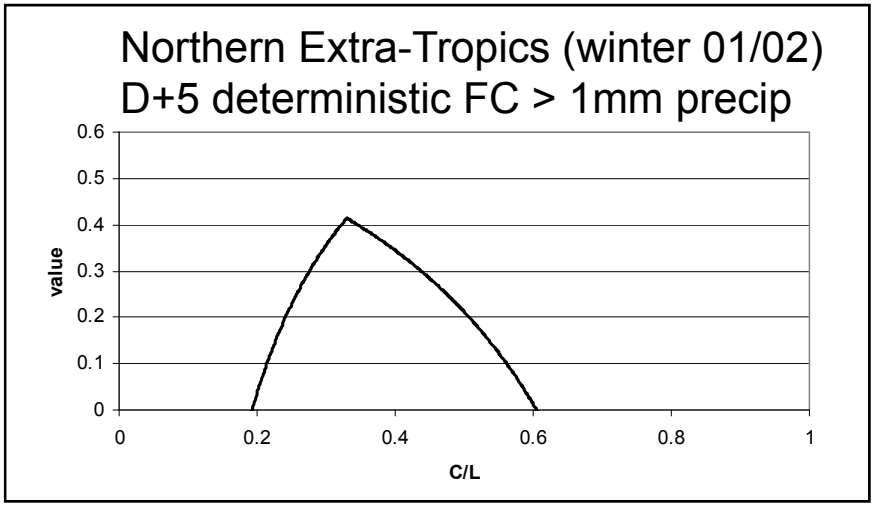

Potential economic value

Northern Extra-Tropics (winter 01/02) D+5 FC > 1mm precipitation

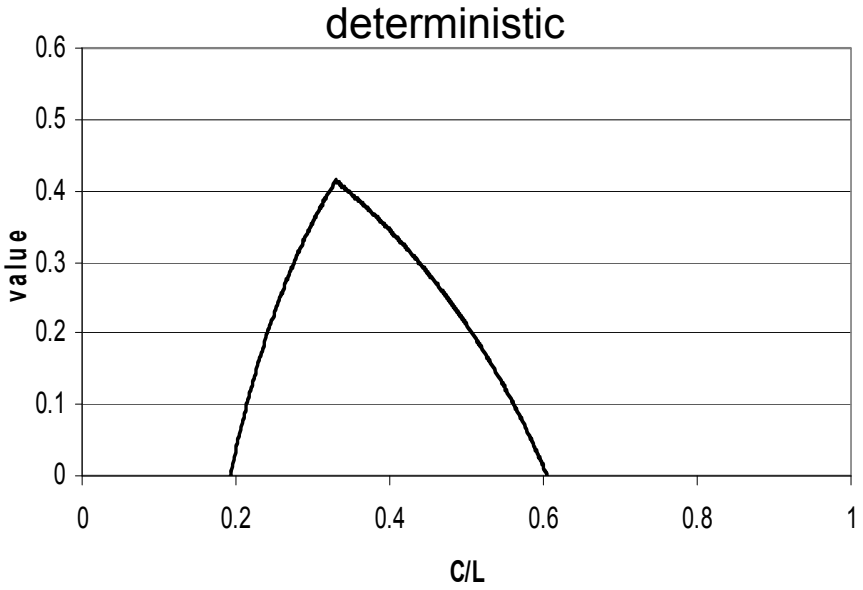

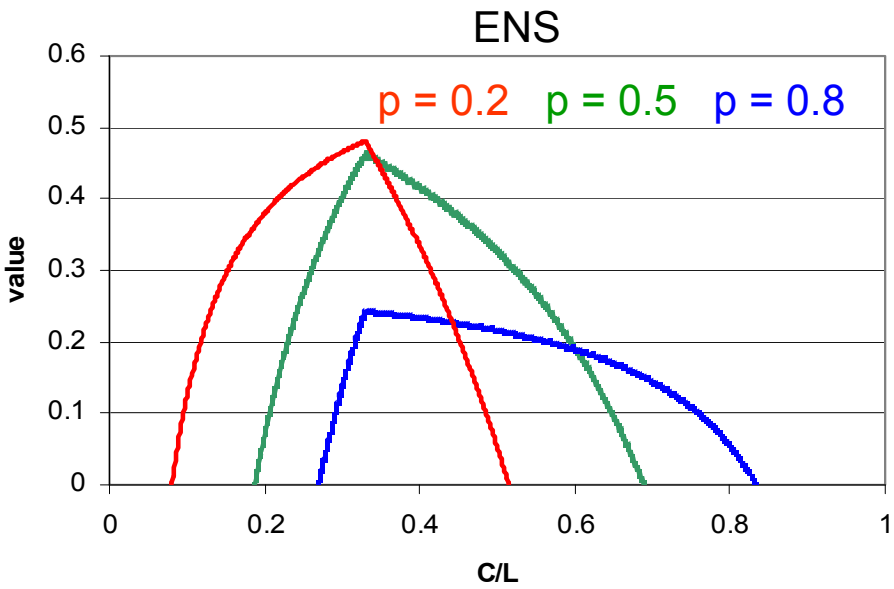

ENS: when each user chooses
the most appropriate probability threshold

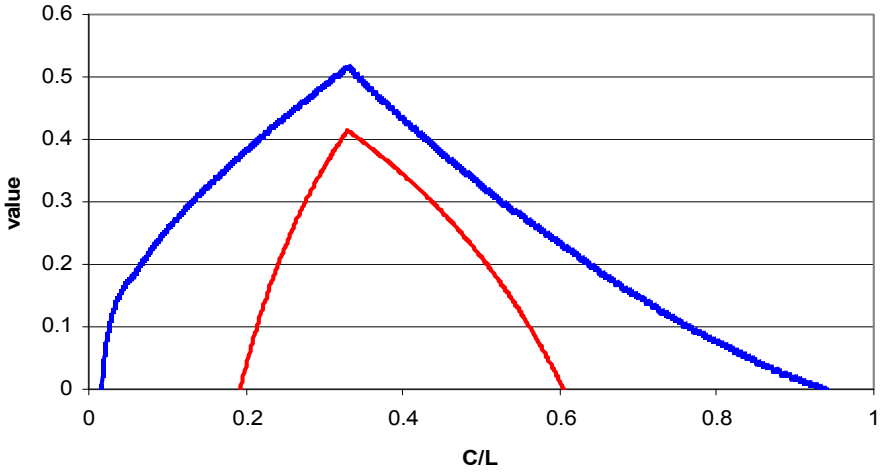

Brier Skill Score, Europe

T2m

Anomaly: >8K >4K <-4K <-8K

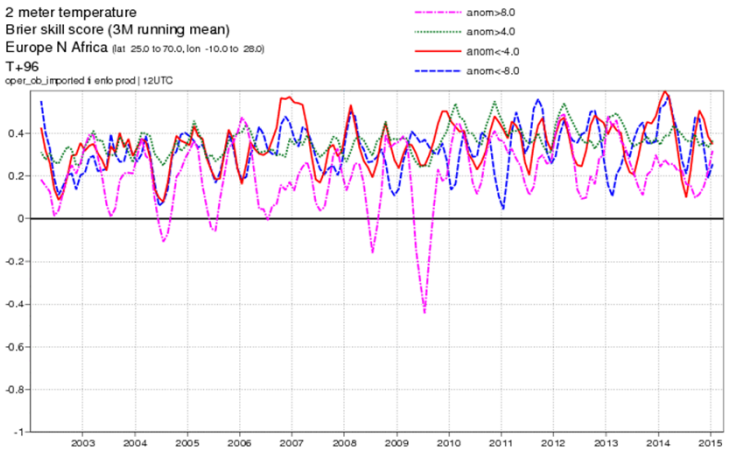

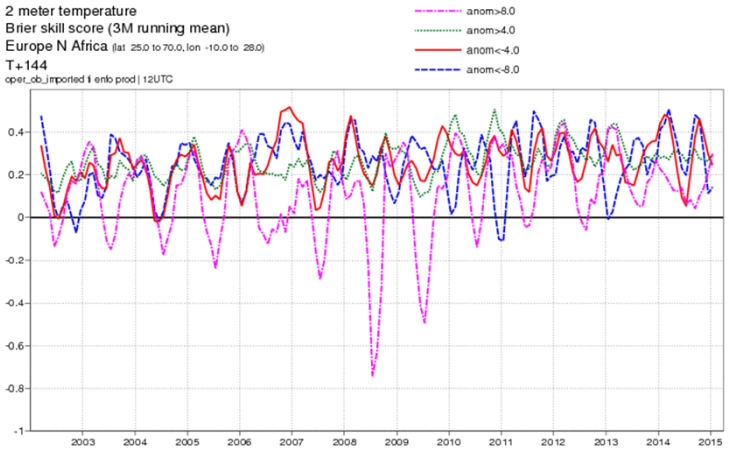

Prec24

Anomaly: >20mm >10mm >5mm >1mm

+96h

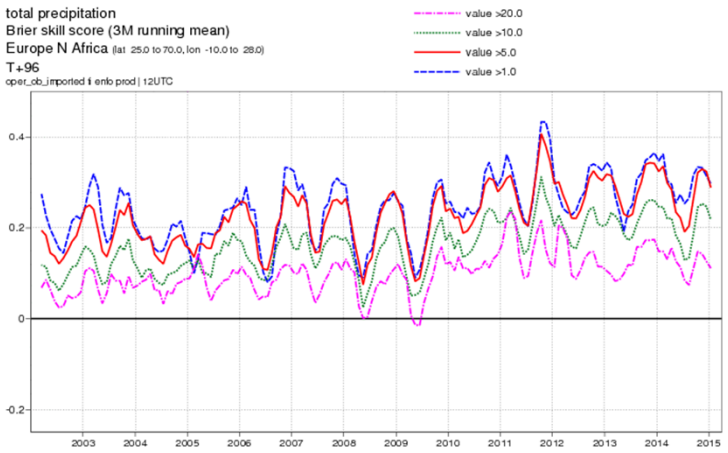

+144h

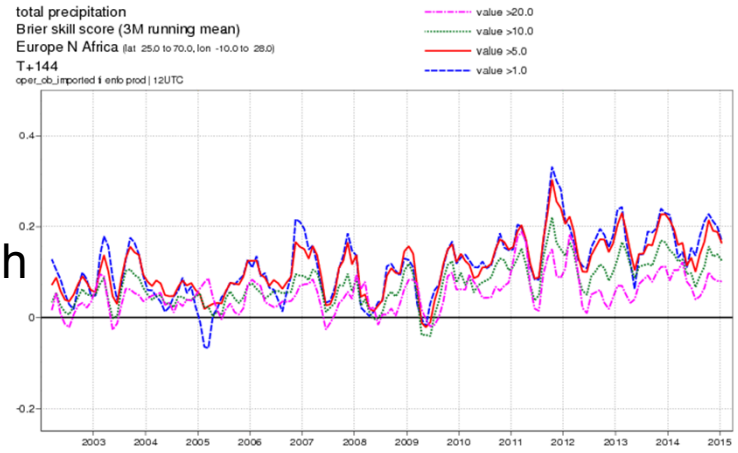

Brier Skill Score, +96h, starting from 1995. Against Analyses and observations in Europe

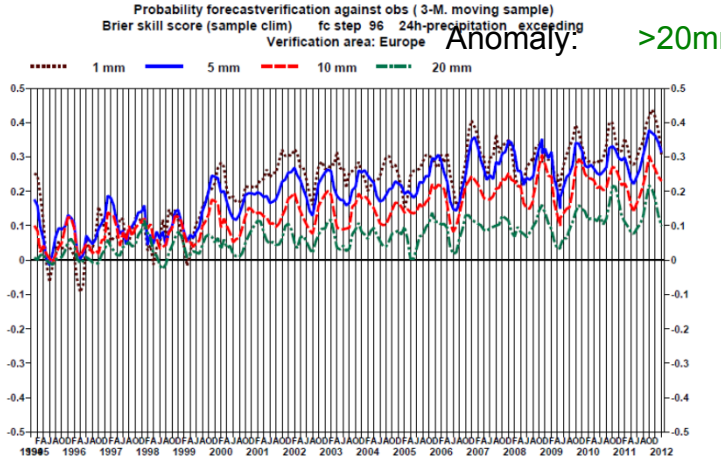

Anomaly: >20mm >10mm >5mm >1mm

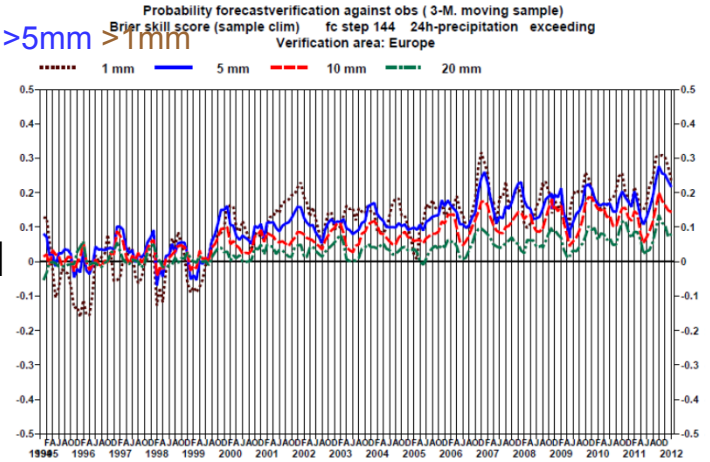

24h N obs

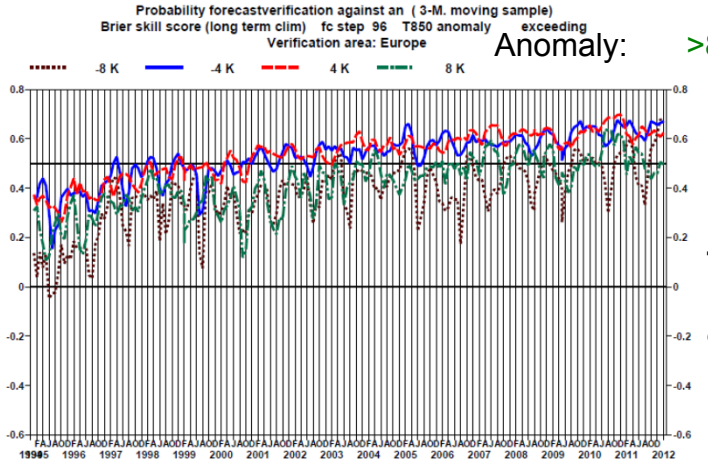

Anomaly: >8K >4K <-4K <-8K

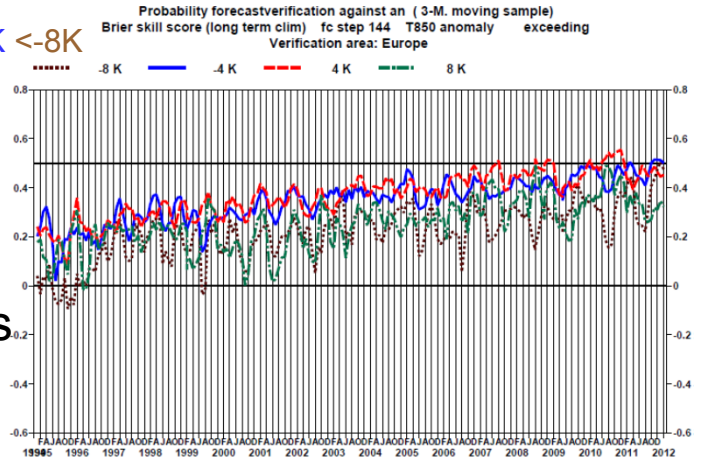

T850 analyses

+96h

+144h

Brier Skill Score, against analyses and observations in Europe. Wind speed, 10m.

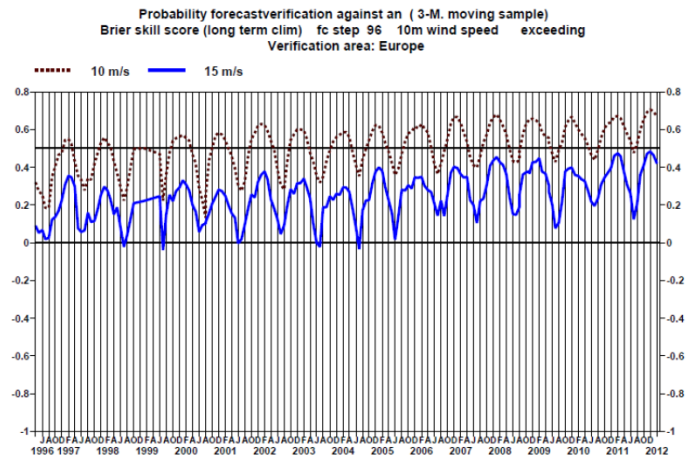

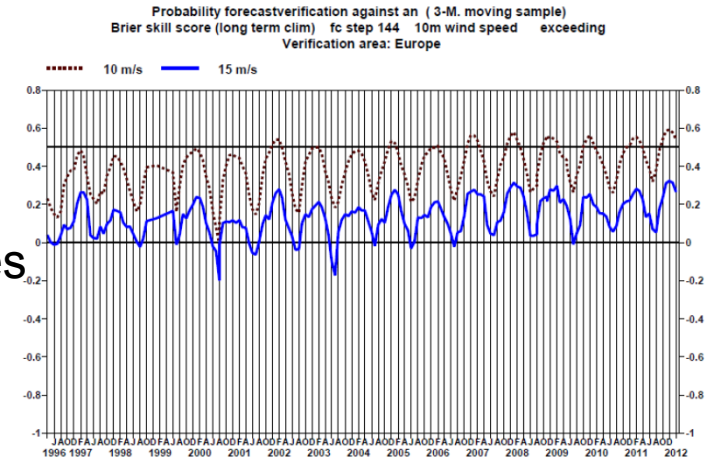

analyses

>15m/s

>10m/s

obs

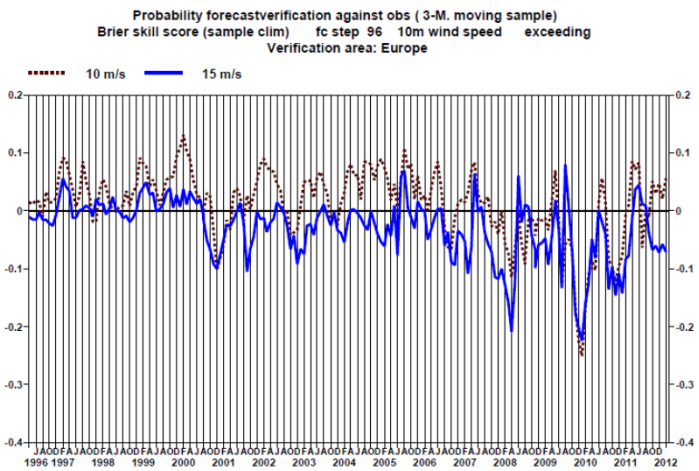

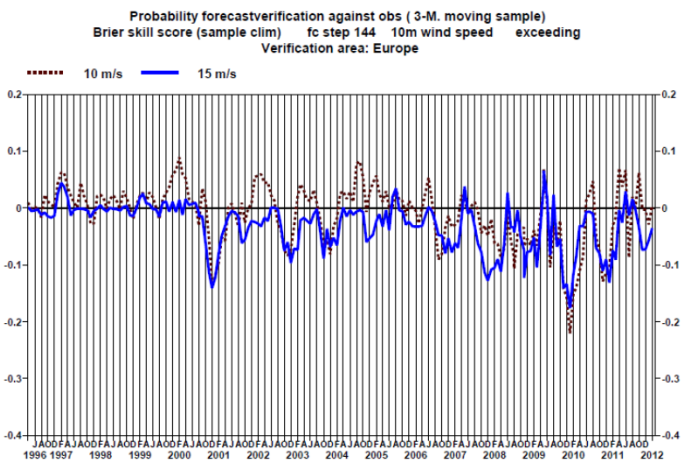

+96h

+144h

The forecast length (days) when CRPSS reaches smaller values than a given threshold for 24h precip and T 850hPa for NH and Europe

Precip
0.1
12m MA

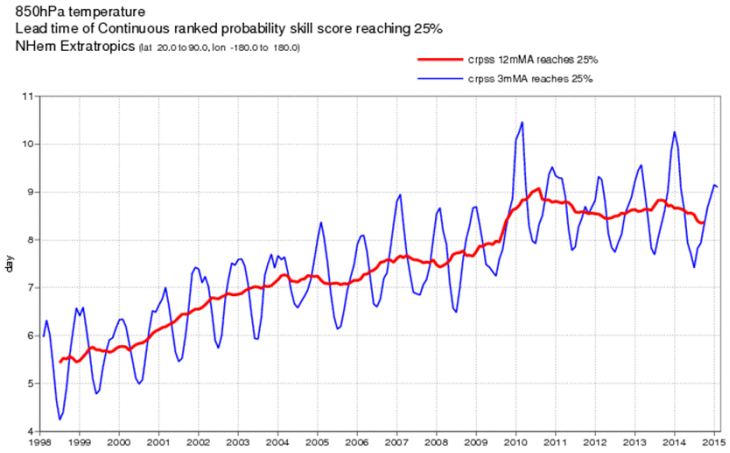

T 850
0.25
3m MA
12m MA

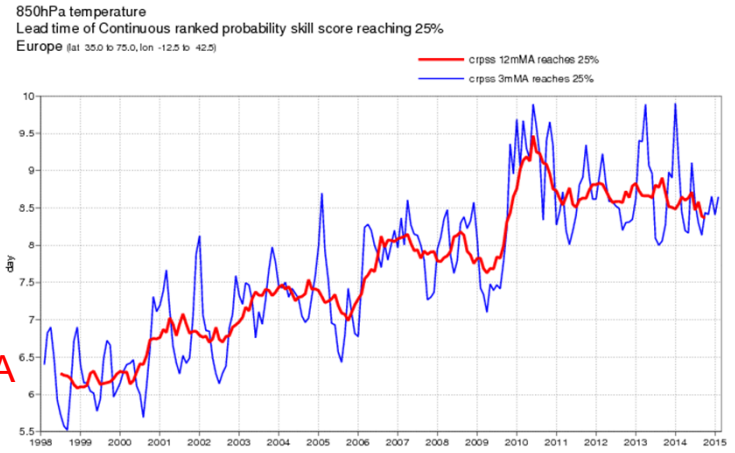

NH Extratropics

Europe

Reliability-diagram and forecast sharpness, winter 2015

ff10m

+96h

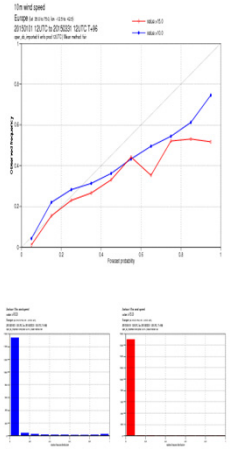

>15m/s

>10m/s

+144h

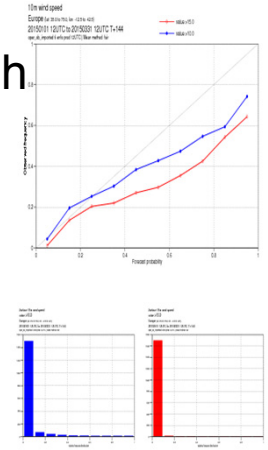

+240h

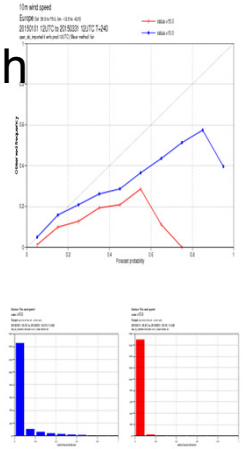

Precip

>20mm >10mm >5mm >1mm

+96h

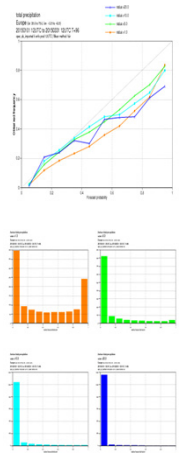

+144h

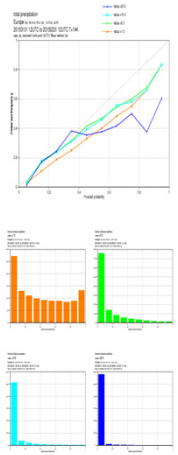

+240h

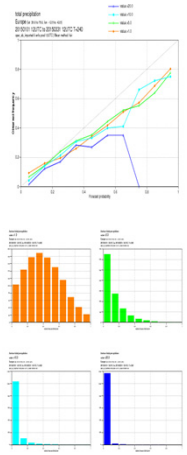

Reliability-diagram and forecast sharpness, winter 2015

T2m

>8K >4K <-4K <-8K

+96h

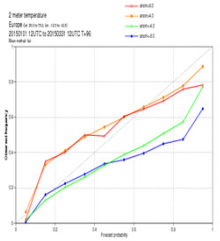

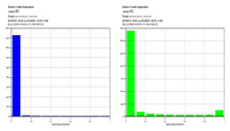

+144h

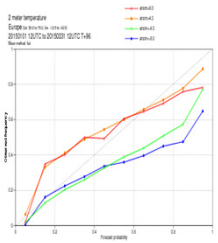

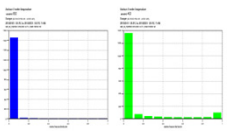

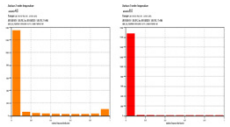

+240h

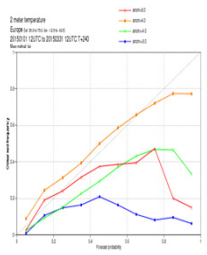

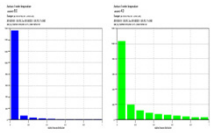

Expected Value of + 144h forecasts of 24h precipitation in Europe with user's c/L. Winter 2015

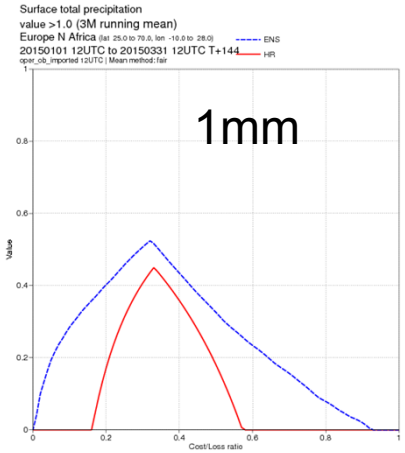

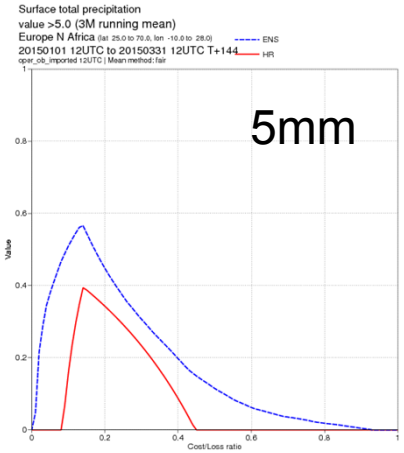

ENS

HighRes